Search for the neutral Higgs boson in $H \to WW^* \to l\nu l\nu$ decays with the ATLAS experiment

Phuong Nguyen Dang

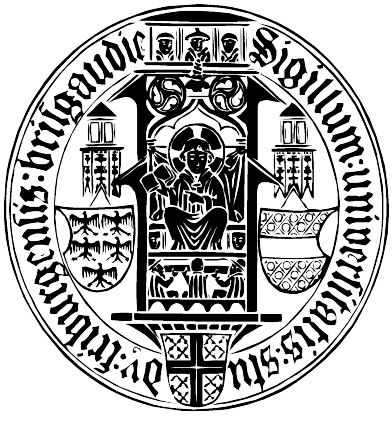

Freiburg 2016

Search for the neutral Higgs boson in $H \to WW^* \to l\nu l\nu$ decays with the ATLAS experiment

Phuong Nguyen Dang

Dissertation
an der Fakultät für Mathematik und Physik
der Albert–Ludwigs–Universität
Freiburg im Breisgau

vorgelegt von
Phuong Nguyen Dang

Freiburg, den 27.10.2016

Dekan:	Prof. Dr. Gregor Herten
Referent:	Prof. Dr. Karl Jakobs
Koreferent:	Prof. Dr. Marc Schumann
Prüfer:	Prof. Dr. Karl Jakobs
	Prof. Dr. Markus Schumacher
	Prof. Dr. Harald Ita

Tag der mündlichen Prüfung: 22.21.2016

Contents

1 Introduction **1**

2 Theoretical Overview **3**

2.1 The Standard Model of Particle Physics . . . 3

2.1.1 Elementary Particles and Interactions . . . 3

2.1.2 Symmetry and Gauge Invariance . . . 5

2.1.3 Electromagnetic Interactions . . . 5

2.1.4 Strong Interactions . . . 7

2.1.5 Weak Interactions and Electroweak Unification . . . 8

2.2 The Higgs Mechanism . . . 10

2.2.1 Spontaneous Symmetry Breaking . . . 10

2.2.2 Higgs Couplings to Fermions . . . 12

2.3 The Standard Model Higgs Boson at the LHC . . . 13

2.3.1 Proton-Proton Collision . . . 13

2.3.2 Luminosity . . . 15

2.3.3 Standard Model Cross Sections at LHC . . . 15

2.3.4 Higgs Boson Production . . . 16

2.3.5 Higgs Boson Decay Modes . . . 19

3 The Large Hadron Collider and ATLAS Detector **21**

3.1 The Large Hadron Collider . . . 21

3.1.1 Data Taking at LHC . . . 22

3.2 The ATLAS Detector . . . 24

3.2.1 ATLAS Coordinate System . . . 24

3.2.2 Inner Detector . . . 26

3.2.3 Calorimeter System . . . 28

3.2.4 Muon Spectrometer . . . 31

3.2.5 Trigger System . . . 32
3.2.6 Luminosity Measurement . . . 33

4 Event Reconstruction and Object Identification 35
4.1 Track and Vertex Reconstruction . . . 35
4.1.1 Track Reconstruction . . . 35
4.1.2 Primary Vertex Reconstruction . . . 36
4.2 Electron Reconstruction and Identification . . . 36
4.2.1 Electron Reconstruction . . . 36
4.2.2 Electron Identification . . . 37
4.2.3 Electron Isolation . . . 37
4.3 Muon Reconstruction and Identification . . . 39
4.3.1 Muon Reconstruction and Identification . . . 39
4.3.2 Muon Identification . . . 40
4.3.3 Muon Isolation . . . 40
4.4 Jet Reconstruction and Identification . . . 42
4.4.1 Jet Reconstruction . . . 42
4.4.2 b-Jet Identification . . . 43
4.5 Missing Transverse Momentum . . . 46
4.6 Overlap Removal . . . 47

5 Search for the Higgs Boson in the $H \to WW^* \to l\nu l\nu$ Decay Mode using $\sqrt{s} = 7$ TeV and 8 TeV Data from the LHC Run 1 49
5.1 Physics Process of the $H \to WW^* \to l\nu l\nu$ Decay Mode . . . 49
5.1.1 Signature of the $H \to WW^* \to l\nu l\nu$ Decay Mode . . . 49
5.1.2 Background Processes . . . 51
5.2 Run 1 Data and Simulation Samples . . . 53
5.2.1 Data Samples . . . 53
5.2.2 Simulation Samples . . . 55
5.3 Event Selection and Background Determination . . . 57
5.3.1 Object Selection . . . 57
5.3.2 Selection of $H \to WW^* \to l\nu l\nu$ Candidate Events . . . 60
5.3.3 Background Estimations . . . 66
5.4 Systematic Uncertainties . . . 72
5.4.1 Theoretical Uncertainties . . . 73
5.4.2 Experimental Uncertainties . . . 75
5.4.3 Uncertainties on backgrounds normalization . . . 75
5.5 Statistical Treatment . . . 76
5.6 Results of the Run 1 Analysis . . . 77
5.6.1 Fit results . . . 77
5.6.2 Observation of the $H \to WW^* \to l\nu l\nu$ decay mode . . . 82

5.6.3 Higgs couplings to fermions and vector bosons 84
5.6.4 Exclusion limits 85
5.6.5 Higgs production cross sections 85

6 Estimation of W + jets Background in the Run 1 Analysis with the Matrix Technique 89
6.1 Methodology 90
6.1.1 Basic ideas 90
6.1.2 Matrix technique for estimating the W + jets background in the $H \to WW^* \to l\nu l\nu$ analysis 93
6.1.3 Matrix equations for the $\mu\mu$ channel 94
6.1.4 Matrix equations for the $e\mu$ and μe channels 95
6.1.5 Matrix equations for the ee channel 95
6.2 Application of the matrix method 96
6.2.1 Datasets and event selection 96
6.2.2 Monte Carlo closure test 96
6.3 Systematic uncertainties 101
6.3.1 $\mu\mu$ channel 101
6.3.2 $e\mu$ channel 102
6.3.3 μe channel 102
6.3.4 ee channel 102
6.3.5 Total systematic uncertainty 102
6.4 Data extraction results and comparison with the alternative fake factor method 103
6.4.1 $\mu\mu$ channel 104
6.4.2 $e\mu$ channel 104
6.4.3 μe channel 105
6.4.4 ee channel 105

7 Search for the $H \to WW^* \to l\nu l\nu$ Decays in the Gluon-Fusion Channel using $\sqrt{s} = 13$ TeV Data from the LHC Run 2 107
7.1 Data and Monte Carlo Samples 107
7.1.1 Data Samples 107
7.1.2 Monte Carlo Samples 108
7.2 Object Selection 111
7.2.1 Event Selection 111
7.2.2 Lepton Selection 111
7.2.3 Optimization of Lepton Isolation 111
7.2.4 Jet Selection 113
7.2.5 Optimization of b-tagging 113
7.2.6 Missing Transverse Momentum 114

7.3 ggF Analysis . . . 115
7.3.1 Analysis Overview . . . 115
7.3.2 Validation of the Selection Criteria . . . 116
7.3.3 Selection of $H \to WW^* \to l\nu l\nu$ Candidate Events . . . 119
7.3.4 Background Estimation . . . 125
7.3.5 Normalization Factors . . . 126
7.4 Systematic Uncertainties . . . 140
7.4.1 Theoretical Uncertainties . . . 140
7.4.2 Experimental Uncertainties . . . 143
7.5 Results of the Run-2 Analysis . . . 144
7.5.1 Summary of the Event Selection . . . 144
7.5.2 Fit Procedure . . . 144
7.5.3 Performance of the Fit . . . 150
7.5.4 Results . . . 157
7.5.5 Discussion of the Results . . . 157

8 Summary **161**

A Additional plots for the matrix method **163**

B Additional plots at pre-selection level **179**

Acknowledgements **192**

1 Introduction

The Standard Model of particle physics is a theory which describes the elementary particles and their interactions. Although the Standard Model describes many experimental results with high accuracy, it still has weaknesses. The three electroweak bosons ($W^{\pm}$ and Z^0) were discovered experimentally in 1983. The ratio of their masses was found to be as predicted in 1968 by S. Glashow, A. Salam and S. Weinberg. However, adding simple mass terms for the W and Z bosons to the equations of the Standard Model would violate its gauge symmetries and are thus forbidden. A mechanism was proposed in 1964 by R. Brout, F. Englert and P. Higgs as the simplest solution to attribute mass not only to the $W^{\pm}$ and Z^0 bosons but also to quarks and leptons while preserving the gauge symmetries of the Standard Model. This theoretical model, known as the *"Englert-Brout-Higgs mechanism"* or *"Higgs mechanism"*, indicates the existence of one additional particle, the *Higgs boson*. This particle is an excitation of a quantum field (*Higgs field*) which causes *spontaneous symmetry breaking* of the electroweak symmetry of the vacuum. Since the 1980s, many experimental searches for the Higgs boson were carried out at LEP and Tevatron but without success.

The *Large Hadron Collider* (LHC) was built by the *European Organization for Nuclear Research* (CERN) between 1998 and 2008 with the major motivation of searching for the Higgs boson. Two multi-purpose detector systems, ATLAS (*A Toroidal LHC ApparatuS*) and CMS (*Compact Muon Solenoid*), were installed at the LHC to search independently for the Higgs boson and new phenomena beyond the Standard Model. The Higgs boson is produced at the LHC mainly via the gluon fusion and vector-boson fusion processes. The decay of the Higgs boson into a W boson pair, which subsequently decays into leptons and neutrinos, provides a sensitive signature of the Higgs boson and subsequent determinations of its properties.

In this thesis, a search for the Higgs boson produced in the gluon fusion production mode and decaying in the $H \to WW^* \to l\nu l\nu$ channel is presented. The data used for this search were collected by the ATLAS detector in two periods: the first period

(Run 1) during the years 2011−2012 with a centre-of-mass energy of 7 TeV and 8 TeV, respectively; and the second one during the years 2015−2016 with a centre-of-mass energy of 13 TeV. The main focus of this thesis is on the data-driven estimation of the W + jets background using a so-called matrix technique in Run 1. In the final signal region, this background is as large as the expected signal contribution and furthermore has a very similar shape distribution in the final observable. Therefore, it is very important to reliably determine the shape and normalization of the W+jets background in the signal region. This thesis proposes a new method which provides a way to determine the W+jets background with smaller systematic uncertainties compared to the prediction used previously. Furthermore, in Run 2 the measurement of the Higgs boson signal strength in the $H \to WW^* \to l\nu l\nu$ decay channel produced via gluon fusion is investigated for the first time. Several studies on object and topology selection criteria optimization, signal-free control regions and signal-strength extraction were done and are presented in this thesis.

The structure of this thesis is as follows: a theoretical overview on the Standard Model, Higgs mechanism and Higgs boson production at the LHC is presented in Chapter 2. The experimental setup, the LHC and the ATLAS experiment are described in Chapter 3. The event reconstruction and object definition which are relevant for the $H \to WW^* \to l\nu l\nu$ analysis are described in Chapter 4. The search for the Higgs boson in the $H \to WW^* \to l\nu l\nu$ decay channel is presented in Chapter 5. This Run-1 search is based on data corresponding to integrated luminosities of 4.5 fb^{-1} and 20.3 fb^{-1} collected at centre-of-mass energies of 7 TeV and 8 TeV, respectively. A dedicated study of the matrix technique for the estimation of the W+jets background in Run 1 is presented in Chapter 6. For Run 2, the analysis of the gluon fusion production mode with the subsequent $H \to WW^* \to l\nu l\nu$ decay is discussed in Chapter 7. The first results of this analysis correspond to an integrated luminosity of 5.8 fb^{-1} at a centre-of-mass energy of 13 TeV. The thesis closes with a final summary given in Chapter 8.

2

Theoretical Overview

This chapter gives a brief introduction to the Standard Model of particle physics and the mathematical description of the Higgs mechanism. At the beginning, an introduction to quantum field theory and to the Standard Model of particle physics is given in Section 2.1, based on the detailed description presented in Refs. [1–4]. Then the motivation, predicted production and decay modes of the corresponding Higgs boson are discussed in Section 2.2. Furthermore, the phenomenological aspects of proton-proton collisions and the predicted cross sections of Higgs boson production are also presented in Section 2.3.

2.1 The Standard Model of Particle Physics

The Standard Model (SM) of particle physics is a theory which describes the elementary particles and their interactions, based on the symmetry group $SU(3) \otimes SU(2) \otimes U(1)$. This theory was developed in the second half of the 20th century, by incorporating the Glashow-Weinberg-Salam theory (electro-weak interaction) with quantum chromodynamics (strong interaction).

In the Standard Model, particle masses are introduced by an idea known as the *"Englert-Brout-Higgs mechanism"* or simply *"Higgs mechanism"*. It gives rise to the appearance of a scalar particle which is called *"Higgs boson"*. The Standard Model is very successful in describing particle physics experiments with high precision. It should be noted that gravity is not included into a quantum field theory so far. It also does not play a significant role at the current experimental particle interaction energies.

2.1.1 Elementary Particles and Interactions

The particles considered as elementary particles are those which do not appear to have any further substructure. In the Standard Model, these particles are known as *leptons*

and *quarks*. Each particle is characterized by a unique set of quantum numbers. They are organized in a three-fold family structure of increasing mass shown in Table 2.1.

Table 2.1: Overview of known lepton and quark families in the Standard Model (the masses are taken from Ref. [5]).

	Particle	Symbol	Mass	Charge [e]
Leptons	Electron	e	0.511 MeV	± 1
	Muon	μ	105.7 MeV	± 1
	Tau	τ	1.777 GeV	± 1
	Electron neutrino	ν_e	< 2 eV	0
	Muon neutrino	ν_μ	< 0.19 MeV	0
	Tau neutrino	ν_τ	< 18.2 MeV	0
Quarks	Up	u	$2.3^{+0.7}_{-0.5}$ MeV	$+2/3$
	Down	d	$4.8^{+0.5}_{-0.3}$ MeV	$-1/3$
	Charm	c	1.28 ± 0.03 GeV	$+2/3$
	Strange	s	95 ± 5 MeV	$-1/3$
	Top	t	$173.21 \pm 0.51 \pm 0.71$ GeV	$+2/3$
	Bottom	b	4.18 ± 0.03 GeV	$-1/3$

There are six types of leptons and six types of quarks. Each of them has its own antiparticle with the same mass but opposite charge quantum number. All fermions take part in the weak interaction while only quarks take part in the strong interaction since they carry so-called *colour charge*. Quarks and charged fermions also participate in the electromagnetic interactions.

All stable matter is made up of the first generation quarks (up and down quarks) and electrons. The others are unstable and decay into lighter particles. And it should be noted that quarks do not exist as free particles but are confined within hadrons containing either a quark and an anti-quark (mesons) or three quarks (baryons) due to the strong interaction.

In the Standard Model, neutrinos are considered as massless particles, but many recent experiments have shown that neutrinos have small but non-zero masses. However, since their masses are tiny, they still do not affect much the predictions of the Standard Model.

All interactions in Standard Model (strong, weak and electromagnetic interactions) are mediated by bosons, which are listed in Table 2.2. The bosons for strong interaction are gluons which couple to the colour charges of quarks. The boson for the electromagnetic interaction is photon. The weak interaction is mediated by three bosons, $W^\pm$ and Z^0.

Table 2.2: Overview of known bosons of the Standard Model that mediate the strong, electromagnetic and weak interactions (Ref. [5]).

Particle	Symbol	Mass	Charge [e]	Interaction
Gluon	g	0 (theoretical)	0	Strong
Photon	γ	$< 10^{-18}$ eV	$< 10^{-46}$	Electromagnetic
W boson	W	80.385 ± 0.015 GeV	± 1	Weak
Z boson	Z	91.188 ± 0.002 GeV	0	Weak

All fermions and bosons discussed so far have been observed experimentally in high energy physics experiments over the last decades [5].

2.1.2 Symmetry and Gauge Invariance

In physics, an invariant is a property of a system which remains unchanged under some transformation [6]. For example, if a system is invariant under translations in space, its momentum is conserved. The connection between symmetries and conservation laws is known as Noether's theorem. This principle is also extended to quantum physics where symmetries are described by groups.

In quantum field theory, particles are described as excited states of an underlying physical field. The dynamics of the fields (particles) are determined by a Lorentz-invariant Lagrangian $\mathcal{L}$, which yields the action

$$S = \int d^4x \mathcal{L} \tag{2.1}$$

The equations of motion can be determined by minimizing this action. The structure of the Lagrangian can be derived using symmetry arguments under which the equations of motion are invariant. The interaction Lagrangian of the Standard Model may be written as the sum of two parts

$$\mathcal{L}_{SM} = \mathcal{L}_{QCD} + \mathcal{L}_{EW}, \tag{2.2}$$

where $\mathcal{L}_{QCD}$ represents quantum chromodynamics and $\mathcal{L}_{EW}$ representing the electroweak part.

2.1.3 Electromagnetic Interactions

The electromagnetic interaction Lagrangian $\mathcal{L}_{QED}$ can be derived from the Lagrangian describing a free Dirac fermion with mass m

$$\mathcal{L}_{free} = \bar{\psi}(i\gamma^\mu \partial_\mu - m)\psi \tag{2.3}$$

where ψ is the spinor field representing fermions and γ^μ denotes the *Dirac γ-matrices*.

The $\mathcal{L}_{free}$ is invariant under a global U(1) gauge transformation

$$\psi(x) \to \psi'(x) = e^{iQ\theta}\psi(x) \tag{2.4}$$

where $Q\theta$ is an arbitrary real constant, Q is the electromagnetic charge and θ is the phase.

However, the free Lagrangian is not invariant under local phase transformation where the phase depends on the space-time coordinate such that $\theta = \theta(x)$. The necessary and sufficient condition for the system to be also invariant under local transformations is to introduce a new vector field $A_\mu(x)$, transforming as

$$A_\mu(x) \to A'_\mu(x) = A_\mu(x) - \frac{1}{e}\partial_\mu\theta \tag{2.5}$$

and to define the covariant derivative as

$$\partial_\mu \to D_\mu = \partial_\mu + ieQA_\mu(x), \tag{2.6}$$

which has the required property of transforming like the field itself.

The Lagrangian now becomes

$$\begin{aligned}\mathcal{L} &= i\bar{\psi}(x)\gamma^\mu D_\mu\psi(x) - m\bar{\psi}(x)\psi(x) \\ &= \mathcal{L}_{free} - eQA_\mu(x)\bar{\psi}(x)\gamma^\mu\psi(x).\end{aligned} \tag{2.7}$$

It is now invariant under local phase transformation.

The vector field A_μ may be interpreted as the photon field which couples to fermions with charge $-Q$. An additional term corresponding to the kinetic energy of the photon,

$$\mathcal{L}_{kin} = -\frac{1}{4}F_{\mu\nu}(x)F^{\mu\nu}(x), \tag{2.8}$$

can be added. This term needs to be invariant under the same local phase transformation as A_μ, so it is defined as

$$F_{\mu\nu} = \partial_\mu A_\nu - \partial_\mu A_\nu. \tag{2.9}$$

Thus, the requirement of local phase invariance on the free fermion Lagrangian leads to the Lagrangian of *quantum electrodynamics* (QED)

$$\mathcal{L}_{QED} = \underbrace{\bar{\psi}(i\gamma^\mu\partial_\mu - m)\psi}_{\text{Kinetic energy and mass of } \psi(x)} \underbrace{- eQA_\mu(x)\bar{\psi}(x)\gamma^\mu\psi(x)}_{\text{Interaction}} \underbrace{- \frac{1}{4}F_{\mu\nu}(x)F^{\mu\nu}(x)}_{\text{Kinetic energy of } A_\mu} \tag{2.10}$$

The addition of a mass term $\frac{1}{2}m^2 A_\mu A^\mu$ is prohibited since it would violate gauge invariance. Hence the gauge particle, the photon, is predicted to be massless.

2.1.4 Strong Interactions

The strong interaction between quarks and gluons is described by *quantum chromodynamics* (QCD) [7–9]. Under this theory, quarks have an additional quantum number called *colour charge* (*red*, *green* and *blue*). The anti-quarks have anti-colour charges which are *anti-red*, *anti-green* and *anti-blue*. However, all observed particles are colourless.

Similar to QED, the free Lagrangian in this case is given by

$$\mathcal{L}_{free} = \bar{q}(i\gamma^\mu \partial_\mu - m)q \tag{2.11}$$

here

$$q = \begin{pmatrix} q_r \\ q_b \\ q_g \end{pmatrix}$$

is the quark colour field and q_r, q_b and q_g are the three colour fields carrying colour charges (r, b, g corresponding to red, blue and green). The symmetry group of QCD is SU(3), hence a local phase transformation transforms the quark colour field q is

$$q(x) \to q'(x) = e^{i\alpha_a(x)T_a} q(x) \tag{2.12}$$

with eight traceless, linearly independent 3×3 matrices T_a.

In analogy to QED, the covariant derivative is given by

$$D_\mu = \partial_\mu + igT_a G^a_\mu \tag{2.13}$$

where the 8 gauge fields transform as

$$G^a_\mu \to G^a_\mu - \frac{1}{g}\partial_\mu \alpha_a - f_{abc}\alpha_b G^c_\mu \tag{2.14}$$

The additional term compared to the QED with the analog on real structure constants f_{abc} results from the non-Abelian structure of QCD and leads to a self-interaction among gluons.

The structure of SU(3) is also the reason why not all of the T_a commute. The commutation relation is given by

$$[T_a, T_b] = i f_{abc} T_c. \tag{2.15}$$

A possible choice for the T_a are the Gell-Mann matrices $\lambda_a/2$. The resulting Lagrangian is then given by

$$\mathcal{L}_{QCD} = \underbrace{\bar{q}(i\gamma^\mu\partial_\mu - m)q}_{\text{Kinetic energy and mass of } q(x)} \underbrace{- g(\bar{q}\gamma^\mu T_a q)G^a_\mu}_{\text{Interaction}} - \underbrace{\frac{1}{4}G^a_{\mu\nu}G^{\mu\nu}_a}_{\text{Kinetic energy of } G^a_\mu} \tag{2.16}$$

where $G^a_{\mu\nu} = \partial_\mu G^a_\nu - \partial_\nu G^a_\mu - g f_{abc} G^b_\mu G^c_\nu$.

Like the photon in QED, gluons have to be massless to keep local gauge invariance.

Contrary to QED, the coupling strength of QCD increases with decreasing energy of a process. As a result, at high energies or short distances, the strong interaction between quarks and gluons are weak and these quarks and gluons can be considered as being *asymptotically free*. However, at very low energies or large distances, the strong interaction becomes very strong and thus quarks or gluons cannot exist as free particles. This confinement leads to the fact that only hadrons, but no single quarks, are observed in experiments.

2.1.5 Weak Interactions and Electroweak Unification

The weak interaction is responsible for radioactive β decay. It was combined with the electromagnetic interaction to form the electroweak interaction by Glashow, Salam and Weinberg (GSW-model) in the 1960s [10–12]. It is based on the gauge symmetry group $\mathrm{SU}(2)_L \otimes \mathrm{U}(1)_Y$ where L refers to left-handed fields and Y is the weak hypercharge.

All fermions in the SM are subject to the electro-weak interaction. The fermions are spinor fields ψ and there are three generations of left- and right-handed chiral fermions $\psi_{L,R}$ which are given by the projections

$$\psi_{L,R} = \frac{1}{2}(1 \mp \gamma^5)\psi. \tag{2.17}$$

Experimental observations show that weak interaction distinguish between left-handed and right-handed fermions. Under the action of the $\mathrm{SU}(2)_L$ group, the left-handed fermions transform as doublets of two leptons or quark weak eigenstates of the same generation. The right-handed fermions transform as singlets and are not affected by actions of the $\mathrm{SU}(2)_L$ group. All fermions carry weak hypercharge Y.

The weak isospin and hypercharge fulfill the Gell-Mann-Nishima relation, which links them to the physically observable electric charge via $Q = I_3 + Y/2$. Table 2.3 gives an overview of all SM fermions and their electroweak quantum numbers (electric charge Q, weak isospin T, its third component T_3 and hypercharge Y).

The left-handed isospin doublets ψ_L and the right-handed isospin singlet ψ_R trans-

form under the action of the $\mathrm{SU}(2)_L \otimes \mathrm{U}(1)_Y$ direct product group as follows

$$\psi_L \to \psi'_L = e^{i\alpha^a(x)T_a + i\beta(x)Y}\psi_L,\ a = 1,2,3 \tag{2.18}$$

$$\psi_R \to \psi'_R = e^{i\beta(x)Y}\psi_R \tag{2.19}$$

where $\alpha^a(x)$ and $\beta(x)$ are local phases and $T_a/2$ and Y are the generators of the $SU(2)_L$ and $U(1)_Y$ groups, respectively.

Since there are now four gauge parameters, $\alpha^a(x)$ and $\beta(x)$, there are as well four different gauge fields and the covariant derivative is defined as

$$D_\mu = \partial_\mu + i\frac{g}{2}W^a_\mu T_a + i\frac{g'}{2}B_\mu Y \tag{2.20}$$

where W^a_μ(a = 1, 2, 3) and B_μ denote the gauge fields related to the 3 + 1 degrees of freedom of the $\mathrm{SU}(2)_L \otimes \mathrm{U}(1)_Y$ symmetry group. The coupling constants g and g' determine the strength of the coupling to the $\mathrm{SU}(2)_L$ gauge fields and the $\mathrm{U}(1)_Y$ gauge field, respectively.

Table 2.3: Overview of the quantum numbers of the Standard Model fermions in the Glashow-Weinberg-Salam model (Ref. [1]).

	Generation			Quantum numbers			
	1^{st}	2^{nd}	3^{rd}	I	I_3	Y	$Q[e]$
Leptons	$\begin{pmatrix}\nu_e\\ e^-\end{pmatrix}_L$	$\begin{pmatrix}\nu_\mu\\ \mu^-\end{pmatrix}_L$	$\begin{pmatrix}\nu_\tau\\ \tau^-\end{pmatrix}_L$	1/2	1/2	−1	0
				1/2	−1/2	−1	−1
	$\bar{e}_R$	$\bar{\mu}_R$	$\bar{\tau}_R$	0	0	−2	−1
Quarks	$\begin{pmatrix}u\\ d'\end{pmatrix}_L$	$\begin{pmatrix}c\\ s'\end{pmatrix}_L$	$\begin{pmatrix}t\\ b'\end{pmatrix}_L$	1/2	1/2	1/3	2/3
				1/2	−1/2	1/3	−1/3
	u_R	c_R	t_R	0	0	4/3	2/3
	d_R	s_R	b_R	0	0	−2/3	1/3

The corresponding field strength tensors of the gauge fields are given by

$$W^{\mu\nu}_a = \partial_\mu W^a_\nu - \partial_\nu W^a_\mu - g\varepsilon_{abc}W^b_\mu W^c_\nu \tag{2.21}$$

$$B_{\mu\nu} = \partial_\mu B_\nu - \partial_\mu B_\mu \tag{2.22}$$

where ε_{abc} denotes the totally antisymmetric tensor. The Lagrangian that is invariant under local $\mathrm{SU}(2)_L \otimes \mathrm{U}(1)_Y$ transformations is found to be

$$\mathcal{L}_{EW} = \sum_j i\bar{\psi}^j_L\gamma_\mu D_\mu \psi^j_L + \sum_j i\bar{\psi}^k_R\gamma_\mu D_\mu \psi^k_R - \frac{1}{4}W^a_{\mu\nu}W^{\mu\nu}_a - \frac{1}{4}B_{\mu\nu}B^{\mu\nu} \tag{2.23}$$

where the sum in i and k runs over all doublets and singlets listed in Table 2.3. Since the field strengths $W^a_{\mu\nu}$ contain a quadratic piece, the Lagrangian gives rise to cubic and quartic self-interactions among the gauge fields.

Experiments show that the gauge fields $W^{\mu\nu}_a$ and B_μ do not carry the right quantum numbers to be directly identified with the experimentally observed $W^\pm$ and Z bosons and the photon. Instead, a linear combination of these gauge fields leads to the physically observable states according to:

$$W^\pm_\mu = \frac{1}{\sqrt{2}}(W^1_\mu \mp iW^2_\mu), \tag{2.24}$$

$$Z_\mu = \cos\theta_W W^3_\mu - \sin\theta_W B_\mu, \tag{2.25}$$

$$A_\mu = \sin\theta_W W^3_\mu + \cos\theta_W B_\mu. \tag{2.26}$$

where $W^\pm_\mu$ and Z_μ denote the fields of the weak gauge bosons, A_μ the photon field and θ_W the weak mixing angle. The combinations above allow to relate the electric charge e and the electroweak couplings by

$$e = g\sin(\theta_W) = g'\cos(\theta_W) \tag{2.27}$$

2.2 The Higgs Mechanism

Experiments show that the fermions and gauge bosons such as W and Z bosons are massive which is not described in the SM Lagrangian. In order to include these masses, the Lagrangian has to be extended without violating the gauge invariance. This can be achieved via the Higgs mechanism which exploits the principle of spontaneous symmetry breaking to generate the mass terms [13–16].

2.2.1 Spontaneous Symmetry Breaking

The spontaneous symmetry breaking allows to include mass terms without breaking local gauge invariance by introducing the so-called *Higgs field* Φ, a weak isospin doublet of complex scalar fields with hypercharge $Y = 1$

$$\Phi = \begin{pmatrix} \phi^+ \\ \phi^0 \end{pmatrix} = \frac{1}{\sqrt{2}} \begin{pmatrix} \phi_1 + i\phi_2 \\ \phi_3 + i\phi_4 \end{pmatrix} \tag{2.28}$$

which contains four real scalar fields ϕ_i. It is subject to a potential

$$V(\Phi) = \mu^2\Phi^\dagger\Phi + \lambda\left(\Phi^\dagger\Phi\right)^2. \tag{2.29}$$

In combination with the covariant derivative as given in Eq. 2.20, this leads to the

Lagrangian

$$\begin{aligned}\mathcal{L}_H &= (D_\mu\Phi)^\dagger(D_\mu\Phi) - V(\Phi) \\ &= |(i\partial_\mu - gT\cdot W_\mu - g'\frac{Y}{2}B_\mu)\Phi|^2 - \mu^2\Phi^\dagger\Phi + \lambda\left(\Phi^\dagger\Phi\right)^2\end{aligned} \tag{2.30}$$

where $|\,|^2 = (\,)^\dagger(\,)$. $\mathcal{L}_H$ is invariant under local $\mathrm{SU}(2)_L\otimes\mathrm{U}(1)_Y$ transformations. The first term describes the coupling of the electroweak gauge fields and the Higgs field. By choosing $\lambda > 0$, which is required by vacuum stability, and $\mu^2 < 0$, a potential of the form illustrated in Figure 2.1 is obtained. There is an infinite set of degenerate states with minimum energy, satisfying

$$\Phi^\dagger\Phi = -\frac{\mu^2}{2\lambda}. \tag{2.31}$$

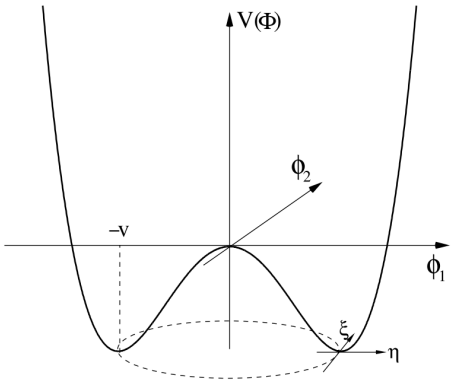

Figure 2.1 *The Higgs potential (taken from Ref. [17])*

By choosing a particular ground state, the symmetry gets spontaneously broken. This is because the vacuum state has a lower symmetry than the potential $V(\Phi)$ itself. An appropriate choice of a particular minimum is

$$\phi_1 = \phi_2 = \phi_4 = 0, \quad \phi_3^2 = -\frac{\mu^2}{\lambda} = v^2 \tag{2.32}$$

where v is called the *vacuum expectation value* of the Higgs field.

Obviously, this ground state is no longer gauge invariant but the Lagrangian itself still obeys the full symmetry. The $\mathrm{SU}(2)_L\otimes\mathrm{U}(1)_Y$ symmetry gets spontaneously broken to the electromagnetic subgroup $\mathrm{U}(1)_{QED}$, which by construction still remains a true symmetry of the vacuum. The excitations over the ground state can be parametrised in the general form

$$\Phi(x) = \frac{e^{iT_a\theta^a(x)}}{\sqrt{2}}\begin{pmatrix}0\\ v+H(x)\end{pmatrix} \tag{2.33}$$

with four real fields denoted as $\theta^a(x)$ and $H(x)$. The important point is that the local $\mathrm{SU}(2)_L$ invariance of the Lagrangian allows to rotate away any dependence on $\theta^a(x)$.

These three fields are the would-be massless Goldstone bosons associated with the spontaneous symmetry breaking. Taking the physical, unitary gauge $\theta^a(x) = 0$ and substituting the resulting parametrisation of $\Phi(x)$ along with the covariant derivative as defined in Eq. 2.20 in the Lagrangian of Eq. 2.30, $\mathcal{L}_H$ takes the form

$$\mathcal{L}_H = \frac{1}{2}\partial_\mu H \partial^\mu H + (v+H)^2\left(\frac{g^2}{4}W_\mu^\dagger W^\mu + \frac{g^2}{8\cos^2\theta_w}Z_\mu Z^\mu\right) - \lambda v^2 H^2 - \lambda v H^3 - \frac{\lambda}{4}H^4 \tag{2.34}$$

In this representation, the fields are expressed in the physical weak boson fields $W_\mu^\pm$ and Z_μ. Due to the non-zero value of v, the second term of the Lagrangian contains bilinear terms in the weak boson fields. These terms can be interpreted as mass terms for the electro-weak gauge bosons as follows

$$m_W = m_Z \cos\theta_w = \frac{vg}{2}, \quad m_\gamma = 0 \tag{2.35}$$

It can be seen from Eq. 2.35 that the masses m_W and m_Z are related to each other via θ_w. Since the existence of the $W^\pm$ and Z^0 bosons has been discovered experimentally with mass values $m_W \approx 80.4$ GeV and $m_Z \approx 91.2$ GeV, the value of θ_w is about 30°.

2.2.2 Higgs Couplings to Fermions

It can be shown that the Higgs boson has exactly the right quantum numbers to form an $SU(2)_L$ and $U(1)_Y$ singlet in the vertex $-\lambda_f \bar{\psi}_L \phi \psi_R$, where λ_f is a so-called Yukawa coupling.

A term in the Lagrangian can be constructed that couples the Higgs doublet to the fermion fields

$$\begin{aligned}\mathcal{L}_{fermion} &= -\lambda_f\left[\bar{\psi}_L\phi\psi_R + \bar{\psi}_R\phi\psi_L\right] \\ &= -\underbrace{\frac{\lambda_f v}{\sqrt{2}}\bar{\psi}\psi}_{\text{fermion mass term}} - \underbrace{\frac{\lambda_f}{\sqrt{2}}h\bar{\psi}\psi}_{\text{fermion-higgs interaction}}\end{aligned} \tag{2.36}$$

The Yukawa coupling is often expressed as

$$\lambda_f = \sqrt{2}\frac{m_f}{v}. \tag{2.37}$$

The couplings grow with the particle masses. The mass of the Higgs boson is connected with the vacuum expectation value v and the parameter λ by $m_H = \sqrt{2\lambda v}$. Since λ is unknown, the mass of the Higgs boson can not be predicted by theory. However, it can be constrained by several theoretical considerations, such as

- ***Unitarity Constraint*** comes from requiring that the scattering matrix for the scattering of gauge ($W^\pm$ and Z^0) and Higgs bosons is unitary. This requirement leads to the upper bound $m_H \lesssim 800$ GeV.

- ***Triviality Constraint*** comes from the fact that in a simplistic theory in which there is only a real scalar field with a quartic self-coupling, the corrected self-coupling increases monotonically with the energy scale and the theory becomes non-perturbative.
- ***Vacuum Stability Constraint*** focus on small Higgs boson masses for which the top quark contribution to λ becomes dominant, and gives lower bounds for the Higgs boson mass.
- ***Fine-Tunning*** originates from the high-order corrections of the Higgs boson mass. Figure 2.2 shows the regions with fine-tuning less than 1% and 10% as well as the triviality, vacuum stability and electro-weak high-precision data constraints.

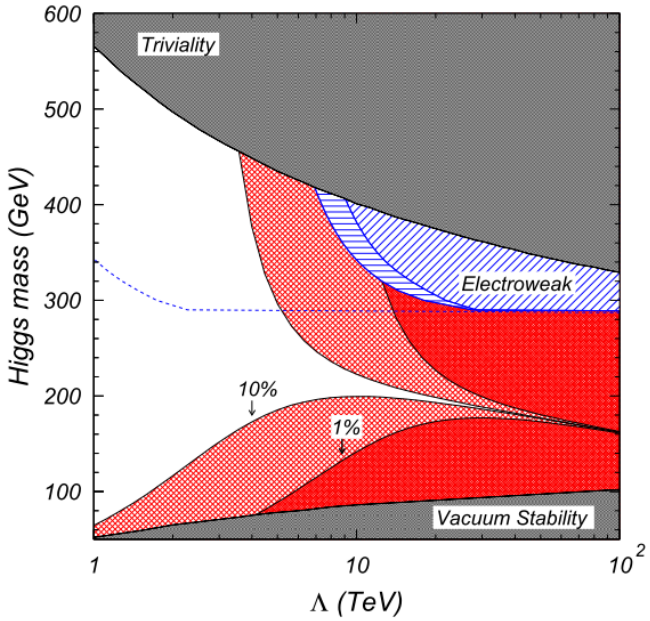

Figure 2.2 *Plot in the $m_H - \Lambda$ plane showing the fine-tuning contours (red) and bounds from triviality, vacuum stability and electroweak precision data constraints. The darkly hatched region marked "1%" represents tunings of greater than 1 part in 100; the "10%" region means greater than 1 part in 10 (taken from Ref. [18]).*

2.3 The Standard Model Higgs Boson at the LHC

This section focuses on the production and decay modes of a Standard Model Higgs boson in proton-proton collisions at the LHC.

2.3.1 Proton-Proton Collision

The proton is a subatomic particle with a positive electric charge of $+1e$ (e is the elementary charge). In the Standard Model of particle physics, protons are considered as particles composed of point-like constituents called *"partons"*.

In proton-proton collisions, these constituents interact with each other. The scattering processes at high energy can be classified as either hard or soft. The *soft scattering processes* appear with small momentum transfer between the interacting partons. However, *hard scattering processes* are characterized by a large momentum transfer and particle production (e.g. the production of Higgs bosons or W and Z bosons) belong to these processes.

Figure2.3 illustrates the interaction of two partons from two incomming protons. In this example, the interacting partons produce a Z^0/γ^* final state. Due to confinement, the proton remnants will hadronize into hadrons which are colour-neutral states. These additional hadrons are referred to as the *underlying event*.

The incoming partons carry colour charge, thus bremsstrahlung can occur. Emissions related to the incoming partons are called *initial state radiation* (ISR) and those related to the outgoing objects are called *final state radiation* (FSR). Both bremsstrahlung emissions can lead to additional reconstructed jets in the detector which might modify the event final state topology.

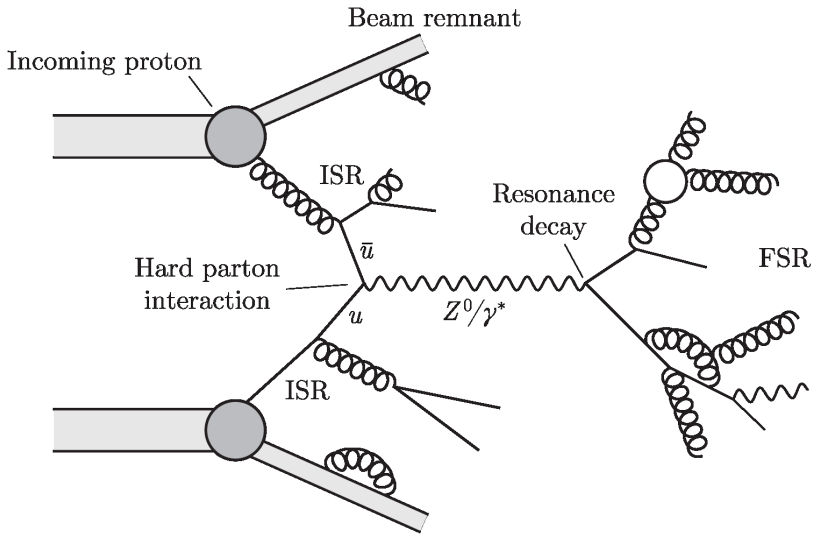

Figure 2.3 *Illustration of a proton-proton collision.*

Since collisions are made to occur between bunches containing about 10^{11} protons, multiple proton-proton interactions can occur in one bunch-crossing. These additional interactions, which are mainly soft inelastic hadronic interactions, are called *minimum bias events*. They constitute the so-called *in-time pileup* contributions. In case the response time of individual detector components is larger than the spacing between two bunches, also contributions from previous bunch crossings can overlay with those from the current bunch crossing. This contribution is called *out-of-time pileup*.

2.3.2 Luminosity

The quantity that measures the ability of a particle accelerator to produce the required number of interactions is called the *luminosity* [19]. For a given type of events occuring at a collider, the rate (number of events per second) relates to the cross section σ and the instantaneous luminosity L delivered by the accelerator as follows

$$R = \frac{\mathrm{d}N}{\mathrm{d}t} = \sigma \cdot L \tag{2.38}$$

The unit of the luminosity is therefore $\mathrm{cm}^{-2}\mathrm{s}^{-1}$.

Asumming that there are two bunches containing n_1 and n_2 particles with identical Gaussian profiles with standard deviations σ_x and σ_y in the horizontal and vertical directions with respect to the beam axis, respectively. When these two bunches collide head-on with a frequency f, the instantaneous luminosity is given by

$$L = f\frac{n_1 n_2}{4\pi\sigma_x\sigma_y} \tag{2.39}$$

The total number of events in a given period of data taking is obtained by integration of the rate R over time

$$N = \sigma \cdot \int L\mathrm{d}t = \sigma \cdot \mathbf{L} \tag{2.40}$$

where $\mathbf{L}$ is the integrated luminosity which is used to quantify the amount of proton-proton collisions. Cross sections are usually measured in units of *barn* (1 barn = 10^{-24} cm^2).

2.3.3 Standard Model Cross Sections at LHC

The calculation of cross sections involving initial hadrons can be done by applying the factorization theorem. The cross section of a hard scattering process of hadrons A and B to the final state X can be expressed by

$$\sigma_{AB} = \sum_{a,b} \int \mathrm{d}x_a \mathrm{d}x_b f_{a/A}(x_a, Q^2) f_{b/B}(x_b, Q^2) \hat{\sigma}_{ab\to X} \tag{2.41}$$

where $\hat{\sigma}_{ab\to X}$ is the partonic cross section involving the initial state partons a and b, which can be achieved with perturbative QCD calculations. This cross section can be expanded as

$$\hat{\sigma}_{ab\to X} = \hat{\sigma}_0 \left(1 + c_1(\mu_F, \mu_R)\alpha_s(Q^2, \mu_R^2) + c_2(\mu_F, \mu_R)\alpha_s^2(Q^2, \mu_R^2) + \cdots\right) \tag{2.42}$$

where $\hat{\sigma}_0$ is the leading-order partonic cross section, α_s is the strong coupling constant depending on the momentum transfer Q^2 and the renormalization and factorization

scales μ_F and μ_R. It is sensible to choose μ_F and μ_R values of the order of the typical momentum scales of the hard scattering process, e.g. for the process $q\bar{q} \to Z \to l^+l^-$ the standard choice is μ_F and μ_R equal to the invariant mass of the lepton pair.

The *parton distribution functions* (PDFs) given by $f_{a/A}(x_a, Q^2$ and $f_{b/B}(x_b, Q^2)$ describe the probability to find a parton $a(b)$ carrying the momentum fraction $x_a(x_b)$ of the hadron $A(B)$. They are determined from experimental data, Figure 2.4 shows the PDFs of the proton determined by the MSTW group [20] for two different scales $Q^2 = 10$ GeV^2 and $Q^2 = 10^4$ GeV^2.

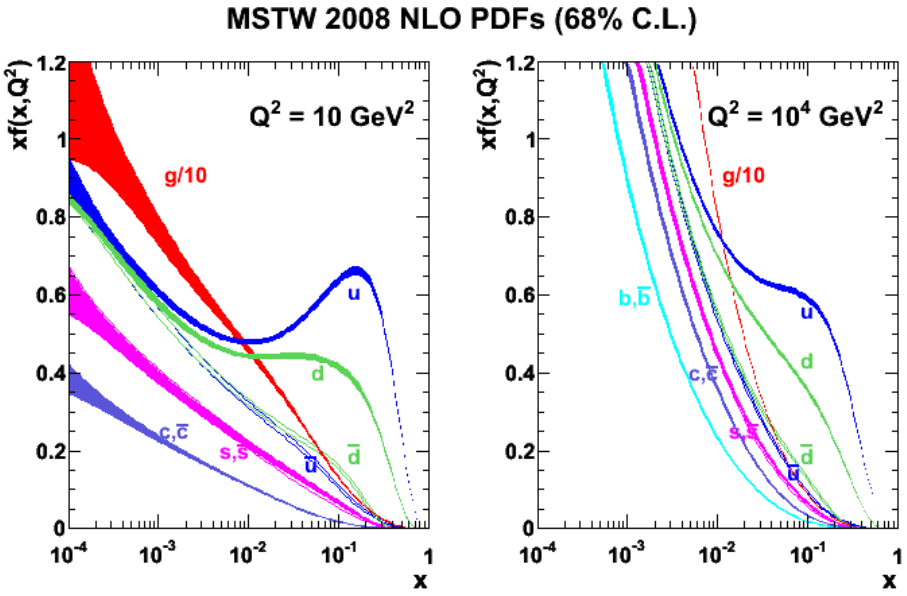

Figure 2.4 *Parton distribution functions determined by the MSTW group for two different scales $Q^2 = 10$ GeV^2 (left) and $Q^2 = 10^4$ GeV^2 (right) (taken from Ref. [20]).*

The formalism described previously can be used to obtain predictions for some important Standard Model cross sections at proton-proton colliders. An overview of cross sections of some processes as a function of the centre-of-mass energy at colliders such as the Tevatron and LHC is shown in Figure 2.5.

It can be seen that the total inelastic cross section is about five orders of magnitude higher compared to the production cross section of W or Z bosons, and about ten to eleven orders of magnitude higher compared to the production cross section of the Higgs boson. Thus, very high luminosities are needed to produce a suffcient rate of these rare processes.

2.3.4 Higgs Boson Production

Within the Standard Model, several processes contribute to Higgs boson production in proton-proton collisions at the LHC, which are

- ***Gluon-gluon fusion*** ($gg \to H$): two gluons form a quark (mostly top-quark) loop, which then radiates a Higgs boson.

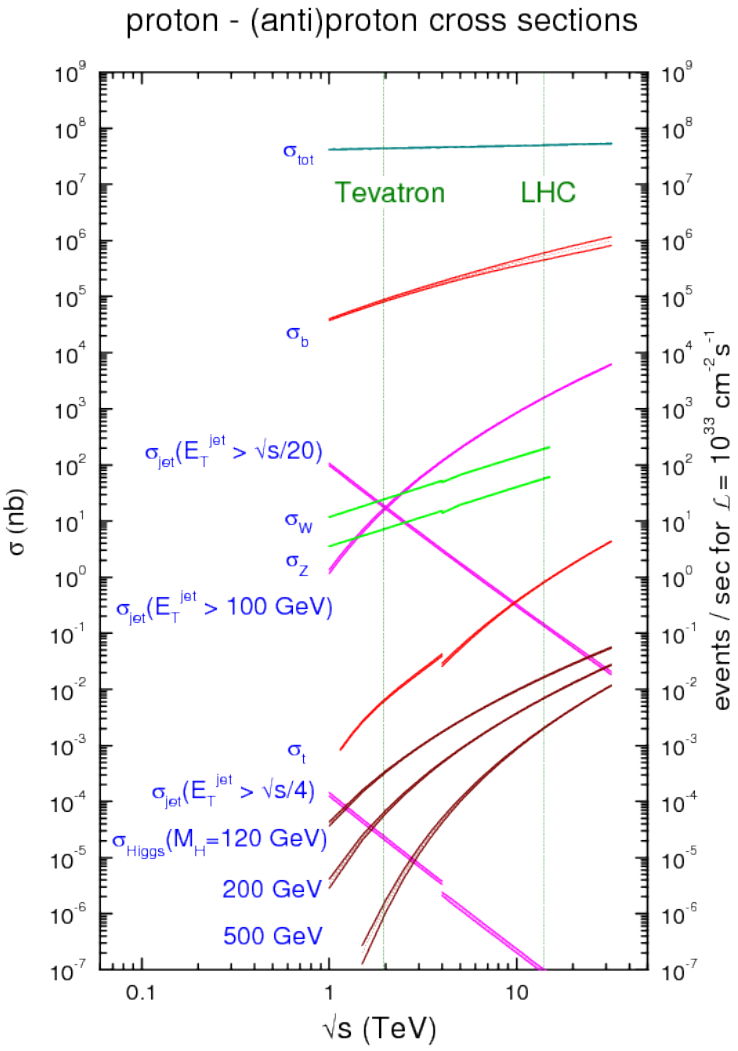

Figure 2.5 *Standard Model cross-section predictions at hadron-hadron colliders such as Tevatron and LHC (taken from Ref. [21]).*

- ***Vector-boson fusion*** ($qq' \to qq'H$): two fermions (or anti-fermions) interact and radiate a virtual vector boson each, which collide to form a Higgs boson.
- ***Higgs-strahlung process*** ($qq' \to WH$ or ZH): associated production with weak bosons.
- ***Associated production with top-quarks*** ($gg \to \bar{t}tH$): two gluons split into a heavy quark−antiquark pair. A quark and antiquark from each pair then combine to produce a Higgs boson.

The Feynman diagrams illustrating these production processes are shown in Figure 2.6.

The cross sections for the individual production channels as a function of the Higgs boson mass are shown in Figure 2.7a for a centre-of-mass energy of $\sqrt{s} = 8$ TeV. The total production cross sections for different centre-of-mass energies of $\sqrt{s} = 7$, 8 and 14 TeV are shown in Figure 2.7b as a function of the Higgs boson mass.

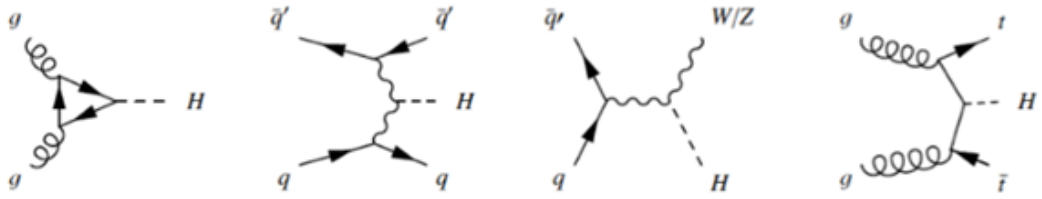

Figure 2.6 *The main Higgs production processes (from left to right): gluon-gluon fusion, vector boson fusion, Higgs-strahlung process and associated production with top quarks.*

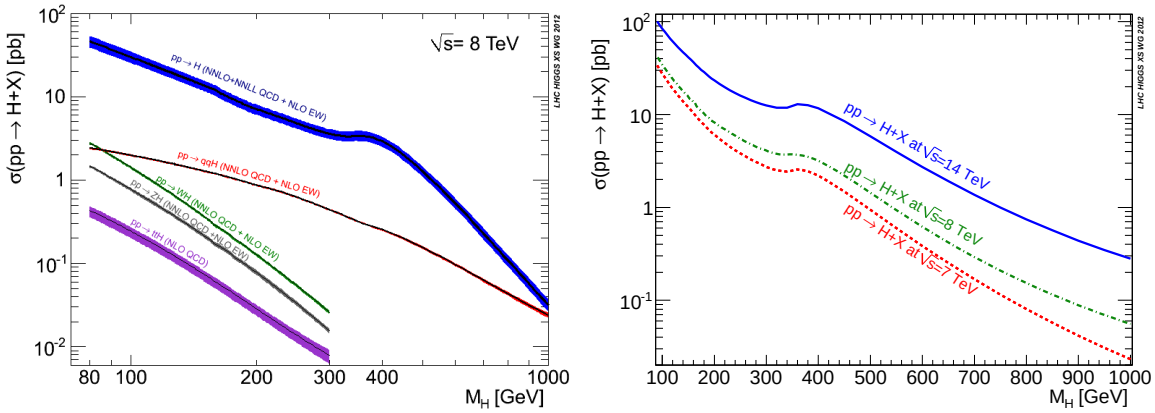

(a) ***(b)***

Figure 2.7 *(a) Cross sections for the dominant Standard Model Higgs boson production processes in proton-proton collisions at the LHC at a centre-of-mass energy of $\sqrt{s}$ = 8 TeV as a function of the Higgs boson mass. (b) Total cross sections for the Standard Model Higgs boson at the LHC for centre-of-mass energies of $\sqrt{s}$ = 7, 8 and 14 TeV as a function of the Higgs boson mass (taken from Ref. [22]).*

For Higgs boson masses below 1 TeV, the gluon-gluon fusion mode is the most dominant one among these processes. The next important production process is vector-boson fusion which becomes comparable to the gluon-gluon fusion for very large Higgs boson mass. A characteristic feature of the vector-boson fusion is the presence of two forward jets from the two outgoing quarks which makes it distinguishable from the gluon-gluon fusion. The associated production with vector-bosons or a $t\bar{t}$ pair have a significant contribution only in the very low Higgs boson mass range. When the Higgs boson mass increases, these processes have much smaller cross sections compared to the two leading ones. The vector bosons or the top-quark pair in the final states can be used as an additional signature to identify Higgs bosons from these production modes.

The leading order contribution to the gluon-gluon fusion cross section is proportional to the strong coupling constant α_s^2. The *next-to-leading-order* (NLO) corrections [23–25] are large and increase the leading-order cross section by about 80−100% at the LHC. The *next-to-next-to-leading-order* (NNLO) corrections [26–28] have been calculated using the infinite top-quark mass limit, leading to an additional increase of the cross section of about 25%. Full NLO QCD and electro-weak corrections [29, 30]

and approximate NNLO QCD corrections [31] are used to calculate the vector-boson fusion cross section. The associated WH/ZH cross sections are calculated up to NNLO QCD corrections [32, 33] and NLO electro-weak corrections [34]. The cross section for the associated production with a $t\bar{t}$ pair are estimated at NLO in QCD [35–37].

2.3.5 Higgs Boson Decay Modes

In order to identify the produced Higgs boson, one has to consider its decay products. An overview of the possible decay branchings as a function of the Higgs boson mass is shown in Figure 2.8. The possible decay channels are listed below

- Fermion − anti-fermion pairs ($f\bar{f}$)
- Massive gauge boson pairs (WW or ZZ)
- Massless gauge boson pairs (gg or $\gamma\gamma$)

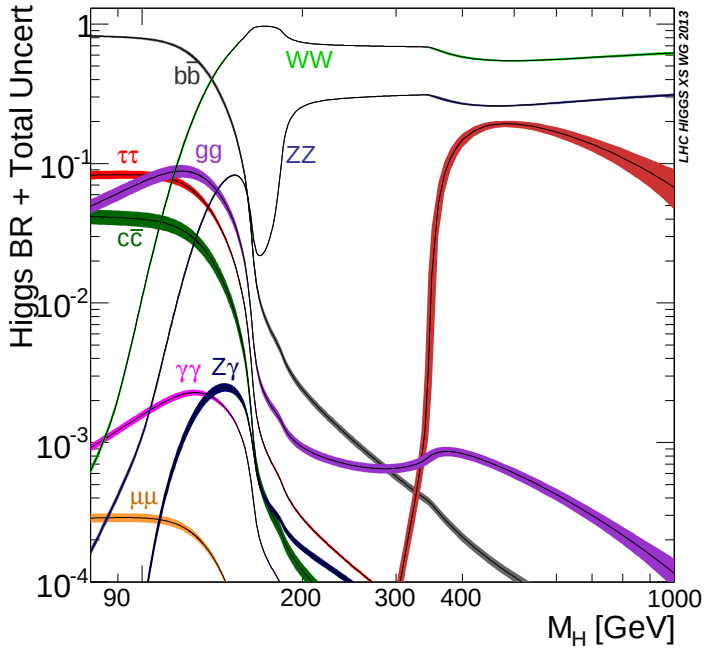

Figure 2.8 *Branching ratios of the different Standard Model Higgs boson decay modes as a function of the Higgs boson mass (taken from Ref. [22])*

From Figure 2.8, the combination of the various decay channels gives sensitivity to a Standard Model Higgs boson over a broad range of the Higgs boson mass. However, due to the environment of hadronic collisions, some of the decay modes are less accessible than others. For example, as shown in Figure 2.8 at relatively low Higgs boson masses, decays of Higgs boson to $b\bar{b}$ are dominant. However, due to the contribution of $b\bar{b}$ production via QCD processes, it is very difficult to perform a search for Higgs boson decays to $b\bar{b}$.

Processes with leptons, e.g. electrons and muons, or photons in the final state are more beneficial in the environment of hadronic collisions since they provide a clean

signature. Thus, the highest sensitivity is expected for searches focusing on three channels, which are $H \to \gamma\gamma$, $H \to ZZ^* \to 4l$ and $H \to WW^* \to l\nu l\nu$. The $H \to \mu\mu$ also provides a clean signature with two high energetic muons, however, the probability of this decay mode is rather small (about 0.04%).

It should be noted that the $H \to \gamma\gamma$ decay mode is mainly sensitive to low Higgs boson masses in the range of 110 GeV to 140 GeV while the $H \to ZZ^* \to 4l$ and $H \to WW^* \to l\nu l\nu$ channels are sensitive over a much broader range.

The $H \to ZZ^* \to 4l$ channel is interesting since the Higgs boson mass can be fully reconstructed using the four leptons in the final state. However, the low branching ratio of the $ZZ^* \to 4l$ decay mode leads to a low number of expected events and a significant amount of data must be collected and analyzed to identify a possible signal.

The $H \to WW^* \to l\nu l\nu$ channel is characterized by the decay products of the W boson pair, each W boson can decay either into a quark and anti-quark or into a charged lepton and the corresponding neutrino. It is simpler to focus only on leptonic decays, as the dilepton requirement is able to suppress many hadronic backgrounds. Therefore, the signature of this channel will be two isolated, opposite charged leptons and large missing transverse energy caused by the neutrinos escaping detection. The branching ratio of this decay mode becomes dominant in the large Higgs boson mass range ($m_H > 2m_W$), making it an attractive search option. Due to the presence of neutrinos, the mass resolution of this channel is too coarse to be able to reconstruct the Higgs boson mass with high precision. However, it is sensitive to the search for the Higgs boson over a large range of masses.

3

The Large Hadron Collider and ATLAS Detector

The following chapter gives an overview of the experimental setup. First, a description of the LHC is given in Section 3.1. Afterwards, the main components of the ATLAS detector, namely the tracking detectors, the electromagnetic and hadronic calorimeters and the muon chambers, are briefly discussed in Section 3.2.

3.1 The Large Hadron Collider

The *Large Hadron Collider* (LHC) is the largest and most powerful particle accelerator in the world up to date. It is located at the *European Organization for Nuclear Research* (CERN) at the Swiss-French border and near to Geneva city. It lies in a tunnel that has a circumference of about 27 km and is buried about 50 to 175 meters below ground. A schematic illustration of the LHC accelerator complex is shown in Figure 3.1.

The LHC is designed to accelerate bunches of protons or ions and bring them to collision at specific interaction points. At the interaction points, several experiments are located as shown in Figure 3.1, each experiment investigates some properties of those collisions. These experiments are

- ***The ALICE experiment*** studies the properties of the quark-gluon plasma, by using heavy ion beams such as lead (Pb) in the LHC.
- ***The ATLAS experiment*** performs high-precision measurements of the Standard Model and searches for new physics at the TeV scale.
- ***The CMS experiment*** addresses the same physics as ATLAS, but these two experiments were designed and operated by two different teams.
- ***The LHCb experiment*** is dedicated to the study of b-physics, such as CP violation, rare decays of charm and beauty-flavored hadrons.

The detectors in ATLAS and CMS are multi-purpose detectors, whereas ALICE and

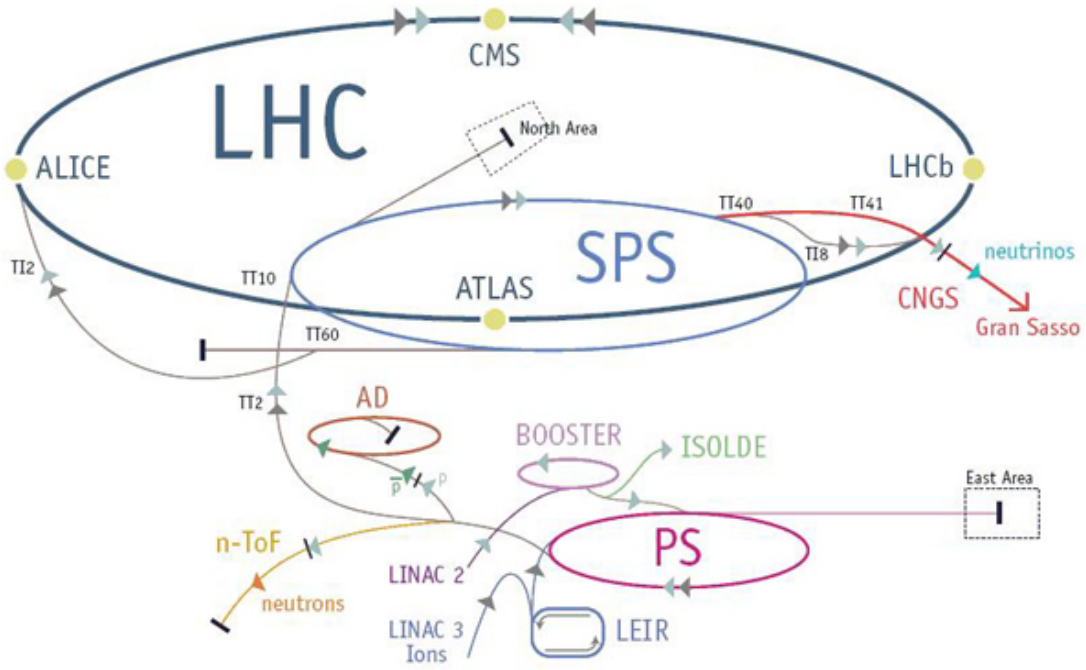

Figure 3.1 *Layout of the CERN accelerator complex (taken from Ref. [38]).*

LHCb are designed to analyze specific physics processes.

The protons used in the LHC are from a bottle of hydrogen gas at one end of a linear accelerator (*Linac2*). From there they are accelerated up to energies of about 50 MeV. They then enter to the *Proton Synchrotron Booster* (PSB), the *Proton Synchrotron* (PS) and the *Super Proton Synchrotron* (SPS), where they reach up to energies of 1.4 GeV, 25 GeV and 450 GeV, respectively. At the end of this chain, the protons are injected into the LHC ring and accelerated to the collision energy.

At the LHC, protons arrive in bunches, each bunch contains about 10^{11} protons. The size of each bunch is about 16 μm in diameter and about 8 cm in length at the interaction points in the experiments. In order to accelerate and keep the proton bunches in the LHC ring, 1232 super-conducting dipole magnets were installed. They are operated at a temperature of about 1.9 K (-271.3 °C) to generate a magnetic field with a strength of ≈ 8.33 T. The proton beams are focused by using 392 quadrupole magnets with lengths ranging from 5 to 7 meters, which provide magnetic field gradients of about 200 T/m each. The distance between two proton bunches, the *bunch spacing*, is designed to be 25 ns, which corresponds to a bunch crossing frequency of 40 MHz.

3.1.1 Data Taking at LHC

The LHC is designed to reach a centre-of-mass energy of $\sqrt{s} = 14$ TeV, which means an energy of 7 TeV per beam. The first circulation of proton beams of the LHC was in autumn of 2008. However, just a few days after that, the beams were interrupted

by a magnet quench incident. About one year later, the operations were resumed in November 2009, and the first proton-proton collisions were recorded. Collisions at a centre-of-mass energy $\sqrt{s} = 7$ TeV were successfully produced in March 2010, and the planned research programs began. The 7 TeV energy was used during 2011 and increased to 8 TeV in 2012. After 27 months of delivering data, the LHC was shutdown for about two years and continued to provide data at the unprecedented energy of 13 TeV since 2015 [39].

The values of some characteristic parameters of the LHC operation from 2011 to 2016 are summarized in Table 3.1. The integrated luminosity of proton-proton collisions delivered by the LHC are also shown in Figure 3.2.

Table 3.1: Overview of machine parameters of the LHC operation during the data taking periods from 2011 to 2016 compared to the design values.

	2011	2012	2015	2016	Design
Centre-of-mass energy	7 TeV	8 TeV	13 TeV	13 TeV	14 TeV
Peak luminosity [$\mathrm{cm^{-2}s^{-1}}$]	3.65×10^{33}	7.73×10^{33}	5.1×10^{33}	13.3×10^{33}	10^{34}
Protons per bunch ($\times 10^{11}$)	0.6−1.2	1.48	1.2	–	1.15
Number of bunches	200−1380	1380	2244	–	2808
Collisions / bunch-crossing	9.1	20	20	20	22
Time between bunches [ns]	75 and 50	50	50-25	25	25

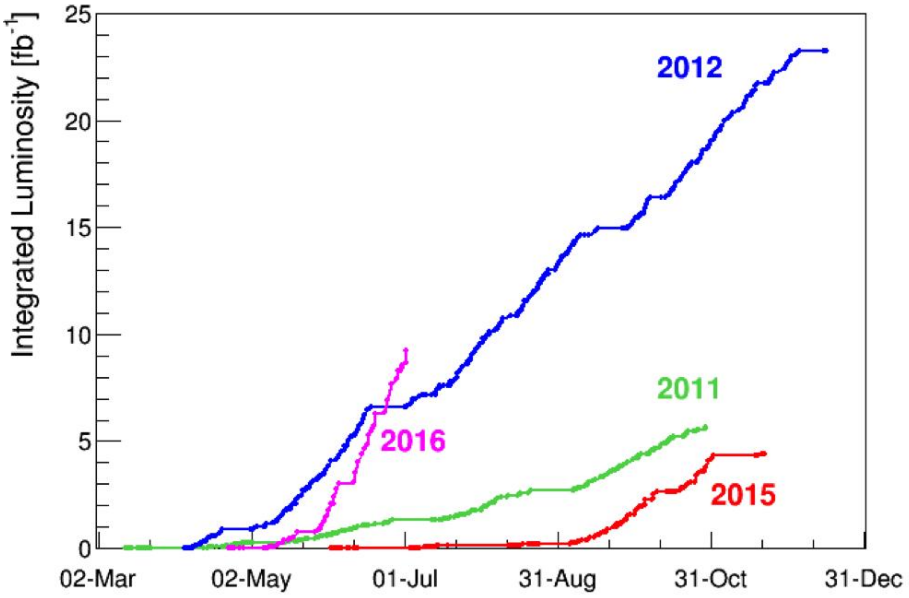

Figure 3.2 *The integrated luminosity delivered by the LHC in 2011, 2012, 2015 and 2016 (taken from Ref. [40]).*

3.2 The ATLAS Detector

The ATLAS (**A** **T**oroidal **L**HC **A**pparatu**S**) experiment is designed to perform high-precision measurements of the Standard Model and searches for new physics. The ATLAS detector is a multi-purpose detector which is installed at one of the interaction points of the LHC accelerator ring. The dimensions of the detector are 25 m in height and 44 m in length, and the overall weight of the detector is approximately 7000 tons [41]. A cut-away view of the overall layout is shown in Figure 3.3. The requirements of particle-identification capabilities led to a set of general requirements for the ATLAS detector, such as

- Fast, radiation-hard electronics and sensor elements.
- Large acceptance in pseudorapidity with almost full azimuthal angle coverage.
- Good charged-particle momentum resolution and reconstruction efficiency.
- Good electromagnetic calorimetry for electron and photon identification and measurements.
- Good muon identification and momentum resolution over a wide range of momenta.
- Highly efficient triggering on low transverse-momentum objects with sufficient background rejection.

The ATLAS detector consists of several sensitive material layers and has a forward-backward symmetric structure around the beam pipe. The main components of this detector are categorized into four categories

- *The tracking system* is closest to the interaction point, and measures the tracks of charge particles.
- *The calorimeter system* measures the energy of particles.
- *The muon system* reconstructs muons and measures their momenta.
- *The magnet system* bends charged particles in the tracking and muon systems, allowing their momenta to be measured.

With all these components being operative, all known particles, except neutrinos, can be detected. The following sections provide a brief overview on the individual detector components and their functionality. A more detailed description can be found in Refs. [41–43].

3.2.1 ATLAS Coordinate System

A coordinate system is used to uniquely identify directions and positions within the ATLAS detector volume (Figure 3.4). This coordinate system has the origin at the nominal interaction point, and the z-axis as the LHC beam direction. The positive x-axis is defined as pointing from the interaction point to the centre of the LHC ring and the positive y-axis is defined as pointing upwards. The azimuthal angle ϕ is measured as usual around the beam axis, and the polar angle θ is the angle from the beam

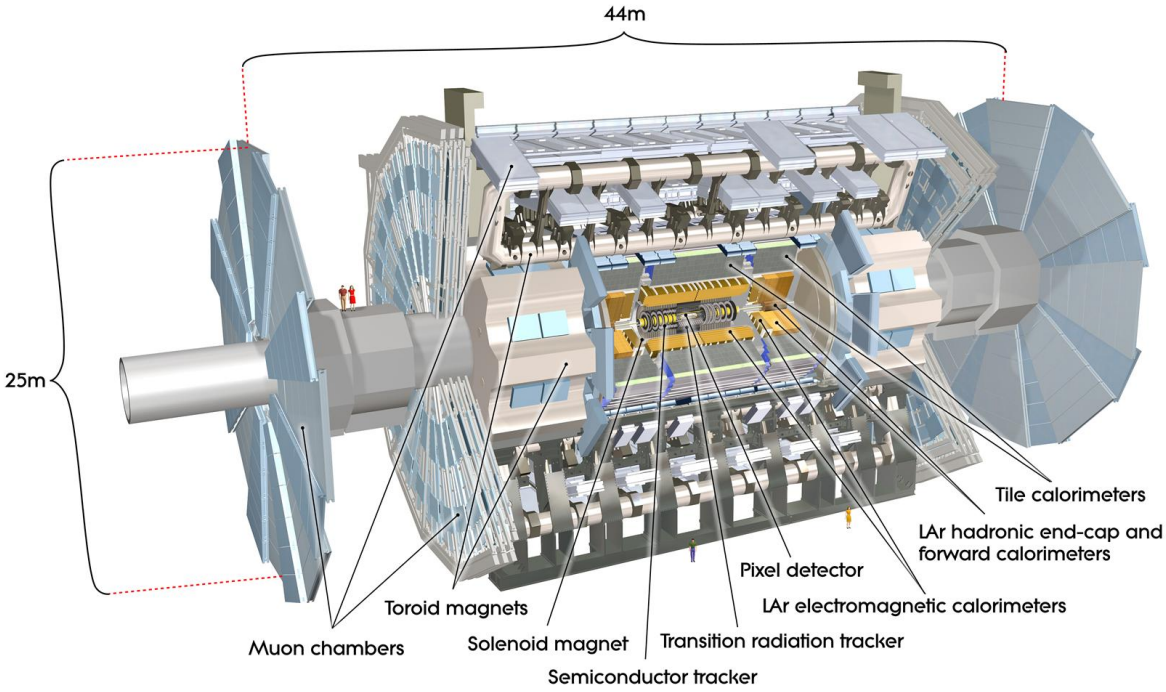

Figure 3.3 *The cut-away view of ATLAS detector and the individual subsystems (taken from Ref. [41]).*

axis [41]. The pseudorapidity η is defined as

$$\eta = -\ln[\tan(\theta/2)]. \tag{3.1}$$

This quantity is preferred over the polar angle θ because differences in η are Lorentz invariant under boosts along the beam axis. In the case of massive object (e.g. jets), the rapidity y is used

$$y = \frac{1}{2}\ln\frac{E + p_z}{E - p_z} \tag{3.2}$$

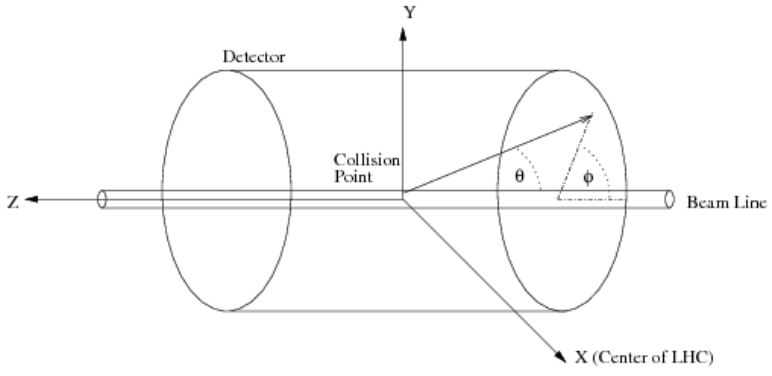

Figure 3.4 *Illustration of the ATLAS coordinate system (taken from Ref. [44]).*

The transverse momentum is calculated from the three-momentum $\vec{p}$ as

$$p_T = |\vec{p}|\sin\theta \tag{3.3}$$

The distance ΔR in the pseudorapidity−azimuthal angle space is defined as

$$\Delta R = \sqrt{(\Delta\phi)^2 + (\Delta\eta)^2} \tag{3.4}$$

where $\Delta\phi$ and $\Delta\eta$ are the distances of ϕ and η respectively.

3.2.2 Inner Detector

The ATLAS *Inner Detector* (ID) is the closest part to the beam pipe. It is designed to provide precise measurements of the direction and transverse momentum of charged tracks above a given p_T threshold (usually 0.5 GeV, but as low as 0.1 GeV in some studies). The Inner Detector covers the pseudorapidity range $|\eta| < 2.5$ and provides electron identification over $|\eta| < 2.0$ with a wide range of energies (between 0.5 GeV and 150 GeV). The resolution of transverse momentum measurement in the Inner Detector is $\frac{\sigma_{pT}}{p_T} = 0.5\% p_T \oplus 1\%$ [41, 43].

A cut-away view of the ATLAS Inner Detector is shown in Figure 3.5. The Inner Detector is contained within a cylindrical envelope of length 7 m and of radius 1.15 m, within a solenoidal magnetic field of 2 T. Figure 3.6 shows the structural elements of the Inner Detector. It consists of three independent subsystems, namely the *Pixel Detector* (PD), the *Semi-Conductor Tracker* (SCT) and the *Transition Radiation Tracker* (TRT).

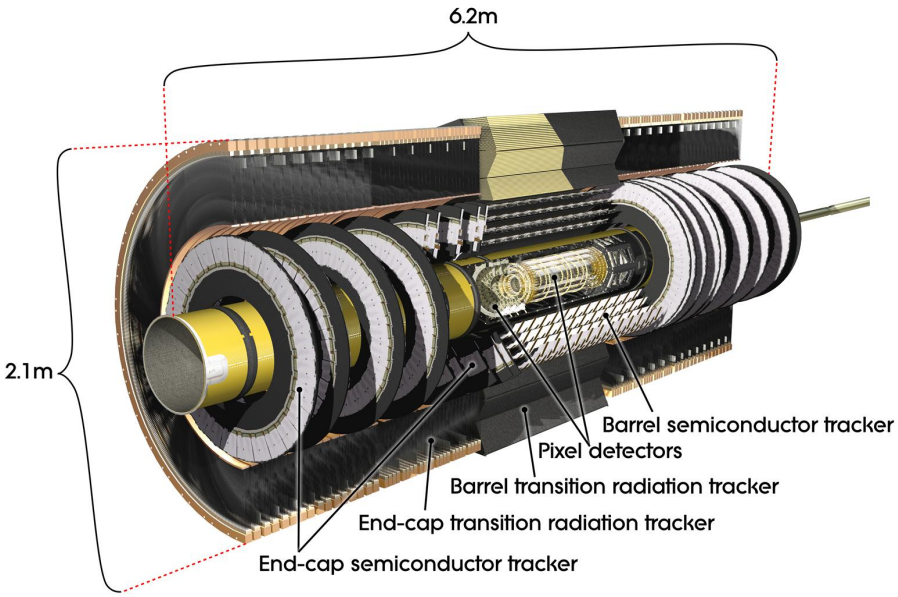

Figure 3.5 *Cut-away view of the ATLAS Inner Detector (taken from Ref. [41]).*

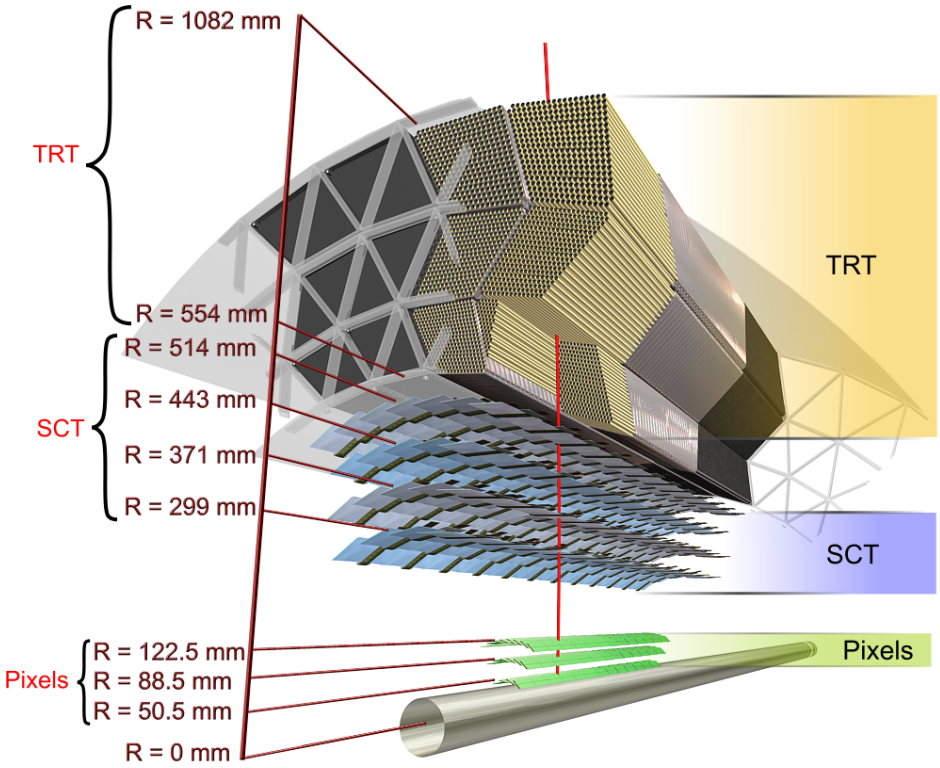

Figure 3.6 *Drawing showing the structural elements of Inner Detector (taken from Ref. [41]).*

Pixel Detector

The pixel detector is close to the beam pipe and contains 1744 silicon sensor modules (external dimensions 19×63 mm^2) arranged in three layers with radii of 5.05, 8.85 and 12.25 cm. Each module contains a total of 47232 pixels. The nominal pixel size is 50×400 μm^2 in $(R-\phi)\times z$ and it has a thickness of 250 μm thickness. The pixel modules are arranged on concentric cylinders around the beam axis in the barrel region and are located on disks perpendicular to the beam axis in the end-cap region. Communication between the modules and the read-out system is realized with 46080 readout channels. The innermost layer of pixels, the so-called *B-layer*, is as close as 5 cm to the beam pipe.

The pixel detector is responsible for the reconstruction of secondary vertices and for the identification of jets originating from b-quarks (*b-tagging jets*). The spatial resolution for the single-point measurement are 10 μm in the $(R-\phi)-$plane and 115 μm in z.

Semi-Conductor Tracker

Outside of the pixel detector is the SCT. It is built of four nested barrel layers of p-in-n type micro-strip sensors that are glued together with a stereo angle of 40 mrad. The radii of these layers are approximately 30, 37, 44 and 51 cm from the beam pipe. The SCT consists of 2122 and 1976 modules in the barrel and the end-cap regions with a

total of 15912 sensors. Each sensor has a thickness of 285 μm and contains 768 active silicon strips. The strips have a length of 12 cm and an average strip pitch of 80 μm each. Two additional strips at the edge of each sensor are inactive.

The SCT barrel and end-cap modules are arranged such that a particle that traverses through the SCT will cross at least four module layers. The spatial resolution for measurement in R$-\phi$ is 17 μm and in z-direction is 580 μm.

Transition Radiation Tracker

The outermost part of the Inner Detector is the TRT. The basic elements of the TRT are the 4-mm diameter polyimide drift (straw) tubes. The TRT consists of three rings that cover the central detector region with a total number of 73 layers and 52544 straw tubes. Two additional sets of 12 and 8 wheels are placed at the end-cap regions, each of the wheels consists of eight layers of straw tubes with a total number of 122880 straws per end-cap.

The tubes are made from wound kapton and carbon fibres. In the centre of each tube, a gold-plated tungsten wire with a diameter of 31 μm is located. The gas mixture inside the tubes is 70% Xe, 27% CO_2 and 3% O_2, which can be ionized by charged particles crossing the tubes. If a charged particle passes through the boundary between two layers with different dielectric media, it will emits photons. Those photons interact with the gas in the tubes and create an amount of free charges. Since the intensity of emitted photons is roughly proportional to the Lorentz factor $\gamma = E/mc^2$, it can be used to identify the type of particle passing through. The TRT only provides information in $(R - \phi)$ direction with the spatial resolution 130 μm per straw.

3.2.3 Calorimeter System

The ATLAS calorimeter system is designed to measure the energy of passing through particles. However, due to the high granularity, not only the amount of energy but also the lateral and longitudinal shapes of energy depositions can be measured. This information can be used to distinguish different types of particles. An overview of the ATLAS calorimeters is shown in Figure 3.7.

The Liquid Argon (LAr) calorimeters are housed in three cryostats, one barrel and two end-cap cryostats. The barrel cryostat contains the electromagnetic barrel calorimeter, while the two end-cap cryostats each contain an *electromagnetic end-cap calorimeter* (EMEC), a *hadronic end-cap calorimeter* (HEC) and a *forward calorimeter* (FCal) to cover the region closest to the beam [41].

Electromagnetic Calorimeter

The *electromagnetic calorimeter* (EMCal) is constructed from accordion-shaped kapton electrodes and lead absorber plates in combination with liquid Argon serving as

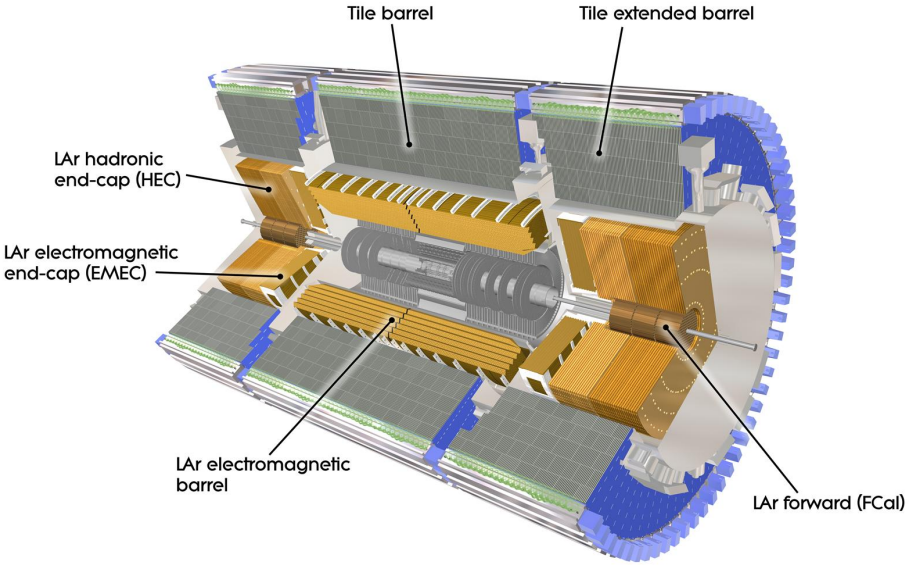

Figure 3.7 *Cut-away view of the ATLAS calorimeter system (taken from Ref. [41]).*

active material. If a high-energetic particle passes through the calorimeter, it interacts with the liquid Argon and absorber plates, creating a shower of low-energetic charged particles such as electrons, positrons or photons. This shower ionizes the liquid Argon and the produced free charges which are measured at the kapton electrodes.

The EMCal is divided into barrel and two end-cap components. The barrel component consists of two identical half-barrels separated by a small gap of 4 mm at z = 0 covering the central region up to $|\eta| < 1.47$. The two end-caps, each built of two coaxial wheels, cover the region $1.375 < |\eta| < 3.2$.

All of the barrel and end-cap components consist of up to three layers. Figure 3.8 shows the three layers of accordion-shaped electrodes in the barrel module. The first of these layers, the *strip layer*, has a very high granularity $\Delta\eta \times \Delta\phi = 0.003 \times 0.1$ allowing good γ/π^0 and e/π distinctions. The second layer has granularity $\Delta\eta \times \Delta\phi = 0.025 \times 0.025$ and a thickness of about $16X_0$. Most of the energy of the electromagnetic showers is deposited in this layer. The third and final layer owns a depth of about $2X_0$ and a granularity $\Delta\eta \times \Delta\phi = 0.050 \times 0.025$. This layer helps to distinguish between electromagnetic and hadronic showers. In the end-cap region, the calorimeter is segmented in two sections in depth and has a coarser longitudinal granularity than for the rest of the acceptance.

In the region of $|\eta| < 1.8$, there is a *presampler* consisting of an active liquid-Argon layer with a thickness of 1.1 cm in the barrel and 0.5 cm in the end-caps. It is used to correct for the energy lost by electrons and photons by interactions with material in the Inner Detector.

The intrinsic resolution of energy measurements with the electromagnetic calorimeter

measured using electron, photon and pion beams [45, 46] is

$$\frac{\sigma(E)}{E} = \frac{a}{\sqrt{E}} \oplus b, \quad \text{with} \begin{cases} a = 10\%, b = 0.3\% & \text{(barrel)} \\ a = 10.0 - 12.5\%, b = 0.6\% & \text{(end-caps)} \end{cases} \tag{3.5}$$

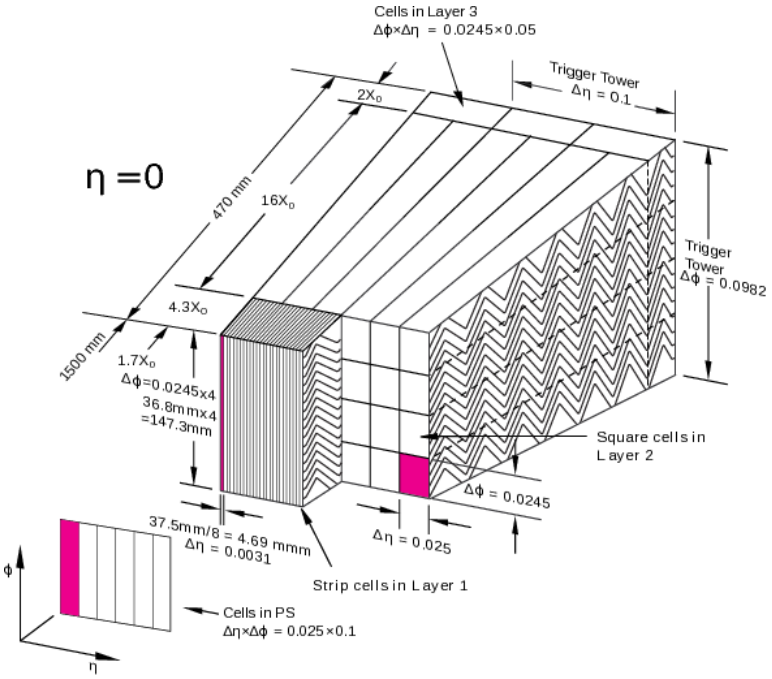

Figure 3.8 *Sketch of the barrel module of the electromagnetic calorimeter displaying the accordion-shaped electrodes with three layers (taken from Ref. [41]).*

Hadronic Calorimeter

The *hadronic calorimeter* (HCal) surrounds the electromagnetic one. It is used to measure the energy of hadrons (e.g. neutrons, protons, pions,...).

In the region of $|\eta| < 1.7$, a *tile calorimeter* (TileCal) is used, with three sets of barrel sections, each containing three layers. Plastic scintillator tiles are used as the active material and steel as the absorber. Particles passing through the calorimeter interact with the materials and produce low-energetic particles, which subsequently produce photons in the scintillator plates. These photons are collected at the edges of each tile and read out into two separate photomultiplier tubes by wavelength-shifting fibres. The typical granularity of the TileCal is $\Delta\eta \times \Delta\phi = 0.1 \times 0.1$ in the first and second layer and $\Delta\eta \times \Delta\phi = 0.1 \times 0.2$ in the third layer.

The $1.5 < |\eta| < 3.2$ range is covered by the *hadronic end-cap calorimeter* (HEC). The HEC consists of two wheels on each side of the barrel. Each wheel is divided into two sections with a total of four layers per end-cap. The wheels consist of liquid argon as active material and flat copper plates used as absorber material. The granularity of

the HEC is $\Delta\eta \times \Delta\phi = 0.1 \times 0.1$ in the region of $|\eta| < 2.5$ and $\Delta\eta \times \Delta\phi = 0.2 \times 0.2$ for larger values of η.

The *forward calorimeter* (FCal) covers the region $3.1 < |\eta| < 4.9$. The FCal consists of three layers per end-cap and uses liquid argon as active material. The first layer is made of copper and is used to measure the energy of electrons and photons while the second and third layers are made of tungsten and dedicated to the energy measurement of hadrons. The granularity of the FCal is $\Delta\eta \times \Delta\phi = 0.2 \times 0.2$.

The intrinsic resolution of energy measurements with the hadronic calorimeter measured using a pion beams [41] is

$$\frac{\sigma(E)}{E} = \frac{a}{\sqrt{E}} \oplus b, \quad \text{with} \begin{cases} a = 52\%, b = 3\% & \text{(EMCal and TileCal)} \\ a = 71\%, b = 5.8\% & \text{(HEC)} \\ a = 94\%, b = 7.5\% & \text{(FCal)} \end{cases} \tag{3.6}$$

3.2.4 Muon Spectrometer

The *muon spectrometer* (MS) is the outermost part of ATLAS detector. It is designed to detect muons that traverse through the Inner Detector and the calorimeter systems without being absorbed and to measure their momenta. An overview of the muon detector system is shown in Figure 3.9.

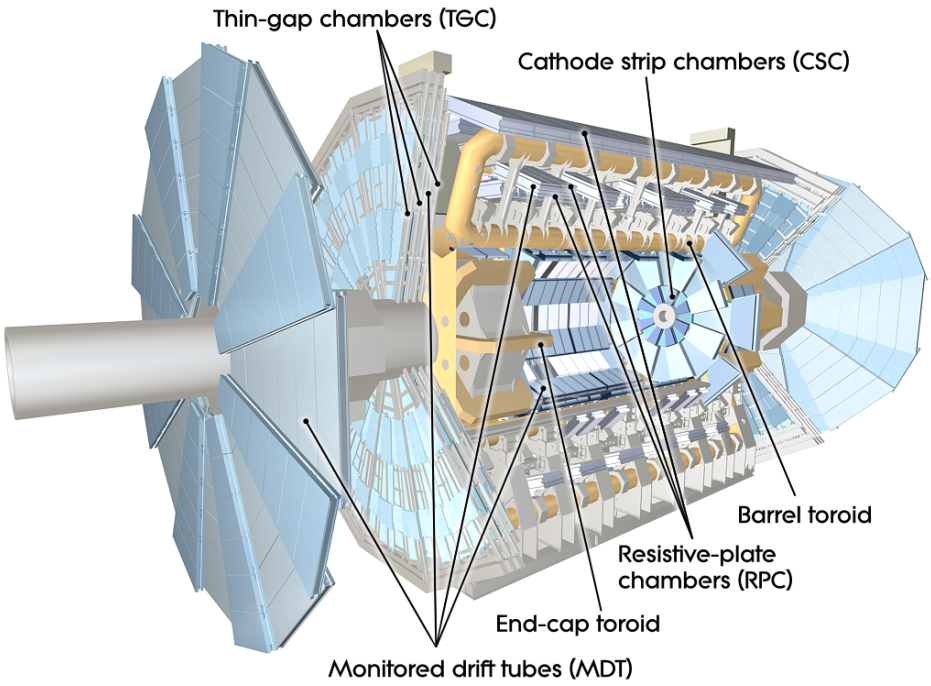

Figure 3.9 *The muon detector system of the ATLAS detector (taken from Ref. [41]).*

The muon spectrometer covers the pseudorapidity range up to $|\eta| < 2.7$ and allows for identification of muons with momenta above 3 GeV. It achieves a transverse momentum

resolution of $\sigma_{p_T}/p_T = 10\%$ for muons with energies of 1 TeV.

A toroidal magnetic system, consisting of eight large air-core toroid magnets in the barrel region $|\eta| < 1.4$ and two end-cap magnets in $1.6 < |\eta| < 2.7$, provides a magnetic field which causes the muons to be deflected and allows to measure their momenta. The field strength created by the magnetic system varies from 0.15 T to 2.5 T in the barrel region and from 0.2 T to 3.5 T in the end-cap region.

In the barrel region, the muon spectrometer consists of three cylindrical layers at radii of about 5, 7.5 and 10 m from the z-axis. Each of the layers consists of sixteen chambers which provide the information to precisely reconstruct the trajectories of charged particles and to measure their momenta. The momentum measurement is performed by the *monitored drift tube chambers* (MDT). These chambers cover a pseudorapidity range up to $|\eta| < 2.7$, except for the innermost layer which is limited to $|\eta| < 2.0$. For the innermost region $2.0 < |\eta| < 2.7$, the *cathode-strip chambers* (CSC), which are multi-wire proportional chambers, are used to provide higher rate capability and time resolution in the forward region.

In the end-cap regions, the muon chambers are constructed as four large wheels perpendicular to the z-axis that are positioned in front and behind the two end-cap magnets at distances of $|z| \approx 7.4$, 10.8, 14 and 21.5 m from the interaction point.

In addition, the muon spectrometer also includes independent trigger chambers that cover the η range up to 2.4 to provide fast information on the multiplicity of muon tracks and their approximate momenta. In the $|\eta| < 1.05$ region, the trigger chambers consist of three layers of *resistive plate chambers* (RPC) which are built of two resistive plates placed in parallel to each other at a distance of 2 mm. For the range $1.05 < |\eta| < 2.4$, the trigger chambers consist of four layers of *thin gap chambers* (TGC) which are multi-wire proportional chambers. They provide not only trigger information but also bunch-crossing and muon-coordinate information in the direction orthogonal to those of the tracking chambers.

3.2.5 Trigger System

Due to the high luminosity of 10^{34} cm^{-2}s^{-1} designed for LHC, the proton−proton interactions will occur at a rate of about 1 GHz. Recording every event is simply not possible due to data readout and transfer abilities. In addition, most collision events only involve low momentum transfers and hence are not interesting for the ATLAS experiment. Therefore, the ATLAS collaboration has developed a three stage trigger system to filter out the potentially relevant interaction processes. The three stages of this system are denoted as *Level 1* (L1), *Level 2* (L2) and *Level 3* (L3) or *event filter* (EF). The work flow of the trigger system is summarized in Figure 3.10.

The L1 trigger system is implemented at hardware level to select events using reduced information from various sub-detectors. This level brings the event rate down to 75 kHz. Only a subset of the ATLAS detector systems, providing reduced-granularity

information from the calorimeter and muon systems (RPCs and TGCs), is used at this stage. Based on this information, events that contain particular signatures are pre-filtered. Trigger objects such as electrons, photons, jets and hadronically decaying τ-leptons, missing and total transverse energy are reconstructed using coarse detector information. *Regions of interests* (RoIs) are defined as the regions of the detector where interesting signatures are recognized in the event. The RoIs are further analyzed by the *central trigger processor* (CTP) and a final L1 trigger decision is made.

The L2 trigger is software-based. It is seeded by the RoIs from L1 and refines the event information stored in RoIs by acquiring additional information from the detector components. The decisions based on these informations reduce the event rate to about 1 kHz.

The final online selection is made by the EF. At this stage, reconstruction algorithms are used to analyze the information from the calorimeter using its full granularity, the muon spectrometer and the complete Inner Detector to fully reconstruct an selected event. The event rate is reduced to about 400 Hz, at which the events are finally recorded.

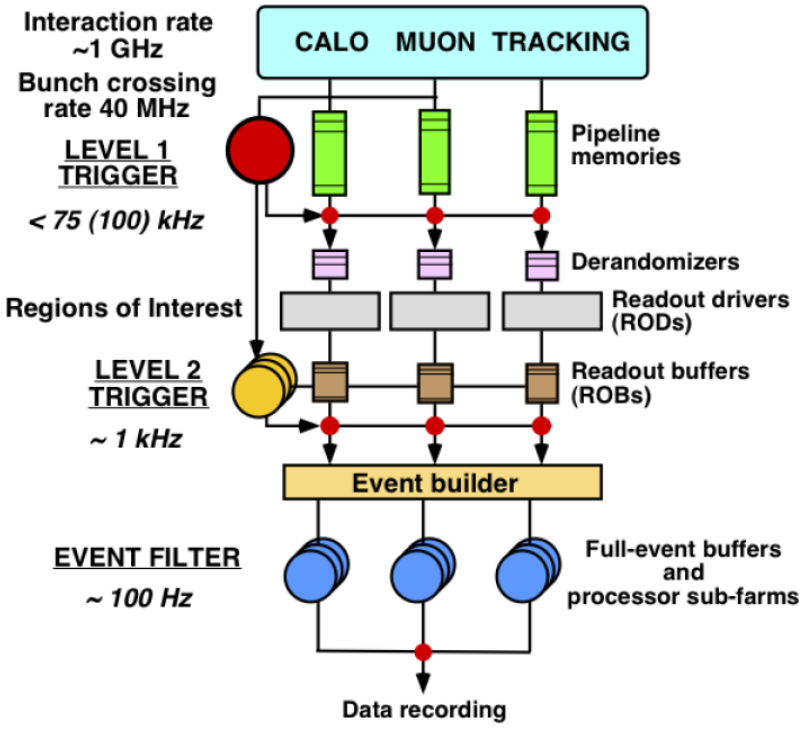

Figure 3.10 *The ATLAS trigger chain (taken from Ref. [47]).*

3.2.6 Luminosity Measurement

The luminosity measurement for the ATLAS experiment is performed by using additional detectors which are placed at large distances to the interaction point and close to the beam axis in order to measure event activities in the very forward directions.

There are two primary detectors, namely LUCID and BCM used to determine bunch-by-bunch luminosity measurements.

The LUCID Detectors

The luminosity monitor LUCID used in ATLAS experiment is made of two detectors placed around the beam-pipe on both forward ends. Those detectors are located at a distance of $z = \pm 17$ m on each side of the interaction point. Each detector is composed of 16 photomultipliers close to the beam-pipe and 4 quartz fibre bundles read by photomultipliers in a shielded location. By analyzing the pulse-height of the tube signals, the number of particles that pass the LUCID detector can be computed at each bunch crossing. Since this number is proportional to the number of proton$-$proton interactions that took place in a bunch crossing the instantaneous luminosity can be determined.

The BCM Detectors

The *Beam Conditions Monitor* (BCM) [48] consists of four small diamond sensors located on each side of the ATLAS detector at $z = \pm 1.84$ m. The sensors are arranged around the beam pipe in a cross pattern. The BCM is designed to detect early signs of beam instabilities and to issue a beam-abort request in case beam losses start to risk damage to ATLAS detectors. Additionally, the fast readout of the BCM provides a measurement of bunch-by-bunch luminositiy in the ATLAS detector at $|\eta| = 4.2$. It provides an independent cross-check to the results obtained with the LUCID detector.

4

Event Reconstruction and Object Identification

The physics objects recorded by the ATLAS detector need to be identified and reconstructed by using all information from the detector. This section describes the procedures used for reconstructing physics objects which are electrons, muons, jets and missing transverse energy. These objects are of interest for the $H \to WW^* \to l\nu l\nu$ analysis.

4.1 Track and Vertex Reconstruction

4.1.1 Track Reconstruction

The track reconstruction is important as input for the reconstruction of charged particles such as muons, electrons, taus and jets. Charged particle tracks can be measured up to $|\eta| < 2.5$. The track reconstruction is basically divided into three stages [49]

- In a first step, the raw data from pixel and SCT detectors are converted into clusters and the TRT raw timing information is converted into calibrated drift-circles.
- In the next step, various track finding algorithms are used. One of the algorithms is the *inside-outside scheme* which is is used to combine the individual signals in the inner detector components, denoted as hits, to form a combined particle track. Another additional algorithm is called *back-tracking* which is used to reconstruct additional tracks of charged particles mainly produced at some distance to the interaction point. This gives an improvement of the tracking effciency for tracks originating from conversions or long-lived particle decays [50].
- In the last step, the dedicated vertex finding and fitting algorithms are used to reconstruct primary vertices of the events.

4.1.2 Primary Vertex Reconstruction

A *primary vertex* is a position of the primary interaction point of the proton-proton collision. It can be reconstructed by grouping the tracks of those charged particles that might have been produced in the same interaction. Furthermore, the number of reconstructed vertices provides a direct measure of in-time pile-up on an event-by-event basis. The procedure of primary vertex reconstruction is described as follow [51]

- First, all reconstructed tracks satisfying certain quality criteria are extrapolated towards the beam line.
- A vertex seed is determined by looking for the global maximum in the distribution of their z-coordinates at the point of closest approach to the nominal interaction point.
- An adaptive vertex fitter is designed to reconstruct the vertex position [52].
- A χ^2 fit is performed, those tracks for which the fit yields $\chi^2 < 49$ are considered to be associated to that vertex. The remaining tracks are used to seed a new vertex.
- The above procedure is repeated until no additional vertex is found.

4.2 Electron Reconstruction and Identification

4.2.1 Electron Reconstruction

The reconstruction of electrons is initiated from energy deposits in the electromagnetic calorimeter, and then matched with reconstructed tracks in the inner detector. Electron identification is restricted to objects within the range $|\eta| < 2.47$ due to the inner detector acceptance, excluding the $1.37 < |\eta| < 1.52$ region as this is the transition region between the barrel and the end-cap of the electromagnetic calorimeter.

The electron reconstruction algorithm starts from defining clusters of energy deposit in electromagnetic calorimeter cells. The clusters are reconstructed by a *sliding-window* algorithm. This algorithm is based on rectangular towers of 3×5 cells on the $(\Delta\eta \times \Delta\phi)$ plane, at the second calorimeter layer. A window with fixed size of 5×5 towers moves across the $(\Delta\eta \times \Delta\phi)$ plane and forms clusters if the total transverse energy E_T inside the window is above 2.5 GeV.

The electron candidates are defined if at least one reconstructed track from the inner detector matches to the cluster. The matching tracks are extrapolated to the middle layer of the calorimeter and must not be matched to a conversion process $\gamma \to e^+e^-$ when testing the geometrical distance between the track impact point and the cluster position. The maximum allowed distance in η-direction is 0.05, and in ϕ-direction 0.1 on the side where the track bends due to the magnetic field and 0.05 on the opposite side. An additional requirement on the ratio of cluster energy to track momentum $E/p < 10$ is applied in order to reject hadrons reconstructed as electron candidates.

The electromagnetic cluster is then refined using a larger cluster size 3×7 (5×5) in the barrel (end-caps). The cluster energy is re-computed with taking into account the energy loss in the material in front and beyond the electromagntic calorimeter, the measured energy of the reconstructed cluster and the lateral energy leakage outside the cluster. The four-momentum of electron is computed using the cluster energy and the associated track direction.

4.2.2 Electron Identification

The electron identification relies on a cut-based selection using variables that include calorimeter, tracker and combined information to separate between isolated electrons and jets (faking electrons). Three sets of selections are defined with increasing background rejection power, each set contains the preceding one [53]

- The `Loose` identification is based on shower shapes of the second electromagnetic calorimeter layer and the hadronic calorimeter.
- The `Medium` identification furthermore includes information from the strip layer, track quality requirements and tighter track-to-cluster matching constraints.
- The `Tight` identification adds requirements on the ratio of cluster energy to track momentum E/p, the number of low and high energetic hits in the TRT, the number of hits in the innermost layer (B-layer) and information on reconstructed vertices of γ conversions.

The cuts are optimized in bins of cluster E_T and η. The expected jet rejection rate obtained from Monte Carlo simulation is 1/500, 1/5000 and 1/50000, respectively. In addition, a re-optimized menu is defined for electrons providing three additional operating points (`Loose++`, `Medium++` and `Tight++`) with improved performance for a higher pile-up environment.

Furthermore, a *multi-variate analysis* (MVA) *likelihood* (LH) technique is used in order to have better background rejection. This technique is based on the combined evaluation of several properties during the selection decision.

The electron identification efficiencies are obtained by using $Z \to ee$ events. The data to Monte Carlo simulation ratios (scale factors) are derived to correct the Monte Carlo efficiency predictions. Figure 4.1 shows the electron identification efficiency measurements at $\sqrt{s} = 13$ TeV as a function of transverse energy E_T and η.

4.2.3 Electron Isolation

Electrons produced from decays of heavy particles like W or Z bosons are usually isolated from other neutral or charged particles. Several variables can be defined to reflect the degree of isolation which depends on the specific analysis needs. Detailed studies of the variables can be found in Ref. [53].

The track-based isolation variables are sensitive to contributions from additional

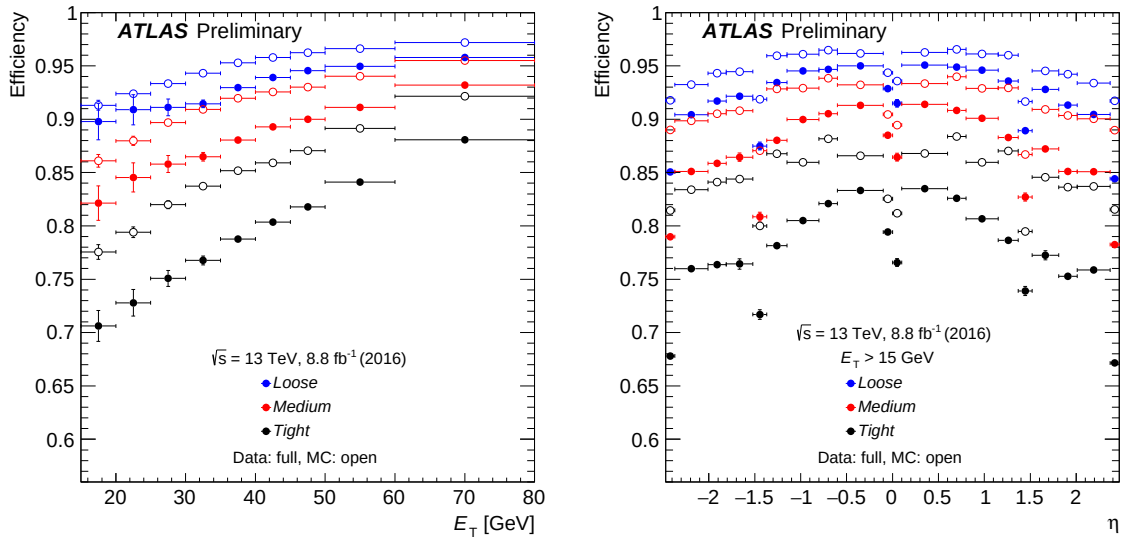

Figure 4.1 *Electron identification efficiency in $Z \to ee$ events as a function of transverse energy E_T (left) and η (right). The efficiency is shown for three operating points that are based on a likelihood approach,* ***Loose****,* ***Medium*** *and* ***Tight****. The efficiencies have been measured in 88 pb^{-1} of data recorded by the ATLAS experiment in 2016 at $\sqrt{s} = 13$ TeV, and are compared to MC simulation (taken from Ref. [54]).*

charged particles. They are defined as a scalar sum of all the transverse momenta of selected tracks in a varying cone of maximum size ΔR_{iso} around the electron candidate

$$P_T^{cone\,\Delta R_{iso}} = \sum_{track} p_T^{track} \tag{4.1}$$

where the electron track itself is excluded from the sum. Only tracks that satisfy $p_T > 1$ GeV and are associated to the same primary vertex with the electron are taken into account.

The calorimeter-based isolation variables are sensitive to energy contributions from additional charged and neutral particles. They are computed from the energy deposited in a cone of radius ΔR_{iso} around the electron candidate

$$P_T^{cone\,\Delta R_{iso}} = \left(\sum_{topoclusters} E_T \right) - E_T(5 \times 7 \text{ cells}) \tag{4.2}$$

where the energy in 5×7 cells of the electron cluster is removed.

Figure 4.2 shows the track-based and calorimeter-based isolation variables using a varying cone size of $\Delta R = 10$ GeV$/E_T$ (maximum 0.4) and a cone size of $\Delta R = 0.4$, respectively. There are two main effects which can bias the isolation computation: the lateral leakage of the electron cluster into the isolation cone, and the energy deposited from other collisions before and during the bunch crossing of interest (i.e. pile-up). Dedicated corrections for these effects are documented in Ref. [55].

While a larger cone size contains more energy in case of misidentified jets, a smaller

cone size is more robust against energy deposits from pile-up. It is found that a cone of $R_{iso} = 0.3$ around the electron gives the best trade-off between high discrimination power and robustness against pile-up [55].

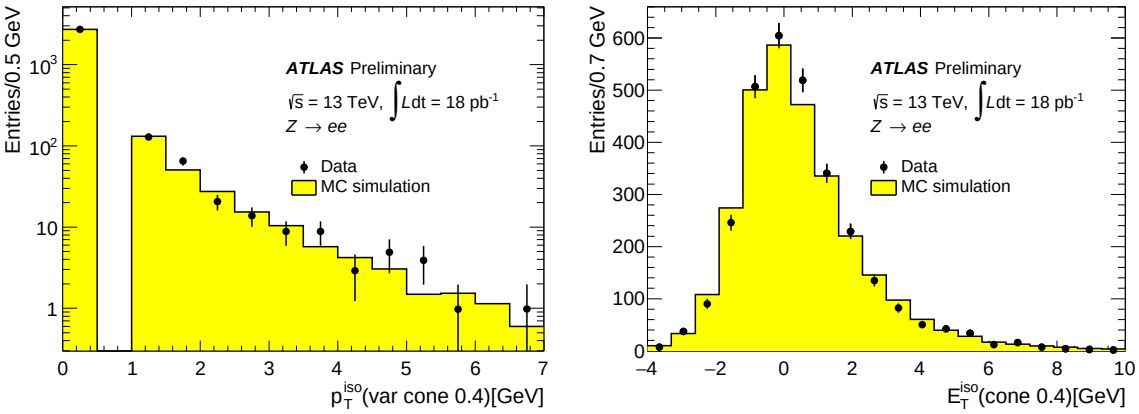

Figure 4.2 *Electron isolation distributions from $Z \to ee$ events for electrons with $E_T = 40{-}50$ GeV, using data recorded in June and July 2015. The p_T^{iso} (left plot) is the sum of the transverse momentum of the tracks with $p_T > 1$ GeV in a varying cone of $\Delta R = 10$ GeV/E_T(lepton) (maximum 0.4) around the electron, excluding the track of the electron itself. The E_T^{iso} (right plot) is the sum of energies of clusters around the electron in a cone with radius $\Delta R = 0.4$, excluding cells in a window of $\Delta\eta \times \Delta\phi = 0.125 \times 0.175$ around the electron cluster barycenter (taken from Ref. [56]).*

4.3 Muon Reconstruction and Identification

4.3.1 Muon Reconstruction and Identification

The reconstruction of muons is performed using the information from the muon spectrometer and the inner detector. There are different strategies to identify muons [57]

- *Combined* (CB) muons are based on combination of tracks reconstructed independently in the inner detector and the muon spectrometer. The matching of the tracks is performed by a χ^2 test.
- *Segment-tagged* (ST) muons are identified if the tracks measured in the inner detector and extrapolated to the muon spectrometer are associated with at least one local track segment in the MDT or CSC chambers.
- *Calorimeter-tagged* (CT) muons are identified if if the tracks measured in the inner detector can be matched to an energy deposit in the calorimeter compatible with a minimum-ionizing particle.
- *Extrapolated* (ME) muons are reconstructed from tracks measured in the muon spectrometer. The multiple scattering process and energy loss of the muon in the calorimeter is also taken into account.

Among those types, CB muons give the highest purity. The ST muons give higher efficiency than CB ones as they can recover muons which did not cross enough precision

chambers and low-p_T muons which only reach the inner layer of the muon chambers. The reconstruction of CB, CT and ST muons is restricted within the range $|\eta| < 2.7$ due to the inner detector acceptance. In the ATLAS experiment, there are three main algorithm chains for reconstructing CT, ST and CB muons [57]

- *Staco* (chain 1): it is required that the muon momentum is measured in both the inner detector and the muon spectrometer. The momentum of the combined muon is then calculated as the weighted average of the independent momentum measurements.
- *MuID* (chain 2): instead of statistical combination, a fitting to all muon hits in the inner detector and the muon spectrometer is performed. The fit includes recovery of missing or wrongly assigned spectrometer hits, mostly arising from missing or low quality information of the muon spectrometer in the transverse projection.
- *MUON* (chain 3): a unified reconstruction program has been developed to incorporate the best features of the two previous chains.

4.3.2 Muon Identification

The muon identification is performed by applying quality requirements that suppress background, mainly from pion and kaon decays, and selecting prompt muons with high efficiency while guaranteeing a robust momentum measurement. Four muon identification selections are provided [58]

- The `Medium` identification uses only ME and CB tracks with requirements on number of hits, difference between the ratio of the charge and momentum of the muons measured in the inner detector and muon spectrometer (*q/p significance*).
- The `Loose` identification uses all types of muons, ME and CB muons satisfy the `Medium` requirements while CT and ST muons are restricted to a small central region.
- The `Tight` identification uses only CB muons that satisfy the `Medium` requirements.
- The `High-`p_T identification uses CB muons passing the `Medium` selection with an additional requirement on the number of muon spectrometer hits.

The muon reconstruction efficiencies are obtained by using $Z \to \mu\mu$ events. Figure 4.3 shows the muon reconstruction efficiency measurements at $\sqrt{s} = 13$ TeV as a function of η.

4.3.3 Muon Isolation

Muons from hadronic decays are accompanied by additional particles. Thus, a powerful quantity to reject those muons is the isolation. Similar to the electron isolation described in Section 4.2.3, the tracking-based isolation is a scalar sum of the transverse

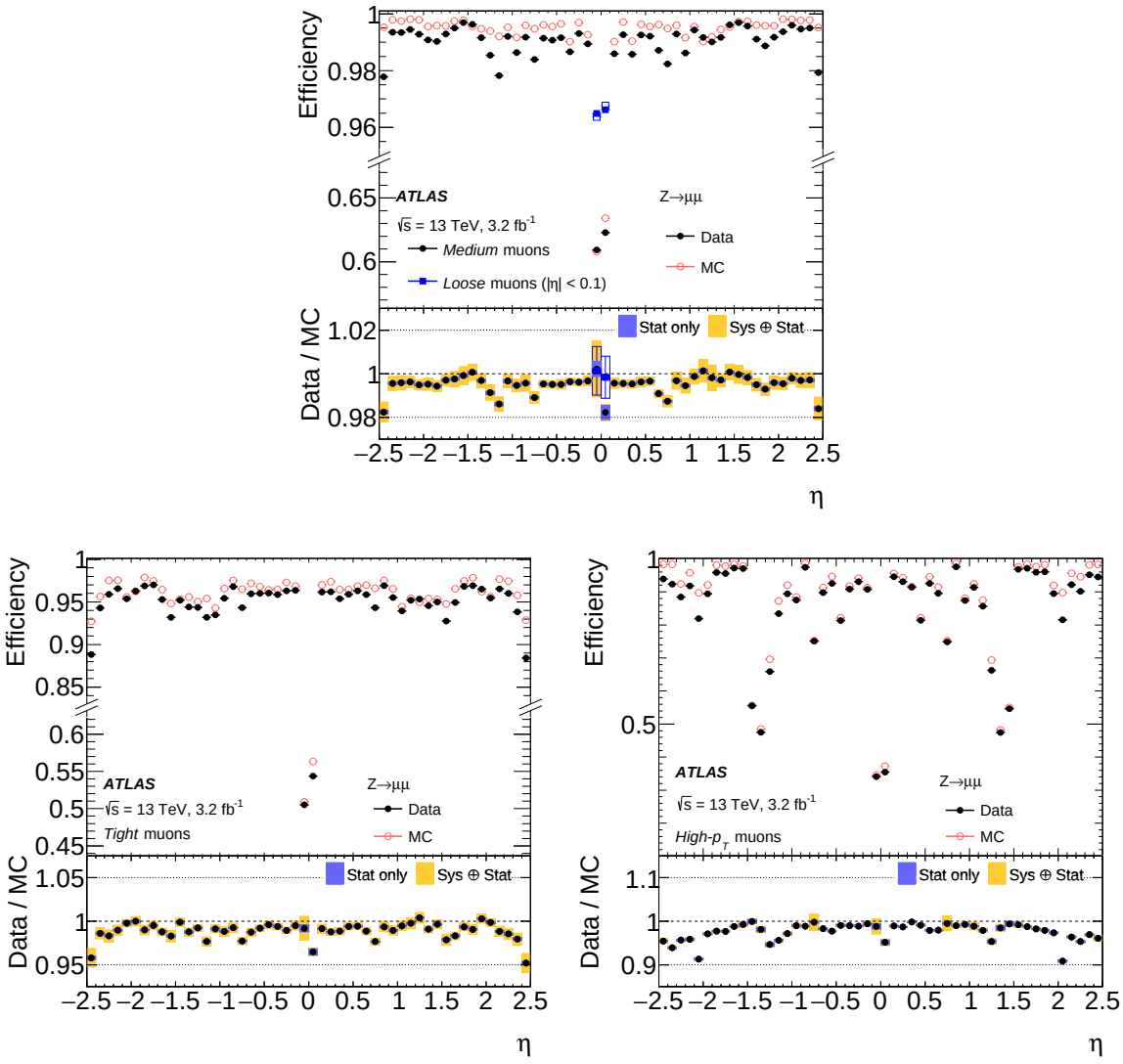

Figure 4.3 *Muon reconstruction efficiency as a function of η measured in $Z \to \mu\mu$ events for muons shown for the* `Medium` *and* `Loose` *(top),* `Tight` *(bottom left) and* `High-`p_T *(bottom right) muon selections (taken from Ref. [58]).*

momenta of the tracks in a varying cone of ΔR_{iso} around the muon, excluding the muon track itself. And the calorimeter-based isolation is calculated by adding up the energy measured in the calorimeter topoclusters within a cone of ΔR_{iso} around the muon, excluding the energy in the cells associated to the muon after corrections for leakage and pile-up effects.

The measured and simulated relative isolation variables divided by the p_T of the probe muons are shown in Figure 4.4.

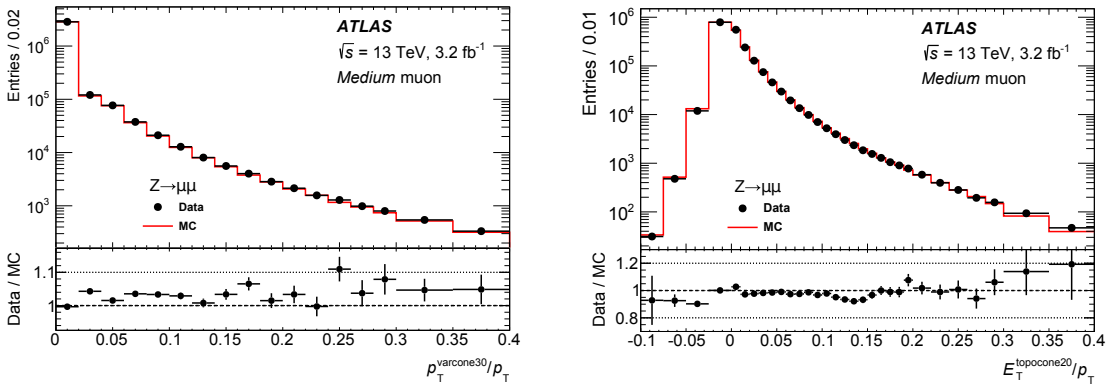

Figure 4.4 *Distribution of the track-based (left) and calorimeter-based (right) relative isolation variables measured in $Z \to \mu\mu$ events. Muons are selected by the* `Medium` *identification algorithm (taken from Ref. [58]).*

4.4 Jet Reconstruction and Identification

4.4.1 Jet Reconstruction

There are many algorithms and methods in the ATLAS experiment to reconstruct and calibrate hadronic jets, which are described in detail in Refs. [59, 60]. In this analysis, jet objects are reconstructed based on the *anti-k_T* algorithm.

The reconstruction of jets starts from a *topological cluster* which is seeded by calorimeter cells with a energy at least four times higher than the *root-mean-square* (RMS) of the noise distribution. Neighbouring cells will be added to the cluster if their *signal-to-noise-ratios* are above a threshold and serve as additional seeds to iteratively expand the cluster.

The anti-k_T algorithm evaluates the resolution variables d_{ij} between objects i and j and d_{iB} between object i and the beam (B)

$$\begin{aligned} d_{ij} &= \min\left(1/p_{T,i}^2, 1/p_{T,j}^2\right) \frac{\Delta R_{ij}^2}{R^2} = \min\left(1/p_{T,i}^2, 1/p_{T,j}^2\right) \frac{\Delta\eta_{ij}^2 + \Delta\phi_{ij}^2}{R^2} \\ d_{iB} &= p_{T,i}^{-2} \end{aligned} \tag{4.3}$$

where $p_{T,i}$ is the transverse momentum of object i and R is a fixed distance parameter which is chosen to be 0.4 for the jets used in this analysis.

The clustering proceeds by identifying the smallest of these distances. If the smallest is d_{ij} the two objects i and j are recombined, whereas if it is d_{iB} i is called a jet and removed from the list. The cycle goes on until no objects are left over. This is done in a way that soft p_T objects tend to cluster with hard ones before they cluster among themselves. If there is a second hard object in the event, two formed hard objects will share a boundary which depends on the ratio of energy of the two particles. The behaviour of the anti-k_T algorithm at a parton-level event is illustrated in Figure 4.5.

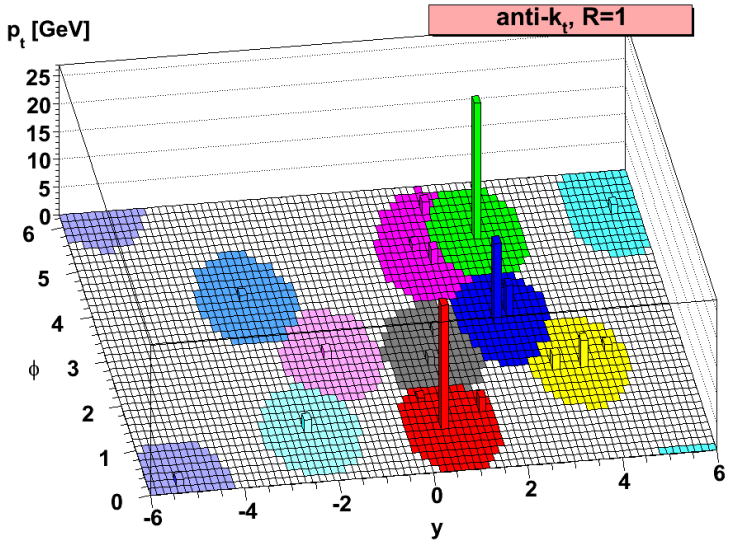

Figure 4.5 *A sample parton-level event (generated with HERWIG [61]) with the anti-k_T algorithm, together with many random soft "ghosts", illustrating the "active" catchment areas of the resulting hard jets (taken from Ref. [59]).*

The calorimeter response to hadrons is lower than its response to electrons or photons. Therefore, several jet calibration schemes have been developed [43]. The energy of the reconstructed clusters is calibrated using the *Local Cluster Weighting* (LCW) scheme. The electromagnetic scale calibration is used as the baseline calibration and energy corrections for hadronic clusters are derived using simulated pion events. In addition, corrections for a lower calorimeter response for hadronic particles compared to electromagnetic ones (*"calorimeter non-compensation"*), signal losses due to noise threshold and energy lost in non-instrumented regions are also applied.

The misreconstructed jets, *"fake jets"* or *"bad jets"*, arise from hardware problems, LHC beam conditions and cosmic-ray showers. Two main types of misreconstructed jets are jets not associated to in-time energy depositions in the calorimeters, and jets coming from real energy depositions in calorimeter regions which have not yet been properly calibrated [62]. The jet cleaning cuts on jet-energy fractions and jet time (t_{jet}) are applied to reject these bad jets.

4.4.2 b-Jet Identification

Jets originating from b-hadrons (denoted as *"b-jets"*) play an important role in the Higgs boson searches. They are distinguished from gluon or light quark jets by using *"b-tagging"* algorithms. This tagging is applied to jets reconstructed by the anti-k_T algorithm with a distance parameter of $\Delta R = 0.4$. The jets are generally required to have $p_T > 20$ GeV and $|\eta| < 2.5$. Several properties of b-jets can be used to distinguish them from the other gluon or lighter quark jets: the lifetime of b-hadrons is relatively long (∼1.5 ps), thus it can travel several millimeters before decaying. A b-hadron most

likely decays into a c-hadron which decays further into lighter quarks, therefore a large number of charged particle tracks are associated to a b-jet. All of these reconstructed tracks will have a large impact parameters and the decay vertex of the b-hadron can be reconstructed in many cases. Figure 4.6 illustrates the characteristics of a b-hadron decay.

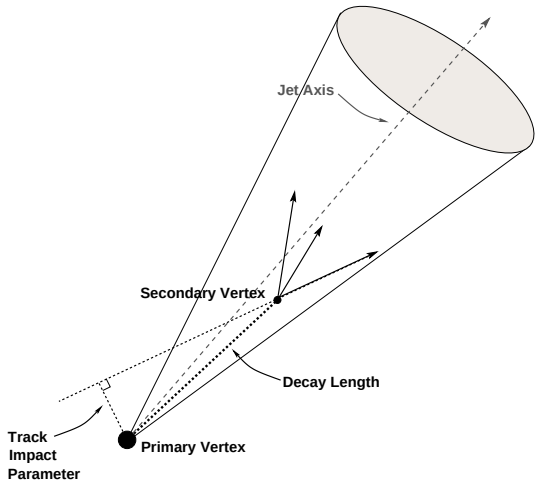

Figure 4.6 *A secondary vertex with a significant decay length indicates the presence of a b-quark in the jet. The secondary vertex is reconstructed from tracks with a large impact parameter significance with respect to the primary vertex. (taken from Ref. [63]).*

Several algorithms to identify jets originating from b-hadrons has been developed [64], some of them are

- The `IP3D` algorithm is one of the impact-parameter based algorithms, compares selected input variables to pre-defined two-dimensional probability functions obtained from simulation for both the b- and light jet hypotheses.
- The `SV0` and `SV1` algorithms aim to reconstruct the vertex of the b- or c-hadron decay.
- The `JetFitter` algorithm is one of the vertex- and lifetime-based tagging algorithms. It aims to reconstruct the complete decay chain of b-hadrons using Kalman filter.
- The `JetFitterCombNN` algorithm uses an artificial neural network to combine the `IP3D` and `JetFitter` algorithms.
- The `MV1` algorithm further combines the `IP3D`, `JetFitterCombNN` and `SV1` algorithms in a neural network.

A tagging algorithm is characterized by the efficiency ϵ_b by which a jet originating from a b-hadron is tagged and by the probability of mistakenly tagging a jet originating from a light-flavour parton (u-, d-, s-quark or gluon) as a b-jet, referred to as *mistag rate*. The b-tagging efficiency is measured in an inclusive sample of jets containing muons and in top-quark pair events with one or two leptons in the final state [65], and the mistag rate is measured in an inclusive jet sample [66]. The results of these measurement were shown in Figure 4.7 and Figure 4.8.

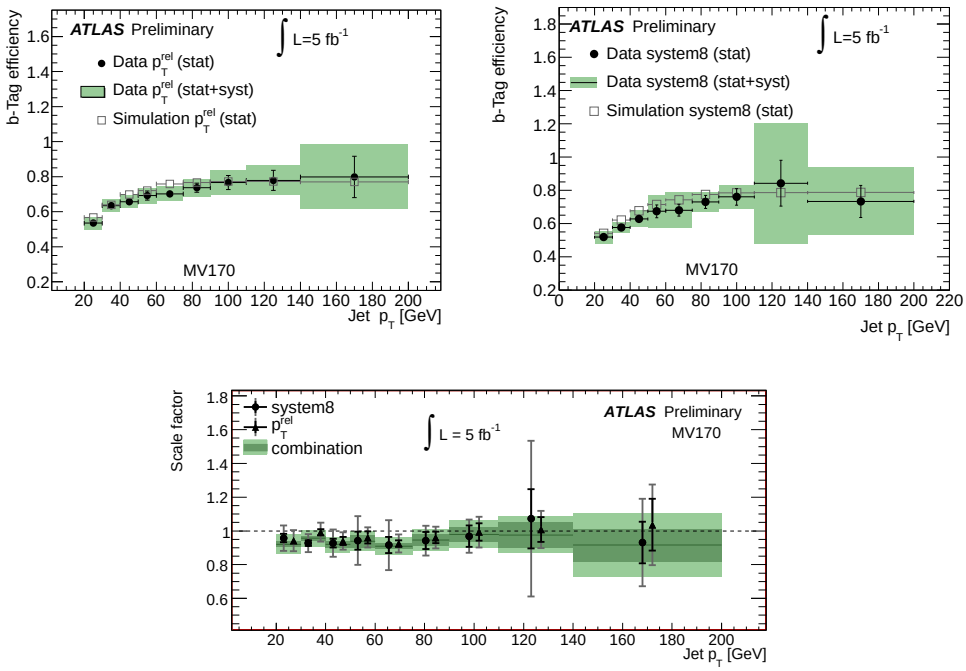

Figure 4.7 *The b-tagging efficiency in data and simulation for the 70% efficiency working point of the* `MV1` *algorithm (MV170) as a function of the jet p_T using "p_T^{rel}" (top left) and "system8" (top right) methods. The correction factors for both methods and their combination are shown in the bottom plot (taken from Ref. [65]).*

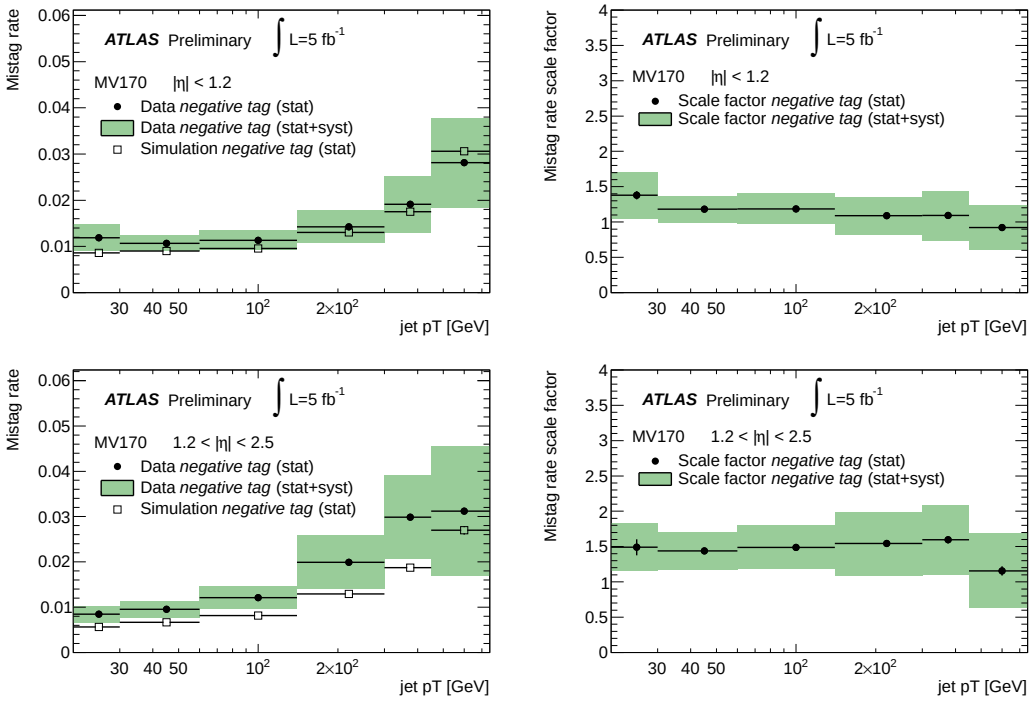

Figure 4.8 *The mistag rate within the pseudorapidity range $|\eta| < 1.2$ (top left) and $1.2 < |\eta| < 2.5$ (top right) as a function of the jet p_T using "negative tag" method. The correction factors for the mistag rate is shown within $|\eta| < 1.2$ (bottom left) and $1.2 < |\eta| < 2.5$ (bottom right) (taken from Ref. [66]).*

4.5 Missing Transverse Momentum

In proton-proton collision, since the undetectable particles such as neutrinos or weakly-interacting particles in final state are not directly recorded in the ATLAS system, there is an imbalance in the momentum distribution in the transverse plane. The missing transverse momentum, denoted as E_T^{miss}, is computed from the negative vector sum of the momenta of all objects reconstructed in an event [67]. It also takes into account the contributions from energy deposits and low-p_T tracks which are not assigned to any reconstructed objects (soft term). The $E_{x(y)}^{miss}$ components are calculated as

$$E_{x(y)}^{miss} = E_{x(y)}^{miss,e} + E_{x(y)}^{miss,\gamma} + E_{x(y)}^{miss,\tau} + E_{x(y)}^{miss,jets} + E_{x(y)}^{miss,\mu} + E_{x(y)}^{miss,soft} \tag{4.4}$$

where each object term is given by the negative vectorial sum of the momenta of the respective calibrated objects: electrons (e), photons (γ), hadronically decaying τ-leptons, jets and muons (μ). The $soft$ term is reconstructed from objects not passing the object selection cuts, which are either track-based (inner detector tracks) or calorimeter-based (calorimeter signals) soft terms.

The value of E_T^{miss} is then calculated as

$$E_T^{miss} = \sqrt{(E_x^{miss})^2 + (E_y^{miss})^2} \tag{4.5}$$

and the azimuthal angle

$$\phi_T^{miss} = \arctan\left(E_y^{miss}/E_x^{miss}\right) \tag{4.6}$$

To estimate the event activity, the quantity $\sum E_T$ is used

$$\sum E_T = \sum p_T^e + \sum p_T^\gamma + \sum p_T^\tau + \sum p_T^{jets} + \sum p_T^\mu + \sum p_T^{soft} \tag{4.7}$$

The performance of E_T^{miss} reconstruction studied with $Z \to \mu\mu$ events is shown in Figure 4.9. The Monte Carlo simulation gives a reasonable agreement with data for $Z \to \mu\mu$ events. The resolution of the E_T^{miss} measurement is shown in Figure 4.10, it is limited by the finite resolution of the energy measurements, the presence of inactive material and the limited solid angle coverage of the detector.

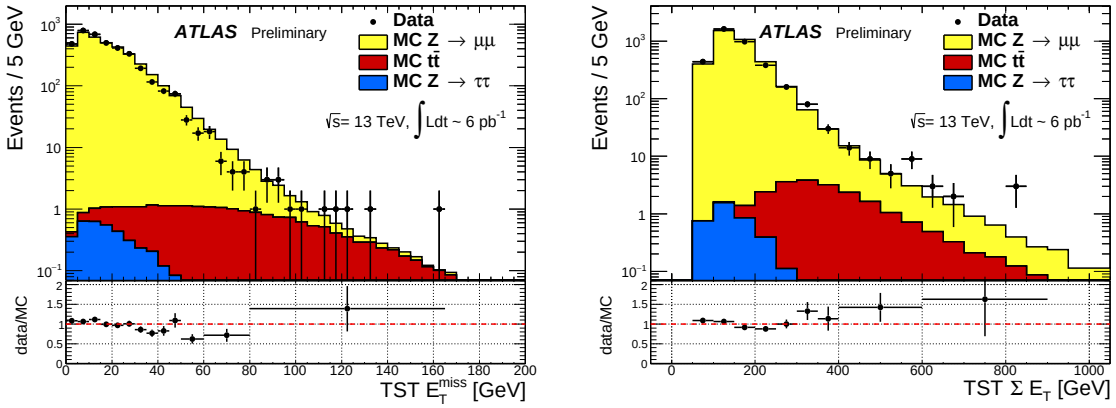

Figure 4.9 *Distributions of track-based soft-term E_T^{miss} (left) and $\sum E_T$ in $Z \to \mu\mu$ events. The expectation from MC simulation is superimposed and normalized to data, after each MC sample is weighted with its corresponding cross-section (taken from Ref. [67]).*

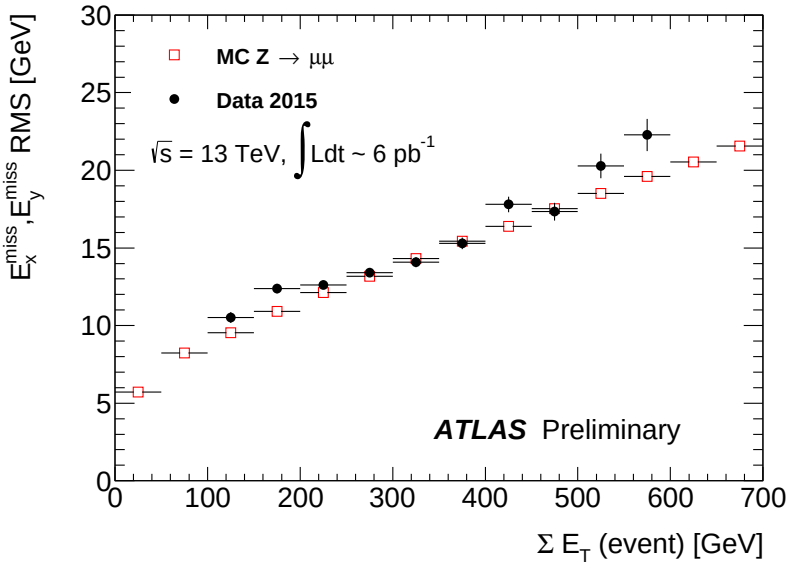

Figure 4.10 *Distributions of track-based soft-term E_x^{miss}, E_y^{miss} resolution as a function of $\sum E_T$ in $Z \to \mu\mu$ events. The data (black circles) and MC simulation (red squares) are overlaid. (taken from Ref. [67]).*

4.6 Overlap Removal

In case two or more objects are reconstructed nearby in the η-ϕ plane, a so-called *"overlap removal"* procedure is applied to avoid double counting between these objects. For the $H \to WW^* \to l\nu l\nu$ analysis, this procedure is

- If an electron is within $\Delta R < 0.1$ of any muon, the electron is removed since it indicates a case that the muon has undergone bremsstrahlung within the inner detector or calorimeter.
- If an electron is within $\Delta R < 0.05$ of any muon, the whole event is removed.
- If two electrons are separated by $\Delta R < 0.1$, the lower p_T electron is removed

since an electron can produce a secondary electron which has lower p_T.

- If an electron is within $\Delta R < 0.3$ of a jet, the jet is removed since a high p_T electron can be reconstructed as a jet.
- If a muon is within $\Delta R < 0.3$ of a jet, the muon is removed.

This procedure is summarized in Table 4.1.

Table 4.1: Summary of overlap removal procedure.

Objects	ΔR	Remove
$\mu - e$	< 0.1	electron
$\mu - e$	< 0.05	event
$e - e$	< 0.1	lower p_T electron
$e - jet$	< 0.3	jet
$\mu - jet$	< 0.3	muon

5

Search for the Higgs Boson in the $H \to WW^* \to l\nu l\nu$ Decay Mode using $\sqrt{s} = 7$ TeV and 8 TeV Data from the LHC Run 1

This chapter gives an overview of the analysis processes related to the search for the Standard Model Higgs boson in the $H \to WW^* \to l\nu l\nu$ channel ($l = e, \mu$) using the complete data samples taken at $\sqrt{s}$ = 7 TeV and 8 TeV. This chapter is organized as follows: Section 5.1 describes the characteristics of the signal process and various background processes which can contribute to the analysis. A detailed description of the data and Monte Carlo samples collected by the ATLAS experiment used in the analysis is given in Section 5.2. The object and event selection employed is provided in Section 5.3. The sources and evaluation of dominant systematic uncertainties considered are covered in Section 5.4. Section 5.5 presents the statistical treatment and Section 5.6 presents the results of the analysis.

5.1 Physics Process of the $H \to WW^* \to l\nu l\nu$ Decay Mode

5.1.1 Signature of the $H \to WW^* \to l\nu l\nu$ Decay Mode

The signature of the channel is characterized by the decay products of the W bosons as shown in Figure 5.1. Both W bosons decay leptonically into two isolated, oppositely charged leptons (either electrons, muons or taus) and neutrinos which cause large missing transverse momentum.

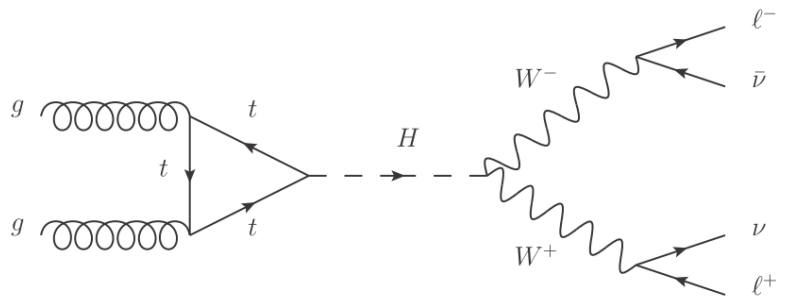

Figure 5.1 *Leading order Feynman diagram of a Higgs boson produced via gluon-gluon fusion decaying to a pair of W bosons, which in turn decay leptonically.*

There are four final states considered in this analysis: $e\nu e\nu$, $\mu\nu\mu\nu$, $e\nu\mu\nu$ and $\mu\nu e\nu$ which are denoted as ee, $\mu\mu$, $e\mu$ and μe, respectively. The difference between $e\mu$ and μe in this analysis is that the $e\mu$ has events which have the electron's p_T higher than the muon's one and vice versa. The major part of the signal is via direct $W \to e\nu$ and $W \to \mu\nu$ decays, however, a small contribution via an intermediate τ lepton ($\tau \to e\nu$ or $\tau \to \mu\nu$) is implicitly included. In addition, there may be jets in the final state created by VBF production or gluon radiation. Therefore, the analysis is categorized into jet multiplicities which are denoted as the $N_{jet} = 0$, $N_{jet} = 1$ and $N_{jet} \geq 2$ categories.

Due to the presence of neutrinos in the final state, it is not possible to fully reconstruct the invariant mass from all decay products to observe a Higgs boson mass peak. Thus, a transverse mass m_T [68], which is computed from the leptons and the missing transverse momentum, is used to test for the presence of a signal.

Since the Higgs boson is a spin-0 particle, the charged leptons tend to be emitted in the same direction, with the two neutrinos produced in the opposite direction to balance the di-lepton system as shown in Figure 5.2. The lepton and anti-lepton in the final state are preferably emitted in the same direction. The two neutrinos tend to go into the opposite direction to the leptons resulting in a large missing transverse momentum.

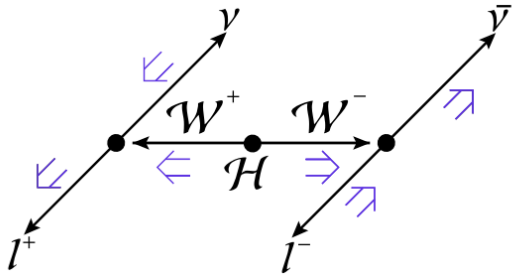

Figure 5.2 *Illustration of the $H \to WW^* \to l\nu l\nu$ decay, showing the directions of particle motion with the thin arrows (black), and the spin projections with the double arrows (blue).*

5.1.2 Background Processes

By focusing on the leptonic decays of the W bosons, many background processes which contain oppositely charged leptons and missing transverse energy in the final state have to taken into account. The most important backgrounds are the non-resonant WW production, top-quark pairs, Z/γ^*+jets (Drell-Yan process), W+jets and WZ/ZZ/Wγ production. A precise knowledge of the background processes is important to achieve an effective reduction of the individual components while retaining most of the expected signal events.

WW production

The dominant background to the $H \to WW^* \to l\nu l\nu$ search arises from WW boson pairs which are mainly produced through quark−antiquark annihilation at the LHC. The leading order Feynman diagrams for the s-channel and t-channel quark−antiquark annihilation and the gluon fusion production mechanism are shown in Figure 5.3. It has exactly the same final state, with similar kinematics, although the opening angle between the charged leptons can be used to characterize the process. The WW process tends to have a larger separation between the charged leptons than those from the Higgs boson signal.

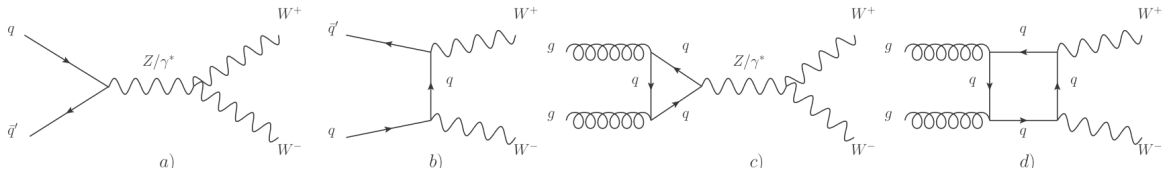

Figure 5.3 *Leading order Feynman diagrams illustrating the production of WW boson pairs at the LHC through in the s-channel (a) and in the t-channel (b) and through gluon fusion mediated by quark loops ((c) and (d)).*

Top-quark production

Top-quark pairs ($t\bar{t}$) are produced through both gluon-gluon and quark−antiquark annihilation as illustrated by the leading order Feynman diagrams in Figure 5.4. Single top quarks are also produced via weak interaction as shown in Figure 5.5 which are the t-channel, s-channel production and the associated production of a W boson and a top quark (denoted as Wt).

Top quarks almost decay into a W boson and a b-quark. Therefore, the top-quark pair and Wt production modes can result in a final state containing WW pairs produced in association with additional jets originating from b-quarks or initial state radiation.

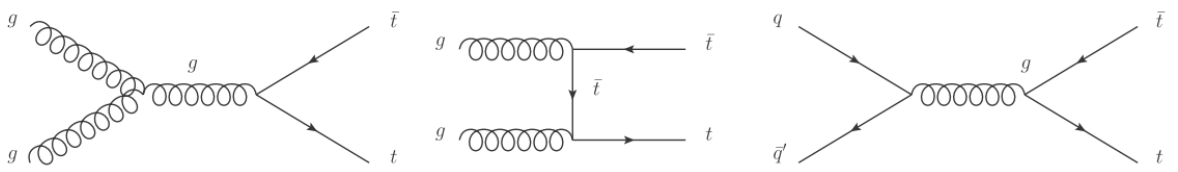

Figure 5.4 *Feynman diagrams illustrating top-quark pair production.*

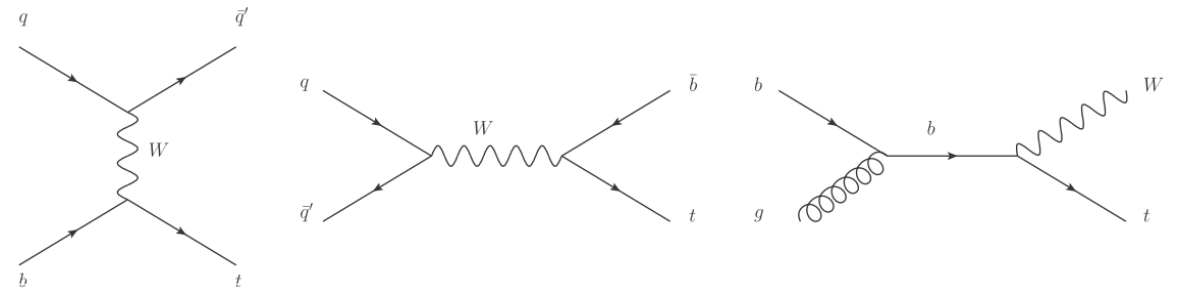

Figure 5.5 *Feynman diagrams illustrating the three production mechanisms of single top quarks.*

Z/γ^*+jets production

The Z/γ^*+jets background mostly affects the ee and $\mu\mu$ channels but has a non-negligible contribution to the $e\mu$ channel through leptonically decaying τ-leptons in the final state. Two oppositely charged leptons, created from the leptonic decay of a Z boson produced in association with jets, can result the signal signature. Even though these events contain only true missing transverse momentum in case of $Z/\gamma^* \to \tau\tau$ decays, missing transverse momentum can still be present due to neutrinos originating from heavy quark decays (from the associated jets), and also from a mismeasurement of the charged leptons or associated jets.

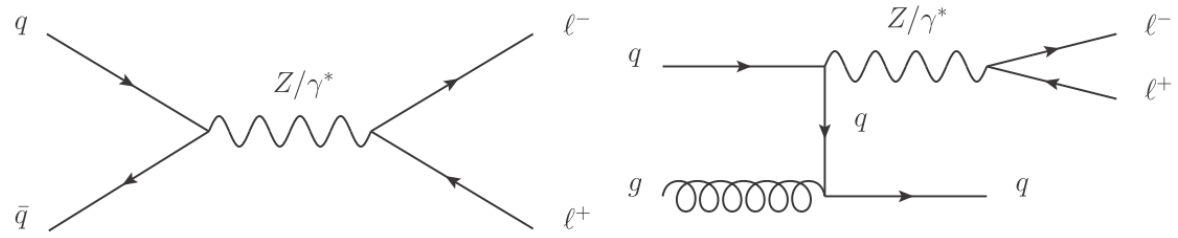

Figure 5.6 *Feynman diagrams illustrating the Drell-Yan production process.*

W+jets and QCD production

In pp collisions, a W boson can be produced in association with jets as shown in Figure 5.7. This process constitutes a background if the W boson decays leptonically and an accompanying jet is misidentified as a prompt lepton. The QCD background refers to multi-jet production, in which two of the jets are misidentified as leptons. Since

the rate of misidentification is low and there is a requirement of large missing transverse momentum, these backgrounds are quite small compared to the other processes.

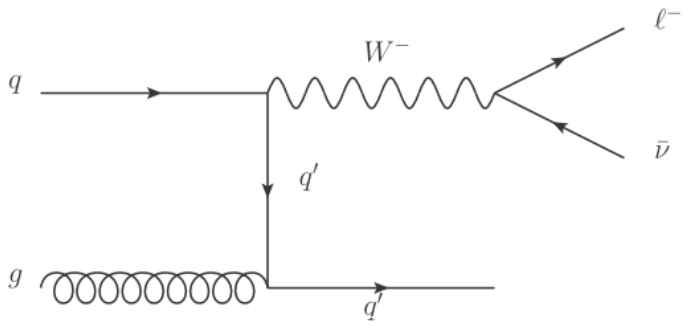

Figure 5.7 *Feynman diagrams illustrating the production of a W boson in association with a jet.*

WZ/ZZ/Wγ production

The last source of background to the $H \to WW^* \to l\nu l\nu$ signal comprises WZ, ZZ and Wγ events. These processes contain charged leptons and missing transverse energy induced by leptonically decaying W bosons. In case of the $W\gamma$ process a photon can produce a secondary electron. These background contributions are significantly reduced by vetoing events with three or more identified leptons.

5.2 Run 1 Data and Simulation Samples

5.2.1 Data Samples

The Run 1 data samples used for this analysis were collected by the ATLAS experiment at centre-of-mass energy of 7 TeV in 2011 and of 8 TeV in 2012. An integrated luminosity $\int L dt = 4.5$ fb^{-1} and $\int L dt = 20.3$ fb^{-1} from the 7 TeV and 8 TeV datasets, respectively, are used in this analysis. The luminosity has an uncertainty of $\pm 1.8\%$ for the 7 TeV data and $\pm 2.8\%$ for 8 TeV data. The mean number of interactions per bunch crossing increased during the data taking period. It is shown for the 2011 and 2012 data in Figure 5.8.

The main focus of this chapter is on the $\sqrt{s} = 8$ TeV dataset but in some sections the analysis based on the $\sqrt{s} = 7$ TeV datasets is incorporated.

Data quality

Not all the data collected are usable due to the detector conditions at runtime, and only data from a *"good runs list"* (GRL) are included for analysis. A GRL is an indicator to ensure stable beam conditions, and all subdetector and trigger systems were operating correctly. The recorded data are grouped into periods corresponding to the detector

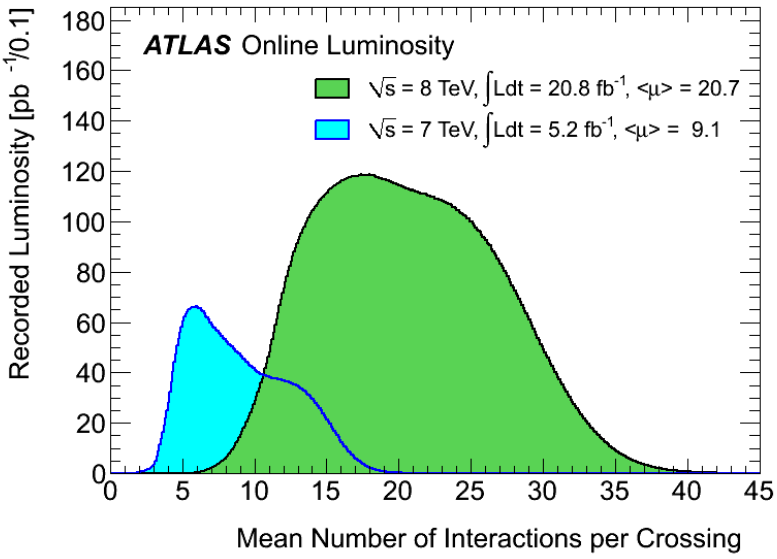

Figure 5.8 *The luminosity-weighted distribution of the mean number of interactions per crossing for the 2011 and 2012 data (taken from Ref. [69]).*

requirements during that time. Table 5.1 shows the integrated luminosities and running hours corresponding to each data-taking periods in 2011 and 2012.

Table 5.1: ATLAS data-taking periods and their corresponding integrated luminosities and running hours in 2011 and 2012.

	Period	Integrated luminosities (pb^{-1})	Running hours
2011	A	0.0000	6.08
	B	0.0133	19.22
	D	0.1855	139.03
	E	0.0527	24.20
	F	0.1593	53.95
	G	0.5721	158.22
	H	0.2867	82.68
	I	0.3639	92.35
	J	0.2403	46.96
	K	0.6850	118.27
	L	1.5536	188.65
	M	1.1548	125.31
2012	A	0.9102	110.04
	B	5.6244	410.02
	C	1.5378	114.74
	D	3.6270	253.97
	E	2.8592	178.90
	G	1.4512	94.05
	H	1.6814	99.80
	I	1.1725	67.84
	J	3.0233	181.18
	L	1.0115	56.91

Event cleaning

Besides GRL, a number of event conditions needs to be satisfied:

- ***LAr Error Flag***: noise bursts can occur in the LAr calorimeters, the ATLAS software will automatically flag them, and the events with this flag will be removed from the analysis.
- ***LAr Hole Cleaning***: events containing a jet with $p_T > 25$ GeV which intersects a faulty area of the LAr calorimeter are removed.
- ***Missing Energy Cleaning***: events containing a so-called *"bad jet"* (see Section 4.4) are removed if the bad jet has $p_T > 20$ GeV.

Triggers

This analysis uses events selected with triggers that require the presence of a single lepton or two leptons (dilepton). The EF triggers used for the 7 TeV and 8 TeV analyses are presented in Table 5.2 and 5.3.

Table 5.2: Summary of the EF triggers used for the 7 TeV dataset.

Period	ee	$\mu\mu$	$e\mu$
B − I	e20_medium	mu18_MG	e20_medium || mu18_MG
J	e20_medium	mu18_MG_medium	e20_medium || mu18_MG_medium
K	e22_medium	mu18_MG_medium	e22_medium || mu18_MG_medium
L − M	e22vh_medium	mu18_MG_medium	e22vh_medium || mu18_MG_medium

Table 5.3: Summary of the EF triggers used for the 8 TeV dataset.

ee	$\mu\mu$	$e\mu$
e24vhi_medium ||	mu24i_tight ||	e24vhi_medium ||
e60_medium ||	mu36_tight ||	e60_medium || mu24i_tight ||
2e12Tvh_loose ||	mu18_tight_mu8_EFFS	mu36_tight ||
2e12Tvh_loose1_L2StarB		e12Tvh_medium_mu8

5.2.2 Simulation Samples

The Monte Carlo (MC) generators used to model signal and background processes at $\sqrt{s} = 8$ TeV are listed in Table 5.4. For most of the background processes, the same generators are used as for the $\sqrt{s} = 7$ TeV analysis except for ZZ, WZ and Wγ events which use the POWHEG generator.

In this analysis, the signal contributions considered include the dominant gluon-gluon fusion production process (denoted as ggF), the vector-boson fusion production process (denoted as VBF) and the Higgs-strahlung process (denoted as VH). The $t\bar{t}H$ production mechanism is negligible due to its smaller cross section.

Only the $H \to WW^* \to l\nu l\nu$ ($l = e, \mu$) channels are considered with the inclusion of a small contribution from leptonic τ decays. The branching fraction for the decay as a function of m_H is calculated using PROPHECY4F [70, 71] with HDECAY [72].

Table 5.4: MC generators used to model the signal and background processes, and the corresponding cross sections at $\sqrt{s} = 8$ TeV, given for $m_H = 125$ GeV in the case of the signal processes (taken from Ref. [73]).

Process	Generator	$\sigma \cdot$ Br (pb)
ggF	POWHEG [74]+PYTHIA8 [75]	0.441
VBF	POWHEG [30]+PYTHIA8	0.035
WH/ZH	PYTHIA8	0.025
$q\bar{q}/g \to WW$	POWHEG+PYTHIA6	5.68
$gg \to WW$	GG2WW [76]+HERWIG [61]	0.16
Electroweak $WW + 2$ jets	Sherpa	0.039
$t\bar{t}$	MC@NLO [77]+HERWIG	238.1
tW/tb	MC@NLO [77]+HERWIG	28
tqb	AcerMC [78]+PYTHIA [79]	88
inclusive W	ALPGEN [80]+HERWIG	$37 \cdot 10^3$
inclusive $Z/\gamma^\star$	ALPGEN [80]+HERWIG	$16 \cdot 10^3$
$Z^{(\star)}Z^{(\star)} \to 4l$	POWHEG+PYTHIA8	0.73
$W(Z/\gamma^\star)(m_{(Z/\gamma^\star)} > 7)$ GeV	POWHEG+PYTHIA8	3.63
$W(Z/\gamma^\star)(m_{(Z/\gamma^\star)} < 7)$ GeV	MADGRAPH [81–83]+PYTHIA	14.3
$W\gamma$	ALPGEN [80]+HERWIG	369

Signal Samples

The ggF signal cross section is computed up to next-to-next-to-leading order (NNLO) in QCD [23, 25, 27, 28, 84, 85]. Next-to-leading order (NLO) electroweak (EW) corrections are also applied [86, 87], as well as QCD soft-gluon resummations up to next-to-next-to-leading log (NNLL) [88]. More details of these calculations are presented in Refs. [89–91].

The VBF signal cross section is computed with approximate NNLO QCD corrections [31] and full NLO QCD and EW corrections [29, 92, 93].

The VH cross section is calculated up to NNLO QCD corrections [32, 33] and NLO EW corrections [34].

Background Samples

The number of ($\sigma \cdot$ Br) quoted for the inclusive Z/γ^* (Drell-Yan process, denoted as DY) corresponds to the range of invariant mass of the two lepton system $m_{ll} < 10$ GeV.

Kinematic criteria are also applied in the event generation of Wγ and Wγ^*, with

$W \to l\nu$ and $\gamma^* \to ll$. For Wγ events, the photon must have $p_T > 8$ GeV and must be separated from the charged lepton by $\Delta R = \sqrt{(\Delta\eta)^2 + (\Delta\phi)^2} > 0.25$. For $W\gamma^*$, at least two leptons must have $p_T > 5$ GeV (p_T denotes the transverse momentum with respect to the beam line) and $|\eta| < 3$ for ee and $\mu\mu$, and $|\eta| < 5$ for $\tau\tau$ events. For WZ a requirement that there are at least two charged leptons with $p_T > 5$ GeV and $|\eta| < 2.8$ is applied. The $ZZ \to 4l$ process is generated with the requirement $m_{ll} > 4$ GeV.

For most processes, separate programs are used to generate the hard scattering process and to model the parton showering (PS), hadronization, and the underlying event (UE). PYTHIA8 [75] or PYTHIA6 [79] are used for the signal and some of the background processes. HERWIG [61] is used for the hadronization and PS while JIMMY [94] is used for the modelling of the UE.

The ALPGEN+HERWIG generator with the MLM matching scheme [95] is used to model the W+jets, Z/γ^*+jets and $W\gamma$ processes. SHERPA [96] is used for both the hard-scattering process and the PS modelling for VBF processes.

The cross sections for the $W\gamma$ and $W\gamma^*$ processes are normalized to the MCFM [97] NLO predictions. These normalization factors are 1.15 for $W\gamma$ and 2.01 for $W\gamma^*$.

The parton distribution function (PDF) set from CT10 [98] is used for POWHEG and MC@NLO generators. CTEQ6L1 [99] is used for ALPGEN, MADGRAPH, PYTHIA6 and PYTHIA8 generators.

The acceptances and efficiencies are obtained from a full simulation using GEANT4 [100]. In cases of $q\bar{q}, gq \to WW$ and single top processes, a fast simulation is used to increase significantly the number of generated events. The MC simulation incorporates the event pile-up conditions in the collected data, including both the effects of multiple pp collisions in the same bunch crossing (denoted as in-time pile-up) and in the nearby bunch crossings (denoted as out-of-time pile-up).

5.3 Event Selection and Background Determination

This section presents the selection of $H \to WW^* \to l\nu l\nu$ candidate events. The object and candidate event selections are described in Sections 5.3.1 and 5.3.2. The methods to determine and normalize the background contributions for W+jets, top and WW events are presented in Section 5.3.3.

5.3.1 Object Selection

Electrons

Table 5.5 shows the summary of the electron selection criteria for the 2011 (7 TeV) and 2012 (8 TeV) datasets. The electron candidates are identified using the `Tight++` selection criteria for the 2011 analysis. In the 2012 analysis, electrons are identified using the *"Very Tight Likelihood"* (`VTLH`) criteria for $E_T < 25$ GeV and the so-called

`Medium++` criteria for $E_T > 25$ GeV. The electrons are required to be in the range of $|\eta| < 2.47$ excluding the region $1.37 < |\eta| < 1.52$, which covers the transition region between the barrel and end-cap calorimeters. Both the tracking and calorimeter based isolation criteria are optimized leading to a p_T dependence for the isolation requirements.

Table 5.5: Summary of the electron selection criteria for the 2011 and 2012 datasets.

Selection criteria	2011 dataset	2012 dataset
Geometrical acceptance	$\|\eta\| < 2.47$ excluding $1.37 < \|\eta\| < 1.52$	
Transverse momentum	$p_T > 15$ GeV	
Overlap removal (e/μ)	$\Delta R(e,\mu) < 0.1$	
Identification criteria	`Tight++`	`VTLH` (`Medium++`) for $E_T < 25$ GeV ($E_T > 25$ GeV)
Track reconstruction	Default	Gaussian Sum Filter
Overlap removal (e/μ)	–	$\Delta R(e,\mu) < 0.1$
Impact parameter		
– Transverse	$\|d_0/\sigma(d_0)\| < 10$	$\|d_0/\sigma(d_0)\| < 3$
– Longitudinal	$\|z_0\| < 1$ mm	$\|z_0 \sin\theta\| < 0.4$ mm
Isolation ($\Delta R < 0.3$)		
– Track	$\sum p_T^{trk}/p_T < 0.13$	$\sum p_T^{trk}/p_T < 0.12\,(0.16)$ for $p_T < 25$ GeV ($p_T > 25$ GeV)
– Calorimeter	$\sum E_T^{cell}/p_T < 0.14$	$\sum E_T^{cell}/p_T < 0.16$

Muons

Table 5.6 shows the summary of the muon selection criteria for the 2011 (7 TeV) and 2012 (8 TeV) datasets. Muons are reconstructed by the *Staco combined* algorithm which matching tracks reconstructed in the inner detector and in the muon spectrometer [101]. The muons are required to be in the range $|\eta| < 2.5$. Like the electron selection, both the tracking and calorimeter based isolation criteria are optimized and tightened, resulting in p_T dependent requirements.

Jets

Table 5.7 shows the summary of the jet selection criteria for the 2011 (7 TeV) and 2012 (8 TeV) datasets. Jets are reconstructed using the *anti-k_t* algorithm with a distance parameter $R = 0.4$ [102]. The jets are required to have $p_T > 25$ GeV in the central region ($|\eta| < 2.4$) and $p_T > 30$ GeV in the forward region ($2.4 < |\eta| < 4.5$). The increased threshold in the forward region reduces the contribution from fake jets produced by pile-up. In addition, a *jet vertex fraction* (JVF) requirement is applied

Table 5.6: Summary of the muon selection criteria for the 2011 and 2012 datasets.

Selection criteria	2011 dataset	2012 dataset
Identification criteria	*Staco combined*	
Transverse momentum	$p_T > 15$ GeV	
Geometrical acceptance	$\|\eta\| < 2.4$	$\|\eta\| < 2.5$
Impact parameter		
– Transverse	$\|d_0/\sigma(d_0)\| < 3$	$\|d_0/\sigma(d_0)\| < 3$
– Longitudinal	$\|z_0\| < 1$ mm	$\|z_0 \sin\theta\| < 1$ mm
Isolation ($\Delta R < 0.3$)		
– Track	$\sum p_T^{trk}/p_T < 0.13$	$\sum p_T^{trk}/p_T < 0.15$
		$\sum p_T^{trk}/p_T < 0.01 p_T - 0.105$)
– Calorimeter	$\sum E_T^{cell}/p_T < 0.14$	$\sum E_T^{cell}/p_T < 0.2$
		$\sum E_T^{cell}/p_T < 0.014 p_T - 0.15$
Overlap removal (μ/j)	–	$\Delta R(\mu, j) < 0.3$

for jets with $p_T > 20$ GeV to suppress pile-up fake jets. The JVF [103] is computed as

$$JVF = \frac{\sum p_T(\text{tracks of jet associated to primary vertex})}{\sum p_T(\text{all tracks of jet})} \tag{5.1}$$

Since it relies on tracking information, it is only applied to jets with $|\eta| < 2.4$.

Table 5.7: Summary of the jet selection criteria for the 2011 and 2012 datasets.

Selection criteria	2011 dataset	2012 dataset
Reconstruction algorithm	*anti-k_t*, $R = 0.4$	
Geometrical acceptance	$\|\eta\| < 4.5$	
Overlap removal (j/e)	$\Delta R(e, \mu) < 0.3$	
Quality criteria	`Loose`	
Transverse momentum	$p_T > 25(30)$ GeV	$p_T > 25(30)$ GeV
	for $(2.75 < \|\eta\| < 3.25)$	for$\|\eta\| < 2.5$ ($\|\eta\| > 2.5$)
Jet Vertex Fraction	$\|$JVF$\| > 0.75$	$\|$JVF$\| > 0.5$
b-tagging		
Tagging algorithm	`JetFitterCombNN`	`MV1`
Working point	80%	85%

Missing transverse momentum

The missing transverse momentum can be reconstructed either from the calorimeter (E_T^{miss}), from the tracking (p_T^{miss}) or from the combination of both detector parts ($p_T^{miss,J-TRK}$). For $p_T^{miss,J-TRK}$, the track-based jet objects are replaced by the corresponding calorimeter-based one. To reduce the presence of E_T^{miss} arising from mis-

measured objects (both leptons and jets), the relative missing transverse momentum is projected onto the axis of the closest hard object

$$E_{T,rel}^{miss} = \begin{cases} E_T^{miss} \cdot \sin(\Delta\phi) & \Delta\phi < \frac{\pi}{2} \\ E_T^{miss} & \Delta\phi \geq \frac{\pi}{2} \end{cases} \tag{5.2}$$

where $\Delta\phi$ is the angle between E_T^{miss} and the nearest reconstructed object. The same methodology is applied to track based p_T^{miss} to get $p_{T,rel}^{miss}$.

5.3.2 Selection of $H \to WW^* \to l\nu l\nu$ Candidate Events

As mentioned in Section 5.1, the $H \to WW^* \to l\nu l\nu$ candidate event selection depends on the jet multiplicity as well as on the rate and the composition of the backgrounds. For $N_{jet} \leq 1$, the signal is dominant by the ggF process and WW events dominate the background composition. For $N_{jet} \geq 2$, the signal is mostly from the VBF process and $t\bar{t}$ is the dominating background.

To separate between signal and background processes, a set of kinematic quantities is used:

- Dilepton invariant mass

$$\begin{aligned} m_{ll} &= \sqrt{(E_{l_1} + E_{l_2})^2 - (\vec{p}_{l_1} + \vec{p}_{l_2})^2} \\ &= \sqrt{E_{l_1}^2 - p_{l_1}^2 + E_{l_2}^2 - p_{l_2}^2 + 2 \cdot E_{l_1} \cdot E_{l_2} - 2 \cdot p_{l_1} \cdot p_{l_2} \cdot \cos\theta} \\ &\simeq \sqrt{2 \cdot E_{l_1} \cdot E_{l_2}(1 - \cos\theta)} \\ &\text{for } m_{l_{1,2}} \ll E_{l_{1,2}} \end{aligned} \tag{5.3}$$

  with $m_{l_{1,2}}$, $E_{l_{1,2}}$ and θ denoting the mass, the energy and the opening angle of the leptons, respectively.
- Dilepton transverse momentum

$$p_T^{ll} = |\vec{p}_T^{\,ll}| = |\vec{p}_T^{\,l1} + \vec{p}_T^{\,l2}| \tag{5.4}$$

- Difference of azimuthal angular between the leptons

$$\Delta\phi_{ll} = \phi_{l1} - \phi_{l2} \text{ in interval } [-\pi, \pi] \tag{5.5}$$

- Difference of pseudorapidity between the leptons

$$\Delta\eta_{ll} = \eta_{l1} - \eta_{l2} \tag{5.6}$$

- Transverse mass of the dilepton and E_T^{miss} system

$$m_T = \sqrt{(E_T^{ll} + E_T^{miss})^2 + |\vec{p}_T^{\,ll} + \vec{p}_T^{\,miss}|^2} \tag{5.7}$$

  where $E_T^{ll} = \sqrt{|\vec{p}_T^{\,ll}|^2 + m_{ll}^2}$.
- Single-lepton transverse mass

$$m_T^l = \sqrt{2(E_T^{miss} p_T{}^l - \vec{p}_T^{\,l} \cdot \vec{E}_T^{miss})} \tag{5.8}$$

- Total transverse momentum

$$p_T^{tot} = |\vec{p}_T^{\,l1} + \vec{p}_T^{\,l2} + \vec{p}_T^{\,miss} + \sum_{jet} \vec{p}_T^{\,jet}| \tag{5.9}$$

- Invariant di-tau mass: it can be constructed in $(ee, \mu\mu, e\mu, \mu e)$ channels by the *collinear approximation* which is assumed that the lepton originating from the τ decay is collinear with the emitted neutrino,

$$m_{\tau\tau} = \frac{\sqrt{(E_{l_1} + E_{l_2})^2 - (\vec{p}_{l_1} + \vec{p}_{l_2})^2}}{\sqrt{x_1 \cdot x_2}} \tag{5.10}$$

  where x_1 and x_2 are the energy fractions of the neutrinos in $\tau\tau \to l\nu l\nu$ events.
- Fractional hadronic recoil

$$f_{recoil} = \frac{|\sum_{soft-jets} |JVF| \cdot \vec{p}_T|}{p_T^{ll(+jet)}} \tag{5.11}$$

  where $p_T^{ll(+jet)}$ is the transverse momentum of the dilepton system in the $N_{jet} = 0$ channel and the total transverse momentum of the two leptons and of the jet in the $N_{jet} = 1$ category.

Pre-selection

For all jet multiplicities, a set of selections is applied to takes advantage of the topological configuration of the two leptons.

The pre-selection requires exactly two oppositely charged leptons with $p_T > 22$ GeV and 10 GeV for the leading and sub-leading leptons, respectively. The contributions from J/ψ and Υ decays are rejected by requiring the dilepton mass $m_{ll} > 12$ GeV for the ee and $\mu\mu$ channels and $m_{ll} > 10$ GeV for the $e\mu$ and μe channels. The Drell-Yan process in the ee and $\mu\mu$ channels is suppressed by requiring a Z-mass veto ($|m_{ll} - m_Z| > 15$ GeV). The analysis is then divided into $N_{jet} = 0$, $N_{jet} = 1$ and $N_{jet} \geq 2$ categories.

Figure 5.9 shows the multiplicity distribution of jets in the $e\mu$, μe, ee and $\mu\mu$ channels

for 8 TeV events after the pre-selection. Table 5.8 summarizes the selection in this analysis.

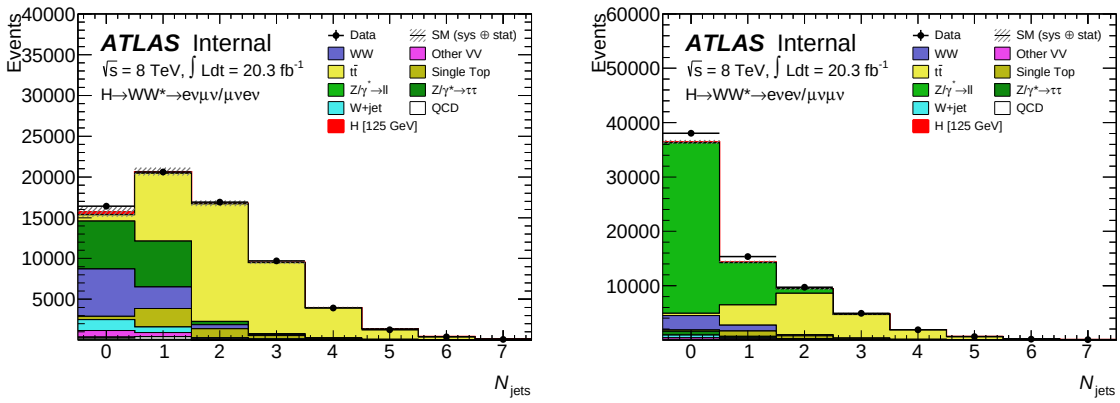

Figure 5.9 *Jet multiplicity for events in 8 TeV data. The plots are shown for the eμ, μe (left) and ee, μμ (right) channels after the pre-selection.*

$\mathbf{N}_{jet} = \mathbf{0}$

In the $N_{jet} = 0$ analysis, the missing transverse momentum is required to be large. For $e\mu$ and μe, the selection is $p_T^{miss} > 20$ GeV. For ee and $\mu\mu$, the selection is tighter, $E_{T,rel}^{miss} > 40$ GeV and $p_{T,rel}^{miss,J-TRK} > 40$ GeV, because of the large DY background from $Z/\gamma^* \to ll$.

The transverse momentum of the dilepton system is required to be large, $p_T^{ll} > 30$ GeV.

For ee and $\mu\mu$ events, the hadronic recoil is required to be small, $f_{recoil} < 0.1$.

The azimuthal gap between $\vec{p}_T^{ll}$ and $\vec{E}_T^{miss}$ is required not to be small in order to remove potentially pathological events where the missing transverse momentum is in the same direction with one lepton, $\Delta\phi_{ll,MET} > \pi/2$.

$\mathbf{N}_{jet} = \mathbf{1}$

In the $N_{jet} = 1$ analysis, the DY treatment is similar to that in the $N_{jet} = 0$ one, while additional selections further suppress top and $Z/\gamma^* \to \tau\tau$ backgrounds. For the DY reduction, the $E_{T,rel}^{miss}$ and p_T^{miss} requirements are the same as in $N_{jet} = 0$ case, but the $p_{T,rel}^{miss,J-TRK}$ is reduced to 35 GeV.

The top-quark background is suppressed by rejecting events with a heavy-flavour jet with a multi-variate b-tagging algorithm [105].

The $Z/\gamma^* \to \tau\tau$ background in $e\mu$ and μe is suppressed using an invariant di-tau mass [106] $|m_{\tau\tau} - m_Z| \geq 25$ GeV.

In case of the $e\mu$ and μe channels, a requirement is applied to the transverse mass of a single lepton $m_T^l > 50$ GeV, since this m_T^l quantity tends to have small values for the DY background and large values for the signal process.

Table 5.8: List of selection criteria for the analysis of the 8 TeV data. The criteria specific to the $e\mu$, μe, ee and $\mu\mu$ channels are noted as such; otherwise, they apply to both. Pre-selection applies to all N_{jet} modes. The rapidity gap is the y range spanned by the two leading jets. The m_{ll} split is at 30 GeV. Energies, masses, and momenta are in units of GeV (taken from Ref. [104]).

Category	$N_{jet} = 0$	$N_{jet} = 1$	$N_{jet} \geq 2$
Pre-selection	Two isolated leptons ($\ell = e, \mu$) with opposite charge Leptons with $p_{\mathrm{T}}^{\mathrm{lead}} > 25$ and $p_{\mathrm{T}}^{\mathrm{sublead}} > 10$ $e\mu + \mu e$: $m_{ll} > 10$ $ee + \mu\mu$: $m_{ll} > 12$, $\lvert m_{ll} - m_Z \rvert > 15$		
Missing transverse momentum and hadronic recoil	$e\mu + \mu e$: $p_T^{miss} > 20$ $ee + \mu\mu$: $E_{T,rel}^{miss} > 40$ $ee + \mu\mu$: $p_{T,rel}^{miss,J-TRK} > 40$ $ee + \mu\mu$: $f_{recoil} < 0.1$	$e\mu + \mu e$: $p_{T,rel}^{miss} > 20$ $ee + \mu\mu$: $E_{T,rel}^{miss} > 40$ $ee + \mu\mu$: $p_{T,rel}^{miss,J-TRK} > 40$ $ee + \mu\mu$: $f_{recoil} < 0.1$	$e\mu + \mu e$: $p_T^{miss} > 20$ $ee + \mu\mu$: $p_T^{miss} > 40$ $ee + \mu\mu$: $E_T^{miss} > 45$ -
General selection	- $\Delta\phi_{ll,MET} > \pi/2$ $p_T^{ll} > 30$	$N_{b\text{-jet}} = 0$ $\max(m_T^l) > 50$ $e\mu + \mu e$: $Z/\gamma^* \to \tau\tau$ veto	$N_{b\text{-jet}} = 0$ p_T^{tot} inputs to BDT $e\mu + \mu e$: $Z/\gamma^* \to \tau\tau$ veto
VBF topology	- - - -	- - - -	m_{jj} inputs to BDT Δy_{jj} inputs to BDT $\sum m_{lj}$ inputs to BDT $\sum C_l$ inputs to BDT
$H \to WW^* \to l\nu l\nu$ topology	$m_{ll} < 55$ $\Delta\phi_{ll} < 1.8$ $e\mu + \mu e$: split m_{ll} Fit m_T	$m_{ll} < 55$ $\Delta\phi_{ll} < 1.8$ $e\mu + \mu e$: split m_{ll} Fit m_T	m_{ll} inputs to BDT $\Delta\phi_{ll}$ inputs to BDT - m_T inputs to BDT

$N_{jet} \geq 2$

In the $N_{jet} \geq 2$ analysis, the event selection follows that in $N_{jet} = 1$ case, with some modifications. The DY background is suppressed by requiring $p_T^{miss} > 20$ GeV for $e\mu$ and μe, and both $p_T^{miss} > 40$ GeV and $E_T^{miss} > 45$ GeV for ee and $\mu\mu$.

The VBF analysis has different approach than the ggF analysis in $N_{jet} \leq 1$ category. This analysis uses a multi-variate analysis (MVA) which called *Boosted Decision Tree* (BDT) method to extract limits and measure the strength of couplings to the Higgs bosons.

A cross-check analysis is performed using cut-based selections on some of the variables that are used as inputs to the BDT. In this cross-check, the VBF-specific selections use the kinematics of the two highest-p_T jets (leading jets) in the event. Their rapidity gap is required to be large, $|\Delta y_{jj}| > 3.6$, and their invariant mass is required to be high, $m_{jj} > 600$ GeV. The activity in the rapidity gap between the leading jets is restricted to reduce the contribution from processes where the jets are produced via QCD radiation, i.e. events with a jet with $p_T > 20$ GeV inside the rapidity gap are vetoed. This restriction is known as *"central-jet veto"* and is applied to the jet centrality quantity, defined as

$$C_{j3} = \left| \eta_{j3} - \frac{\sum \eta_{jj}}{2} \right| / \frac{\Delta\eta_{jj}}{2} \tag{5.12}$$

where η_{j3} is the pseudorapidity of an additional jet, $\sum \eta_{jj} = \eta_{j1} + \eta_{j2}$ and $\Delta\eta_{jj} = \eta_{j1} - \eta_{j2}$. The centrality of any additional jet in the event is required to be $C_{j3} > 1$.

The leptons are required to be within the rapidity gap via the lepton centrality (C_l) which is defined similarly to that for additional jet. A requirement of $C_l < 1$ is applied to each lepton in the BDT and cross-check analyses.

The top-quark background is suppressed by requiring b-jet veto $N_{b-jet} = 0$ with $p_T > 20$ GeV.

Signal region selection

The two variables, m_{ll} and m_T, are used to further separate the signal from the background processes. The m_{ll} distribution for $N_{jet} \leq 1$ is shown in Fig. 5.10. The signal-to-background (S/B) ratio in this distribution is varying, so the sample is further subdivided for a signal extraction at $m_{ll} = 30$ GeV for $N_{jet} \leq 1$ categories.

The m_T distribution is used to measure the signal strength. The statistical treatment is described later in Section 5.5. Figure 5.11 shows the expected signal and the composition of the expected background for the different N_{jet} categories and decay channels. The details of the normalization of the background events are discussed in the next section. The highest S/B is in a region of m_T around m_H: $0.75m_H < m_T < m_H$ for $N_{jet} \leq 1$ and $m_T < 1.2m_H$ for $N_{jet} \geq 2$.

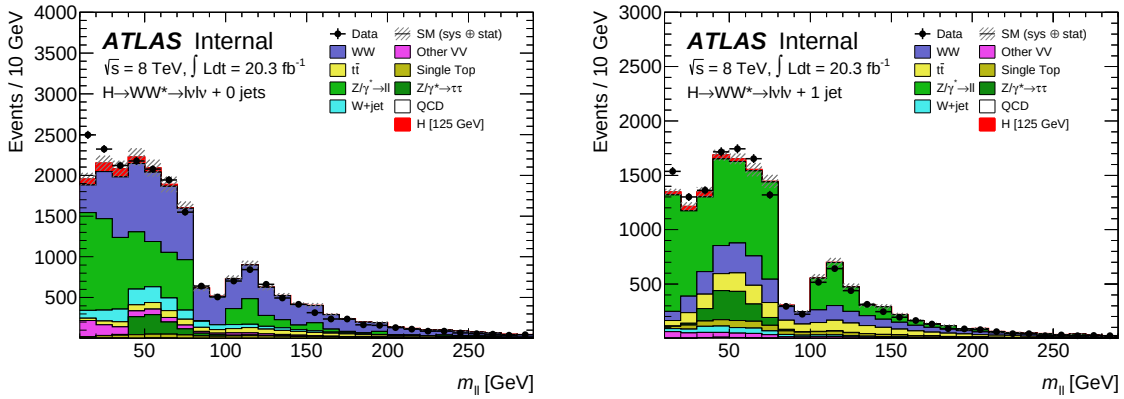

Figure 5.10 *Distributions of m_{ll} in the 8 TeV data before the $m_{ll} < 55$ GeV cut. The plots are shown in the $N_{jet} = 0$ (left) and $N_{jet} = 1$ (right) categories. The distributions have been normalized to the data.*

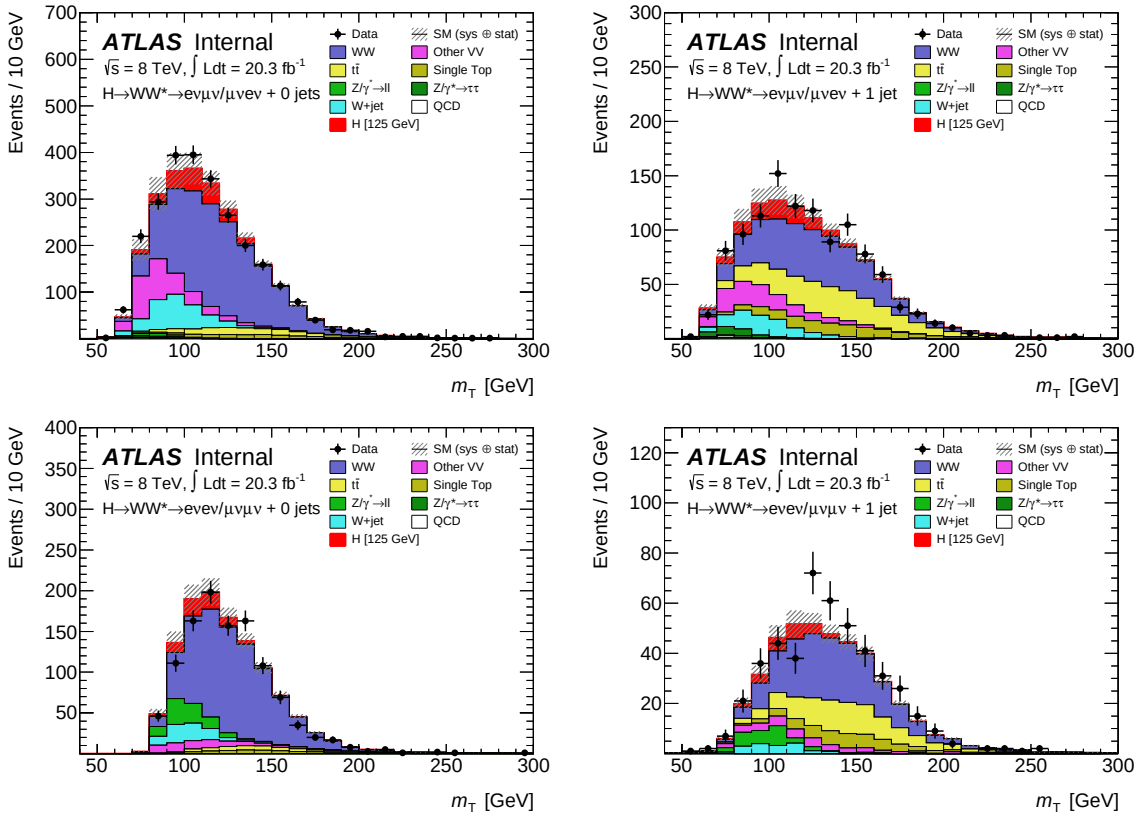

Figure 5.11 *Distributions of m_T in the 8 TeV data signal regions. The plots are shown for the $e\mu$, μe (top) and ee, $\mu\mu$ (bottom) channels in the $N_{jet} = 0$ (left) and $N_{jet} = 1$ (right) categories. The distributions have been normalized to the data.*

In the VBF analysis, eight variables are used for the BDT, which ar m_{jj}, Δy_{jj}, m_{ll}, $\Delta\phi_{ll}$, p_T^{tot}, m_T, sum of lepton centralities ($\sum C_l = C_{l1} + C_{l2}$), and sum of invariant masses of lepton and jet $\sum_{lj} m_{lj}$. Figure 5.12 shows the distributions of m_{jj}, Δy_{jj}, C_{l1} and $\sum_{lj} m_{lj}$ variables. The BDT is trained after the preselection and the $N_{b-jet} = 0$ requirement. More details on the BDT analysis can be found in Ref. [104].

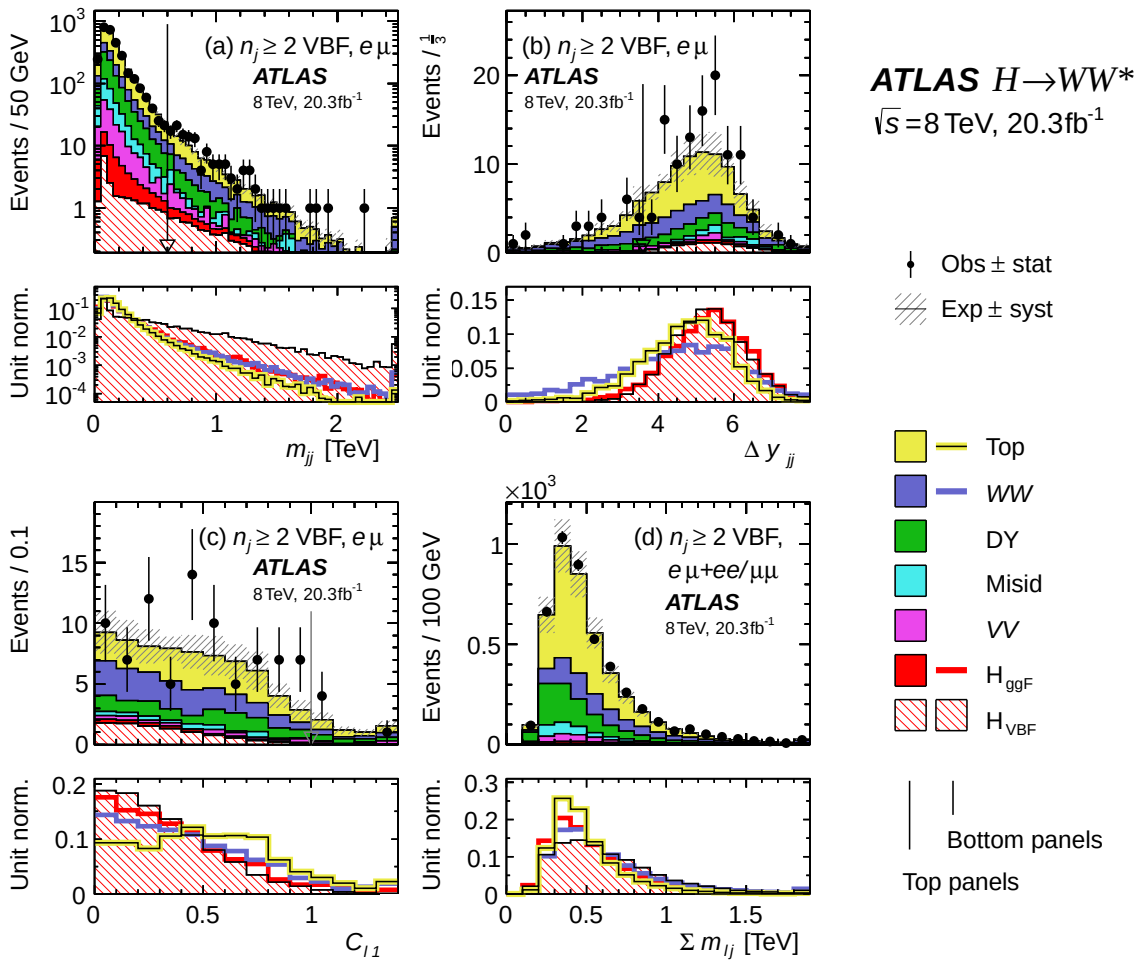

Figure 5.12 *Distributions of (a) m_{jj}, (b) Δy_{jj}, (c) C_{l1} and (d) $\sum m_{lj}$ for the $N_{jet} \geq 2$ VBF-enriched category. The distributions have been normalized to the data. The plot in (a) is made after requiring all selections up to m_{jj}, (b) up to Δy_{jj} and (c) up to C_{l1} requirements in the cross-check analysis. There is no selection made on the variable in (d) since it is only used as an input to the training of the BDT.*

5.3.3 Background Estimations

Important background processes for this analysis are WW, $t\bar{t}$, single top-quark production, $Z/\gamma^* \rightarrow \tau\tau$, W+jets, and diboson processes other than WW, collectively referred to as VV and including Wγ^*, Wγ, WZ, and ZZ events. The control regions (CRs) are used to determine the correct normalization factors (NFs) for the Monte Carlo predictions of Z/γ^*+jets, top and WW processes. The extracted normalization factors and the corresponding uncertainties are described briefly in the following paragraphs.

WW estimation

The WW background is the dominant background in $N_{jet} = 0$. It has a similar size as the top-quark background in $N_{jet} = 1$, and it is still significant in the $N_{jet} \geq 2$ category.

Table 5.9: Event selection criteria used to define the control regions. Every control region starts from the pre-selection. The top quark "aux." lines describe auxiliary data control regions used to correct the normalization found in the main control region. The control region for the W+jets and multi-jet backgrounds follow the signal region selection but with modified lepton selection.

CR	$N_{jet} = 0$	$N_{jet} = 1$
WW	$55 < m_{ll} < 110$ GeV	$m_{ll} > 80$ GeV
	$\Delta\phi_{ll} < 2.6$	$\lvert m_{\tau\tau} - m_Z \rvert > 25$ GeV
		b-jet veto
		$m_T^l > 50$ GeV
top quark	no N_{jet} requirement	$N_{b-jet} = 1$
	$\Delta\phi_{ll} < 2.8$	$\max(m_T^l) > 50$ GeV
	$p_T^{ll} > 30$ GeV	$m_{\tau\tau} < m_Z - 25$ GeV
top quark aux.	no N_{jet} requirement	$N_{jet} = 2$
	≥ 1 b-jet required	≥ 1 b-jet required
	$\Delta\phi_{ll} < 2.8$	
	$p_T^{ll} > 30$ GeV	
$Z/\gamma^* \to \tau\tau$	no $E_T^{miss,TRK}$ requirement	no $E_T^{miss,TRK}$ requirement
	$m_{ll} < 80$ GeV	$m_{ll} < 80$ GeV
	$\Delta\phi_{ll} > 2.8$	$m_{\tau\tau} > m_Z - 25$ GeV
		b-jet veto
VV	same-sign leptons	same-sign leptons
	all SR cuts	all SR cuts

The predictions in the $N_{jet} \leq 1$ analyses are normalized using control regions. The WW CRs are defined with the same selection as the signal region except that the $\Delta\phi_{ll}$ requirement is removed. For $N_{jet} = 0$ the requirement 50 GeV $< m_{ll} <$ 100 GeV is applied, and for $N_{jet} = 1$ the requirement $m_{ll} > 80$ GeV is applied to the WW CRs [107]. Events from WW contribute about 70% and 40% of the total events in the $N_{jet} = 0$ and $N_{jet} = 1$ CRs, respectively. The resulting NFs for WW are 1.22 $\pm$ 0.03 (stat.) and 1.05 $\pm$ 0.05 (stat.) for the $N_{jet} = 0$ and $N_{jet} = 1$ signal regions, respectively.

The observed and predicted m_T distributions for events in the WW CRs are shown in Fig. 5.13, after applying all normalization factors. The WW and top background estimates for $N_{jet} = 1$ are anti-correlated due to the large contamination of top-quark events in the WW control region.

The WW contribution in the $N_{jet} \geq 2$ category is taken from simulation because it is difficult to define a CR that is sufficiently free of top-quark background, while still retaining a sufficiently large number of events.

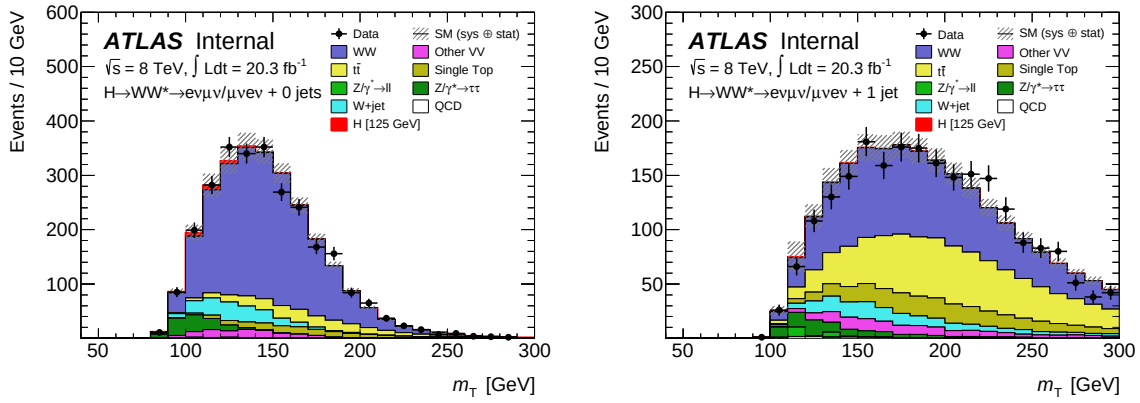

Figure 5.13 *Distributions of m_T in the WW control region in the $N_{jet} = 0$ (left), $N_{jet} = 1$ (right) categories. The distributions have been normalized to the data.*

Top estimation

The top-quark background for the $N_{jet} = 0$ category is estimated using the procedure described in Ref. [103]. The NF is derived from inclusive samples without requirement on the number of jets. The efficiency of the $N_{jet} = 0$ signal region selection is modeled using the MC simulation, and the efficiency α of the jet veto is corrected using the fraction of b-tagged events which have no jets in addition to the b-tagged one. The jet veto survival probability α is applied in quadrature to account for the presence of two jet in tree-level $t\bar{t}$ production. The normalization scale factor for the signal region is therefore given by

$$\beta_{\text{top,0jet}} = \frac{N_{\text{CR,data}}}{N_{\text{CR,MC}}} \cdot \left(\frac{\alpha_{\text{data}}}{\alpha_{\text{MC}}}\right)^2, \tag{5.13}$$

where event yields from non-top-quark events are subtracted from event yields in data using MC simulation or data driven estimates.

For the $N_{jet} = 1$ category, the NF is determined from a control region distinguished from the signal region by requiring that the one jet is b-tagged. To reduce the effect of b-tagging systematic uncertainties, the transfer factor from the CR to the SR is corrected using an effective b-jet tagging scale factor derived from a control region with two jets, at least one of which is b-tagged. The difference in b-tagging efficiency between the regions with one and two jets is accounted for using MC simulation. The normalization scale factor is obtained as

$$\beta_{top,1jet} = \frac{N_{data,1jet,1b-tag}}{N_{MC,1jet,0b-tag}} \cdot \overbrace{\left(\frac{1-\epsilon^{est}_{1jet}}{\epsilon^{est}_{jet}}\right)}^{\alpha} \tag{5.14}$$

where α is the corresponding extrapolation factor. The estimate for the b-tagging

efficiency is given by

$$\epsilon_{1jet}^{est} = \left(\frac{\frac{N_{MC,1jet,1b-tag}}{N_{MC,1jet,0b-tag}+N_{MC,1jet,1b-tag}}}{\frac{N_{MC,2jet,2b-tag}}{N_{MC,2jet,1b-tag}+N_{MC,2jet,2b-tag}}} \right) \cdot \frac{N_{data,2jet,2b-tag}}{N_{data,2jet,1b-tag} + N_{data,2jet,2b-tag}} \tag{5.15}$$

The estimation of the b-tagging efficiency using the 2-jet region is validated through comparison of the jet p_T spectrum shown in Figure 5.14. The resulting normalization factors are 1.08 ± 0.02 (stat.), 1.06 ± 0.03 (stat.) and 1.05 ± 0.03 (stat.) in the $N_{jet} = 0$, $N_{jet} = 1$ and $N_{jet} \geq 2$ categories, respectively.

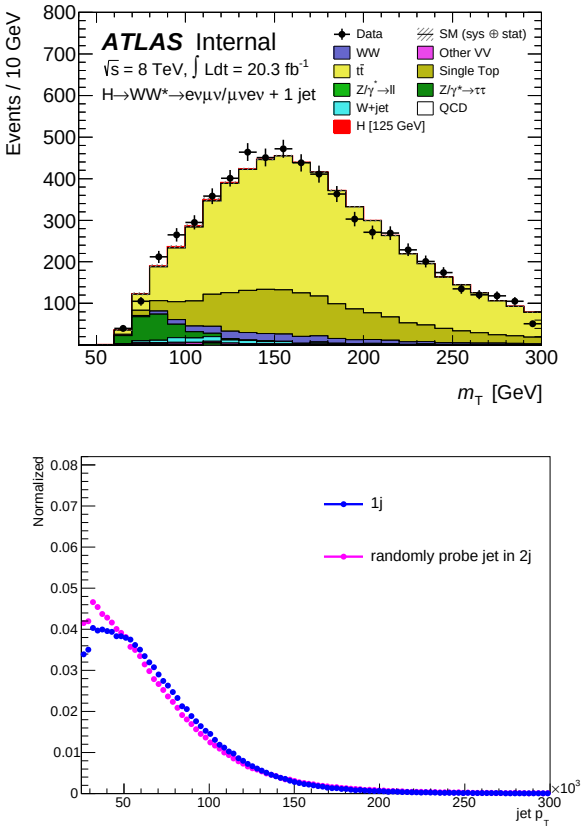

Figure 5.14 *Top-quark control region distributions of m_T (top) and jet p_T (bottom). The m_T plot scales the top-quark contributions with the normalization factor $\beta_{top,1jet}$. The jet p_T plot in compares the jet p_T distribution in top-quark MC in $N_{jet} = 2$ ($2j$ probe) events to $N_{jet} = 1$ ($1j$) events. For each $N_{jet} = 2$ event, one of the two jets is chosen randomly and the p_T of that jet enters the distribution if the other jet is tagged.*

Z/γ^*+jets estimation

In the ee and $\mu\mu$ channels, the contribution of Z/γ^*+jets is estimated by using a data-driven method. In the $N_{jet} \leq 1$ category, the hadronic recoil variable is used for estimating the DY and non-DY processes from data. The events in the CR are divided into two bins: passing (N_{pass}) and failing (N_{fail}) the f_{recoil} cut. The efficiency of the f_{recoil} cut $\alpha = N_{pass}/(N_{pass}+N_{fail})$ is measured from data for both the DY and non-DY

backgrounds. A normalization factor can then be obtained via inverting the matrix

$$\begin{pmatrix} N_{pass} \\ N_{pass} + N_{fail} \end{pmatrix} = \begin{pmatrix} 1 & 1 \\ 1/\alpha_{DY} & 1/\alpha_{\text{non-DY}} \end{pmatrix} \times \begin{pmatrix} B_{DY} \\ B_{\text{non-DY}} \end{pmatrix} \tag{5.16}$$

and solving for B_{DY}, the estimation of DY events in the ee and $\mu\mu$ signal regions. The efficiency for the non-DY backgrounds α_{non-DY} is measured in a sample using $e\mu$ and μe events only in order to increase the purity. The resulting normalization factors are 1.24 ± 0.10 (stat.) in the $N_{jet} = 0$ and 1.50 ± 0.20 (stat.) in the $N_{jet} = 1$ categories.

In $N_{jet} \geq 2$, a so-called *ABCD−method* is used to extrapolate the fraction of DY events into the signal region. Four regions are defined in the $m_{ll} - E_{T,rel}^{miss}$ plane

- Region A: 12 GeV $< m_{ll} <$ 50 GeV and $E_T^{miss} > 45$ GeV (signal region)
- Region B: 12 GeV $< m_{ll} <$ 50 GeV and 20 GeV $< E_T^{miss} > 45$ GeV
- Region C: $|m_{ll} - m_Z| < 15$ GeV and $E_T^{miss} > 45$ GeV
- Region D: $|m_{ll} - m_Z| < 15$ GeV and 20 GeV $< E_T^{miss} > 45$ GeV

The ratios of DY events between regions A/B and C/D are assumed to be constant. An extrapolation to the signal region by using the number of observed events in data is

$$A^{estimated} = B^{observed} \times \frac{C^{observed}}{D^{observed}} \times \alpha, \quad \text{with } \alpha = \frac{(A^{MC}/B^{MC})}{(C^{MC}/D^{MC})} \tag{5.17}$$

where A^{MC}, B^{MC}, C^{MC} and D^{MC} are MC DY events in the respective regions.

In the $e\mu$ and μe channels, the background is estimated using MC simulation. A cross-check with data in $N_{jet} = 0$ was performed using a CR dominated by $Z \to \tau\tau$ decays, which is constructed by requiring 10 GeV $< m_{ll} <$ 80 GeV, $\Delta\phi_{ll} > 2.5$, and $p_T^{ll} < 30$ GeV. A $E_{T,rel}^{miss}$ threshold of 25 GeV is used to calculate the data/MC scale factor which is consistent with unity within the uncertainty of about ±10%.

$\mathbf{Z/\gamma^* \to \tau\tau}$ estimation

The DY background from taus is normalized to the data using a $e\mu$ and μe CRs that is defined by the back-to-back configuration of the leptons [103]. The CR shown in Figure 5.15 has a purity of 94% and 74% for $N_{jet} = 0$ and $N_{jet} = 1$, respectively. For the $N_{jet} = 0$ analysis, the CR is defined after the pre-selection cuts with further requiring $m_{ll} < 80$ GeV and $\Delta\phi_{ll} > 2.8$, resulting in a normalization factor of 1.00 ± 0.02 (stat.). In the $N_{jet} = 1$ case, the CR is also defined after the pre-selection cuts with the invariant di-tau mass $m_{\tau\tau} > (m_Z - 25$ GeV) and the cut $m_{ll} < 80$ GeV is applied. The resulting normalization factor for the $N_{jet} = 1$ case is 1.05 ± 0.04 (stat.).

The $N_{jet} \geq 2$ analysis is similar to the $N_{jet} \leq 1$ one, but requiring $N_{b-jet} = 0$ and $p_T^{tot} < 45$ GeV to define a CR with 67% purity. The resulting normalization factor is found to be 1.24 ± 0.06 (stat.).

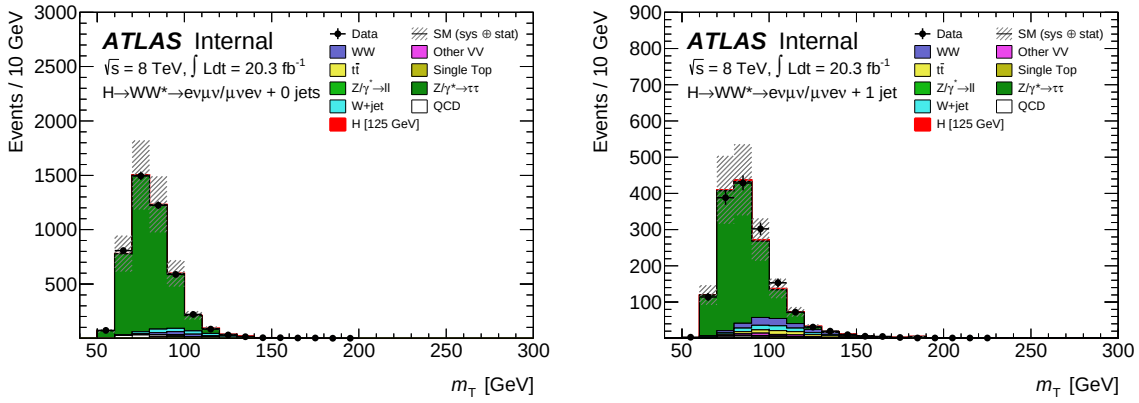

Figure 5.15 *Distributions of m_T in the $Z/\gamma^* \to \tau\tau$ control region in the $N_{jet} = 0$ (left), $N_{jet} = 1$ (right) categories. The distributions have been normalized to the data.*

W+jets estimation

The W+jets background contribution is estimated using a CR in which one lepton satisfies the identification and isolation criteria as described above, and the other lepton (denoted as *anti-identified*) fails these criteria but satisfies a looser selection. The dominant contribution to this background comes from W+jets events in which a jet produces an object which is reconstructed as a lepton. The extrapolation from the CR to the signal region is done by the *"fake factor method"*. In this method, the W+jets background in the signal region is obtained by scaling the number of expected W+jets events in the data CR by a fake factor. The fake factor is defined as the ratio of identified to anti-identified leptons

$$f_l = \frac{N_{id}}{N_{anti-id}} \quad \text{with } l = e, \mu \tag{5.18}$$

f_l is estimated as a function of the p_T and η of the anti-identified lepton using dijet and enriched Z+jets samples (see Figure 5.16).

For the W+jets predictions, two CRs are defined for the $ee/\mu\mu$ and $e\mu/\mu e$ channels separately, with the same selection as that of the SR. The number of events in this W+jets CR $N_{id+antiid}$ is used to estimate the amount W+jets background in the SR:

$$N_{W+jets} = f_l \times N_{id+anti-id} \tag{5.19}$$

The fake factor uncertainty is the main uncertainty on the W+jets background estimation. It is dominated by differences in the jet composition between the dijet and W+jets samples, as observed in MC simulation (see Figure 5.17). The total fake factor uncertainty is ±45% (±40%) for mis-identified electrons (muons).

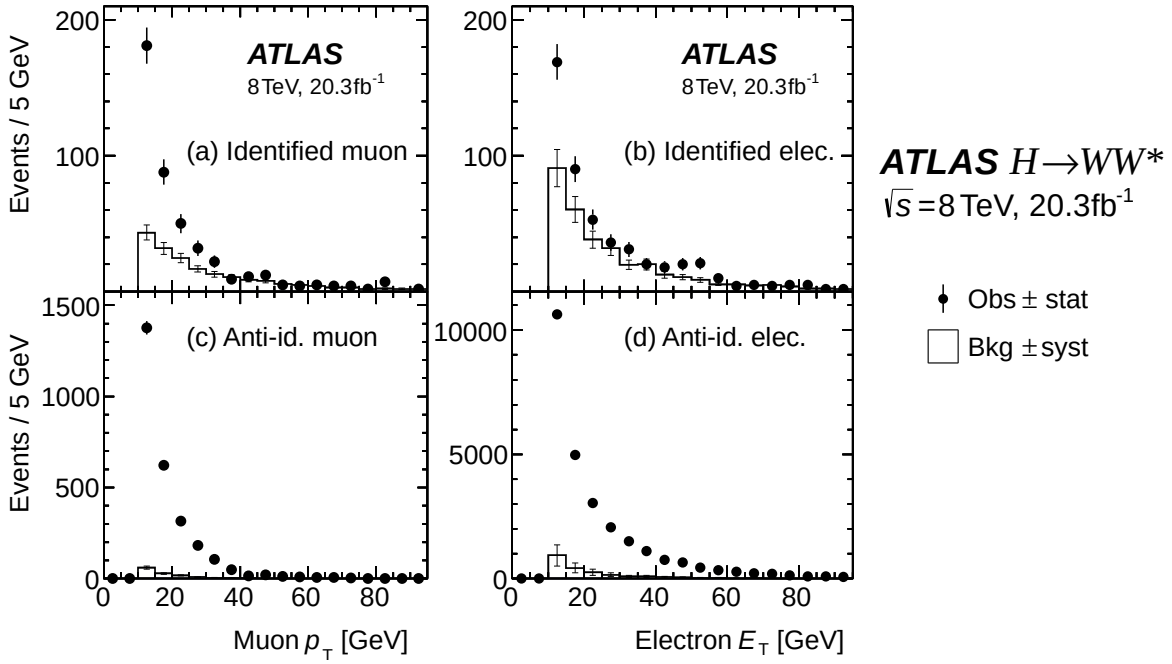

Figure 5.16 *Distributions of lepton p_T in the Z+jets control sample: (a) identified muon, (b) identified electron, (c) anti-identified muon and (d) anti-identified electron.*

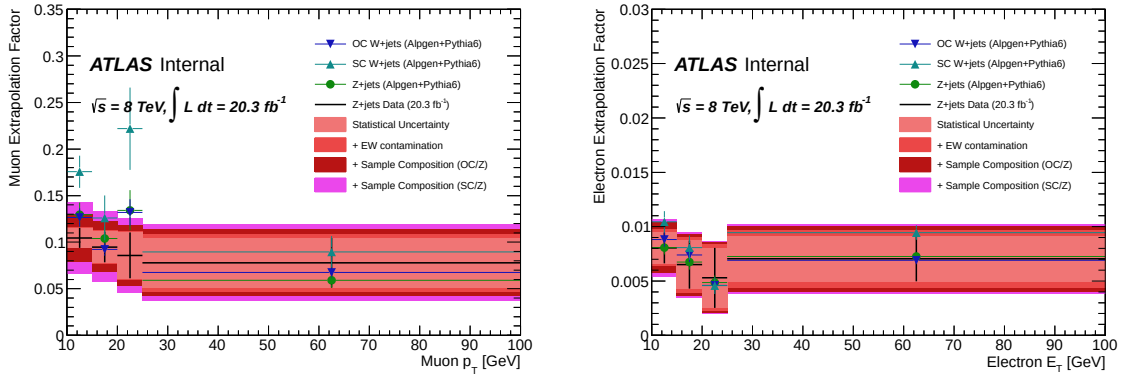

Figure 5.17 *Fake factors f_l for anti-identified muons (left) and electrons (right). The symbols represent the central values of the Z+jets data and the three MC samples: Z+jets, opposite-charge (OC) W+jets, and same-charge (SC) W+jets. The bands represent the uncertainties: Stat. refers to the statistical component, which is dominated by the number of jets identified as leptons in Z/γ^* data; EW is due to the subtraction of other electroweak processes; and Sample is due to the variation of the f_l ratios in Z+jets to OC W+jets or to SC W+jets in the three MC samples.*

5.4 Systematic Uncertainties

The systematic uncertainties on the signal yields and cross section can be divided into two categories: theoretical uncertainties, such as the estimation of the effect of higher-order corrections through variations of the QCD scale inputs to MC calculations, and experimental uncertainties, such as uncertainties on the jet energy scale and the b-jet

tagging efficiency. Some of these uncertainties are correlated between the signal and background predictions, so the impact of each uncertainty is calculated by varying the parameter and recalculating the signal and background yields.

5.4.1 Theoretical Uncertainties

Theoretical uncertainties on the signal production cross sections include uncertainties on the QCD renormalization and factorization scales, the PDF model and underlying event and the parton shower model [108, 109].

To evaluate the uncertainties from the QCD factorization and renormalization scales, the scales are independently varied up and down by a factor of two while keeping their ratio between 0.5 and 2.

For large backgrounds such as WW and top that are evaluated through extrapolation from a signal-depleted CR, theoretical uncertainties are reduced compared to those on the absolute MC normalization. The parameters are defined generally as the ratio of the number of events passing the signal region selection to the number passing the CR selection as evaluated in simulation, $\alpha = N_{\mathrm{SR}}/N_{\mathrm{CR}}$.

For small backgrounds, such as the non-WW diboson backgrounds, the background acceptance is completely evaluated from simulation and the calculated cross sections are used for their normalization. Therefore, the associated theoretical uncertainties are larger than those for backgrounds normalized in CRs [103], but it is not dramatic since these backgrounds are small.

WW background

For WW, the parameters α_{WW}^{0j} and α_{WW}^{1j} denote the extrapolation parameters for $N_{jet} = 0$ and $N_{jet} = 1$, respectively. The uncertainties on these parameters are evaluated according to the prescription of Ref. [109]. The signal extraction procedure relies on the precise knowledge of the modelling by simulation. These corresponding uncertainties are evaluated by comparing the α-value from POWHEG+PYTHIA8 and MCFM. The UE and PS uncertainties are evaluated by comparing the predictions of POWHEG interfaced with PYTHIA8, PYTHIA6, and HERWIG. The total uncertainties are about $\pm 2\%$ and $\pm(4{-}6)\%$ for the $N_{jet} = 0$ and $N_{jet} = 1$ signal regions, respectively.

The WW background in the $N_{jet} \geq 2$ category is predicted by simulation. Two types of contributions result from QCD processes with gluon emissions and from electroweak processes. For the first one, a total uncertainty of $\pm 42\%$ is dominated from QCD scale and PDF variations. For the latter one, a total uncertainty of $\pm 11\%$ is obtained by considering the QCD scale, the interference between QCD and Higgs processes, and the difference between the SHERPA and MADGRAPH generators.

Top-quark background

The dominant uncertainties on the top-quark background for the $N_{jet} = 0$ analysis are the theoretical uncertainties on the component derived from MC simulation. These total to ±10% and include the effects of uncertainties on the QCD scale, initial- and final-state radiation, generator/PS model. The relative normalisation of $t\bar{t}$ and single top, and the interference between single top and $t\bar{t}$, is neglected when using separate $t\bar{t}$ and single top Monte Carlo samples.

For $N_{jet} = 1$, the uncertainty of ±8% on α is evaluated by comparing the simulated $t\bar{t}$ and single top event yields with different QCD tunes for initial- and final-state radiation. For $N_{jet} \geq 2$, the uncertainty of ±15% on α is evaluated by comparing the modelling of various generators after the VBF-related selection.

Z/DY background

A total theoretical uncertainty of ±21% for $Z/\gamma^* \to \tau\tau$ in $N_{jet} = 0$ and ±12% in $N_{jet} = 1$ has been estimated. For $Z/\gamma^* \to ee/\mu\mu$, a total uncertainty on the estimated background yield B_{DY} is found to be ±49% and ±45% for the $N_{jet} = 0$ and $N_{jet} = 1$ categories, respectively.

W+jets background

For the Z+jets and W+jets control samples, the yields predicted by POWHEG+ PYTHIA8, ALPGEN+ PYTHIA6 and ALPGEN+HERWIG are compared. The total systematic uncertainty on the fake factor varies from ±29% to ±61% for anti-identified electrons and from ±25% to ±46% for anti-identified muons.

ggF and VBF signal

The uncertainty on the perturbative calculation of the production cross section for the Higgs signal is one of the leading uncertainties on the measurement of the signal strength μ. For the ggF, the total uncertainty is about ±10% with approximately equal contributions from QCD scale variations and PDF modelling. For the VBF, the contribution to the theoretical uncertainty from QCD scale variations is found to be negligible. The PDF modeling uncertainty is evaluated to be ±2.7%. The total acceptance uncertainty for cut-based analyses for a 125 GeV VBF Higgs is about ±2.4%.

Furthermore, an uncertainty on the jet multiplicity distribution is obtained using the *jet-veto effciency* (JVE) method [110]. The uncertainties on the JVE are ±14% and ±24% for the $N_{jet} = 0$ and $N_{jet} = 1$ categories, respectively.

Table 5.10: Total relative uncertainties on backgrounds that are normalized using control regions. The "Cross-talk" column gives approximate uncertainties on the normalization of other processes in the CR (taken from Ref. [73]).

Estimate	Statistical (%)	Theory (%)	Expermental (%)	Cross-talk (%)	Total (%)
WW					
$N_{jet} = 0$	2.9	1.6	4.4	5.0	7.4
$N_{jet} = 1$	6	5	4	36	37
Top					
$N_{jet} = 1$	2	8	22	16	29
$N_{jet} \geq 2$	10	15	29	19	39

5.4.2 Experimental Uncertainties

The experimental uncertainties affect both the expected signal and background yields, and are primarily associated with the reconstruction efficiency and energy/momentum scale and resolution of the different objects (leptons, jets, and missing momentum) in the event. The most significant contributions are from the jet energy scale and resolution, the b-tagging efficiency, and the uncertainty on the fake factor used to calculate the W+jets background.

The jet energy scale is determined from a combination of test beam, simulation, and in situ measurements. The jet energy scale uncertainty for jets with $p_T > 25$ GeV and $|\eta| < 4.5$ is $\pm(1{-}5)\%$. The uncertainty of jet energy resolution varies from $\pm 5\%$ to $\pm 20\%$ as a function of the jet p_T and η.

The uncertainties of reconstruction, identification, and trigger efficiencies for electrons and muons are estimated using $Z \to ll$, $J/\psi \to ll$, and $W \to l\nu$ decays and are found to be smaller than $\pm 1\%$.

The efficiency of the b-tagging algorithm is determined using samples containing muons reconstructed in the vicinity of jets [111]. The resulting uncertainty on the b-jet tagging efficiency varies between $\pm 5\%$ and $\pm 12\%$ as a function of jet p_T.

The uncertainty on the integrated luminosity is $\pm 3.6\%$ [112].

5.4.3 Uncertainties on backgrounds normalization

For the backgrounds normalized using CRs (WW for the $N_{jet} = 0$ and $N_{jet} = 1$ categories and top for the $N_{jet} = 1$ and ≥ 2), the sources of uncertainty can be grouped into four categories: the statistical uncertainty, the theoretical and experimental uncertainties on the simulation-based extrapolation from the CR to the signal region, and the uncertainty on the other contributing processes in the CR, which are subtracted from the data yield to get the estimated number of events from the targeted background. The resulting total uncertainties from these sources are summarized in Table 5.10.

5.5 Statistical Treatment

To extract the analysis results, a maximum likelihood fit is used. For $N_{jet} \leq 1$ the transverse mass m_T is used in the fit while for the $N_{jet} \geq 2$ the MVA is used instead. In the fit, extrapolation factors (normalization factors NF) from the control regions to the signal regions are used for the backgrounds in order to describe the fitted background rates in the signal region. Moreover, among the various control regions the background rates are extrapolated. For a single m_T bin in a given final state (e.g. lepton flavour and jet multiplicity) the likelihood can be written as a product of conditional Poisson probabilities $P(N|\mu)$

$$\mathcal{L}(\mu, \mu_b) = P(N|\mu \cdot S + \mu_b \cdot b_{SR}^{exp}) \times P(M|\mu_b \cdot b_{CR}^{exp}) \tag{5.20}$$

where b_{CR}^{exp} is the expected background yield in the control region, b_{SR}^{exp} the expected background yield in the signal region, S the expected yield of signal events in the signal region, μ is the signal strength parameter and μ_b the signal strength parameter for the background.

The simple likelihood function is expanded as a product of Poisson probability terms for the signal and control regions in each lepton flavour channel, jet multiplicity and m_T bin. Uncertainties are treated as a set of *nuisance parameters* (referred to as $\vec{\theta}$) with additional constraints.

The full likelihood can be written as

$$\mathcal{L}(\mu, \vec{\theta}) = \left\{ \prod_{k=e\mu,\mu e,ee,\mu\mu} \prod_{j=0}^{n_{jet}} \prod_{i=1}^{N_{bins}} P(N_{ijk}|\mu \cdot S_{ijk} + \sum_{m}^{N_{bg} b_{ijk}}) \right\} \times \left\{ \prod_{i=1}^{N_\theta} N(\widetilde{\theta}|\theta) \right\} \tag{5.21}$$

which contains a product over the m_T bins, a product over lepton flavour and a product over the jets in the final state. The signal and background yields are functions of the nuisance parameters (NPs) θ in a way that their responses to each NP is factorized from the nominal value of the expected rate, e.g.

$$S = S_0 \times \prod \nu(\theta) \tag{5.22}$$

where $\nu(\theta)$ is response function which depends on θ.

The final term $N(\widetilde{\theta}|\theta)$ is the product over the NP. The NP correspond to the various systematic variations and the background estimations in the control regions of the analysis, the collection of the NPs is represented by $\vec{\theta}$. The NPs are divided into four categories

- ***Flat systematic uncertainties***: systematic uncertainties which do not affect the shape of the m_T distribution, take the form $\nu_{flat}(\theta) = \kappa^\theta$ with a Gaussian constraint.

- ***Shape systematic uncertainties***: systematic uncertainties which affect the shape of the m_T distribution. The NP is split into a flat component affecting only the normalization and treated as described above, and a shape component with a Gaussian constraint.
- ***Statistical systematic uncertainties***: uncertainties arise from the MC statistical uncertainty on the number of MC events or data-driven methods.
- ***Uncertainties from background control regions***: originating from the limited size of the data sample in the control region constraining the background normalization. The contamination due to both the signal and the other backgrounds has to be taken into account as well. The constraint is given by a Poisson distribution.

Due to the fact that each category represents a different systematic source, each can affect multiple signal and background rates. Likewise, each signal or background component may possess a different set of NPs. A test statistic q_μ is constructed using the profile likelihood

$$q_\mu = -2\ln\frac{\mathcal{L}(\mu, \hat{\hat{\theta}}_\mu)}{\mathcal{L}(\hat{\mu}, \hat{\theta}_{\hat{\mu}})} \tag{5.23}$$

where $\hat{\mu}$ and $\hat{\theta}_{\hat{\mu}}$ are the parameters that maximize the likelihood and $\hat{\hat{\theta}}_\mu$ corresponds to the conditional maximum likelihood of θ given μ and the data. The constraint $0 \leq \hat{\mu} \leq \mu$ is applied to ensure that the signal is positive and to guarantee a one-sided confidence limit.

The p-value expresses the probability of how the data are compatible with the assumption that the background-only hypothesis is true. It is calculated by integrating over the corresponding sampling distribution

$$p_0 = \int_{q_\mu^{obs}}^{\infty} f(q_\mu|0, \hat{q}_0^{obs})\mathrm{d}q_\mu \tag{5.24}$$

where $f(q_\mu|0, \hat{q}_0^{obs})$ represents the *probability density function* (PDF) under a given assumption on μ. In practice, the PDF for a given hypothesis on μ is obtained using MC pseudo-experiments.

5.6 Results of the Run 1 Analysis

5.6.1 Fit results

The fit is performed over the signal and control regions. For the $e\mu$ and μe channels in the $N_{jet} \leq 1$ categories, each signal region is divided into 12 kinematic regions: two regions in $m_l l$, three regions in $p_T^{sublead}$ and two regions for the subleading lepton flavours. In contrast, the ee and $\mu\mu$ channels only have one region for each $m_l l$ and

$p_T^{sublead}$. Table 5.11 summarizes the m_{ll} and $p_T^{sublead}$ bins used in the fit.

Table 5.11: Signal region categories of the fit in the $N_{jet} \leq 1$ categories. Energy-related quantities are in GeV.

N_{jet}	$\otimes m_{ll}$	$\otimes p_T^{sublead}$	$\otimes l^{sublead}$
$N_{jet} = 0$			
$-\ e\mu/\mu e$	$\otimes[10, 30, 55]$	$\otimes[10, 15, 20, \infty]$	$\otimes[e, \mu]$
$-\ ee/\mu\mu$	$\otimes[12, 55]$	$\otimes[10, \infty]$	
$N_{jet} = 1$			
$-\ e\mu/\mu e$	$\otimes[10, 30, 55]$	$\otimes[10, 15, 20, \infty]$	$\otimes[e, \mu]$
$-\ ee/\mu\mu$	$\otimes[12, 55]$	$\otimes[10, \infty]$	

Table 5.12 shows the postfit yields for all of the fitted categories in the 8 TeV and 7 TeV data analyses. The signal yields are scaled with the observed signal strength derived from the simultaneous combined fit to all of the categories. All of the background processes are normalized to the postfit NFs and additionally their rates take into account the pulls of the nuisance parameters. The uncertainties include both the statistical and systematic components.

For the 8 TeV data analysis, the m_T distributions for the $e\mu/\mu e$ and $ee/\mu\mu$ channels in different m_{ll} and $p_T^{sublead}$ bins in the $N_{jet} \leq 1$ categories are shown in Figures 5.18 and 5.19. In $N_{jet} = 0$ category, the WW process dominates the background contributions. Besides, the VV and W+jets processes are dominant backgrounds in the 10 GeV $< p_T^{sublead} <$ 15 GeV region. Figure 5.20 show the BDT outputs in the $e\mu/\mu e$ and $ee/\mu\mu$ channels, respectively. In Figures 5.20(a) and 5.20(c), the third BDT bin provides the highest purity, with a signal-to-background ratio of approximately 2. The m_T distributions in Figures 5.20(b) and 5.20(d) combines all three BDT bins for the $e\mu/\mu e$ and $ee/\mu\mu$ channels, respectively. Figure 5.21 shows the m_T distributions in the 7 TeV analysis which are similar to those in the 8 TeV analysis but with fewer events. Finally, Figure 5.22 shows the combined m_T distribution, summed over the lepton-flavours in the $N_{jet} \leq 1$ categories for the 7 TeV and 8 TeV data analyses, and the residuals of the data after background subtraction in compared to the expected m_T distribution of an Standard Model Higgs boson with $m_H = 125$ GeV.

Table 5.12: Signal region yields with uncertainties for each N_{jet} category, separated for the 8 and 7 TeV data analyses. The N_{signal} columns show the expected signal yields from the ggF and VBF production modes. The composition columns give the contributions to N_{bkg}.

Channel	Summary				Composition of N_{bkg}						
	N_{obs}	N_{bkg}	N_{signal}		N_{WW}	N_{top}		N_{fakes}		N_{VV}	N_{DY}
			N_{ggF}	N_{VBF}		N_t	$N_{t\bar{t}}$	N_{W+jets}	N_{QCD}		
(a) 8 TeV											
$N_{jet} = 0$	3750	3430±90	300±50	8±4	2250±95	112±9	195±15	360±60	16±5	420±40	78±21
$e\mu$	1430	1280±40	129±20	3.0±2.1	830±34	41±3	73±6	149±29	10.1±3.6	167±21	14±2.4
μe	1212	1106±35	97±15	2.5±0.6	686±29	33±3	57±5	128±31	3.8±1.5	184±23	14±2.4
$ee/\mu\mu$	1108	1040±40	77±15	2.4±1.7	740±40	39±3	65±5	82±16	2±0.5	68±7	50±21
$N_{jet} = 1$	1596	1470±40	102±26	17±5	630±50	150±10	385±20	108±20	8.2±3.0	143±20	51±13
$e\mu$	621	569±19	45±11	7.4±2	241±20	58±4	147±7	51±11	5.7±2.0	53±10	13.8±3.3
μe	508	475±18	35±9	6.1±1.4	202±17	45±3	119±6	37±9	2.3±0.9	60±10	9.3±2.5
$ee/\mu\mu$	467	427±21	22±6	3.6±1.8	184±15	46±4	119±10	19±4	0.2±0.1	31±4	28±12
$N_{jet} \geq 2$, VBF	130	99±9	7.7±2.6	21±3	11±3.5	5.5±0.7	29±5	4.7±1.4	2.8±1.0	4.4±0.9	38±7
(b) 7 TeV											
$N_{jet} = 0$	594	575±24	49±8	1.4±0.2	339±24	20.5±2.1	38±4	74±15	1.3±0.6	79±10	23±6
$e\mu$	185	186±8	19±3	0.5±0.0	116±8	7±1	14±2	19±5	±24	3±4.8	1±
μe	195	193±12	15±2.4	0.5±0.0	95±7	5.3±0.5	10±1	37±9	1.1±0.5	41±6	4.1±0.9
$ee/\mu\mu$	214	196±11	16±3.1	0.5±0.1	128±10	8±1	14±2	18±4	0.2±0.1	14±2	14±5
$N_{jet} = 1$	304	276±15	16±4	3.2±0.3	103±15	22±2	58±6	20±4	3.2±1.6	32±8	38±6
$e\mu$	93	75±4	5.7±1.6	1.2±0.1	33±5	7±1	18±2	5±1	±9	2±2.7	0.4±
μe	91	76±5	4.5±1.2	0.9±0.1	28±4	6±1	16±2	10±2	0.7±0.3	14±4	2.3±0.7
$ee/\mu\mu$	120	125±9	5.3±1.6	1.2±0.2	43±6	9±1	24±3	5±1	2.5±1.4	9±2	33±6
$N_{jet} \geq 2$, VBF	9	7.8±1.8	0.9±0.3	2.7±0.3	1.2±0.4	0.3±0.1	1.6±0.8	0.4±0.1	0.1±0.0	0.5±0.2	3.4±1.5

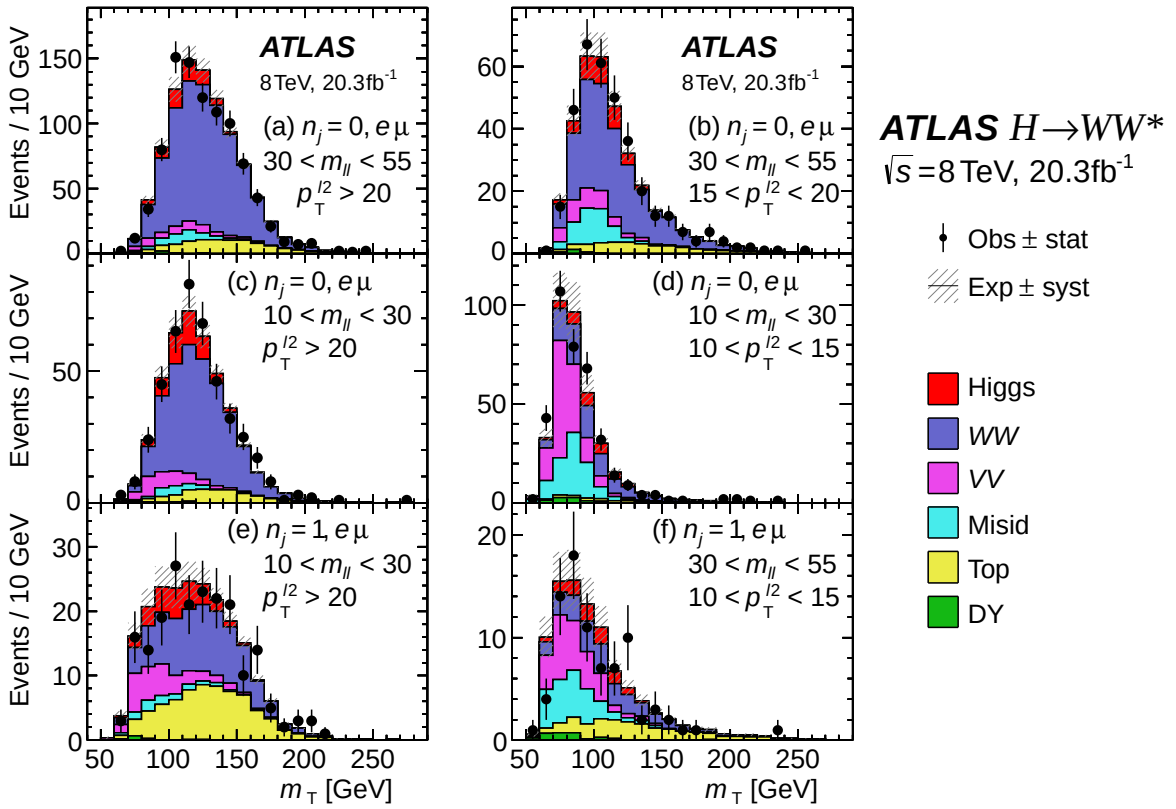

Figure 5.18 *Post-fit m_T distributions in the $e\mu/\mu e$ $N_{jet} \leq 1$ categories with different m_{ll} and $p_T^{sublead}$ bins in the 8 TeV data analysis.*

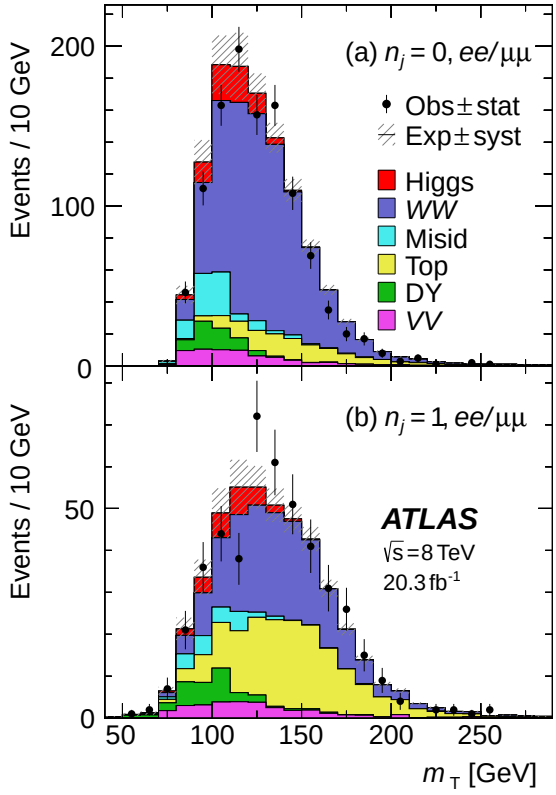

Figure 5.19 *Post-fit m_T distributions in the $ee/\mu\mu$ $N_{jet} \leq 1$ categories in the 8 TeV data analysis.*

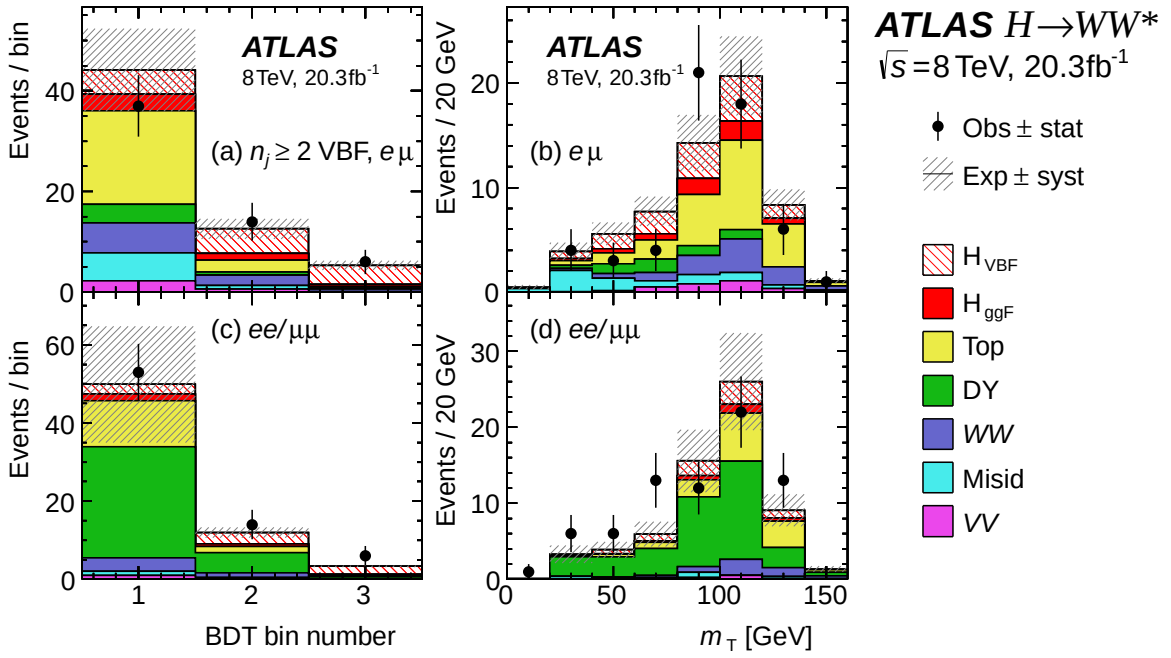

Figure 5.20 *Post-fit BDT and m_T distributions in the $N_{jet} \geq 2$ VBF-enriched categories in the 8 TeV data analysis: (a) BDT output in $e\mu/\mu e$, (b) m_T in $e\mu/\mu e$, c) BDT output in $ee/\mu\mu$, and (d) m_T in $ee/\mu\mu$.*

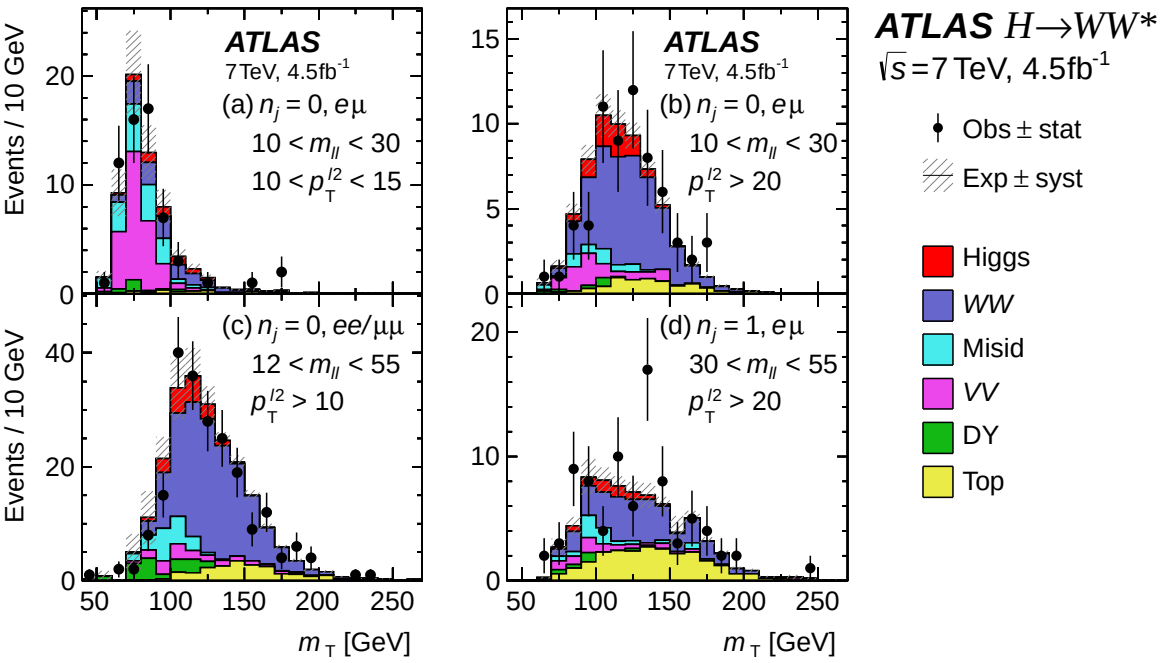

Figure 5.21 *Post-fit m_T distributions in the $e\mu/\mu e$ $N_{jet} \leq 1$ categories with different m_{ll} and $p_T^{sublead}$ bins in the 7 TeV data analysis.*

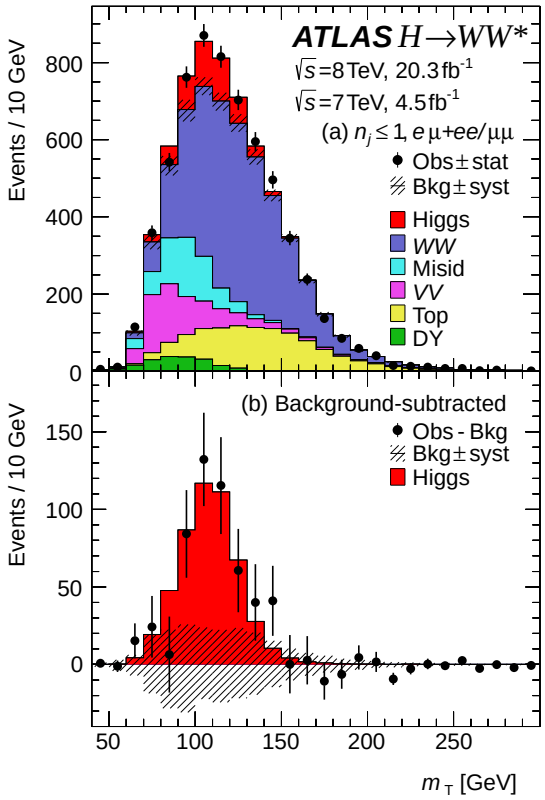

Figure 5.22 *Postfit m_T distributions for $N_{jet} \leq 1$ and for all lepton-flavor samples in the 7 TeV and 8 TeV data analyses. The bottom plot shows the residuals of the data after background subtraction in compared to the expected m_T distribution of an Standard Model Higgs boson with $m_H = 125$ GeV.*

5.6.2 Observation of the $H \to WW^* \to l\nu l\nu$ decay mode

All the final results from the $H \to WW^* \to l\nu l\nu$ analysis using 7 TeV and 8 TeV dataset is combined together to provide a cumulative result. The left plot in Figure 5.23 shows the observed and expected p_0 as a function of m_H. The minimum p_0 value is found at $m_H = 130$ GeV and corresponds to a local significance of 6.1 standard deviations (s.d.). The corresponding expected significance for a Standard Higgs boson is 5.8 s.d. The right plot in Figure 5.23 shows the best-fit signal strength $\hat{\mu}$ as a function of m_H. The observed $\hat{\mu}$ is close to zero for $m_H > 160$ GeV and crosses unity at $m_H = 125.36$ GeV, and from there the observed best-fit of μ takes value

$$\begin{aligned}
\mu &= 1.09 \ {}^{+0.16}_{-0.15}\,(\text{stat.}) \ {}^{+0.08}_{-0.07}\left(\begin{smallmatrix}\text{expt.}\\ \text{syst.}\end{smallmatrix}\right) \ {}^{+0.15}_{-0.12}\left(\begin{smallmatrix}\text{theo.}\\ \text{syst.}\end{smallmatrix}\right) \ \pm 0.03\left(\begin{smallmatrix}\text{lumi.}\\ \text{syst.}\end{smallmatrix}\right) \\
&= 1.09 \ {}^{+0.16}_{-0.15}\,(\text{stat.}) \ {}^{+0.17}_{-0.14}\,(\text{syst.}) \\
&= 1.09 \ {}^{+0.23}_{-0.21}.
\end{aligned} \tag{5.25}$$

The signal strength μ can be further splitted into the ggF signal strength μ_{ggF} and VBF signal strength μ_{VBF}. A profiled likelihood scan is performed to extract the

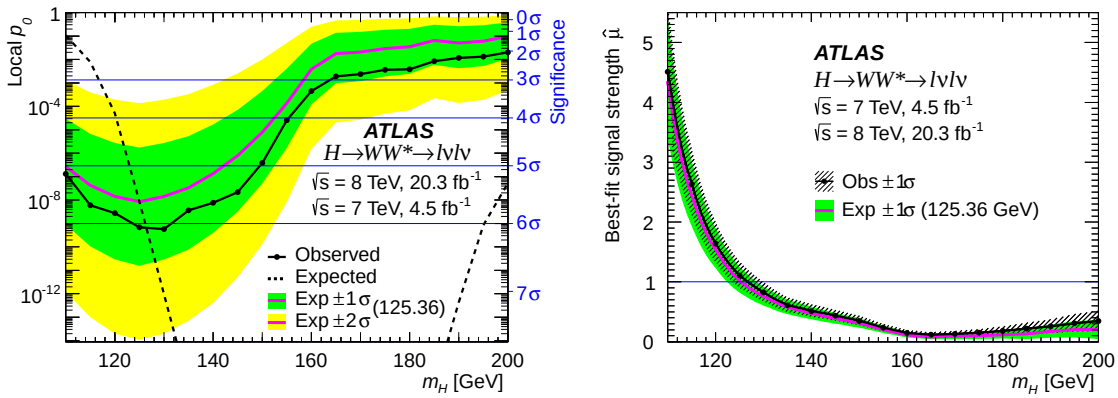

Figure 5.23 *Results for p_0 (left) and best-fit signal strength $\hat{\mu}$ (right) as functions of m_H using combined 7 TeV and 8 TeV data. The expected values for $m_H = 125$ GeV are shown as a black solid lines.*

significance of the VBF signal. The likelihood scan as a function of the ratio μ_{VBF}/μ_{ggF} is shown in Figure 5.24, which gives the best-fit value of

$$\frac{\mu_{VBF}}{\mu_{ggF}} = 1.26\,^{+0.61}_{-0.45}\,(\text{stat.})\,^{+0.50}_{-0.26}\,(\text{syst.}) = 1.26\,^{+0.79}_{-0.53}. \tag{5.26}$$

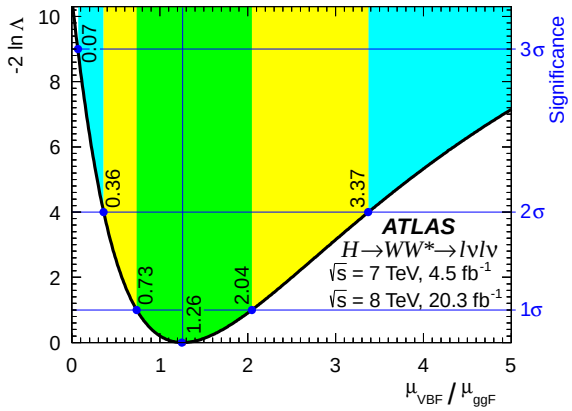

Figure 5.24 *Likelihood scan as a function of μ_{VBF}/μ_{ggF} for $m_H = 125.36$ GeV.*

The value of the likelihood at $\mu_{VBF}/\mu_{ggF} = 0$ gives the significance of the VBF signal at 3.2 s.d. and the corresponding expected significance is 2.7 s.d. The same results can be obtained via a simultaneous fit over the two signal strength in order to check the compatibility with the Standard Model prediction of the ggF and VBF production. The best-fit values are

$$\begin{array}{lllll} \mu_{ggF} & = 1.02 & \pm 0.19 & ^{+0.22}_{-0.18} & = 1.02\,^{+0.29}_{-0.26} \\ \mu_{VBF} & = 1.27\,^{+0.44}_{-0.40} & & ^{+0.29}_{-0.21} & = 1.27\,^{+0.53}_{-0.45}. \\ & (\text{stat.}) & & (\text{syst.}) & \end{array} \tag{5.27}$$

Figure 5.25 shows the two-dimensional likelihood contours as a function of μ_{ggF} and

μ_{VBF}.

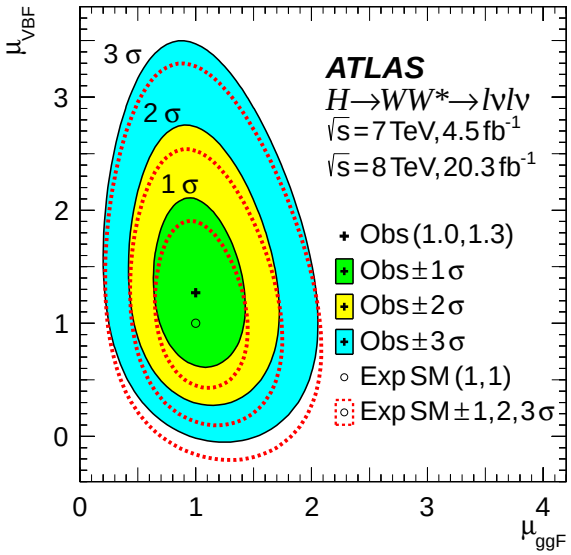

Figure 5.25 *Likelihood scan as a function of μ_{ggF} and μ_{VBF}.*

5.6.3 Higgs couplings to fermions and vector bosons

The values of μ_{ggF} and μ_{VBF} can be expressed as functions of the two newly defined scale factors κ_F (for fermionic couplings) and κ_F (for bosonic couplings) using a leading-order interaction framework [113]

$$\begin{aligned} \mu_{ggF} &\propto \frac{\kappa_F^2 \cdot \kappa_V^2}{(\mathcal{B}_{H\to f\bar{f}} + \mathcal{B}_{H\to gg})\,\kappa_F^2 + (\mathcal{B}_{H\to VV})\,\kappa_V^2} \\ \mu_{VBF} &\propto \frac{\kappa_V^4}{(\mathcal{B}_{H\to f\bar{f}} + \mathcal{B}_{H\to gg})\,\kappa_F^2 + (\mathcal{B}_{H\to VV})\,\kappa_V^2}. \end{aligned} \tag{5.28}$$

With an assumption that there is no non-SM decay mode, the denominator corresponds to the total decay width of the Higgs boson in terms of the fermionic and bosonic decay amplitudes. The likelihood scan as a function of κ_V and κ_F is shown in Figure 5.26. The low discrimination at high values of κ_F implies the insensitive of the ggF production mode at the limit where $\kappa_F \gg \kappa_V$. Therefore, the sensitivity at high κ_F values is driven by the value of μ_{VBF}. The vanishing of VBF process at the limit where $\kappa_F \gg \kappa_V$ is due to the increase of the Higgs boson total width and the decrease of the WW* branching fraction. The best-fit values are

$$\begin{aligned} \kappa_F &= 0.93 \;{}^{+0.24}_{-0.18}\;{}^{+0.21}_{-0.14} &&= 0.93 \;{}^{+0.32}_{-0.23} \\ \kappa_V &= 1.04 \;{}^{+0.07}_{-0.08}\;{}^{+0.07}_{-0.08} &&= 1.04 \;\pm 0.11. \\ & \quad \text{(stat.)} \quad \text{(syst.)} \end{aligned} \tag{5.29}$$

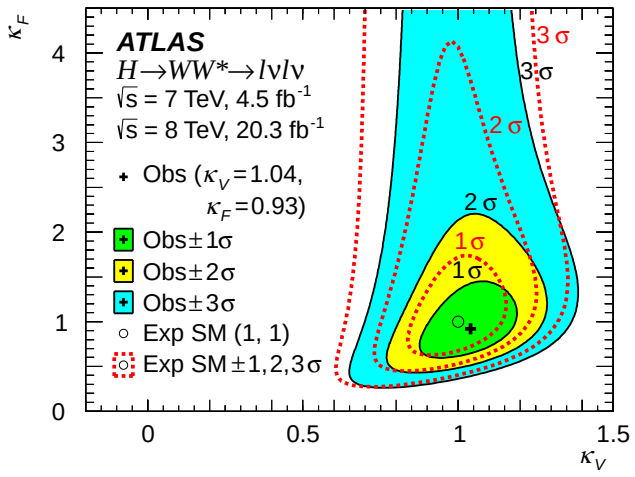

Figure 5.26 *Likelihood scan as a function of κ_V and κ_F.*

5.6.4 Exclusion limits

The exclusion ranges are computed using the modified frequentist method CL_s [114]. A SM Higgs boson of mass m_H is considered excluded at 95% confidence level (C.L.) if the value $\mu = 1$ is excluded at that mass. The analysis results give an observed exclusion range of 132 GeV $< m_H <$ 200 GeV (upper limit of the search range) as shown in Figure 5.27.

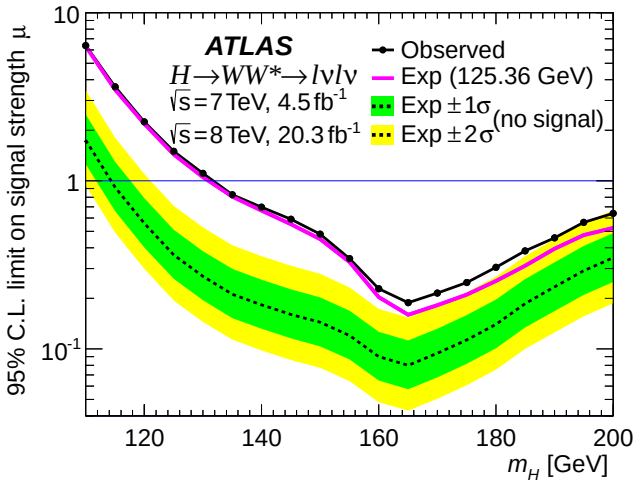

Figure 5.27 *CL_s exclusion plot for 110 GeV $< m_H <$ 200 GeV.*

5.6.5 Higgs production cross sections

The inclusive cross section of the Higgs boson production is defined as

$$\begin{aligned}\left(\sigma \cdot \mathcal{B}_{H\to WW^*}\right)_{obs} &= \frac{(N_{sig})_{obs}}{\mathcal{A}\cdot\mathcal{C}\cdot\mathcal{B}_{WW^*\to l\nu l\nu}} \cdot \frac{1}{\int Ldt} \\ &= \hat{\mu}\cdot\left(\sigma\cdot\mathcal{B}_{H\to WW^*}\right)_{exp}.\end{aligned} \tag{5.30}$$

where $\mathcal{A}$ is the kinematic and geometric acceptance and $\mathcal{C}$ is the ratio of the number of measured events to the number of events produced in the fiducial phase space of the detector.

The inclusive cross sections are calculated for the ggF production process at both 7 TeV and 8 TeV and for the VBF production process only at 8 TeV. The measured signal strengths are

$$\begin{aligned}
\mu_{ggF}^{7\text{TeV}} &= 0.57 \quad {}^{+0.52}_{-0.51} \quad {}^{+0.36}_{-0.34} \quad {}^{+0.14}_{-0.004} \\
\mu_{ggF}^{8\text{TeV}} &= 1.09 \quad \pm 0.20 \quad {}^{+0.19}_{-0.17} \quad {}^{+0.14}_{-0.09} \\
\mu_{VBF}^{8\text{TeV}} &= 1.45 \quad {}^{+0.48}_{-0.44} \quad {}^{+0.38}_{-0.24} \quad {}^{+0.11}_{-0.06} \\
&\qquad\qquad (\text{stat.}) \quad (\text{syst.}) \quad (\text{sig.})
\end{aligned} \tag{5.31}$$

where (sig.) indicates the systematic uncertainties on the signal yields which do not be taken into account for the cross section measurements.

The inclusive cross sections are

$$\begin{aligned}
\sigma_{ggF}^{7\text{TeV}} \cdot \mathcal{B}_{H\to WW^*} &= 2.0 \quad \pm 1.7 \quad {}^{+1.2}_{-1.1} \quad = 2.0 \quad {}^{+2.1}_{-2.0} \quad \text{pb} \\
\sigma_{ggF}^{8\text{TeV}} \cdot \mathcal{B}_{H\to WW^*} &= 4.6 \quad \pm 0.9 \quad {}^{+0.8}_{-0.7} \quad = 4.6 \quad {}^{+1.2}_{-1.1} \quad \text{pb} \\
\sigma_{VBF}^{8\text{TeV}} \cdot \mathcal{B}_{H\to WW^*} &= 0.51 \quad {}^{+0.17}_{-0.15} \quad {}^{+0.13}_{-0.08} \quad = 0.51 \quad {}^{+0.22}_{-0.17} \quad \text{pb.} \\
&\qquad\qquad (\text{stat.}) \quad (\text{syst.})
\end{aligned} \tag{5.32}$$

The predicted cross sections are 3.3 ± 0.4 pb, 4.2 ± 0.5 pb and 0.35 ± 0.02 pb, respectively.

Besides, the fiducial cross sections are also interesting since they can be compared with theoretical predictions with minimal assumptions on the kinematics of the signal and jet multiplicity in the event. The fiducial cross section is defined as

$$\begin{aligned}
\sigma_{fid} &= \frac{(N_{sig})_{obs}}{\mathcal{C}} \cdot \frac{1}{\int L\mathrm{d}t} \\
&= \hat{\mu} \cdot (\sigma \cdot \mathcal{B}_{H\to WW^*\to e\nu\mu\nu})_{exp} \cdot \mathcal{A},
\end{aligned} \tag{5.33}$$

To minimize dependence on the signal model or theoretical uncertainties, only the 8 TeV $e\mu$ and μe events in the $N_{jet} \leq 1$ categories are used. The obtained signal strengths are

$$\begin{aligned}
\mu_{0j,e\mu/\mu e}^{ggF} &= 1.39 \quad \pm 0.27 \quad {}^{+0.21}_{-0.19} \quad {}^{+0.27}_{-0.17} \\
\mu_{1j,e\mu/\mu e}^{ggF} &= 1.14 \quad {}^{+0.42}_{-0.41} \quad {}^{+0.27}_{-0.26} \quad {}^{+0.42}_{-0.17} \\
&\qquad\qquad (\text{stat.}) \quad (\text{syst.}) \quad (\text{sig.})
\end{aligned} \tag{5.34}$$

The corresponding cross sections are

$$\begin{aligned} \sigma^{ggF}_{fid,0j} &= 27.6 \,{}^{+5.4}_{-5.3}\,({\rm stat.})\,{}^{+4.1}_{-3.9}\,({\rm syst.}) = 27.6 \,{}^{+6.8}_{-6.6}\ {\rm fb} \\ \sigma^{ggF}_{fid,1j} &= 8.3 \,{}^{+3.1}_{-3.0}\,({\rm stat.})\,{}^{+2.0}_{-1.9}\,({\rm syst.}) = 8.3 \,{}^{+3.7}_{-3.5}\ {\rm fb.} \end{aligned} \tag{5.35}$$

The predicted cross sections are 19.9 ± 3.3 fb and 7.3 ± 1.8 fb, respectively.

6

Estimation of W + jets Background in the Run 1 Analysis with the Matrix Technique

The W + jets background contributes in the final signal region of the $H \to WW^* \to l\nu l\nu$ (HWW) analysis in a similar amount compared to the Higgs boson signal itself. Moreover, its shape is also comparable to the signal shape in one of the final observables m_T. Therefore, it is very important to reliably determine the shape and normalization of the W+jets background and especially minimize the uncertainty on these quantities.

The W + jets estimation method used in the last publicly available ATLAS HWW analysis [115] is based on the so-called fake factor method. This method calculates the rate that a loosely identified lepton candidate passes all tight identification criteria. It uses dijet and Z+jets samples which are independent from the HWW analysis sample to determine this fake factor. However, the dijet fake lepton factor is not the same as the one in the W + jets sample since the dijet and W + jets samples have different light-flavour and heavy-flavour contributions and moreover have different kinematic and topological distributions. Thus, this method has a large associated systematic uncertainty, called sample dependence uncertainty, of about 50%. It thus far constitutes the second most important systematic uncertainty in the determination of the Higgs boson signal strength, after that of the WW-related uncertainty (driven by the POWHEG − MC@NLO generators difference).

The matrix technique is described in Sec. 6.1. The Monte Carlo closure test to validate the matrix method and its application to data is presented in Sec. 6.2. The estimation of all the uncertainties is explained in Sec. 6.3. Finally, results are presented in Sec. 6.4.

6.1 Methodology

The matrix method presented here provides an alternative way to determine the W + jets background. It estimates each component of the W + jets background from data, based on their different responses to the different lepton identification selection criteria. One big advantage is the absense of the sample dependence uncertainty as in the fake factor method. This is because the extraction is performed directly in the dilepton sample of the main analysis. The main uncertainty of the matrix method is rather statistical. This stems from the fact that the data sample obtained after applying all selection criteria to extract the Higgs boson signal is of a rather limited size. The resulting statistical uncertainty is about 20% using the full ATLAS 2012 $\sqrt{s} = 8$ TeV dataset. The systematic uncertainties arise from the limited available Monte Carlo sample size used to build the extraction matrix, and from the Monte Carlo description of the lepton identification variables. The total uncertainty is estimated to be about 30%.

6.1.1 Basic ideas

The matrix method is based on the idea that one can determine the sample composition at an early pre-selection stage of the analysis (with some lepton identification criteria not yet applied) with sufficient sample size. The identification of the individual components can be done using lepton selection criteria that are assumed to be uncorrelated with the kinematic distributions of interest and the finally applied additional selection criteria. Since each background component responds differently to each lepton identification criteria, an efficiency matrix can be build. And since the remaining analysis selection criteria are assumed to be uncorrelated with the lepton identification criteria, one can use that same matrix to predict the contribution of each background component in the final signal regions. Figure 6.1 shows the sketch of the basic idea of matrix method. All aspects of this technique are explained with simple examples and also in more detail in the following sections.

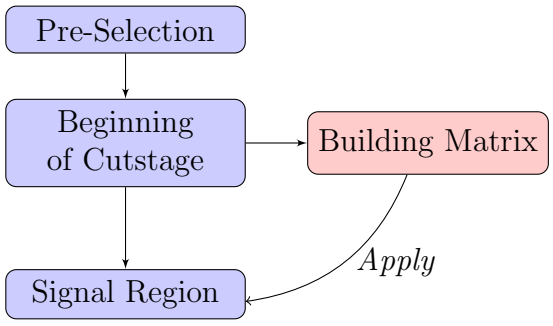

Figure 6.1 *Sketch of the basic idea of matrix method for determining the W + jets background.*

A simple example

The matrix technique in this example will be used for estimating the contribution of two types of lepton candidates. The lepton candidates originating from jets and other sources of background (e.g. photon conversions or leptonic decays of hadrons) are called *"fake"* leptons, and the lepton candidates actually originating directly from decays of heavy gauge bosons are called *"real"* leptons.

Two lepton identification selection criteria are defined, *"loose"* and *"tight"*, where in the "tight" case, additional lepton identification criteria are applied, *e.g.*, selections based on the relative lepton isolation as measured by the inner detector tracking system. The observed number of events in these "loose" and "tight" selection regions can be decomposed as

$$\begin{aligned} N^{loose} &= N^{loose}_{real} + N^{loose}_{fake} \\ N^{tight} &= N^{tight}_{real} + N^{tight}_{fake} \\ &= \epsilon_{real} N^{loose}_{real} + \epsilon_{fake} N^{loose}_{fake} \end{aligned} \tag{6.1}$$

where N^{loose} (N^{tight}) is the number of observed lepton candidates after applying the "loose" ("tight") lepton identification criteria, N^{loose}_{real} (N^{loose}_{fake}) is the true number of "real" ("fake") leptons after applying the "loose" lepton identification criteria, N^{tight}_{real} and N^{tight}_{fake} are the corresponding numbers of leptons after applying the "tight" lepton identification criteria, and ϵ_{real} (ϵ_{fake}) is the efficiency of a "real" ("fake") lepton candidate selected with the "loose" identification criteria to also be passing the "tight" selection. These equations can be rewriten in matrix form as

$$\begin{pmatrix} N^{loose} \\ N^{tight} \end{pmatrix} = \begin{pmatrix} 1 & 1 \\ \epsilon_{real} & \epsilon_{fake} \end{pmatrix} \times \begin{pmatrix} N^{loose}_{real} \\ N^{loose}_{fake} \end{pmatrix}. \tag{6.2}$$

The above efficiency matrix has to be inverted since the goal is to determine the number of "fake" leptons. Solving the equation for this, one finds

$$\begin{pmatrix} N^{loose}_{real} \\ N^{loose}_{fake} \end{pmatrix} = \frac{1}{\epsilon_{fake} - \epsilon_{real}} \begin{pmatrix} \epsilon_{fake} & -1 \\ -\epsilon_{real} & 1 \end{pmatrix} \times \begin{pmatrix} N^{loose} \\ N^{tight} \end{pmatrix}. \tag{6.3}$$

In a real analysis, one could imagine that the efficiencies are determined solely from Monte Carlo. Or, alternatively, one could determine ϵ_{real} with the *"tag-and-probe"* method from a $Z \to ll$ sample and ϵ_{fake} from a dijet sample.

Eq. 6.3 determines the number of "fake" lepton candidates after the "loose" selection. However, the final number of interest is the number of "fake" lepton candidates after the "tight" identification criteria are applied. This number is determined as

$$\begin{aligned} N^{tight}_{fake} &= \epsilon_{fake} N^{loose}_{fake} \\ &= \frac{\epsilon_{fake}}{\epsilon_{real} - \epsilon_{fake}} (\epsilon_{real} N^{loose} - N^{tight}), \end{aligned} \tag{6.4}$$

General case

After considering a simple case with one real and one fake lepton component, one can now move to the more general case in which the fake lepton is comprised of more than one component.

$$N_{fake} = N_{fake1} + N_{fake2} + ... \tag{6.5}$$

In this case, one needs more than one lepton identification variables to separate out each lepton component. Thus, the generalized analogon to Eq. 6.2 is

$$\begin{pmatrix} N^{loose} \\ N^{tight1} \\ N^{tight2} \\ ... \\ N^{tightN} \end{pmatrix} = \begin{pmatrix} 1 & 1 & 1 & ... & 1 \\ \epsilon_{real}^{tight1} & \epsilon_{fake1}^{tight1} & \epsilon_{fake2}^{tight1} & ... & \epsilon_{fakeM}^{tight1} \\ \epsilon_{real}^{tight2} & \epsilon_{fake1}^{tight2} & \epsilon_{fake2}^{tight2} & ... & \epsilon_{fakeM}^{tight2} \\ ... & ... & ... & ... & ... \\ \epsilon_{real}^{tightN} & \epsilon_{fake1}^{tightN} & \epsilon_{fake2}^{tightN} & ... & \epsilon_{fakeM}^{tightN} \end{pmatrix} \times \begin{pmatrix} N_{real}^{loose} \\ N_{fake1}^{loose} \\ N_{fake2}^{loose} \\ ... \\ N_{fakeM}^{loose} \end{pmatrix}. \tag{6.6}$$

Because of the large number of fake component, the efficiencies are estimated from MC instead of building control region for each fake component as in the simple case. Therefore, the systematic uncertainty will mainly come from the incorrect MC description of lepton identification variable cuts.

Method for solving the matrix

A binned maximum likelihood fit is used to solve the matrix equation. This fit method can be used for a binned dataset even if the distributions cannot be easily described by analytic functions. Also, this procedure correctly assumes that all statistical number fluctuations are Poisson distributed. Thus, one can describe the probability P_i to observe the number of events n_i in each bin using Poisson statistics

$$P_i = \frac{e^{-\bar{\mu_i}}(\bar{\mu_i})^{n_i}}{n_i!}. \tag{6.7}$$

The binned maximum likelihood tries to obtain the estimators of n_i by maximizing the joint probability function

$$L = \prod_i P_i \tag{6.8}$$

and instead of using the likelihood function directly, we can use the natural logarithm of it, which is called the log-likelihood function

$$\ln L = \sum_i \ln P_i = \sum_i n_i \ln(\bar{\mu_i}) - \sum_i \bar{\mu_i} - \sum_i \ln(n_i!). \tag{6.9}$$

In this study, the parameters are extracted by maximizing the log-likelihood function using the MINUIT package [116].

6.1.2 Matrix technique for estimating the $W+$jets background in the $H \to WW^* \to l\nu l\nu$ analysis

Suppose the data contain one real and one fake lepton component. Let x be a discriminating variable, e.g., lepton isolation, whose real and fake efficiencies $\varepsilon^{real}(x)$ and $\varepsilon^{fake}(x)$, respectively, are known from Monte Carlo. The total number of real and fake events, N^{real} and N^{fake}, can be estimated from data by solving the matrix equation

$$\begin{pmatrix} N(x_1) \\ N(x_2) \\ ... \\ N(x_n) \end{pmatrix} = \begin{pmatrix} \epsilon_{real}(x_1) & \epsilon_{fake}(x_1) \\ \epsilon_{real}(x_2) & \epsilon_{fake}(x_2) \\ ... & ... \\ \epsilon_{fake}(x_n) & \epsilon_{fake}(x_n) \end{pmatrix} \begin{pmatrix} N^{real} \\ N^{fake} \end{pmatrix}. \tag{6.10}$$

If y is an observable, *e.g.*, m_T, that is statistically independent of x, that is,

$$\begin{aligned} \epsilon_{real}(x,y) &= \epsilon_{real}(x)\epsilon_{real}(y) \\ \epsilon_{fake}(x,y) &= \epsilon_{fake}(x)\epsilon_{fake}(y), \end{aligned} \tag{6.11}$$

then the real and fake distributions of y, $N_{\text{real}}\epsilon_{real}(y)$ and $N_{\text{fake}}\epsilon_{fake}(y)$, are extracted from data without any further assumption as

$$\begin{pmatrix} N(x_1,y) \\ N(x_2),y \\ ... \\ N(x_n,y) \end{pmatrix} = \begin{pmatrix} \epsilon_{real}(x_1) & \epsilon_{fake}(x_1) \\ \epsilon_{real}(x_2) & \epsilon_{fake}(x_2) \\ ... & ... \\ \epsilon_{real}(x_n) & \epsilon_{fake}(x_n) \end{pmatrix} \begin{pmatrix} N_{\text{real}}\epsilon_{real}(y) \\ N_{\text{fake}}\epsilon_{fake}(y) \end{pmatrix}. \tag{6.12}$$

The generalization of the above equations to several real and fake sources as well as many x and y variables is straightforward. In the following, the real component always consists of the sum of all processes containing two prompt and isolated leptons. Depending on the studied di-lepton channel, the fake components are different processes each containing one prompt isolated lepton from the W boson decay, and one non-isolated lepton of background origin. Thus the x variables are always lepton identification variables. The observables y will always be event kinematic quantities such as

- m_T: the event transverse mass,
- m_{ll}: the di-lepton invariant mass,
- $\Delta\phi_{ll}$: the opening angle between the two leptons in the plane perpendicular to the proton beam axis, and,
- p_T^{ll}: the transverse momentum of the di-lepton system.

Thus the independence between the x and y variables that is necessary to simplify the matrix equation always holds to a very good approximation.

Since there are more than one decay channel in the HWW analysis, the equations of

the matrix method are also categorized into different channels, the $H \to WW^* \to \mu\nu\mu\nu$ ($\mu\mu$), $H \to WW^* \to e\nu\mu\nu$ ($e\mu$), $H \to WW^* \to \mu\nu e\nu$ (μe) and $H \to WW^* \to e\nu e\nu$ (ee) channels.

6.1.3 Matrix equations for the $\mu\mu$ channel

The real and fake components of this channel are the followings:

- $\mu\mu$: the signal process, the sum of all the sources containing two prompt isolated muons such as Higgs boson decays, WW, WZ, di-leptonic $t\bar{t}$ (the semi-leptonic component is a part of data-driven estimated W + jets background), etc,
- μh: one prompt isolated muon, one non-isolated muon produced in an in-flight decay of a charged pion or kaon (the so-called light-flavor W + jets background),
- μQ: one prompt isolated muon, one non-isolated muon produced in semi-leptonic decay of B or C hadrons (the so-called heavy-flavor W + jets background).

The W + jets background is defined in this channel as the sum of the μh and μQ processes. The discriminating muon identification variables x are

- $p_{T,cone}^{rel}$: muon isolation, defined as the scalar sum of all the track momenta in a cone of size $\Delta R = 0.3$ in the $\eta - \phi$ plane surrounding the muon track (excluding this track itself), divided by the muon track momentum,
- Δp_T: muon momentum imbalance, defined as the relative difference between the muon spectrometer and inner detector momenta, normalized by the inner detector momentum (see Figure 6.2a),
- $|d_0| / \sigma(d_0)$: muon impact parameter significance relative to the interaction vertex in the transverse plane (see Figure 6.2b).

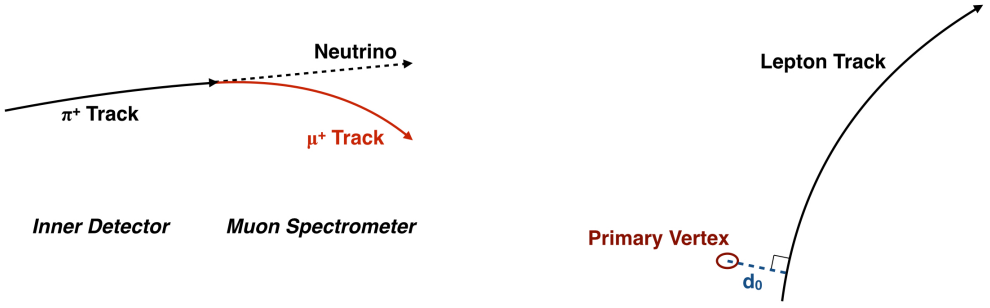

(a) *Momentum imbalance* ***(b)*** *Impact parameter*

Figure 6.2 *Sketches of (a) muon momentum imbalance from pion decay in flight, (b) muon impact parameter.*

The equation to extract the total numbers of signal and background events is

$$\begin{pmatrix} N(\text{STD}) \\ N(p_{T,cone}^{rel}) \\ N(|d_0|/\sigma(d_0)) \\ N(\Delta p_T) \end{pmatrix} = \begin{pmatrix} \varepsilon^{\mu\mu}(\text{STD}) & \varepsilon^{\mu h}(\text{STD}) & \varepsilon^{\mu Q}(\text{STD}) \\ \varepsilon^{\mu\mu}(p_{T,cone}^{rel}) & \varepsilon^{\mu h}(p_{T,cone}^{rel}) & \varepsilon^{\mu Q}(p_{T,cone}^{rel}) \\ \varepsilon^{\mu\mu}(|d_0|/\sigma(d_0)) & \varepsilon^{\mu h}(|d_0|/\sigma(d_0)) & \varepsilon^{\mu Q}(|d_0|/\sigma(d_0)) \\ \varepsilon^{\mu\mu}(\Delta p_T) & \varepsilon^{\mu h}(\Delta p_T) & \varepsilon^{\mu Q}(\Delta p_T) \end{pmatrix} \begin{pmatrix} N^{\mu\mu} \\ N^{\mu h} \\ N^{\mu Q}, \end{pmatrix} \quad (6.13)$$

where $N(p_{T,cone}^{rel})$, $N(|d_0|/\sigma(d_0))$ and $N(\Delta p_T)$ are the numbers of observed events obtained after applying the isolation, impact parameter and momentum imbalance cuts, and $N(\text{STD})$ is the one obtained before any of these cuts. Similarly, the equation to extract the kinematic variables is

$$\begin{pmatrix} N(\text{STD}, y) \\ N(p_{T,cone}^{rel}, y) \\ N(|d_0|/\sigma(d_0), y) \\ N(\Delta p_T, y) \end{pmatrix} = \begin{pmatrix} \varepsilon^{\mu\mu}(\text{STD}) & \varepsilon^{\mu h}(\text{STD}) & \varepsilon^{\mu Q}(\text{STD}) \\ \varepsilon^{\mu\mu}(p_{T,cone}^{rel}) & \varepsilon^{\mu h}(p_{T,cone}^{rel}) & \varepsilon^{\mu Q}(p_{T,cone}^{rel}) \\ \varepsilon^{\mu\mu}(|d_0|/\sigma(d_0)) & \varepsilon^{\mu h}(|d_0|/\sigma(d_0)) & \varepsilon^{\mu Q}(|d_0|/\sigma(d_0)) \\ \varepsilon^{\mu\mu}(\Delta p_T) & \varepsilon^{\mu h}(\Delta p_T) & \varepsilon^{\mu Q}(\Delta p_T) \end{pmatrix} \begin{pmatrix} N^{\mu\mu}\varepsilon^{\mu\mu}(y) \\ N^{\mu h}\varepsilon^{\mu h}(y) \\ N^{\mu Q}\varepsilon^{\mu Q}(y) \end{pmatrix} \tag{6.14}$$

6.1.4 Matrix equations for the $e\mu$ and μe channels

The real and fake components of these two channel are

- $e\mu$: the signal process, the sum of all the sources containing one prompt isolated electron and one prompt isolated muon such as Higgs boson decays, WW, WZ, $t\bar{t}$, etc,
- $h\mu$: one non-isolated electron produced by light flavor hadrons, one prompt isolated muon,
- $\pi^0 Q\mu$: one non-isolated electron produced by heavy flavor hadrons or photon conversion from π^0 decays, one prompt isolated muon,
- eh: one prompt isolated electron, one non-isolated muon produced in a in-flight decay of a charged pion or kaon,
- eQ: one prompt isolated electron, one non-isolated muon produced in semi-leptonic decays of B or C hadrons.

The W +jets background in these analysis channels is the sum of the $h\mu$, $\pi^0 Q\mu$, eh and eQ processes. However, the statistics of fake muon components is quite low, therefore the eQ component will be merged with the eh component in the μe channel; and the two components eh and eQ will be merged with the $\pi^0 Q\mu$ in the $e\mu$ channel. The discriminating variables x used in these two channels are the three variables used in the $\mu\mu$ channel and in addition two more variables

- TRT: fraction of high threshold hits of the electron candidate in the transition radiation tracker (TRT) to a given number of track hits in the TRT,
- BL: number of track hits in the innermost layer of the ATLAS tracking detectors (b-layer).

6.1.5 Matrix equations for the ee channel

The real and fake components of this channel are

- ee: the signal process, the sum of all the sources containing two prompt isolated

electron,

- eh: one prompt isolated electron, one non-isolated electron produced due to light-flavor hadrons faking an electron signature,
- $e\pi^0 Q$: one prompt isolated electron, one non-isolated electron produced by heavy flavor hadrons or photon conversion from π^0 decays.

The W + jets background in this analysis channel is the sum of the eh and the $e\pi^0 Q$ processes. The discriminating variables x are the three variables $p_{T,cone}^{rel}$, TRT and BL as described in the previous section.

6.2 Application of the matrix method

6.2.1 Datasets and event selection

In this study, a dataset corresponding to an integrated luminosity of 20.7 fb^{-1} was analyzed. The results of the extraction of the W + jets background using the matrix method are presented in all four channels: ee, $\mu\mu$, $e\mu$ and μe. There are five major sources of backgrounds (QCD, W +jets, Drell-Yan, top quark and dibosons), which are included in this study. The background processes are modelled using the generators as in Table 5.4.

6.2.2 Monte Carlo closure test

To validate the matrix technique, a Monte Carlo closure test is performed. This test validates that the matrix method is performing correctly. In order to do this test, the matrix elements are built at the same selection stage that one wants to extract the W + jets component. The comparisons are shown for the $\mu\mu$ channel in Table 6.1, for the $e\mu$ channel in Table 6.2, for the μe channel in Table 6.3, and for the ee channel in Table 6.4.

Shape comparisons between Monte Carlo truth information (MC truth) and extracted results using the matrix technique after the pre-selection have been performed. These comparisons are shown for the $\mu\mu$ channel in Figure 6.3, for the $e\mu$ channel in Figure 6.4, for the μe channel in Figure 6.5, and for the ee channel in Figure 6.6. Further comparisons are shown in Appendix A. One can see from these comparisons that the extracted results agree quite well with the MC truth. This validation confirms that the matrix technique works well.

Table 6.1: Comparison between MC truth and extracted results after the pre-selection (top left), $N_{jet} = 0$ (top right), $N_{jet} = 1$ (bottom left) and $N_{jet} \geq 2$ (bottom right) categories in the $\mu\mu$ channel.

Pre-selection		
Source	MC truth	Extracted results
μh	14.83 ± 7.35	14.83 ± 26.78
μQ	121.91 ± 38.41	121.91 ± 51.27
W + jets	136.73 ± 39.11	136.74 ± 57.84
$\mu\mu$	$25\,033.56 \pm 179.17$	$25\,033.46 \pm 111.78$

$N_{jet} = 0$		
Source	MC truth	Extracted results
μh	14.04 ± 7.27	13.98 ± 31.03
μQ	50.36 ± 35.07	50.45 ± 36.13
W + jets	64.40 ± 35.82	64.43 ± 47.62
$\mu\mu$	$11\,117.84 \pm 145.43$	$11\,117.37 \pm 77.57$

$N_{jet} = 1$		
Source	MC truth	Extracted results
μh	0.20 ± 0.20	2.10 ± 0.37
μQ	42.82 ± 14.59	41.60 ± 9.50
W + jets	43.01 ± 14.59	43.69 ± 9.50
$\mu\mu$	5308.99 ± 78.80	5337.29 ± 51.06

$N_{jet} \geq 2$		
Source	MC truth	Extracted results
μh	3.66 ± 1.46	3.71 ± 60.16
μQ	87.52 ± 20.34	87.55 ± 44.13
W + jets	91.18 ± 20.39	91.26 ± 74.61
$\mu\mu$	$18\,940.72 \pm 116.72$	$18\,940.45 \pm 127.19$

Table 6.2: Comparison between MC truth and extracted results after the pre-selection (top left), $N_{jet} = 0$ (top right), $N_{jet} = 1$ (bottom left) and $N_{jet} \geq 2$ (bottom right) categories in the $e\mu$ channel.

Pre-selection		
Source	MC truth	Extracted results
$h\mu$	348.81 ± 62.80	349.77 ± 28.10
$\pi^0 Q\mu$	470.68 ± 71.42	476.66 ± 93.87
eh	443.63 ± 80.61	443.46 ± 27.41
W + jets	1263.12 ± 124.67	1269.89 ± 101.75
$e\mu$	$23\,711.19 \pm 97.37$	$23\,727.74 \pm 176.61$

$N_{jet} = 0$		
Source	MC truth	Extracted results
$h\mu$	190.92 ± 57.12	191.76 ± 30.77
$\pi^0 Q\mu$	236.96 ± 65.68	241.40 ± 68.59
eh	320.57 ± 78.23	320.50 ± 23.46
W + jets	748.45 ± 117.03	753.65 ± 78.76
$e\mu$	4448.19 ± 32.71	4464.16 ± 83.97

$N_{jet} = 1$		
Source	MC truth	Extracted results
$h\mu$	104.45 ± 23.12	104.63 ± 10.17
$\pi^0 Q\mu$	83.75 ± 16.88	83.79 ± 21.84
eh	60.26 ± 15.11	60.26 ± 7.47
W + jets	248.46 ± 32.37	248.68 ± 25.22
$e\mu$	5094.45 ± 43.78	5093.86 ± 70.86

$N_{jet} \geq 2$		
Source	MC truth	Extracted results
$h\mu$	120.26 ± 18.71	120.10 ± 22.06
$\pi^0 Q\mu$	224.28 ± 24.33	230.47 ± 187.64
eh	113.02 ± 18.16	112.75 ± 17.12
W + jets	457.57 ± 35.67	463.32 ± 189.71
$e\mu$	$24\,814.37 \pm 106.25$	$24\,808.47 \pm 314.41$

Table 6.3: Comparison between MC truth and extracted results after the pre-selection (top left), $N_{jet} = 0$ (top right), $N_{jet} = 1$ (bottom left) and $N_{jet} \geq 2$ (bottom right) categories in the μe channel.

Pre-selection		
Source	MC truth	Extracted results
$h\mu$	442.46 ± 76.52	442.46 ± 3.86
$\pi^0 Q\mu$	533.24 ± 69.85	533.08 ± 22.41
$W+$jets	975.70 ± 103.61	975.54 ± 22.74
$e\mu$	$20\,661.65 \pm 93.85$	$20\,662.64 \pm 136.52$

$N_{jet} = 0$		
Source	MC truth	Extracted results
$h\mu$	283.73 ± 71.88	283.74 ± 4.57
$\pi^0 Q\mu$	210.83 ± 52.38	210.77 ± 10.24
$W+$jets	494.56 ± 88.94	494.51 ± 11.21
$e\mu$	4251.59 ± 41.12	4251.80 ± 63.51

$N_{jet} = 1$		
Source	MC truth	Extracted results
$h\mu$	105.28 ± 21.40	105.28 ± 1.58
$\pi^0 Q\mu$	160.93 ± 43.31	160.90 ± 12.35
$W+$jets	266.21 ± 48.30	266.19 ± 12.45
$e\mu$	4270.73 ± 40.44	4270.82 ± 65.01

$N_{jet} \geq 2$		
Source	MC truth	Extracted results
$h\mu$	102.14 ± 19.30	102.14 ± 1.15
$\pi^0 Q\mu$	274.44 ± 20.92	274.40 ± 21.53
$W+$jets	376.57 ± 28.46	376.54 ± 21.56
$e\mu$	$21\,256.61 \pm 98.70$	$21\,256.43 \pm 130.85$

Table 6.4: Comparison between MC truth and extracted results after the pre-selection (top left), $N_{jet} = 0$ (top right), $N_{jet} = 1$ (bottom left) and $N_{jet} \geq 2$ (bottom right) categories in the ee channel.

Pre-selection		
Source	MC truth	Extracted results
eh	235.50 ± 42.64	239.46 ± 2.42
$e\pi^0 Q$	279.87 ± 41.97	289.51 ± 9.42
$W+$jets	515.37 ± 59.83	528.98 ± 9.72
ee	$15\,110.28 \pm 140.83$	$15\,071.59 \pm 88.45$

$N_{jet} = 0$		
Source	MC truth	Extracted results
eh	108.10 ± 35.64	110.51 ± 1.84
$e\pi^0 Q$	90.68 ± 34.96	93.85 ± 4.25
$W+$jets	198.79 ± 49.92	204.35 ± 4.63
ee	6348.12 ± 114.40	6320.94 ± 57.02

$N_{jet} = 1$		
Source	MC truth	Extracted results
eh	62.95 ± 17.08	64.03 ± 1.10
$e\pi^0 Q$	72.16 ± 17.65	75.44 ± 4.79
$W+$jets	135.11 ± 24.56	139.48 ± 4.92
ee	3211.59 ± 61.48	3202.06 ± 42.01

$N_{jet} \geq 2$		
Source	MC truth	Extracted results
eh	135.65 ± 24.48	137.05 ± 1.63
$e\pi^0 Q$	243.74 ± 21.27	246.07 ± 11.71
$W+$jets	379.40 ± 32.43	383.12 ± 11.82
ee	$12\,620.69 \pm 94.08$	$12\,627.56 \pm 79.02$

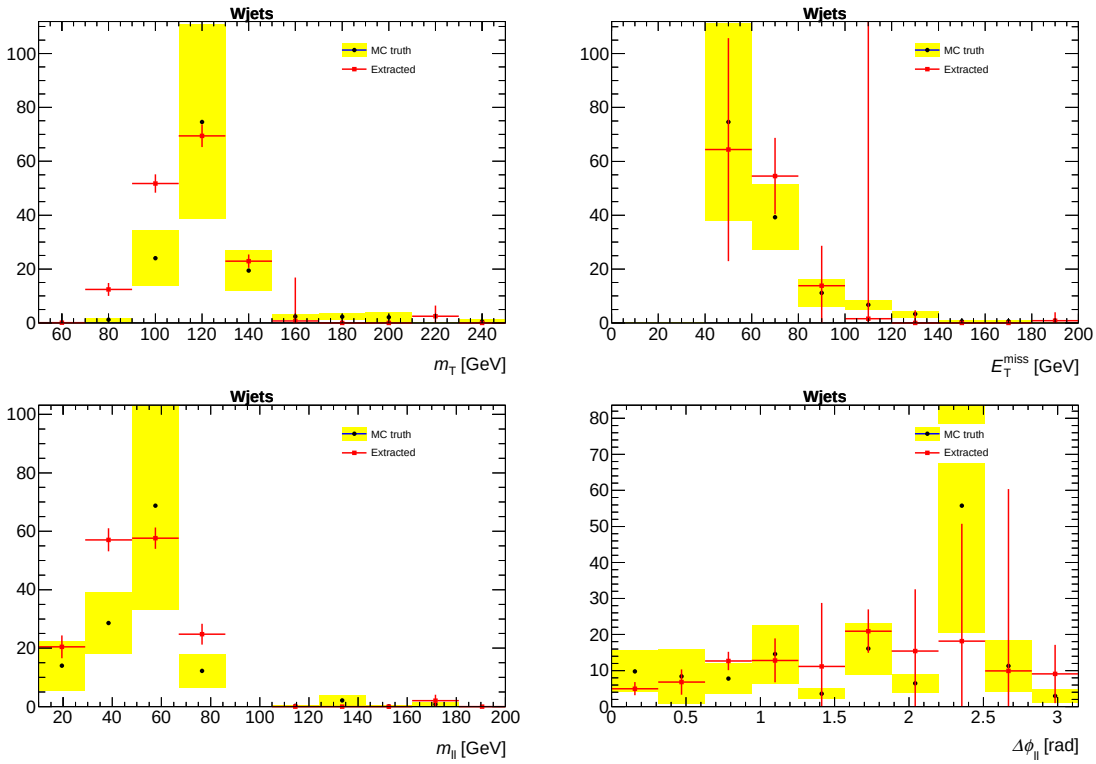

Figure 6.3 *Comparison between MC truth and extracted results for the distributions m_T (top left), E_T^{miss} (top right), m_{ll} (bottom left), and $\Delta\phi_{ll}$ (bottom right) after the pre-selection in the $H \to WW^* \to \mu\nu\mu\nu$ channel.*

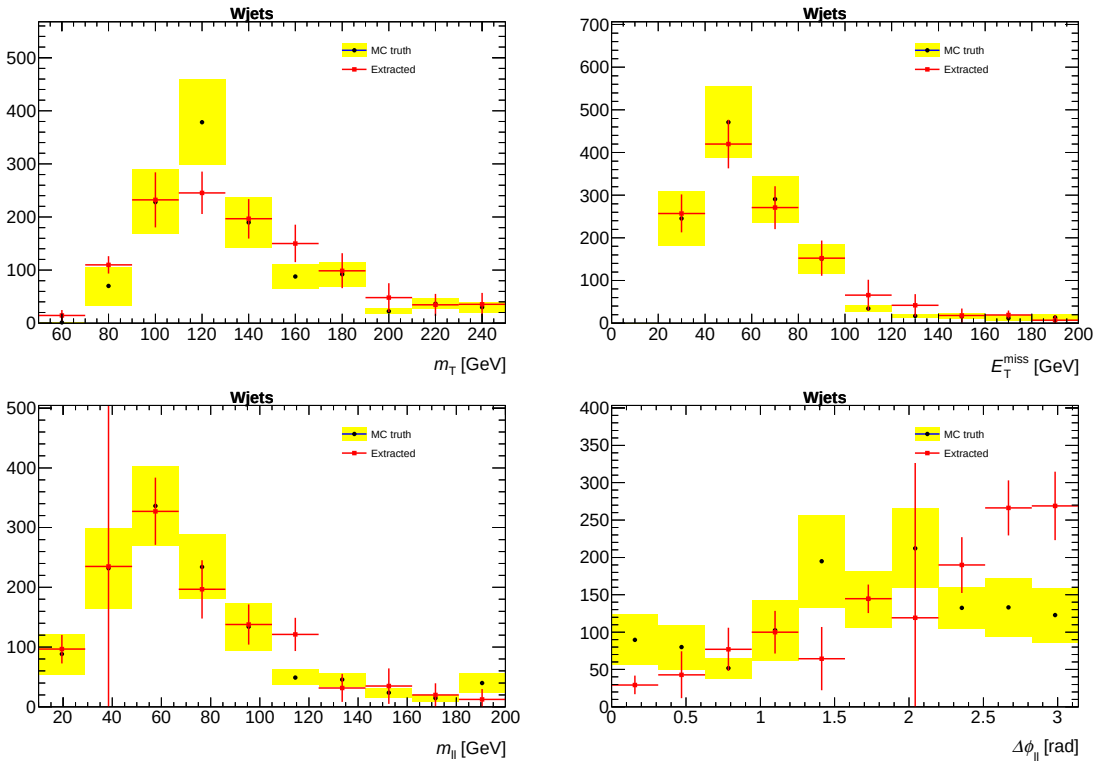

Figure 6.4 *Comparison between MC truth and extracted results for the distributions m_T (top left), E_T^{miss} (top right), m_{ll} (bottom left), and $\Delta\phi_{ll}$ (bottom right) after the pre-selection in the $H \to WW^* \to e\nu\mu\nu$ channel.*

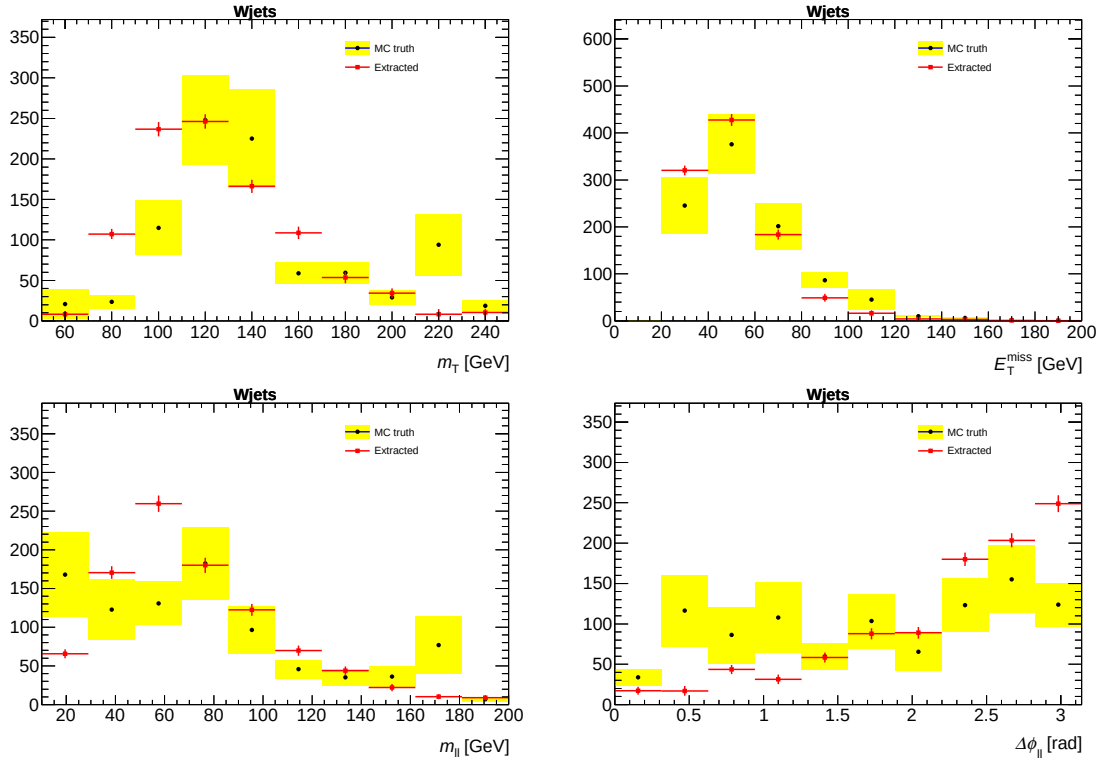

Figure 6.5 *Comparison between MC truth and extracted results for the distributions m_T (top left), E_T^{miss} (top right), m_{ll} (bottom left), and $\Delta\phi_{ll}$ (bottom right) after the pre-selection in the $H \to WW^* \to \mu\nu e\nu$ channel.*

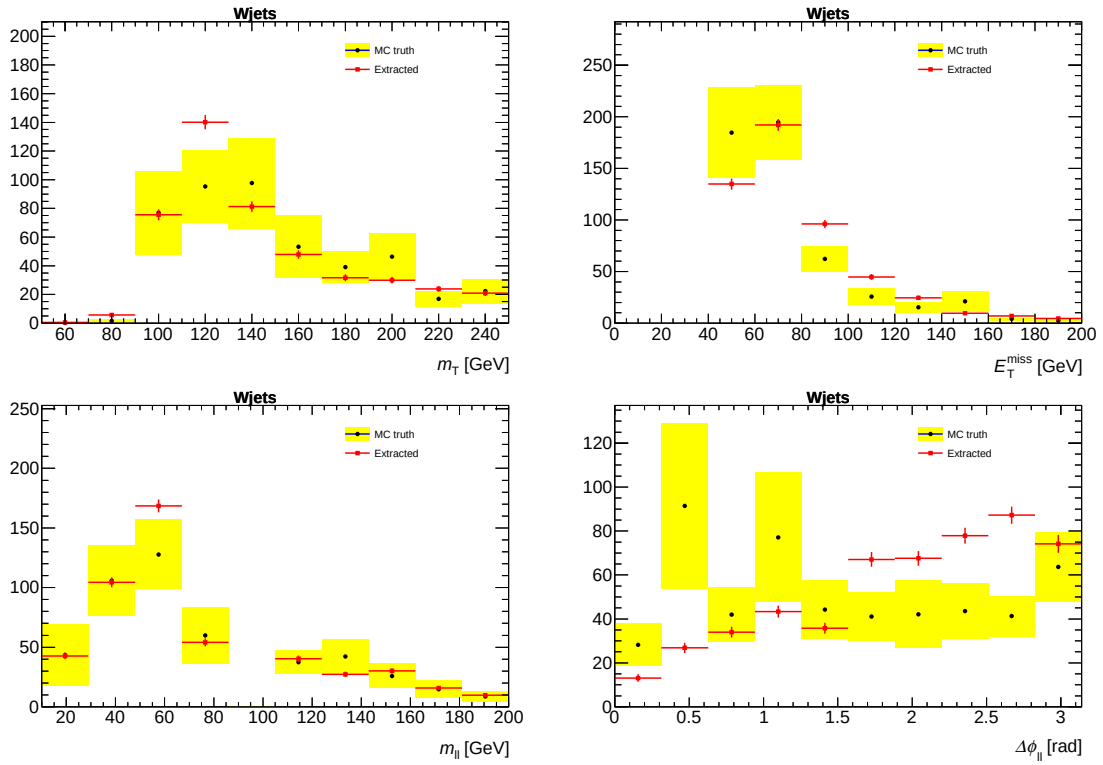

Figure 6.6 *Comparison between MC truth and extracted results for the distributions m_T (top left), E_T^{miss} (top right), m_{ll} (bottom left), and $\Delta\phi_{ll}$ (bottom right) after the pre-selection in the $H \to WW^* \to e\nu e\nu$ channel.*

6.3 Systematic uncertainties

The evaluation of the systematic uncertainties of the matrix method are described in this section. The main systematic uncertainty arises from the imperfect Monte Carlo description of the used lepton identification variables with respect to data. These uncertainties are evaluated for each considered analysis channel in the following by scaling the relevant Monte Carlo lepton identification variable distributions to data at the pre-selection stage in the same-sign region. The matrix elements were then build from the scaled Monte Carlo. The differences of extracted results built from unscaled and scaled Monte Carlo where then determined and used as a systematic uncertainty.

To scale the Monte Carlo lepton identification distributions to data, all these variables were divided into two bins corresponding to the discriminating cut for that variable. The diboson (WZ/ZZ/Wγ) contributions were subtracted from both Monte Carlo and data. The remainder of the Monte Carlo was scaled bin-by-bin to data to match the data perfectly for all considered lepton identification distributions.

6.3.1 $\mu\mu$ channel

There are three lepton identification variables used in this analysis channel: the lepton isolation ($p_{T,cone}^{rel}$), the momentum imbalance (Δp_T) and the impact parameter significance ($|d_0| / \sigma(d_0)$). Table 6.5 shows the comparison of the extracted results with matrix elements built from unscaled and scaled Monte Carlo. The inputs used in this comparison are from both Monte Carlo and data. The resulting uncertainty in the W + jets estimation is determined to be 30% in this analysis channel.

Table 6.5: Systematic uncertainties due to a imperfect MC description of the lepton identification variables in the $\mu\mu$ channel. Shown are extracted numbers for MC and data at four different stages of the event selection for matrices build with unscaled and scaled MC and their relative difference.

Input	Category	No scaling	With scaling	Difference
MC	Pre-selection	136.74 ± 57.84	121.85 ± 38.47	10.9%
	$N_{jet} = 0$	64.43 ± 47.62	62.43 ± 21.89	3.1%
	$N_{jet} = 1$	43.69 ± 9.50	41.66 ± 6.24	4.6%
	$N_{jet} \geq 2$	91.26 ± 74.61	96.77 ± 85.83	6.0%
Data	Pre-selection	238.67 ± 7.31	310.25 ± 12.67	30.0%
	$N_{jet} = 0$	90.57 ± 4.23	117.95 ± 23.24	30.2%
	$N_{jet} = 1$	79.13 ± 7.49	82.57 ± 27.47	4.3%
	$N_{jet} \geq 2$	172.84 ± 8.37	218.61 ± 10.85	26.5%

6.3.2 $e\mu$ channel

The five lepton identification variables used in this analysis are the lepton isolation ($p_{T,cone}^{rel}$), the transition radiation fraction (TRT), the number of B-layer hits (BL), the momentum imbalance (Δp_T), and the impact parameter significance ($|d_0|/\sigma(d_0)$). Table 6.6 shows the comparison of the extracted results with matrix elements built from unscaled and scaled Monte Carlo. The resulting uncertainty in the W + jets estimation is determined to be 30% in this analysis channel.

Table 6.6: Systematic uncertainties due to a imperfect MC description of the lepton identification variables in the $e\mu$ channel. Shown are extracted numbers for MC and data at four different stages of the event selection for matrices build with unscaled and scaled MC and their relative difference.

Input	Category	No scaling	With scaling	Difference
MC	Pre-selection	1269.89 ± 101.75	945.55 ± 80.87	25.5%
	$N_{jet} = 0$	753.65 ± 78.76	513.41 ± 56.88	31.9%
	$N_{jet} = 1$	248.68 ± 25.22	194.91 ± 20.59	21.6%
	$N_{jet} \geq 2$	463.32 ± 189.71	431.37 ± 95.20	6.9%
Data	Pre-selection	1025.46 ± 43.62	703.30 ± 33.19	31.4%
	$N_{jet} = 0$	692.70 ± 91.53	468.89 ± 197.46	32.3%
	$N_{jet} = 1$	191.20 ± 32.47	133.82 ± 35.03	30.0%
	$N_{jet} \geq 2$	418.80 ± 30.92	288.62 ± 50.08	31.1%

6.3.3 μe channel

The uncertainty in μe channel is estimated in the same way as in $e\mu$ channel. Table 6.7 shows the comparison the resulting uncertainty on the W + jets estimation is about 15%.

6.3.4 ee channel

This analysis channel uses the lepton isolation ($p_{T,cone}^{rel}$), the transition radiation fraction (TRT), and the number of hits in the B-layer (BL) as discriminating variables. The systematic uncertainty in this channel is estimated to be 15% as can be deduced from the results shown in Table 6.8.

6.3.5 Total systematic uncertainty

The total resulting systematic uncertainty is summarized in Table 6.9 for all analyzed channels.

Table 6.7: Systematic uncertainties due to a imperfect MC description of the lepton identification variables in the μe channel. Shown are extracted numbers for MC and data at four different stages of the event selection for matrices build with unscaled and scaled MC and their relative difference.

Input	Category	No scaling	With scaling	Difference
MC	Pre-selection	975.54 ± 22.74	883.95 ± 20.84	9.4%
	$N_{jet} = 0$	494.51 ± 11.21	430.04 ± 10.04	13.0%
	$N_{jet} = 1$	266.19 ± 12.45	249.46 ± 11.24	6.3%
	$N_{jet} \geq 2$	376.54 ± 21.56	354.49 ± 20.76	5.9%
Data	Pre-selection	903.30 ± 22.42	823.93 ± 20.54	8.9%
	$N_{jet} = 0$	451.82 ± 10.67	397.04 ± 9.57	12.1%
	$N_{jet} = 1$	243.67 ± 12.09	228.17 ± 10.90	6.4%
	$N_{jet} \geq 2$	394.63 ± 22.20	372.13 ± 21.39	5.7%

Table 6.8: Systematic uncertainties due to a imperfect MC description of the lepton identification variables in the ee channel. Shown are extracted numbers for MC and data at four different stages of the event selection for matrices build with unscaled and scaled MC and their relative difference.

Input	Category	No scaling	With scaling	Difference
MC	Pre-selection	528.98 ± 9.72	450.67 ± 8.22	14.8%
	$N_{jet} = 0$	204.35 ± 4.63	171.10 ± 3.93	16.3%
	$N_{jet} = 1$	139.48 ± 4.92	121.85 ± 4.20	12.6%
	$N_{jet} \geq 2$	383.12 ± 11.82	332.63 ± 9.88	13.2%
Data	Pre-selection	465.12 ± 9.18	396.41 ± 7.75	14.8%
	$N_{jet} = 0$	175.10 ± 4.32	146.69 ± 3.66	16.2%
	$N_{jet} = 1$	114.83 ± 4.49	100.28 ± 3.83	12.7%
	$N_{jet} \geq 2$	440.60 ± 12.50	381.79 ± 10.45	13.3%

Table 6.9: Total resulting systematic uncertainties in all channels.

Channel	Systematic uncertainty
$\mu\mu$	30%
$e\mu$	30%
μe	15%
ee	15%

6.4 Data extraction results and comparison with the alternative fake factor method

The full ATLAS 2012 $\sqrt{s} = 8$ TeV dataset of $20.7\,\text{fb}^{-1}$ is used to extract the W + jets component for each analysis channel. In the following, the results for each of the four

analysis channels are presented with applying the matrix technique to data, together with the number of Monte Carlo W + jets events at same cut stage and the thus-far used fake factor method. The extracted numbers of W + jets background events are shown for each analysis channel at the pre-selection and the three disjoint analysis $N_{jet} = 0$, $N_{jet} = 1$ and $N_{jet} \geq 2$ categories, as well as for the final signal regions in each channel and category. Note that the numbers of W +jets events in the final signal regions are extracted using the matrices that were build in the same analysis channel at the looser selection of the $N_{jet} = 0$, $N_{jet} = 1$ and $N_{jet} \geq 2$ categories.

6.4.1 $\mu\mu$ channel

There is good agreement between the two methods in the $\mu\mu$ channel, however there is still a large difference in the $N_{jet} = 1$ category, as can be seen in Table 6.10. The reasons for this difference have been traced back to the fact that the matrix method uses the categorization into the different number of jet selections at the stage where the matrices are build while these different categories are not considered in the fake factor method. This different category has different topologies and more importantly different compositions of sources for fake lepton candidates.

Table 6.10: Comparison of W + jets estimation results from different methods in the $\mu\mu$ channel. Shown are the matrix method applied to data (second column), Monte Carlo W + jets (third column), and the fake factor method applied to data (fourth column). All are shown for different stages of the selection (first column). The uncertainties given in the table is statistical uncertainties.

Selection stage	Matrix method	Monte Carlo	Fake factor method
Pre-selection	238.67 ± 7.31	136.73 ± 39.11	184.97 ± 15.02
$N_{jet} = 0$	90.57 ± 4.23	64.40 ± 35.82	99.71 ± 11.71
$N_{jet} = 1$	79.13 ± 7.49	43.01 ± 14.59	38.78 ± 8.23
$N_{jet} \geq 2$	172.84 ± 8.37	91.18 ± 20.39	134.05 ± 7.43
$N_{jet} = 0$ signal region	8.40 ± 3.66	4.10 ± 4.10	9.13 ± 0.97
$N_{jet} = 1$ signal region	4.83 ± 1.25	0.35 ± 0.35	2.38 ± 0.70
$N_{jet} \geq 2$ signal region	0.27 ± 2.19	0.00 ± 0.00	0.36 ± 0.28

6.4.2 $e\mu$ channel

Table 6.11 shows the results for the $e\mu$ channel. There are large differences between results from the matrix method and from the fake factor method in the $N_{jet} = 0$ and $N_{jet} \geq 2$ categories. However, the two methods agree with each other in the $N_{jet} = 1$ category.

Table 6.11: Comparison of W+jets estimation results from different methods in the $e\mu$ channel. Shown are the matrix method applied to data (second column), Monte Carlo W + jets (third column), and the fake factor method applied to data (fourth column). All are shown for different stages of the selection (first column). The uncertainties given in the table is statistical uncertainties.

Selection stage	Matrix method	Monte Carlo	Fake factor method
Pre-selection	1025.46 ± 43.62	1263.12 ± 124.67	534.29 ± 8.46
$N_{jet} = 0$	692.70 ± 91.53	748.45 ± 117.03	297.03 ± 5.13
$N_{jet} = 1$	191.20 ± 32.47	248.46 ± 32.37	141.09 ± 4.11
$N_{jet} \geq 2$	418.80 ± 30.92	457.57 ± 35.67	274.24 ± 8.10
$N_{jet} = 0$ signal region	101.91 ± 15.46	203.76 ± 66.58	35.62 ± 1.87
$N_{jet} = 1$ signal region	25.82 ± 5.43	30.99 ± 12.08	22.41 ± 1.60
$N_{jet} \geq 2$ signal region	1.52 ± 1.51	0.31 ± 0.31	0.54 ± 0.42

6.4.3 μe channel

Table 6.12 shows the results for the μe channel. There is good agreement within the uncertainties between results from the matrix method and from the fake factor method at the early cutstages. However, the two methods disagree with each other in the $N_{jet} = 0$ category at the very end of the cutstage.

Table 6.12: Comparison of W+jets estimation results from different methods in the μe channel. Shown are the matrix method applied to data (second column), Monte Carlo W + jets (third column), and the fake factor method applied to data (fourth column). All are shown for different stages of the selection (first column). The uncertainties given in the table is statistical uncertainties.

Selection stage	Matrix method	Monte Carlo	Fake factor method
Pre-selection	903.30 ± 22.42	975.70 ± 103.61	977.57 ± 8.19
$N_{jet} = 0$	451.82 ± 10.67	494.56 ± 88.94	665.97 ± 6.44
$N_{jet} = 1$	243.67 ± 12.09	266.21 ± 48.30	215.18 ± 3.57
$N_{jet} \geq 2$	394.63 ± 22.20	376.57 ± 28.46	259.38 ± 5.48
$N_{jet} = 0$ signal region	52.46 ± 3.92	148.38 ± 51.92	190.72 ± 2.29
$N_{jet} = 1$ signal region	34.51 ± 3.94	94.09 ± 40.65	49.97 ± 1.41
$N_{jet} \geq 2$ signal region	0.35 ± 0.43	0.00 ± 0.00	1.11 ± 0.26

6.4.4 ee channel

Table 6.13 shows the results for the ee channel. There are huge discrepancies between results from two methods at the early cutstages. However, at the end of cutstages, the numbers agree quite well.

Table 6.13: Comparison of W+jets estimation results from different methods in the ee channel. Shown are the matrix method applied to data (second column), Monte Carlo W + jets (third column), and the fake factor method applied to data (fourth column). All are shown for different stages of the selection (first column). The uncertainties given in the table is statistical uncertainties.

Selection stage	Matrix method	Monte Carlo	Fake factor method
Pre-selection	465.12 ± 9.18	515.37 ± 59.83	211.69 ± 3.10
$N_{jet} = 0$	175.10 ± 4.32	198.79 ± 49.92	134.32 ± 2.27
$N_{jet} = 1$	114.83 ± 4.49	135.11 ± 24.56	48.16 ± 1.45
$N_{jet} \geq 2$	440.60 ± 12.50	379.40 ± 32.43	79.45 ± 2.52
$N_{jet} = 0$ signal region	11.51 ± 1.07	58.52 ± 31.21	16.69 ± 0.75
$N_{jet} = 1$ signal region	2.68 ± 0.72	14.61 ± 8.28	2.90 ± 0.42
$N_{jet} \geq 2$ signal region	0.09 ± 0.64	0.00 ± 0.00	0.09 ± 0.03

7

Search for the $H \to WW^* \to l\nu l\nu$ Decays in the Gluon-Fusion Channel using $\sqrt{s} = 13$ TeV Data from the LHC Run 2

The search for the Higgs boson in the decay $H \to WW^* \to l\nu l\nu$ in the ggF, VBF and VH production modes was performed using 25 fb^{-1} of data collected at $\sqrt{s} = 7$ TeV and 8 TeV during the LHC Run 1. In this chapter, the corresponding analysis is described based on a data sample corresponding to an integrated luminosity of 5.8 fb^{-1} taken by the ATLAS detector in 2015 and 2016 at the centre-of-mass energy $\sqrt{s} = 13$ TeV (Run 2 data taking). The data analysis follows closely that of Run 1. A description of the data and Monte Carlo samples collected by the ATLAS experiment used in the analysis is given in Section 7.1. The object and event selection employed for the analysis is provided in Section 7.2. The event selection and preliminary result of the ggF analysis are presented in Sections 7.3 and 7.5, respectively.

7.1 Data and Monte Carlo Samples

7.1.1 Data Samples

The data used in this analysis correspond to an integrated luminosity of 5.8 fb^{-1}. This represents the proton-proton collision data collected in 2015 and the first six months of 2016 at $\sqrt{s} = 13$ TeV with a bunch spacing of 50 ns and 25 ns, which pass data quality checks. The mean number of interactions per bunch crossing increased during the data taking period. It is shown for 2015 and 2016 data in Figure 7.1.

The high-level triggers (HLTs) used in this analysis are listed in Table 7.1. The

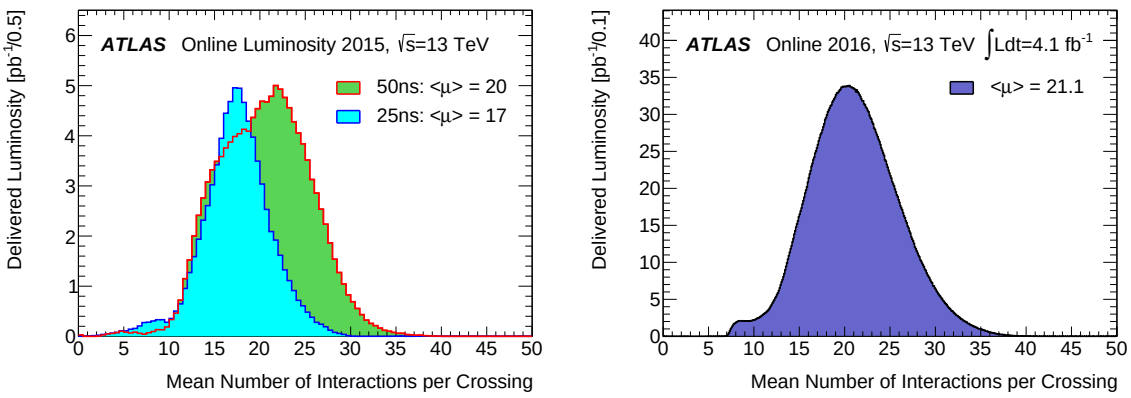

Figure 7.1 *The luminosity-weighted distributions of the mean number of interactions per crossing for the 2015 (left) and 2016 (right) data (taken from Ref. [117]).*

lepton trigger efficiencies are measured using leptonic decays of Z bosons as a function of lepton p_T and η. The single-lepton trigger efficiencies are about 70% for muons with $|\eta| < 1.05$, 90% for muons in the range $1.05 < |\eta| < 2.40$, and $\geq 90\%$ for electrons in the range $|\eta| < 2.40$.

Table 7.1: Summary of the HLT triggers used for the 2015 and 2016 dataset.

Lepton	HLT trigger
	2015
e	HLT_e24_lhmedium_L1EM20VH || HLT_e24_lhmedium_L1EM18VH || HLT_e60_lhmedium || HLT_e120_lhloose
μ	HLT_mu20_iloose_L1MU15 || HLT_mu50
	2016
e	HLT_e24_lhtight_nod0_ivarloose || HLT_e26_lhtight_nod0_ivarloose || HLT_e60_lhmedium_nod0 || HLT_e140_lhloose_nod0
μ	HLT_mu26_ivarmedium || HLT_mu24_ivarmedium || HLT_mu26_imedium || HLT_mu24_imedium

7.1.2 Monte Carlo Samples

The MC generators used to model signal and background processes are listed in Table 7.2. Separate programs are used to generate the hard scattering process and to model the parton showering and hadronisation stages. The CT10 parton distribution function (PDF) set [98] is used for the POWHEG, SHERPA and MADGRAPH samples. The CTEQ6L1 [118] PDF set is used for the PYTHIA8 showering in combination with either the AZNLO [119] or the A14 [120] tune. JIMMY [94] is used for the simulation of the underlying event. The MLM matching scheme is used for the description of the W+jets, Z/γ^*+jets and Wγ processes.

Table 7.2: MC generators used to model the signal and background processes at $\sqrt{s} = 13$ TeV, and corresponding cross sections (given for $m_H = 125$ GeV in the case of the Higgs boson production processes).

Process	Generator	$\sigma \cdot$ Br (pb)
ggF $H \to WW^*$	POWHEG+PYTHIA8	10.4
VBF $H \to WW^*$	POWHEG+PYTHIA8	0.808
WH $H \to WW^*$	POWHEG+PYTHIA8 (MINLO)	0.293
ZH $H \to WW^*$	POWHEG+PYTHIA8 (MINLO)	0.189
Inclusive $W \to l\nu$	POWHEG+PYTHIA8	6.02×10^4
Inclusive $Z/\gamma^\star \to ll$ ($m_{ll} \geq 40$ GeV)	MADGRAPH	6.04×10^3
Inclusive $Z/\gamma^\star \to ll$ ($40 \geq m_{ll} \geq 10$ GeV)	MADGRAPH	8.01×10^3
$(W \to l\nu)\gamma$ ($p_T^\gamma > 10$ GeV)	SHERPA	453
$(Z \to ll)\gamma$ ($p_T^\gamma > 10$ GeV)	SHERPA	175
$t\bar{t}$ leptonic	POWHEG+PYTHIA6	87.6
Wt leptonic	POWHEG+PYTHIA6	7.55
$t\bar{t}W/Z$	MADGRAPH	0.62
tZ non-all-hadronic	MADGRAPH	0.24
$q\bar{q}/g \to WW \to l\nu l\nu$	POWHEG+PYTHIA8	11.2
$Z^{(*)}Z^{(*)} \to 2l2\nu$ ($m_{ll} \geq 4$ GeV)	POWHEG+PYTHIA8	0.925
$q\bar{q}/g \to 2l2\nu$	SHERPA	12.8
$gg \to 2l2\nu$	SHERPA	0.72
$q\bar{q}/g \to l\nu ll$	SHERPA	11.9
$q\bar{q}/g, gg \to llll$	SHERPA	11.5
$WZ \to qqll$	SHERPA	3.76
$ZZ \to qqll$	SHERPA	2.36
Electroweak $WW + 2$ jets ($l\nu l\nu$)	SHERPA	0.012
Electroweak $WZ + 2$ jets ($l\nu ll$)	SHERPA	0.038
Electroweak $ZZ + 2$ jets ($llll$)	SHERPA	0.116
Electroweak $q\bar{q} \to (Z \to \tau\tau)q\bar{q}$	SHERPA	2.54

Signal Samples

In this analysis, only the ggF process is considered to be included in the signal. Contributions from the VBF, VH and $H \to \tau\tau$ are included in the analysis as background. Other small production processes like ttH and bbH are neglected because their contributions are expected to be small.

For the decay of the Higgs boson, only the $H \to WW^* \to l\nu l\nu$ decay channel with two charged leptons ($l = e, \mu$) is considered as signal. The branching fraction for this decay is taken from the HDECAY program. Details of the signal cross-section calculation are discussed in Section 5.2.2.

Background Samples

The main sources of background events result from the production of top-quarks, dibosons, tribosons, Z+jets, W+jets and multi-jets. The $q\bar{q}$-initiated diboson processes

are the main background in this analysis, which are modelled either with POWHEG+ PYTHIA8 or SHERPA. The $q\bar{q}/g \to WW \to l\nu l\nu$ process is modelled by POWHEG+ PYTHIA8 since it provides a better modelling of the observed E_T^{miss} distribution in data. SHERPA is used for the other diboson processes. The loop-induced gg-initiated diboson processes are simulated by SHERPA with zero or one additional jet.

The cross section of the inclusive WW background process is known at NNLO accuracy [121] and includes contributions from $q\bar{q}/g \to WW$ and $gg \to WW$. Since the processes $q\bar{q}/g \to WW$ and $gg \to WW$ are modelled with different generators and a higher order calculation is available for $gg \to WW$, the cross sections of both processes need to be separated.

For the $q\bar{q}/g \to ZZ \to ll\nu\nu$ process, a cut on the invariant mass of the two charged leptons $m_{ll} > 4$ GeV is required. For the $q\bar{q}/g$-initiated diboson processes, there are requirements of $m_{ll} > 2m_l + 250$ MeV for any same-flavour opposite-sign lepton pair and at least two charged leptons must have $p_T > 5$ GeV. For gg-initiated diboson processes, m_{ll} is restricted to be greater than 2 GeV for the $gg \to l\nu l\nu$ and 10 GeV for the $gg \to llll$ final states. SHERPA is also used for the modelling of diboson processes (WW/WZ/ZZ) for the $llll$, $l\nu ll$ and $l\nu l\nu$ with two jets final states as well as the $q\bar{q} \to Zq\bar{q}$ processes with the $Z \to \tau\tau$ decay mode at LO accuracy, and requiring $m_{\tau\tau} > 40$ GeV.

The $t\bar{t}$ and Wt production are generated with POWHEG interfaced to PYTHIA6 for parton showering, using the PERUGIA2012 [122] tune. EvtGen [123] is used for bottom and charm hadron decays. The predicted $t\bar{t}$ production cross section is calculated with the TOP++ program [124] to NNLO in perturbative QCD, including soft-gluon resummation to NNLL order, and assuming a top-quark mass of 172.5 GeV. Both $t\bar{t}$ and Wt samples are required to have at least two charged leptons in the final state. The $t\bar{t}W/Z$ and tZ processes are generated at LO using MADGRAPH5 interfaced with PYTHIA8 ($t\bar{t}W/Z$) and PYTHIA6. The tZ process is required to have three charged leptons in the final state, in which the leptons from the Z boson decay are required to have $m_{ll} > 10$ GeV.

The production of Zγ and Wγ events is modelled using SHERPA at NLO accuracy. For both processes the p_T of the γ is required to be larger than 10 GeV, and the distance in the $\eta - \phi$ plane between γ and leptons $\Delta R > 0.1$. In addition, the leptons from the Z boson decay are required to have $m_{ll} > 2$ GeV. The production of Z bosons in association with jets is modelled by MADGRAPH5 at LO interfaced with PYTHIA8 in the invariant mass range of the two charged leptons $m_{ll} > 10$ GeV. The event overlap between the Zγ and Z+jets samples is removed by rejecting events from the Z+jets sample that contain a photon with $p_T > 10$ GeV and $|\eta| < 2.5$ in the final state.

7.2 Object Selection

This section presents the object selection in the 13 TeV analysis. Object selections in the 7 and 8 TeV analysis are presented in Section 5.3.1.

7.2.1 Event Selection

Events are required to have at least one primary vertex that has more than one associated track with transverse momentum $p_T > 400$ MeV. If there is more than one primary vertex reconstructed in the event, the one with the largest track $\sum p_T^2$ is chosen as the hard-scatter primary vertex and used for calculation of the main physics objects in this analysis.

7.2.2 Lepton Selection

Leptons are required to originate from the primary vertex. The absolute value of the longitudinal impact parameter of the track $|z_0 \sin\theta|$ is required to be less than 0.5 mm, and the significance of the transverse impact parameter $|d_0|/\sigma_{d_0}$ is required to be less than three (five) for muons (electrons).

Electrons are selected from clusters of energy deposits in the calorimeter that match a track reconstructed in the inner detector and identified using a likelihood identification criteria [125]. There are three levels of identification: `LooseLH`, `MediumLH` and `TightLH`, which correspond to approximately 96%, 94% and 88% identification efficiency for an electron with transverse energy of 100 GeV. The electrons used in this analysis are required to have E_T greater than 15 GeV and pass `MediumLH` or `TightLH` selection if their E_T is greater or smaller than 25 GeV. The pseudorapidity of electrons are required to be within the range of $|\eta| < 2.47$, excluding the transition region between the barrel and end-caps ($1.37 < |\eta| < 1.52$).

Muons are reconstructed by combining inner detector and muon spectrometer tracks through an overall fit using the hits of the inner detector track, the energy loss in the calorimeter, and the hits of the track in the muon system. Based on the quality of the reconstruction and identification, muon candidates are defined as `Loose`, `Medium` and `Tight`, with increasing purity. The muon candidates used in this analysis are required to pass the `Tight` selection for 15 GeV $< p_T <$ 25 GeV and to pass the `Medium` selection for $p_T < 25$ GeV within the range $|\eta| < 2.5$.

7.2.3 Optimization of Lepton Isolation

For Run 2 analyse, there are several working points centrally provided for the lepton isolation

- `Loose` isolation is defined such that all leptons independent of their transverse momentum have an isolation efficiency of 99%.
- `Tight` isolation is similar to `Loose` but with an isolation efficiency of 95%.
- `Gradient` isolation is defined as p_T dependent $(0.1143 \times p_T$ [GeV] $+ 92.14)\%$, where the isolation efficiency is larger for leptons with a higher p_T.
- `GradientLoose` isolation is defined as $(0.057 \times p_T$ [GeV] $+ 95.57)\%$. The main difference between this isolation and the `Gradient` one is the efficiency for low p_{T} leptons.
- `LooseTrackOnly` isolation has an efficiency of 99% for all leptons independent of their p_T and applies only a track isolation criteria.

In case of the ggF analysis, the optimal isolation criteria were investigated by looking at the expected event yields of signal, semi-leptonic top-quark and W+jets backgrounds after the event selection for $N_{jet} = 0$ and $N_{jet} = 1$ separately. Many MC samples were still of the MC15a variant at the time of this study, and all numbers were scaled to an integrated luminosity of 4 fb^{-1}. The results are shown in Table 7.3 and are compared to the isolation from Run 1. Since the `Gradient` working point gives the best result for the $N_{jet} = 0$ channel and also good results for the $N_{jet} = 1$ channel, it was chosen as the ggF isolation working point. The selection of leptons for the ggF analysis is also summarized in Table 7.4.

Table 7.3: Comparison of the expected signal yield, the yield of the top-quark background and the W+jets background, and the expected $S/\sqrt{B}$ for the isolation criteria. All numbers were scaled to an integrated luminosity of 4 fb^{-1}.

N_{jet}	0				1			
Isolation	ggF	top	W+jets	$S/\sqrt{B}$	ggF	top	W+jets	$S/\sqrt{B}$
HWWRun1	63.4	70	158	4.23	44.7	264	74	2.62
Tight	66.1	79	243	3.72	46.4	283	92	2.58
Loose	68	86	269	3.66	48.3	301	105	2.58
LooseTrackOnly	69	88	314	3.45	48.8	309	112	2.56
GradientLoose	64.6	75	178	4.20	45.7	275	83	2.60
Gradient	61.5	79	134	4.33	43.4	262	74	2.56

Table 7.4: Lepton selections used in each analysis.

p_T range	Electron ID	Muon ID	Isolation
< 25 GeV	`TightLH`	`Tight`	`Gradient`
> 25 GeV	`MediumLH`	`Medium`	`Gradient`

7.2.4 Jet Selection

Jets are reconstructed from three-dimensional clusters of energy deposits in the calorimeter using the anti-k_t algorithm with distance parameters of $R = 0.4$. The four momenta of the jets are calculated as the sum of the four momenta of their constituents and corrected for losses in passive material, the non-compensating response of the calorimeter, and contributions from pile-up. Jets are required to have $p_T > 25$ GeV for $|\eta| < 2.4$ and $p_T > 30$ GeV for $2.4 < |\eta| < 4.5$.

The *"Jet vertex tagger"* (JVT) [126], which is a multivariable tagger, is used to suppress jets from pile-up events. Jets with $p_T < 50$ GeV and $|\eta| < 2.4$ are required to have $JVT > 0.64$. In addition, jets are discarded if they are within a cone of size $\Delta R < 0.2$ of a lepton candidate or have less than three associated tracks. However, if a jet with three or more associated tracks is within a cone of size $\Delta R < 0.4$ of a muon candidate or within $0.2 < \Delta R < 0.4$ of an electron candidate, the corresponding electron or muon candidate is discarded.

7.2.5 Optimization of b-tagging

The b-jets are identified using the `MV2C10` b-tagging algorithm [127], where the b-tagging efficiency has been determined from $t\bar{t}$ simulated events and the corresponding data. A study to choose the optimal b-tagging working point were done in the $N_{jet} = 1$ category. Thus, many MC samples for this study correspond to the MC15a version of the digitization and reconstruction. All samples have been scaled to a corresponding integrated luminosity of 4 fb^{-1}. The results are shown in Table 7.5 for the b-tagger `MV2c20` in the $N_{jet} = 1$ signal region. It can be seen that $S/\sqrt{B}$ increases with the efficiency of the b-tagging working point since the total background is reduced more than the signal. The best $S/\sqrt{B}$ is achieved with a working point which corresponds to an efficiency of 85% to positively identify a b-jet, while the 90% working point performs worse due to a larger reduction of the signal efficiency.

Table 7.5: Comparison of expected total background sum, the ggF signal yield and the expected $S/\sqrt{B}$ for the different working points of the `MV2c20` tagger. All numbers were scaled to an integrated luminosity of 4 fb^{-1}.

b-tagging working point	Total background	ggF	$S/\sqrt{B}$
no b-jet veto	1067	44.2	1.45
veto with 60% working point	665	43.7	1.81
veto with 70% working point	603	43.4	1.89
veto with 77% working point	557	43.0	1.94
veto with 80% working point	538	42.7	1.96
veto with 85% working point	494	41.6	1.99
veto with 90% working point	444	39.0	1.97

7.2.6 Missing Transverse Momentum

In Run 2, the missing transverse momentum is reconstructed from the transverse momenta of all calibrated selected objects and soft tracks compatible with the primary vertex but not matched to any of the selected objects. This missing transverse momentum is called *track soft term* (TST) missing E_T, denoted as E_T^{miss}. Besides, in the analysis also the "Track missing E_T", $E_T^{miss,TRK}$, is used. The $E_T^{miss,TRK}$ is reconstructed as the negative sum of the momenta of ID tracks ($|\eta| < 2.5$) that satisfy the following selection criteria

- $p_T^{track} > 500$ MeV
- At least 7 hits in the silicon detector and less than two holes in the silicon layers or one hole in the pixel layers
- Requirements on the transverse impact parameter: $d_0 < 1.5$ mm and $d_0/\sigma(d_0) < 3$.

For high p_T, the electron p_T is more precisely measured using the calorimeter than using the track momentum. Therefore, the p_T of an electron track is replaced by the calorimeter cluster measurement. E_T^{miss} gives a very pile-up robust estimation of the missing transverse momentum.

In the ggF analysis, both E_T^{miss} (TST) and $E_T^{miss,TRK}$ are used for m_T calculation and for selection, respectively. The cut on $E_T^{miss,TRK}$ is used to reduce contributions from Drell–Yan background since $E_T^{miss,TRK}$ differentiates better than E_T^{miss} between processes with real missing E_T contributions and processes with fake missing E_T for events with low hadronic activity. In Figure 7.2, E_T^{miss} and $E_T^{miss,TRK}$ are shown in the $N_{jet} = 0$ Top CR before a cut on $E_T^{miss,TRK}$ is applied. It can be observed that the fraction of Drell–Yan to top-quark background is larger for low values of $E_T^{miss,TRK}$ than for low values of E_T^{miss}.

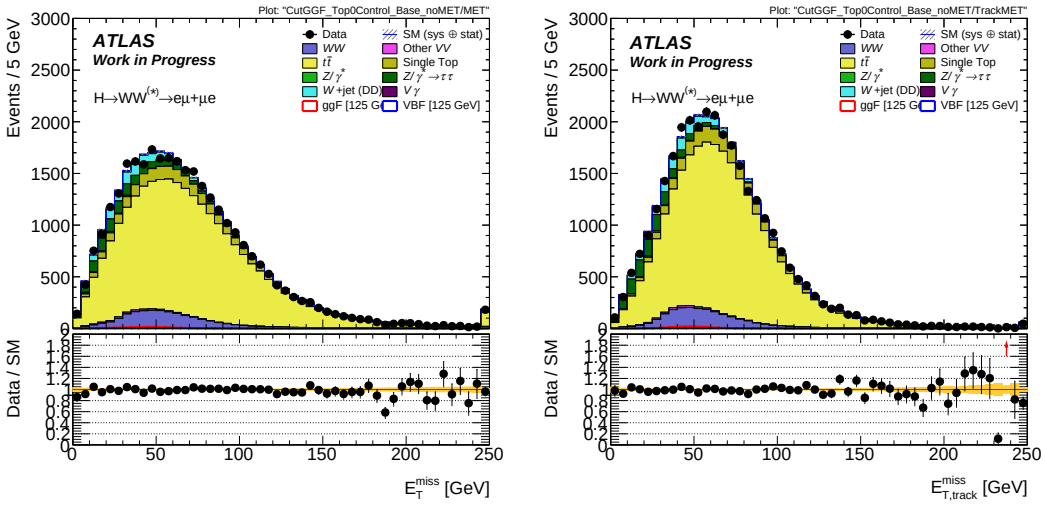

Figure 7.2 *Distributions of E_T^{miss} (left) and $E_T^{miss,TRK}$ (right) in the $N_{jet} = 0$ Top CR without E_T^{miss} cut.*

A study on the resolution of different types of missing E_T reconstruction in the

$N_{jet} = 0$ category was performed at an early stage of Run-2 analysis. There are three types of missing E_T reconstruction in Run 2: calorimeter-based E_T^{miss} using calorimeter-based soft term, calorimeter-based E_T^{miss} using track-based soft term and track-based E_T^{miss} ($E_T^{miss,TRK}$). Figure 7.3 shows a comparison of reconstructed missing E_T resolutions between Run 2 and Run 1. It can be seen that $E_T^{miss,TRK}$ gives the best resolution. Table 7.6 give values of the Run 2 missing E_T resolutions and compares them with the corresponding values in Run 1.

Table 7.6: Comparison of missing E_T resolutions in the $N_{jet} = 0$ category between the Run-2 and Run-1 analyses.

Type	Run 2	Run 1
$E_T^{miss,CST}$ (calo. soft term)	19.2 GeV	–
E_T^{miss} (trk. soft term)	14.6 GeV	15.9 GeV
$E_T^{miss,TRK}$	13.6 GeV	12.4 GeV

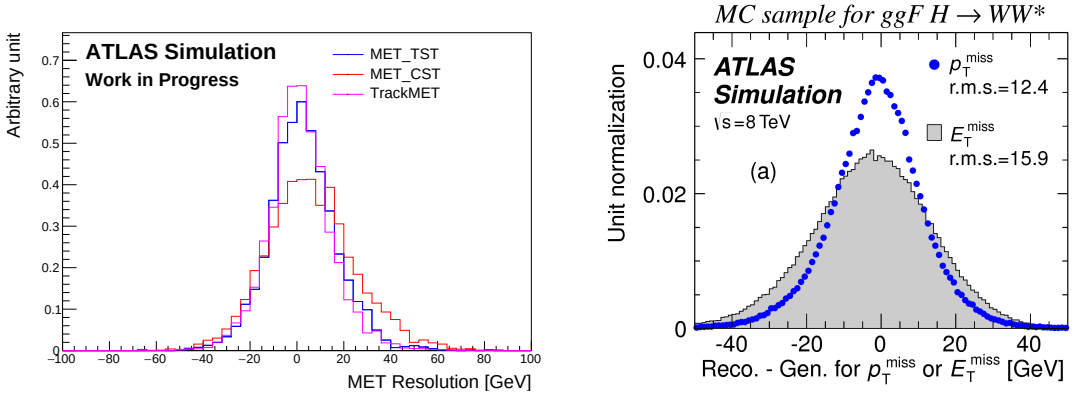

Figure 7.3 *Comparison of the reconstructed missing E_T resolutions in the Run-2 (left) and Run-1 (right) analyses [104]. There is three types of missing E_T: calorimeter-based $E_T^{miss,CST}$ using calorimeter-based soft term (MET_CST), calorimeter-based E_T^{miss} using track-based soft term (MET_TST) and track-based E_T^{miss} (TrackMET).*

7.3 ggF Analysis

7.3.1 Analysis Overview

This analysis focuses on the $N_{jet} \leq 1$ signal regions in the $e\mu$ and μe final states, which provide the highest sensitivity. The $N_{jet} \geq 2$ signal region as well as the same-flavour channels are currently dropped due to limited time. The p_T cut on the subleading lepton is also increased from 10 GeV to 15 GeV, compared to the Run 1 analysis, to suppress background from fake leptons. Numerous background processes contribute to the signal regions, including top ($t\bar{t}$ and Wt), WW, WZ, Wγ^*, ZZ, W+jets, QCD, $Z/\gamma^* \to \tau\tau$, and $Z/\gamma^* \to ee/\mu\mu$. The general analysis strategy is similar to Run 1,

which is discussed in Section 5.3.2, that is to identify signal regions within the dilepton phase space, divide them to further separate signal and background regions, and normalize the expected backgrounds using data as much as possible.

7.3.2 Validation of the Selection Criteria

As mentioned above, the ggF signal region selection is based on the Run 1 analysis. However, since the Run 2 exhibits a higher centre-of-mass energy ($\sqrt{s} = 13$ TeV instead of 8 TeV as in Run 1), the selection criteria may need to change in order to obtain a good signal significance.

The strategy of this study is not to perform a rigorous optimization of all selection criteria, but rather to validate that the selection criteria obtained in the Run 1 analysis are also good selection criteria for the Run 2 analysis. In order to perform this check, the same selection with the identical order of the selection criteria as in Run 1 is used to determine for each variable the optimal cut value. At each selection stage, the selection criteria for the following variable is studied. A significance scan for both an upper and lower cut is performed. Here, the Poisson significance is used, which is defined as

$$S = \sqrt{2\left((s+b)\ln(1+\frac{s}{b}) - s\right)}. \tag{7.1}$$

Distributions for some variables under study are shown in Figure 7.4 for the $N_{jet} = 0$ category and Figure 7.5 for the $N_{jet} = 1$ category. The comparison between current and optimized cut values is shown in Table 7.7.

Table 7.7: Comparison between the Run 1 selections and the newly validated selections in the ggF analysis.

Category	Run 1 cut	Validated cut
$N_{jet} = 0$	$\Delta\phi(ll, MET) > 1.57$	$\Delta\phi(ll, MET) > 2.10$
	$p_T^{ll} > 30\,\text{GeV}$	$p_T^{ll} > 35\,\text{GeV}$
	$m_{ll} < 55\,\text{GeV}$	$m_{ll} < 50\,\text{GeV}$
	$\Delta\phi_{ll} < 1.8$	$\Delta\phi_{ll} < 1.8$
$N_{jet} = 1$	$N_{b-jet} = 0$	$N_{b-jet} = 0$
	$m_T^l > 50\,\text{GeV}$	$m_T^l > 0\,\text{GeV}$
	$m_{\tau\tau} < m_Z - 25\,\text{GeV}$	$m_{\tau\tau} < m_Z - 25\,\text{GeV}$
	$m_{ll} < 55\,\text{GeV}$	$m_{ll} < 50\,\text{GeV}$
	$\Delta\phi_{ll} < 1.8$	$\Delta\phi_{ll} < 1.8$

Most of the optimization results show that one can safely use the Run 1 cut values for the signal region selection, with the exception of the m_T^l cut in the $N_{jet} = 1$ category. However, this m_T^l cut was designed in Run 1 to reduce the background processes that contain non-isolated leptons, especially QCD multi-jet events. As no data-driven

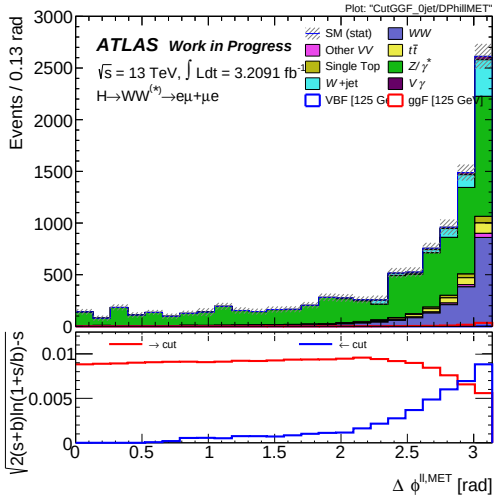

(a) *$\Delta\phi(ll, MET)$ distribution after $N_{jet} = 0$ cut*

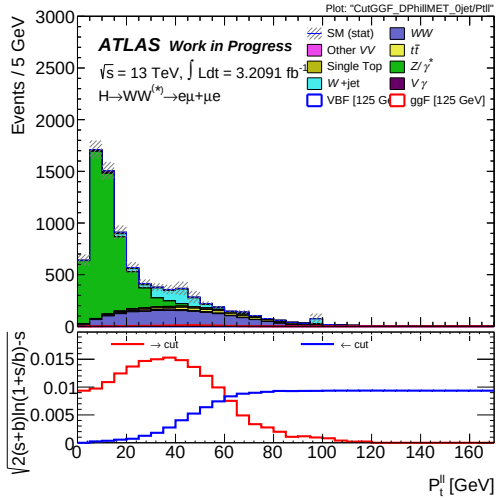

(b) *p_T^{ll} distribution after $\Delta\phi(ll, MET)$ cut*

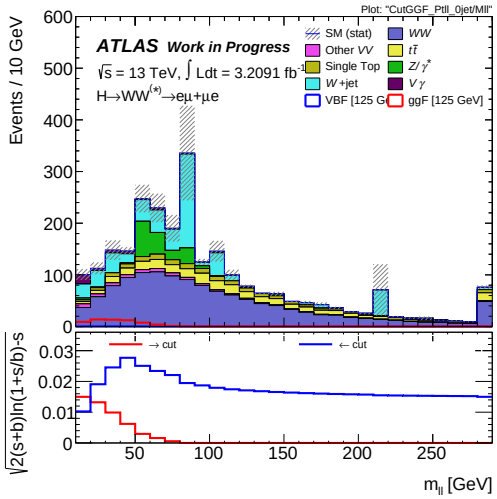

(c) *m_{ll} distribution after p_T^{ll} cut*

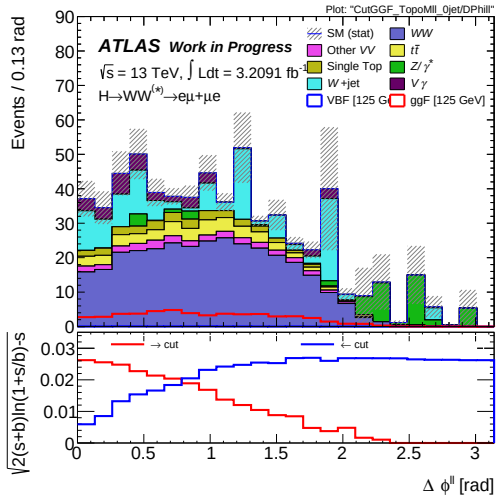

(d) *$\Delta\phi_{ll}$ distribution after m_{ll} cut*

Figure 7.4 *Distributions of $\Delta\phi(ll, MET)$, p_T^{ll}, m_{ll} and $\Delta\phi_{ll}$ variables in the $N_{jet} = 0$ category. The red and blue lines in the significance plot show the Poisson significance for a lower and upper cut, respectively. The cut values which give highest significances were chosen as optimized cut values.*

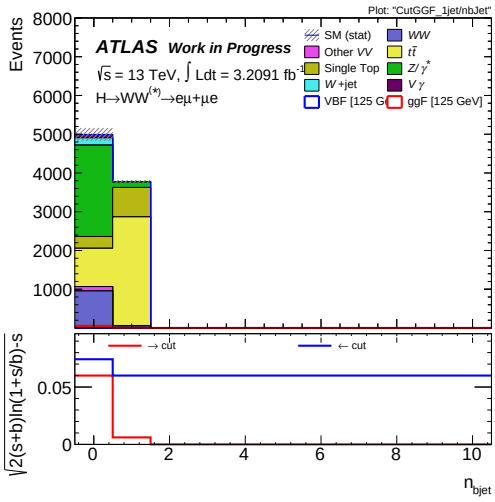

(a) N_{b-jet} *distribution after* $N_{jet} = 1$ *cut*

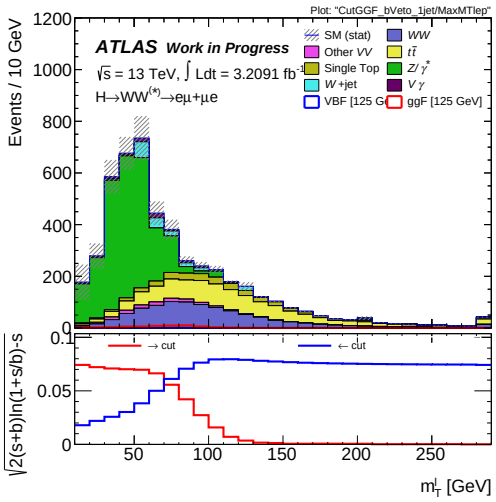

(b) m_T^l *distribution after* N_{b-jet} *cut*

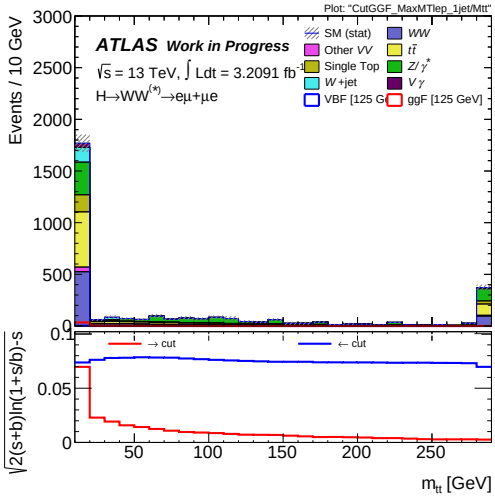

(c) $m_{\tau\tau}$ *distribution after* m_T^l *cut*

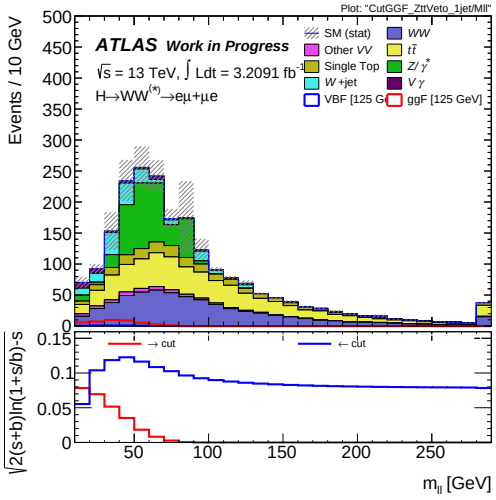

(d) m_{ll} *distribution after* $m_{\tau\tau}$ *cut*

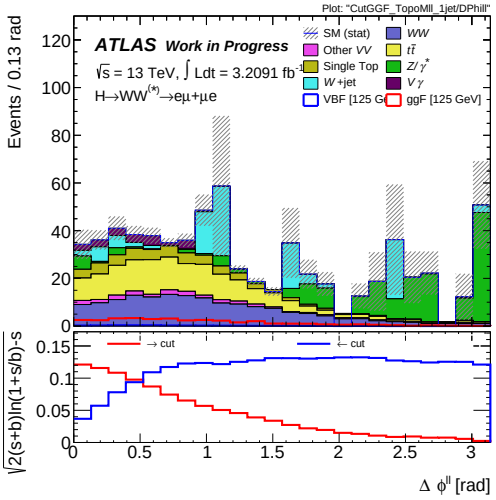

(e) $\Delta\phi_{ll}$ *distribution after* m_{ll} *cut*

Figure 7.5 *Distributions of* N_{b-jet}, m_T^l, $m_{\tau\tau}$, m_{ll} *and* $\Delta\phi_{ll}$ *variables in the* $N_{jet} = 1$ *category. The red and blue lines in the significance plot show the Poisson significance for a lower and upper cut, respectively. The cut values which give highest significances were chosen as optimized cut values.*

lepton-fake estimates were available when this study was performed, it was decided to keep this cut unchanged from the Run 1 value.

7.3.3 Selection of $H \to WW^* \to l\nu l\nu$ Candidate Events

Events are selected from those with exactly one electron and one muon with opposite charge, at least one of the two leptons is required to have $p_T > 25$ GeV. If the leading lepton is a muon in the 2015 dataset the muon is required to have $p_T > 22$ GeV due to the single lepton trigger thresholds [128]. The other (subleading) lepton is required to have $p_T > 15$ GeV. Additional cuts on the dilepton invariant mass $m_{ll} > 10$ GeV and $E_T^{miss,TRK} > 20$ GeV are applied to reject Drell–Yan and multi-jet backgrounds. To give an impression on the modelling, a set of variables at pre-selection level is shown in Figure 7.6 (more plots are in Appendix B).

Figure 7.7 shows the jet multiplicity for $H \to WW^* \to l\nu l\nu$ candidate events. Two non-overlapping signal regions are defined by the number of reconstructed jets: $N_{jet} = 0$ and $N_{jet} = 1$. These separate the data by the dominant background process, which is WW for $N_{jet} = 0$ and a mixture of the WW and top quarks for $N_{jet} = 1$, which improves the sensitivity of the analysis and allows background estimations targeted at each topology.

The selection is summarized in Table 7.8. The p_T threshold used for the jet counting that differentiates the two signal regions is 25 GeV for $|\eta^{jet}| < 2.4$ and 30 GeV for $2.4 < |\eta^{jet}| < 4.5$. The b-jet veto uses jets with $p_T > 20$ GeV. The $\tau\tau$ invariant mass $m_{\tau\tau}$ is calculated using the collinear approximation (see Section 5.3.2).

Background from $Z/\gamma^* \to \tau\tau$ and multi-jets in the $N_{jet} = 1$ category is further reduced with the requirement that at least one of the two leptons must have a single-lepton transverse mass $m_T^l > 50$ GeV.

The discriminating variable in this analysis is the transverse mass m_T. For the definition of m_T and m_T^l, the E_T^{miss} defined in Section 7.2 is used.

In Figures 7.8 and 7.9, the cut variables for the $N_{jet} = 0$ and $N_{jet} = 1$ signal region before the corresponding cut are shown. A blinding criteria is applied for data only: if $m_{ll} < 55$ GeV, then events are rejected with 80 GeV $< m_T <$ 150 GeV for the $N_{jet} = 0$ and 75 GeV $< m_T <$ 150 GeV for the $N_{jet} = 1$ signal region. Due to the blinding criteria, the data points are off but it is still meaningful to compare data to simulation in some regions of phase space, e.g. the tails of m_{ll}. These figures also motivate the application of the subsequent selection cut on the variable that is shown.

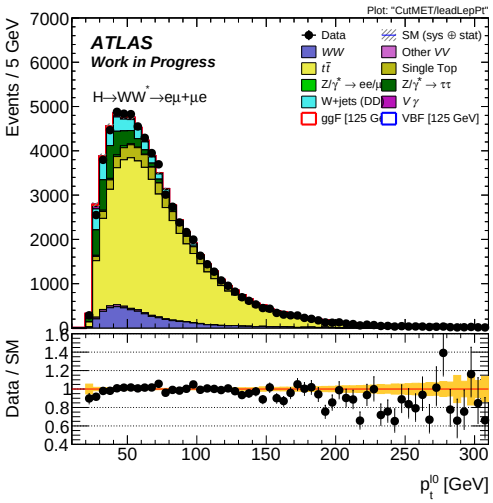

(a) p_T^{lead}

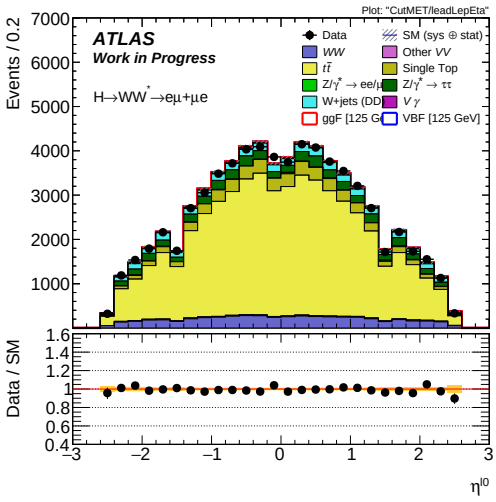

(b) η^{lead}

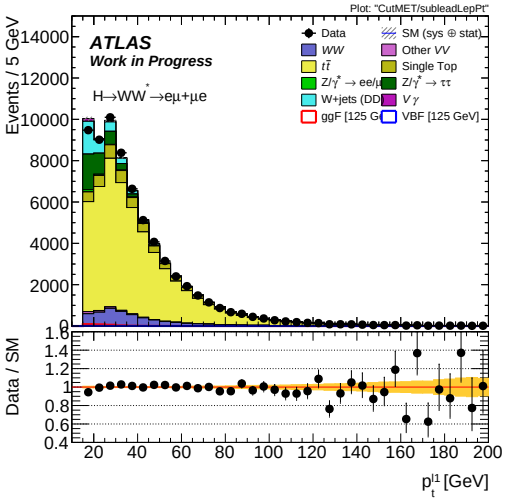

(c) $p_T^{sublead}$

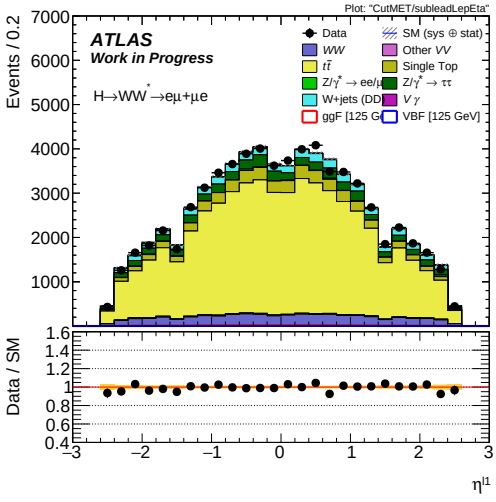

(d) $\eta^{sublead}$

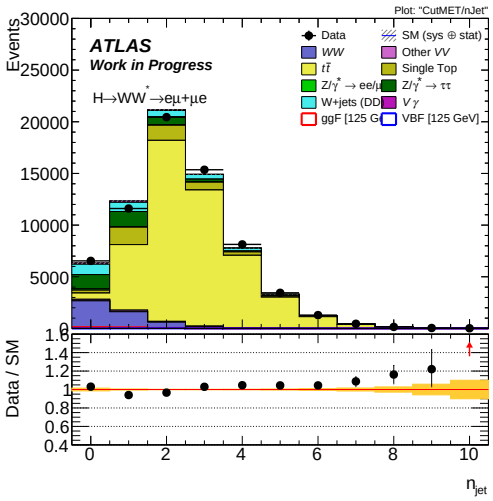

(e) N_{jet}

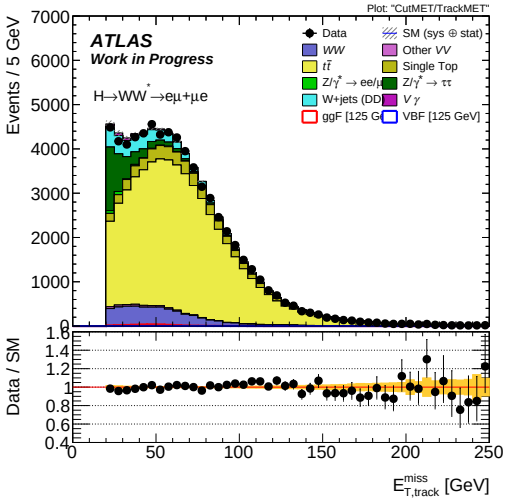

(f) $E_T^{miss,TRK}$

Figure 7.6 *Distributions of* p_T^{lead}, η^{lead}, $p_T^{sublead}$, $\eta^{sublead}$, N_{jet} *and* $E_T^{miss,TRK}$ *at pre-selection level. Signal and background processes are normalized to predictions. The hatched band in the upper plot, and the shaded band in the ratio plot, give the quadrature sum of statistical and experimental systematic rate uncertainties on the signal and backgrounds.*

Table 7.8: Event selection criteria used to define the signal regions in the $e\mu + \mu e$ ggF analysis at $\sqrt{s} = 13$ TeV.

Category	$N_{jet} = 0$	$N_{jet} = 1$
Pre-selection	Two isolated leptons ($l = e, \mu$) with opposite charge $p_T^{lead} > 25$ GeV ($p_T^{lead} > 22$ GeV for muons in 2015), $p_T^{sublead} > 15$ GeV $m_{ll} > 10$ GeV $E_T^{miss,TRK} > 20$ GeV	
background rejection	-	$N_{b-jet} = 0$
	$\Delta\phi(ll, MET) > 1.57$	$\max(m_T^l) > 50$ GeV
	$p_T^{ll} > 30$ GeV	$m_{\tau\tau} < m_Z - 25$ GeV
$H \to WW^* \to l\nu l\nu$ topology	$m_{ll} < 55$ GeV	
	$\Delta\phi_{ll} < 1.8$	

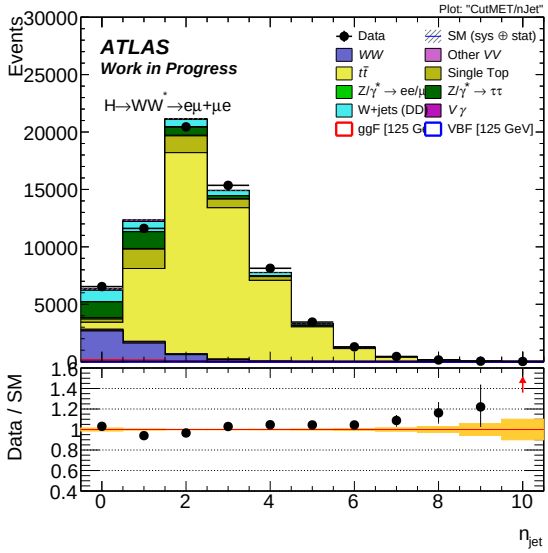

Figure 7.7 *Jet multiplicity for $H \to WW^* \to l\nu l\nu$ candidate events in 13 TeV data at pre-selection level. Signal and background processes are normalized to predictions. The hatched band in the upper plot, and the shaded band in the ratio plot, give the quadrature sum of statistical and experimental systematic rate uncertainties on the signal and backgrounds.*

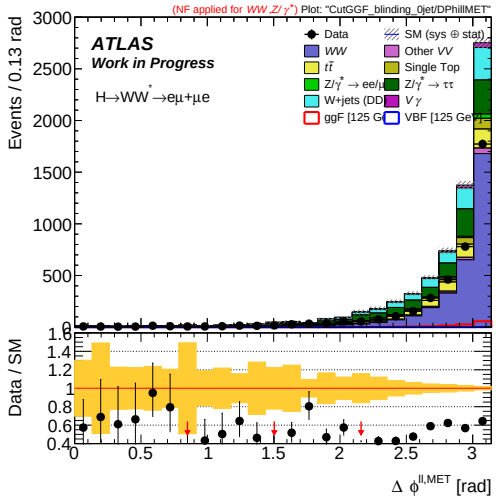

(a) $\Delta\phi_{ll,MET}$ *after the cut* $N_{jet} = 0$

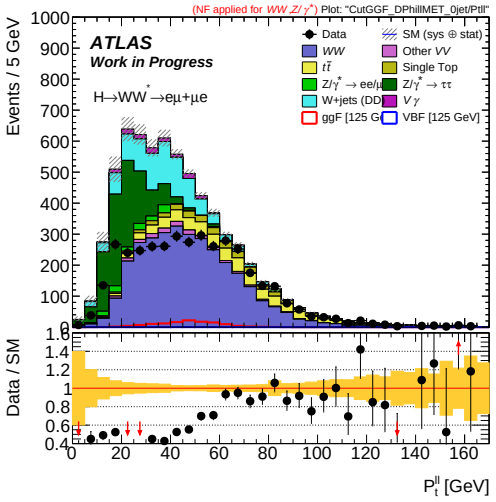

(b) p_T^{ll} *after the cut* $\Delta\phi_{ll,MET} > 1.57$

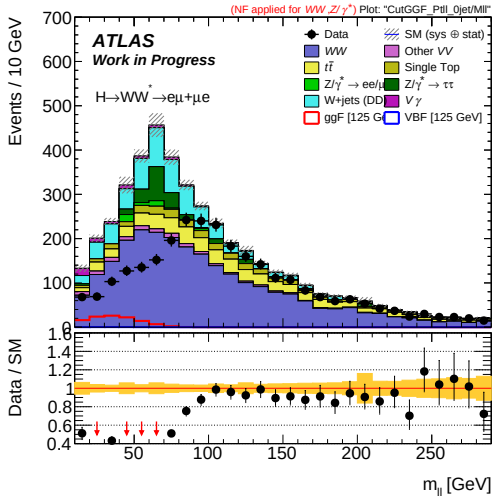

(c) m_{ll} *after the cut* $p_T^{ll} > 30$ *GeV*

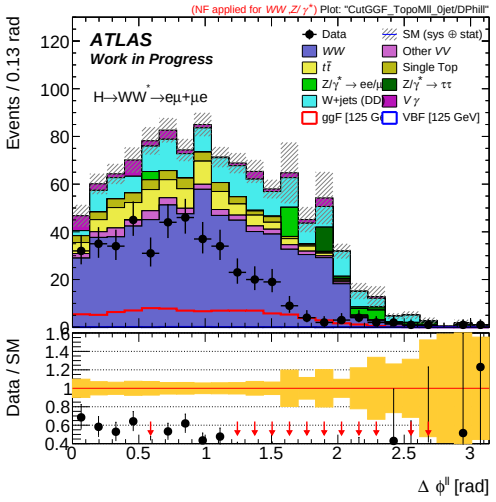

(d) $\Delta\phi_{ll}$ *after the cut* $m_{ll} < 55$ *GeV*

Figure 7.8 *Distributions of the cut variables* $\Delta\phi_{ll,MET}$, p_T^{ll}, m_{ll}, *and* $\Delta\phi_{ll}$ *before the corresponding cut is applied in the* $N_{jet} = 0$ *signal region. The blinding criteria is applied for data in these plots, therefore the data points are off in some regions. The uncertainty band is the quadratic sum of the statistical uncertainty and the experimental systematic rate uncertainties.*

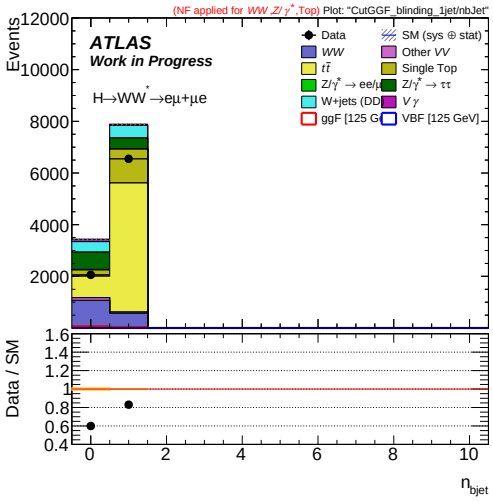

(a) N_{b-jets} *after the cut* $N_{jet} = 1$

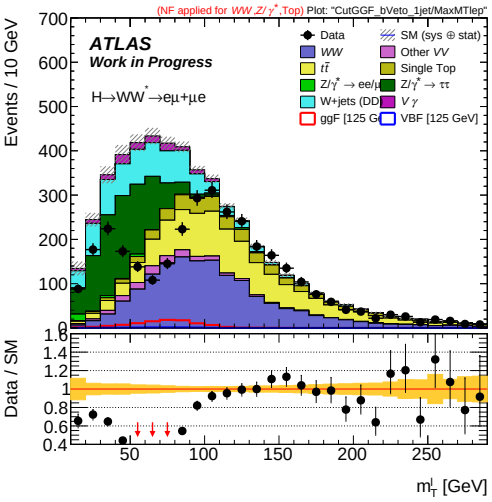

(b) $max(m_T^l)$ *after the b-jet veto*

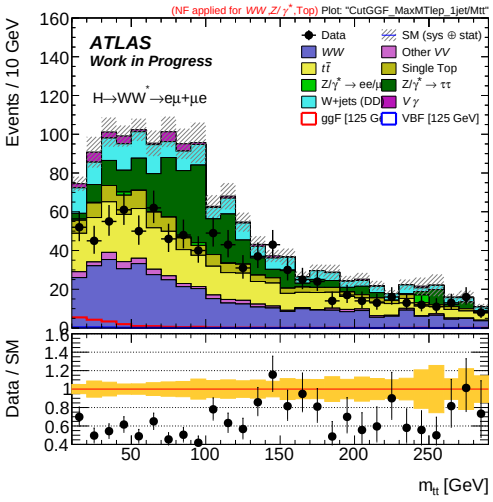

(c) $m_{\tau\tau}$ *after cut* $max(m_T^l) > 50\ GeV$

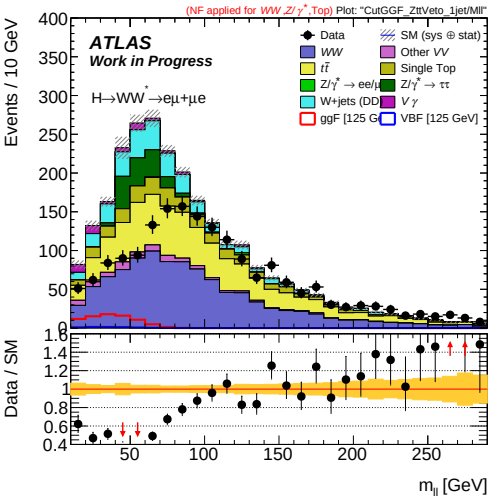

(d) m_{ll} *after the cut* $m_{\tau\tau} < m_Z - 25\ GeV$

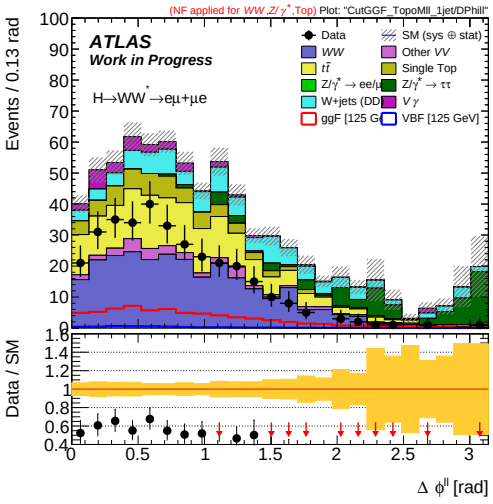

(e) $\Delta\phi_{ll}$ *after the cut* $m_{ll} < 55\ GeV$

Figure 7.9 *Distributions of the cut variables* N_{b-jets}, $max(m_T^l)$, $m_{\tau\tau}$, m_{ll}, *and* $\Delta\phi_{ll}$ *before the corresponding cut is applied in the* $N_{jet} = 1$ *signal region. The blinding criteria is applied for data in these plots, therefore the data points are off in some regions. The uncertainty band is the quadratic sum of the statistical uncertainty and the experimental systematic rate uncertainties.*

7.3.4 Background Estimation

The background estimation strategy is described in detail in Section 5.3.3. The control regions are almost identical to the ones used in the Run-1 analysis (see Table 5.9) but have an increased subleading lepton p_T threshold of 15 GeV.

WW estimation

For the $N_{jet} = 0$ and $N_{jet} = 1$ categories, the WW background is normalized using control regions differentiated from the SR primarily by m_{ll} (see Table 5.9), and the shape is taken from MC simulation. To reduce the contribution of top-quark background in the WW $N_{jet} = 1$ CR, a b-jet veto for jets above a p_T threshold of 20 GeV is applied. Figure 7.10 shows the number of b-jets in the WW $N_{jet} = 1$ CR where the b-jet veto is applied for jets with $p_T > 25$ GeV, this motivates to reject b-jets above 20 GeV. It can be seen that top-quark background is dominating in the $N_{b-jet} = 1$ bin. Distributions for some of the characteristic variables in the WW CR are shown in Figure 7.11 and 7.12 for $N_{jet} = 0$ and Figure 7.13 and 7.14 for $N_{jet} = 1$.

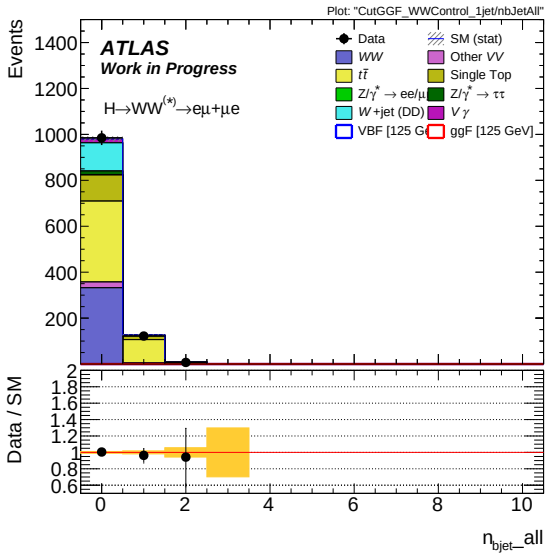

Figure 7.10 *$N_{b\text{-}jet}$ distribution of b-jets with $p_T > 20$ GeV in the WW $N_{jet} = 1$ CR where the b-jet veto is applied for jets with $p_T > 25$ GeV.*

Top estimation

The top-quark background normalization is estimated using control regions for each jet bin, and the shape of the distributions other than N_{jet} is taken from MC simulation. More details on top-quark background normalization can be seen in Section 5.3.3. Distributions for some of the characteristic variables in the top-quark CR are shown in Figure 7.15 and 7.16 for $N_{jet} = 0$ and Figure 7.17 for $N_{jet} = 1$.

Z/γ^*+jets estimation

The $Z/\gamma^* \to \tau\tau$ background normalization is derived from control regions (see Table 5.9), and the shape is taken from MC, for all jet bins. The NFs extracted from $Z/\gamma^* \to \tau\tau$ CRs are applied to all $Z/\gamma^* \to ll$ backgrounds. Distributions for some of the characteristics variables in the $Z/\gamma^* \to \tau\tau$ CR are shown in Figure 7.18 for $N_{jet} = 0$ and Figure 7.19 for $N_{jet} = 1$.

W+jets estimation

The W+jets contribution to the signal region is determined by the fake-factor method (see Section 5.3.3) which scales the number of events in the control sample by a transfer factor measured in a dijet data sample. The extrapolation factor is the ratio of the number of identified leptons to the number of anti-identified leptons, measured in bins of anti-identified lepton p_T and η. To account for differences between the jets associated with W boson and dijet production, the extrapolation factors are measured in Z+jets and dijet samples, and the difference of the two extrapolation factors is taken as a systematic uncertainty on the one measured in dijet data (see Figure 7.20). Other sources of uncertainties on the measurement of the fake factors are the uncertainty associated to the real lepton contamination from electroweak processes (estimated by varying the subtracted MC predictions up and down by 20%) and the uncertainty associated to the lepton charge dependence in W+jets (taken as the difference in fake factors between the same-sign and opposite-sign case derived from MC W+jets).

Diboson estimation

The background from Vγ diboson processes is normalized in the $N_{jet} = 0$ and $N_{jet} = 1$ categories using control regions identical to the signal regions except that the leptons are required to have the same electric charge (*same-sign*). These same-sign control regions currently lack statistics but can still be used for NF calculations. The extracted NFs are then used in the fit. Distributions for some of the characteristic variables in the $V\gamma$ CR are shown in Figure 7.21 for $N_{jet} = 0$ and Figure 7.22 for $N_{jet} = 1$.

7.3.5 Normalization Factors

The normalization from control regions is applied via normalization factors. Except for the normalization of top processes these NFs are applied globaly to the MC prediction of the corresponding process. First of all, top-quark NFs are calculated as described in Section 5.3.3. WW and Drell–Yan background processes are then normalized simultaneously using a matrix inversion method. After subtracting contributions from processes which are not normalized in this procedure, the event yield in data D_i in CR

i can be expressed as

$$D_i = MC_{ij} \cdot NF_j, \tag{7.2}$$

where MC_{ij} denotes the contribution taken from MC of process j to region i and NF_j is the NF of the process. If the number of CRs and processes to be normalized is equal, MC_{ij} is a square matrix and Eq. 7.2 can be solved for the vector (NF_j) via multiplication with the inverse $(MC_{ij})^{-1}$.

After all, the same-sign control regions supply NFs for Vγ, defined as $(N - B')/B$, where N is the number of data events observed in the control region, B is the original predicted background yield in the CR for the target process, and B' is the predicted yield from other processes in the control region.

Due to significant contributions of some backgrounds to control regions of other backgrounds, the order of which NF calculations are performed is relevant. The order of NF calculation is starting with the top, followed by a matrix inversion calculation for WW and Z/DY and finally the same-sign CR. The results of these NF calculations are given in Table 7.9, along with their uncertainties which is determined using a set of toy NFs and to be included as a systematic uncertainty for the final results, unless the CRs are directly included in the fit. This reflects the correlation of each NF across all bins in the fit. Only the $N_{jet} = 0$ top-quark and the Vγ normalization factors are used for the signal extraction. All other CRs are entering the likelihood fit and the backgrounds are renormalized. The NFs in Table 7.9 are mainly used for the normalization of the control plots, cut-based yield tables, and as a cross check.

Table 7.9: Background normalization factors obtained from the control regions.

Control Regions	WW	Top	$Z/\gamma^* \to ll$	Vγ
$N_{jet} = 0$	1.10 ± 0.06	0.91 ± 0.03	0.96 ± 0.03	1.32 ± 0.26
$N_{jet} = 1$	0.88 ± 0.07	1.03 ± 0.03	0.78 ± 0.07	1.37 ± 0.21

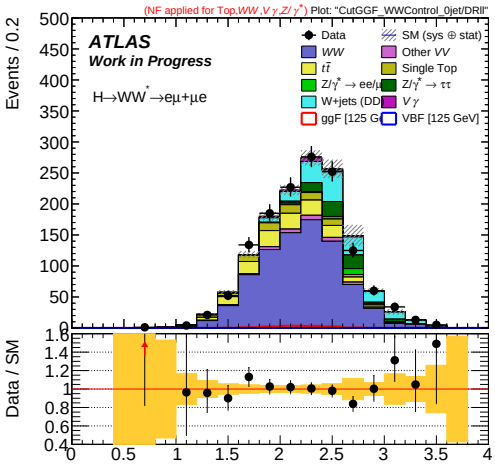

(a) $\Delta R(ll)$

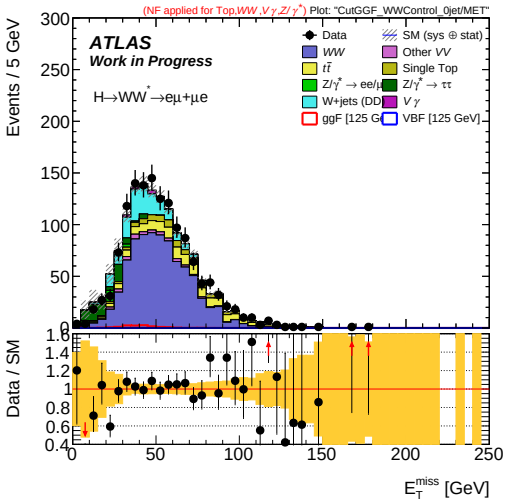

(b) E_T^{miss}

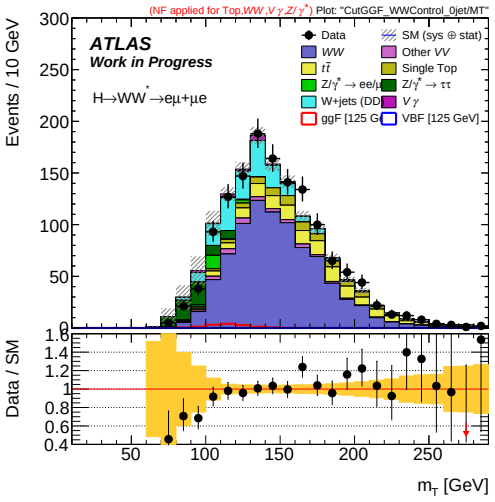

(c) m_T

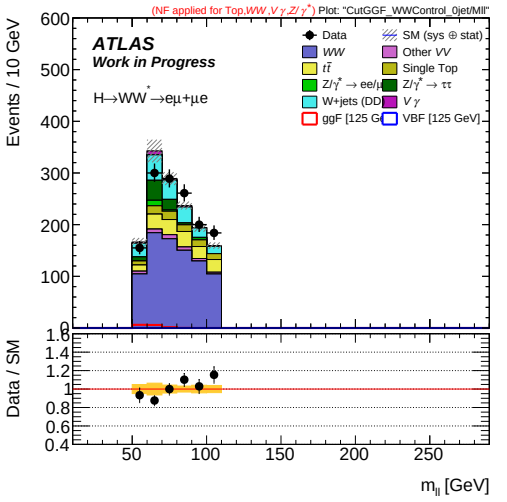

(d) m_{ll}

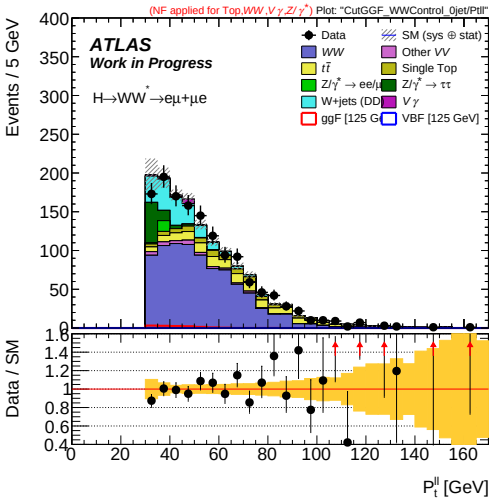

(e) p_T^{ll}

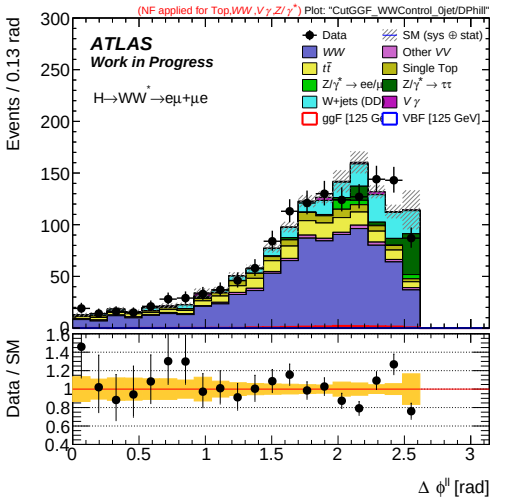

(f) $\Delta\phi_{ll}$

Figure 7.11 *Distributions of* $\Delta R(ll)$, E_T^{miss}, m_T, m_{ll}, p_T^{ll} *and* $\Delta\phi_{ll}$ *in the WW control region in the* $N_{jet} = 0$ *category, from which the WW background in the signal region is normalized. The uncertainty band is the quadratic sum of the statistical uncertainty and the experimental systematic rate uncertainties.*

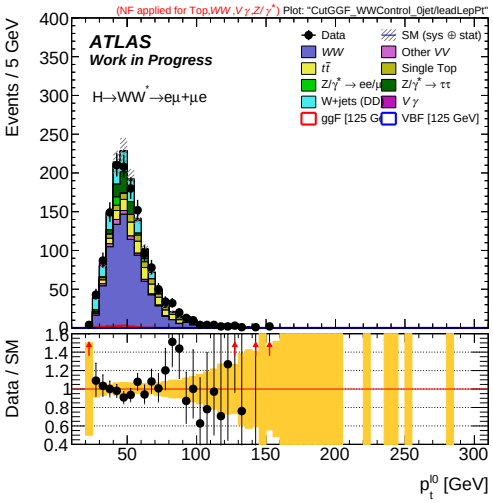

(a) p_T^{lead}

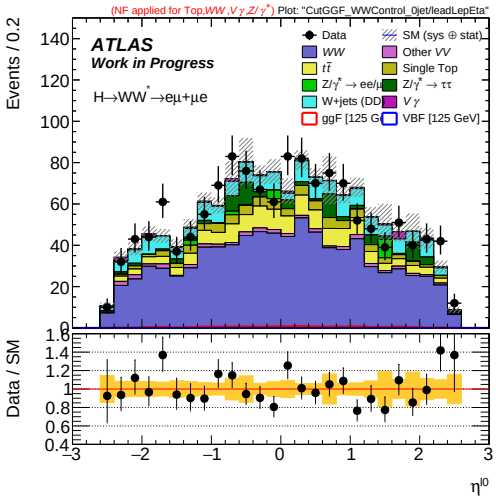

(b) η^{lead}

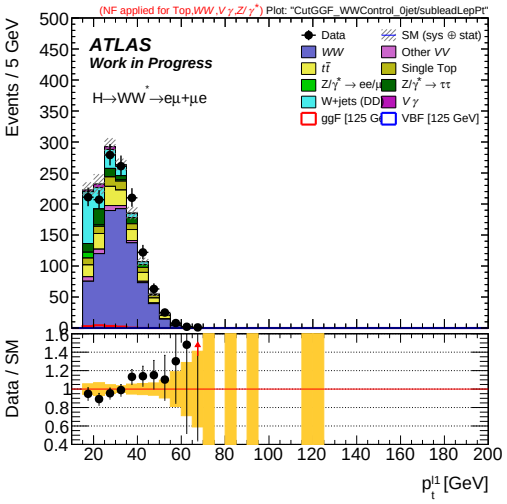

(c) $p_T^{sublead}$

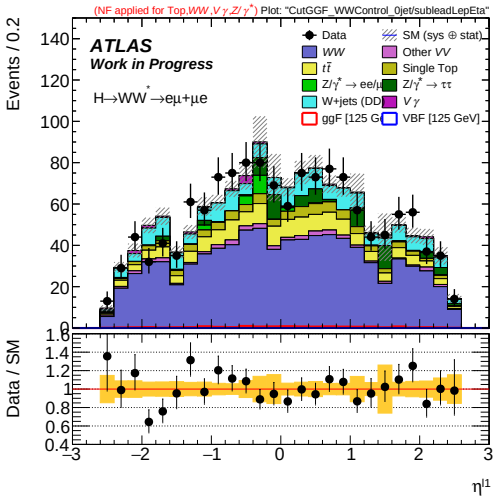

(d) $\eta^{sublead}$

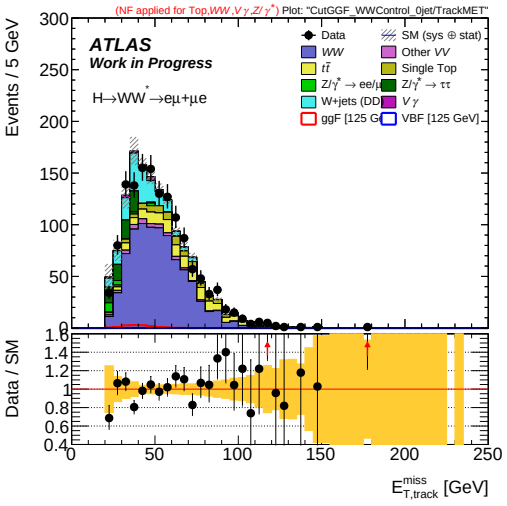

(e) $E_T^{miss,TRK}$

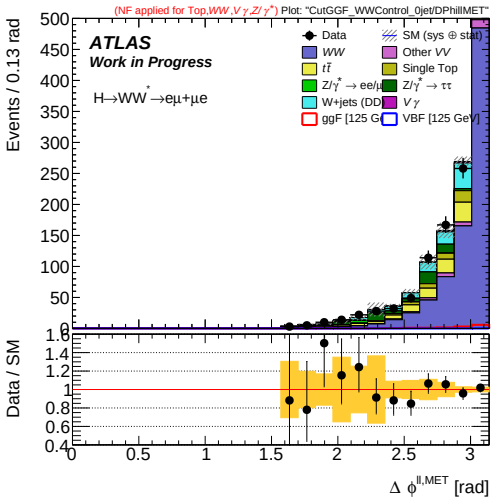

(f) $\Delta\phi_{ll,MET}$

Figure 7.12 *Distributions of p_T^{lead}, η^{lead}, $p_T^{sublead}$, $\eta^{sublead}$, $E_T^{miss,TRK}$ and $\Delta\phi_{ll,MET}$ in the WW control region in the $N_{jet} = 0$ category, from which the WW background in the signal region is normalized. The uncertainty band is the quadratic sum of the statistical uncertainty and the experimental systematic rate uncertainties.*

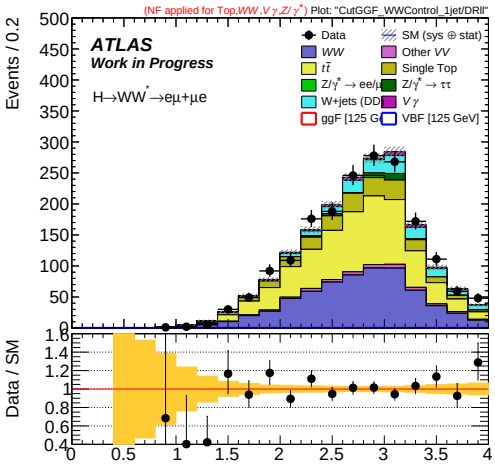

(a) $\Delta R(ll)$

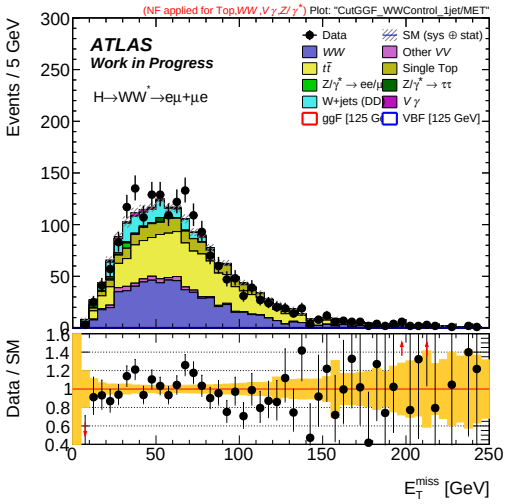

(b) E_T^{miss}

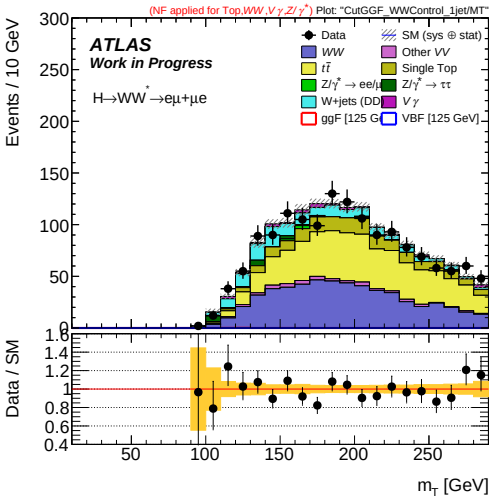

(c) m_T

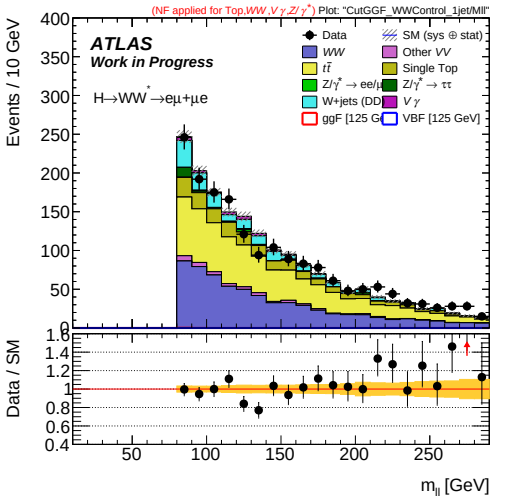

(d) m_{ll}

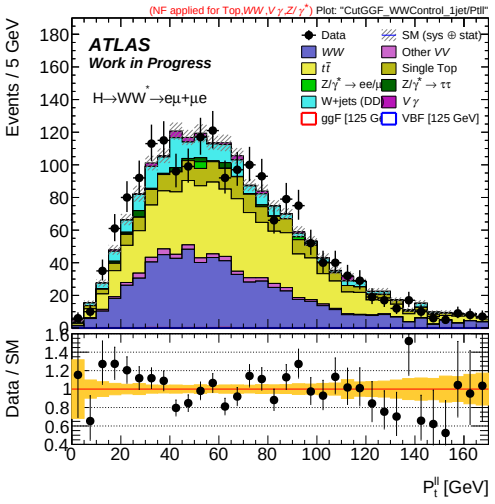

(e) p_T^{ll}

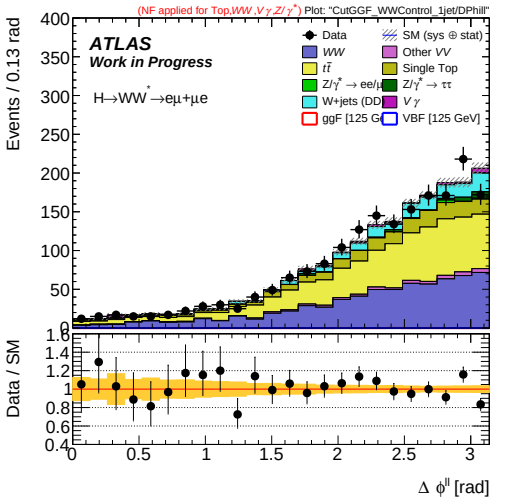

(f) $\Delta\phi_{ll}$

Figure 7.13 *Distributions of* $\Delta R(ll)$, E_T^{miss}, m_T, m_{ll}, p_T^{ll} *and* $\Delta\phi_{ll}$ *in the WW control region in the* $N_{jet} = 1$ *category, from which the WW background in the signal region is normalized. The uncertainty band is the quadratic sum of the statistical uncertainty and the experimental systematic rate uncertainties.*

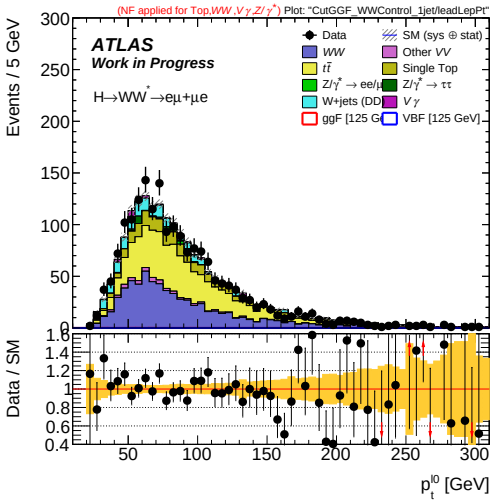

(a) p_T^{lead}

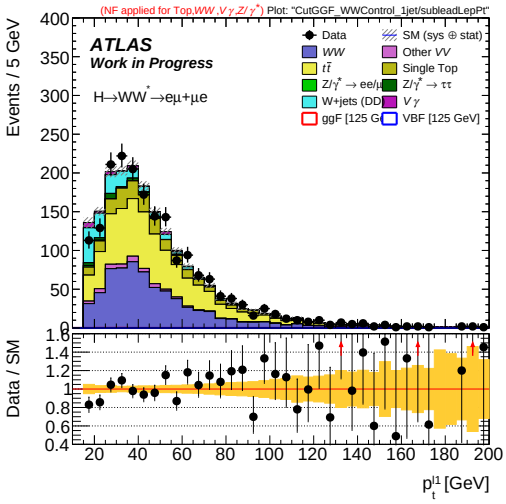

(b) $p_T^{sublead}$

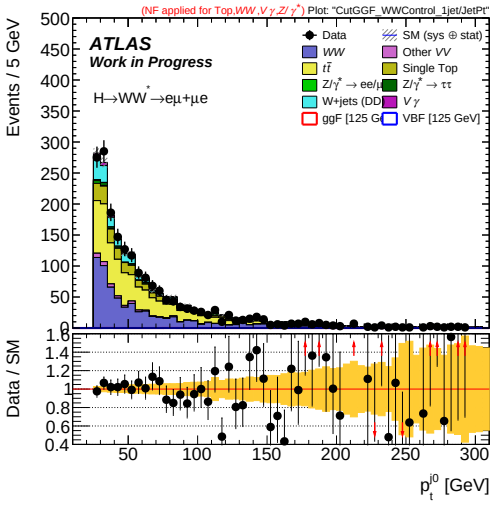

(c) p_T^j

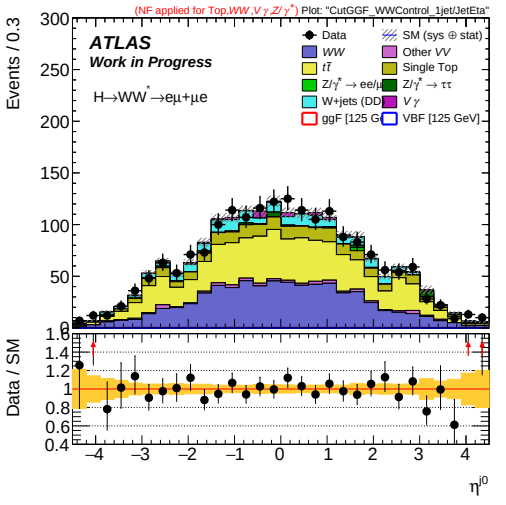

(d) η^j

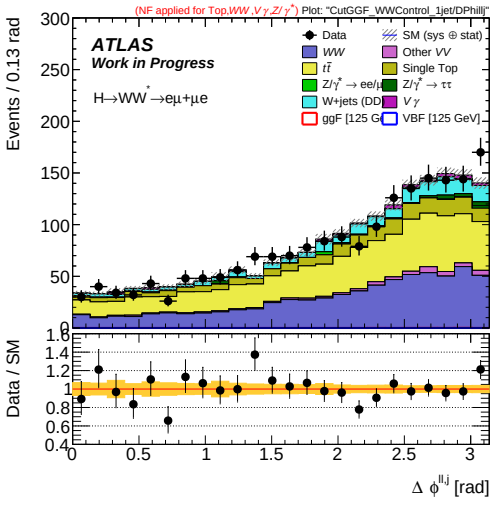

(e) $\Delta\phi_{ll,j_1}$

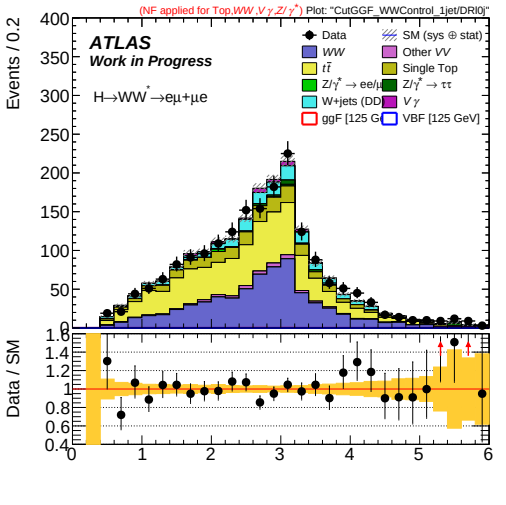

(f) $\Delta R(l^{\text{lead}}, j_1)$

Figure 7.14 *Distributions of p_T^{lead}, $p_T^{sublead}$, p_T^j, η^j, $\Delta\phi_{ll,j_1}$ and $\Delta R(l^{\text{lead}}, j_1)$ in the WW control region in the $N_{jet} = 1$ category, from which the WW background in the signal region is normalized. The uncertainty band is the quadratic sum of the statistical uncertainty and the experimental systematic rate uncertainties.*

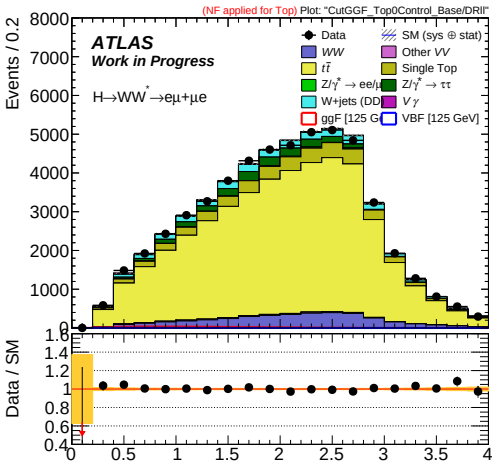

(a) $\Delta R(ll)$

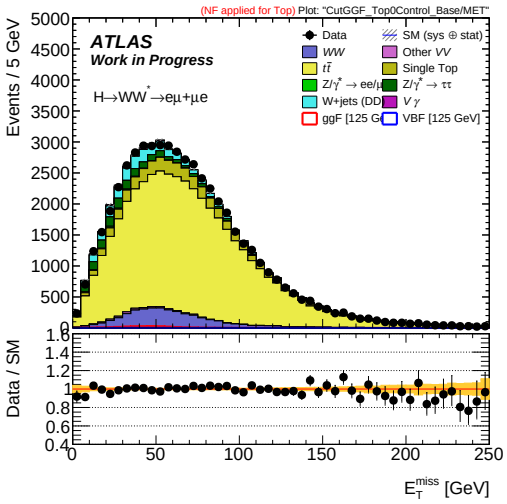

(b) E_T^{miss}

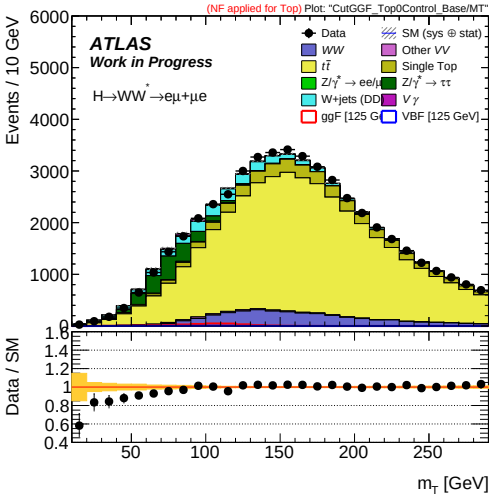

(c) m_T

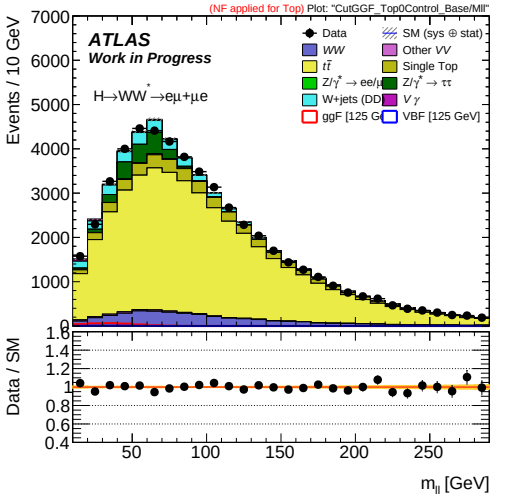

(d) m_{ll}

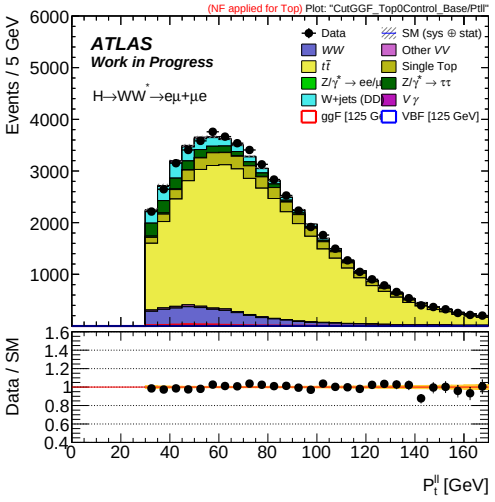

(e) p_T^{ll}

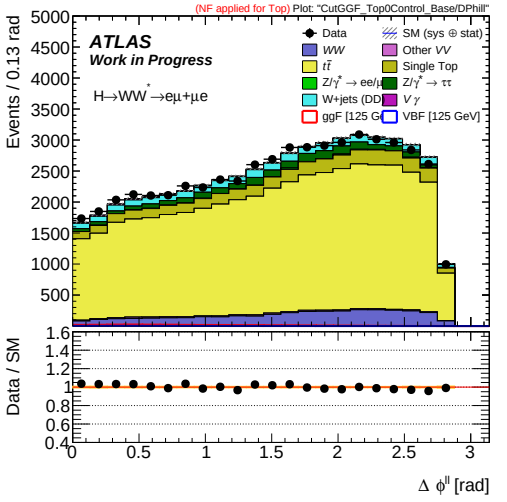

(f) $\Delta\phi_{ll}$

Figure 7.15 *Distributions of* $\Delta R(ll)$, E_T^{miss}, m_T, m_{ll}, p_T^{ll} *and* $\Delta\phi_{ll}$ *in the top-quark control region in the* $N_{jet} = 0$ *category, from which the top-quark background in the signal region is normalized. The hatched band in the upper plot, and the shaded band in the ratio plot, give the quadrature sum of statistical and experimental systematic rate uncertainties on the signal and backgrounds.*

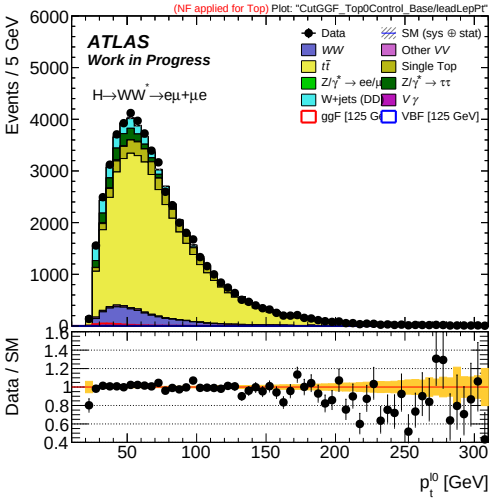

(a) p_T^{lead}

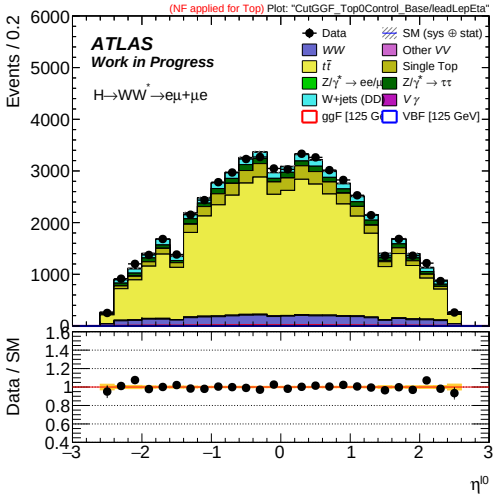

(b) η^{lead}

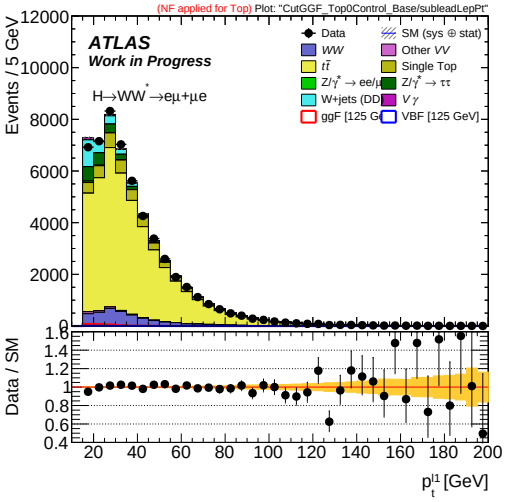

(c) $p_T^{sublead}$

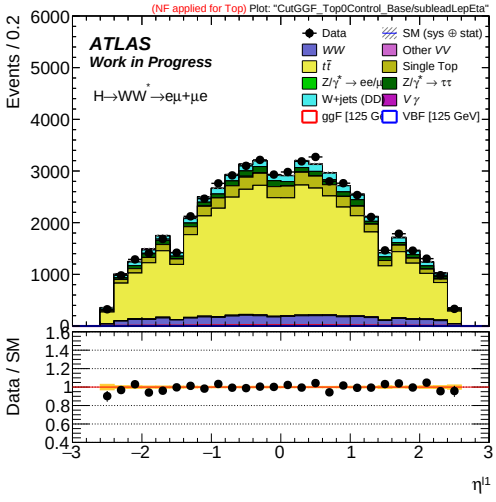

(d) $\eta^{sublead}$

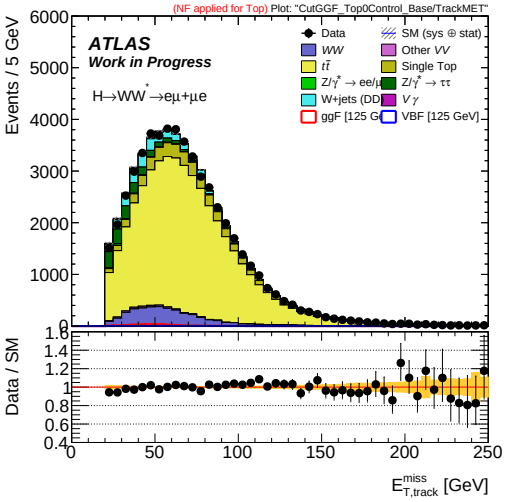

(e) $E_T^{miss,TRK}$

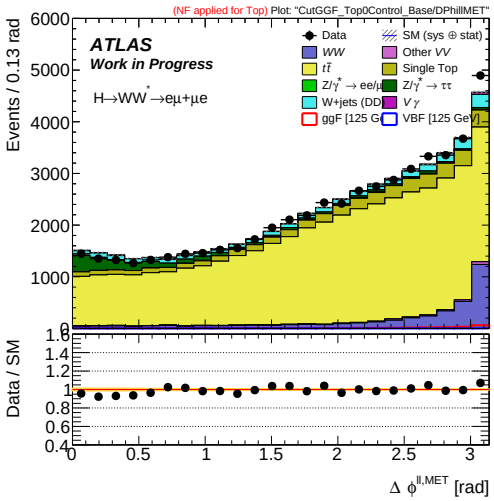

(f) $\Delta\phi_{ll,MET}$

Figure 7.16 *Distributions of p_T^{lead}, η^{lead}, $p_T^{sublead}$, $\eta^{sublead}$, $E_T^{miss,TRK}$ and $\Delta\phi_{ll,MET}$ in the top-quark control region in the $N_{jet} = 0$ category, from which the top-quark background in the signal region is normalized. The hatched band in the upper plot, and the shaded band in the ratio plot, give the quadrature sum of statistical and experimental systematic rate uncertainties on the signal and backgrounds.*

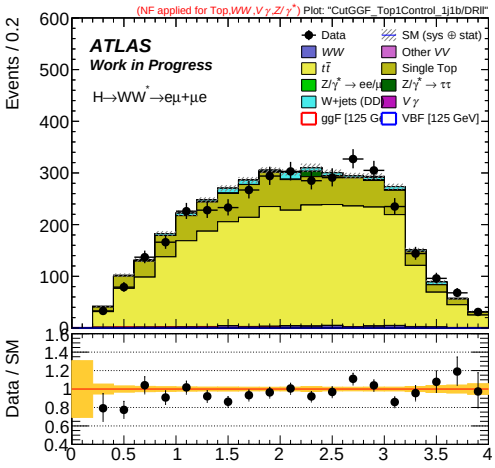

(a) $\Delta R(ll)$

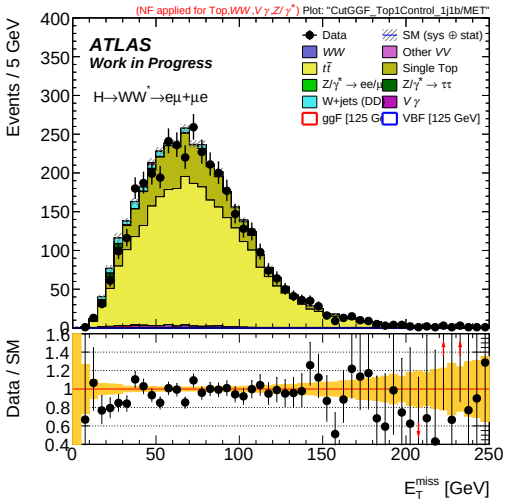

(b) E_T^{miss}

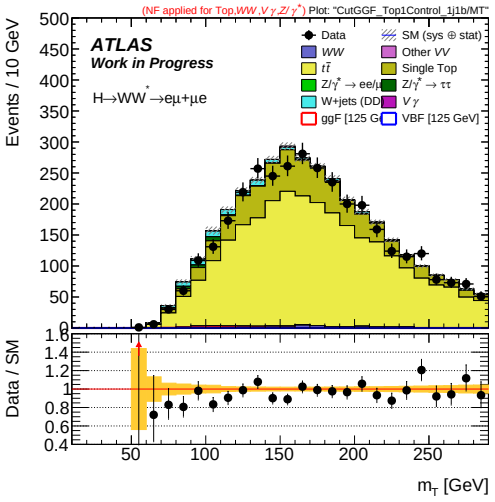

(c) m_T

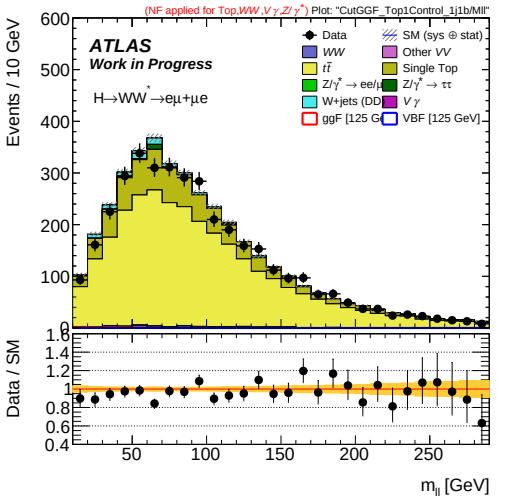

(d) m_{ll}

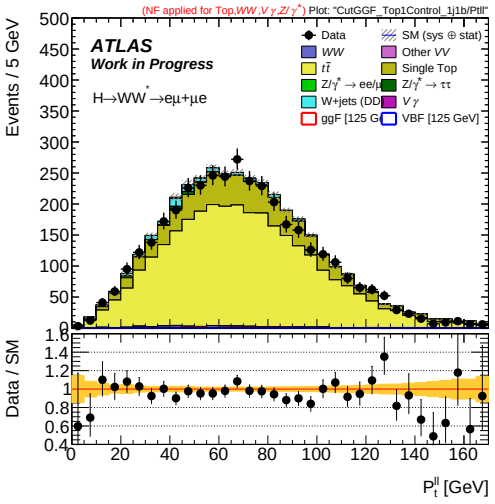

(e) p_T^{ll}

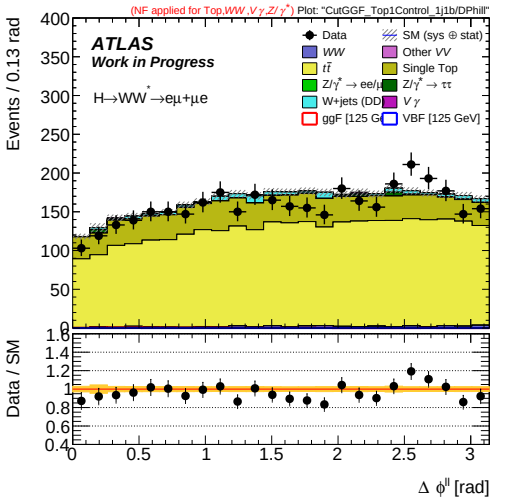

(f) $\Delta\phi_{ll}$

Figure 7.17 *Distributions of* $\Delta R(ll)$, E_T^{miss}, m_T, m_{ll}, p_T^{ll} *and* $\Delta\phi_{ll}$ *in the top-quark control region in the* $N_{jet} = 1$ *category, from which the top-quark background in the signal region is normalized. The hatched band in the upper plot, and the shaded band in the ratio plot, give the quadrature sum of statistical and experimental systematic rate uncertainties on the signal and backgrounds.*

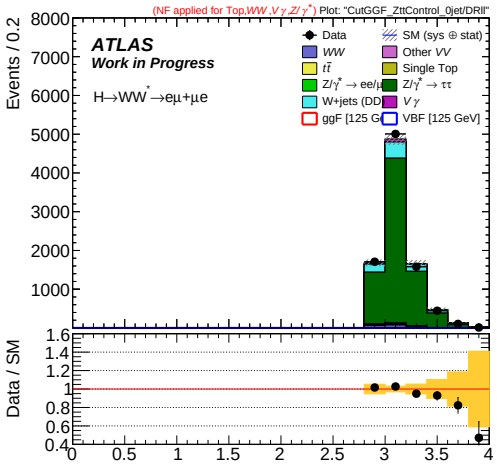

(a) $\Delta R(ll)$

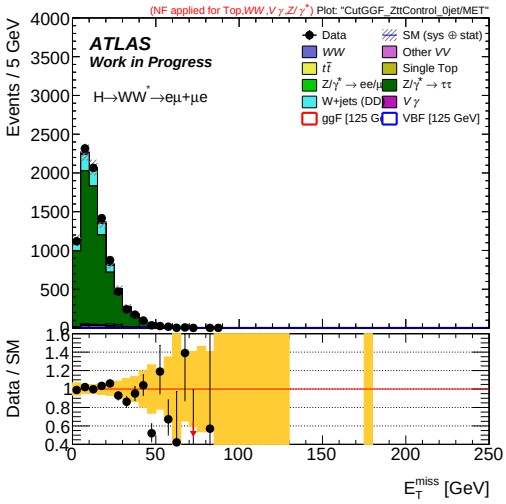

(b) E_T^{miss}

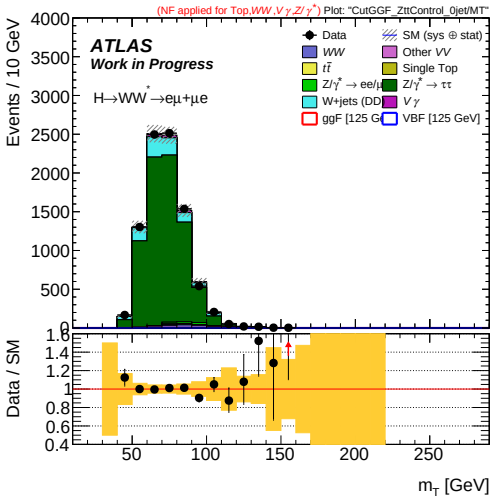

(c) m_T

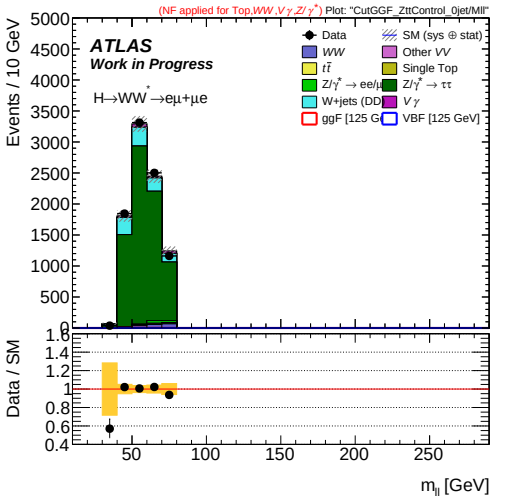

(d) m_{ll}

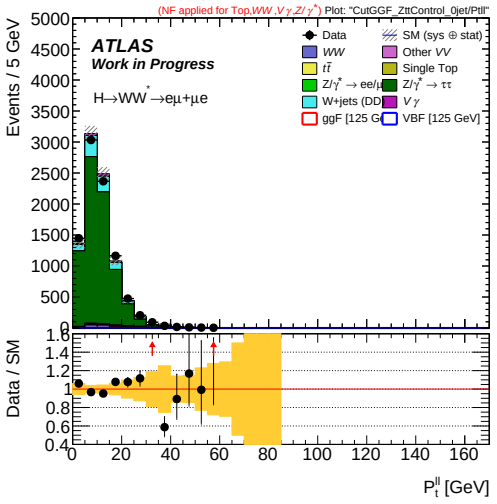

(e) p_T^{ll}

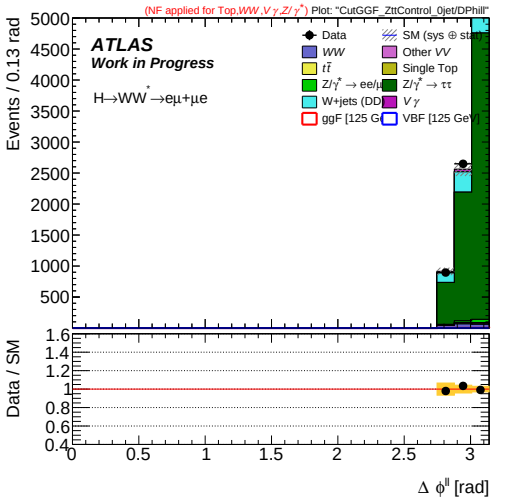

(f) $\Delta\phi_{ll}$

Figure 7.18 *Distributions of $\Delta R(ll)$, E_T^{miss}, m_T, m_{ll}, p_T^{ll} and $\Delta\phi_{ll}$ in the $Z/\gamma^* \to \tau\tau$ control region in the $N_{jet} = 0$ category, from which the $Z/\gamma^* \to \tau\tau$ background in the signal region is normalized. The hatched band in the upper plot, and the shaded band in the ratio plot, give the quadrature sum of statistical and experimental systematic rate uncertainties on the signal and backgrounds.*

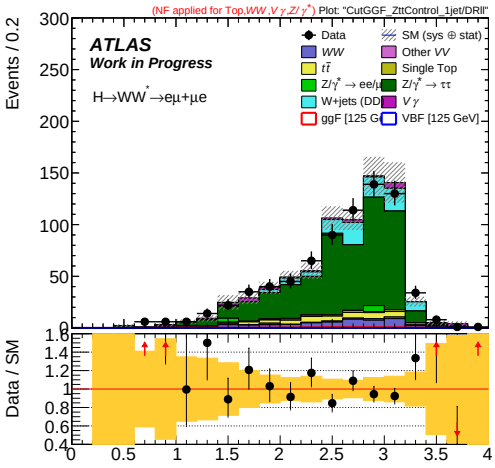

(a) $\Delta R(ll)$

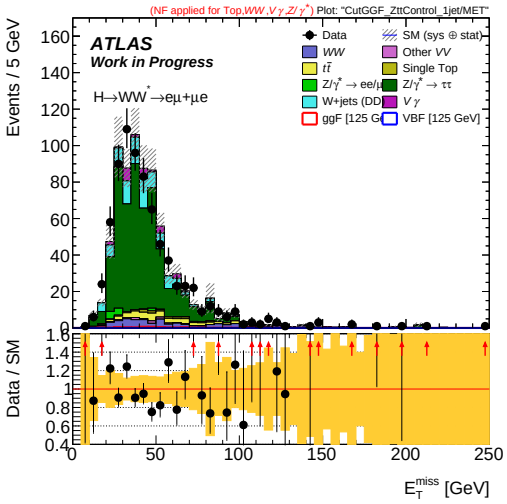

(b) E_T^{miss}

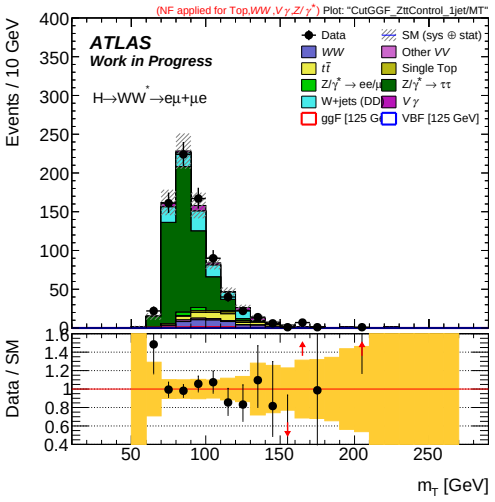

(c) m_T

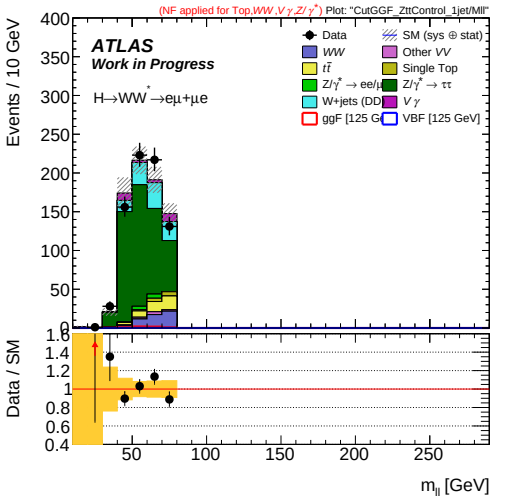

(d) m_{ll}

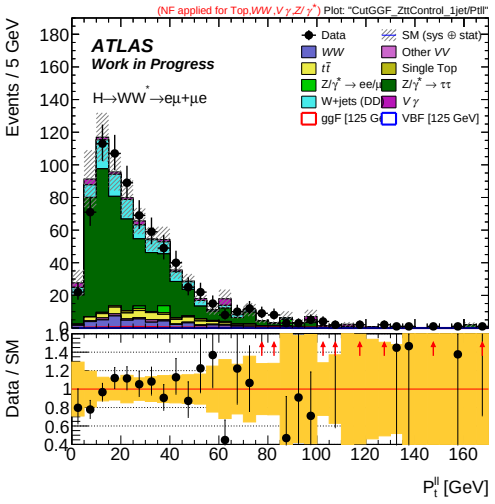

(e) p_T^{ll}

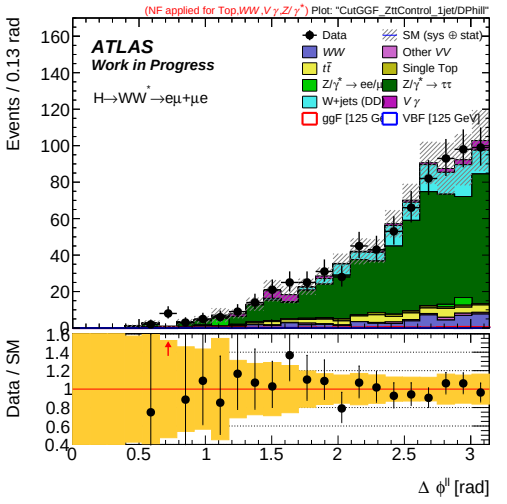

(f) $\Delta\phi_{ll}$

Figure 7.19 *Distributions of* $\Delta R(ll)$, E_T^{miss}, m_T, m_{ll}, p_T^{ll} *and* $\Delta\phi_{ll}$ *in the* $Z/\gamma^*\to\tau\tau$ *control region in the* $N_{jet} = 1$ *category, from which the* $Z/\gamma^*\to\tau\tau$ *background in the signal region is normalized. The hatched band in the upper plot, and the shaded band in the ratio plot, give the quadrature sum of statistical and experimental systematic rate uncertainties on the signal and backgrounds.*

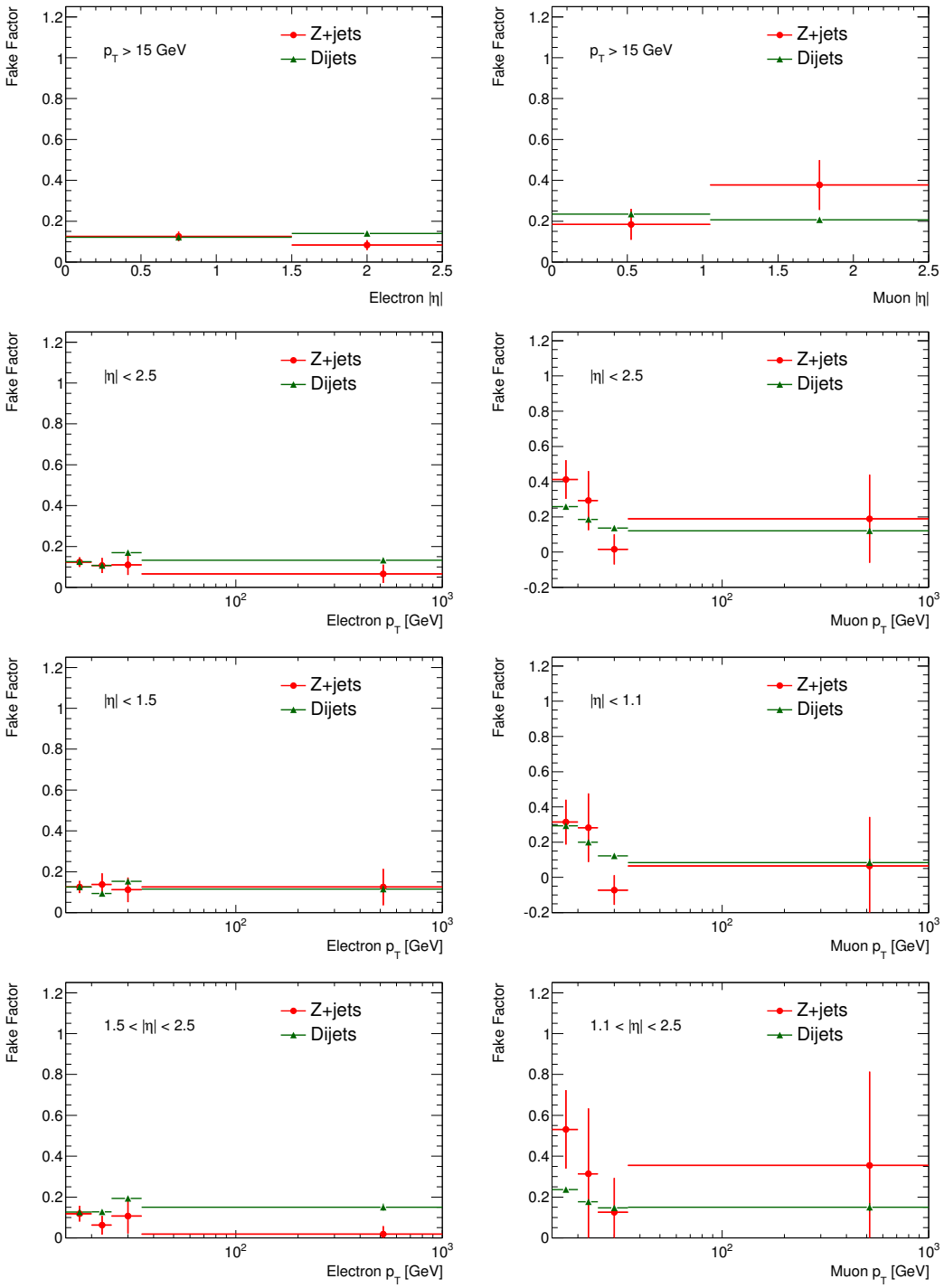

Figure 7.20 *Fake factors obtained in the Z+jets sample with the ones obtained in the dijet sample as a function of the p_T of the electron (left) and muon (right) fake candidates. The first row shows the fake factors averaged over p_T bins, while the second row shows the fake factors averaged over η bins. The third and fourth row shows the fake factors in the central and forward regions, respectively.*

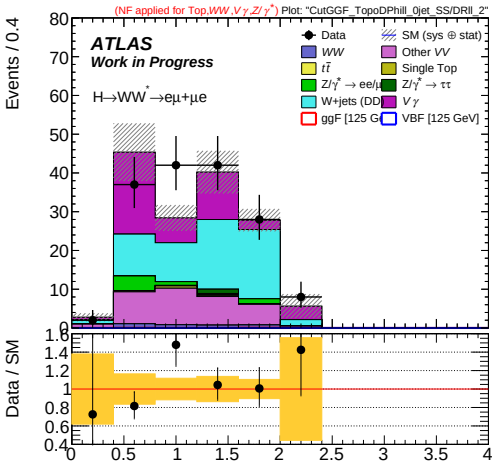

(a) $\Delta R(ll)$

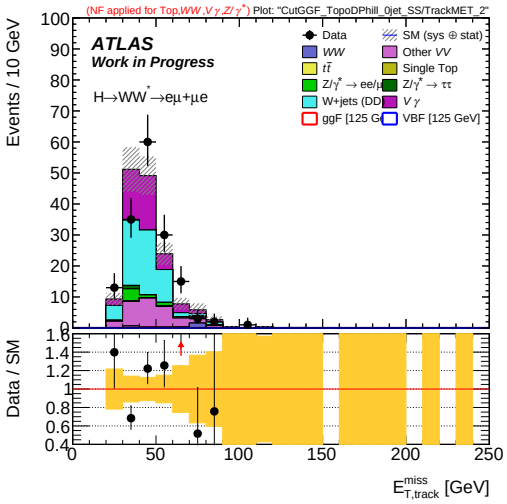

(b) E_T^{miss}

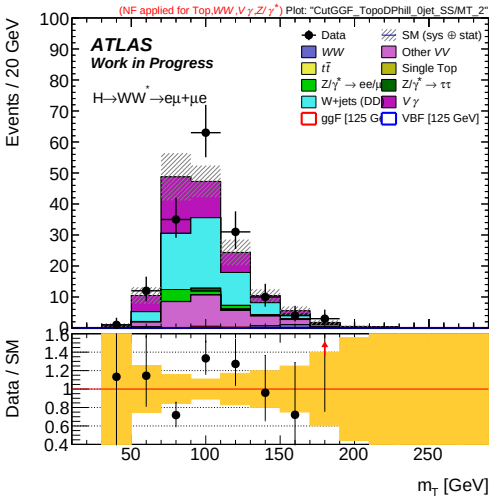

(c) m_T

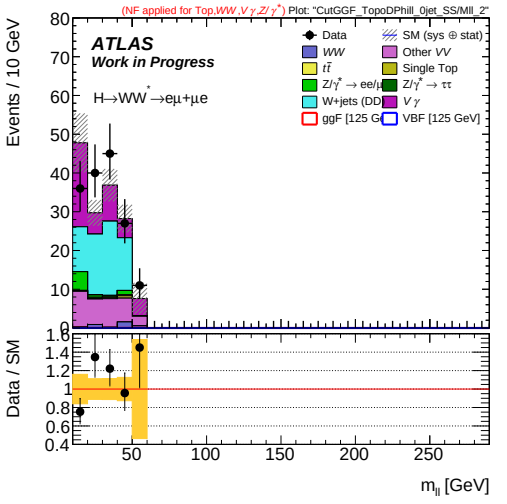

(d) m_{ll}

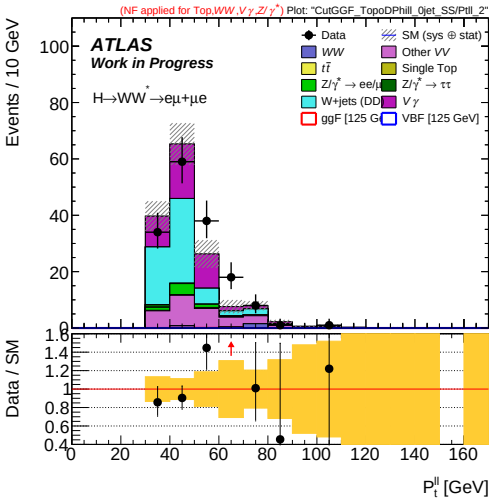

(e) p_T^{ll}

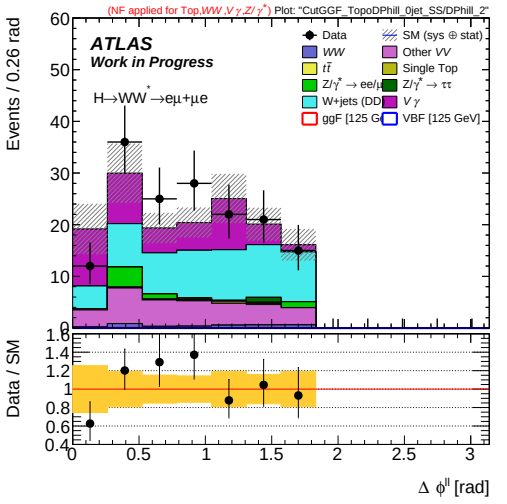

(f) $\Delta\phi_{ll}$

Figure 7.21 *Distributions of* $\Delta R(ll)$, E_T^{miss}, m_T, m_{ll}, p_T^{ll} *and* $\Delta\phi_{ll}$ *in the same-sign control region in the* $N_{jet} = 0$ *category, from which the* $V\gamma$ *background in the signal region is normalized. The hatched band in the upper plot, and the shaded band in the ratio plot, give the quadrature sum of statistical and experimental systematic rate uncertainties on the signal and backgrounds. Only the integrated systematic normalization uncertainty is used in this figure.*

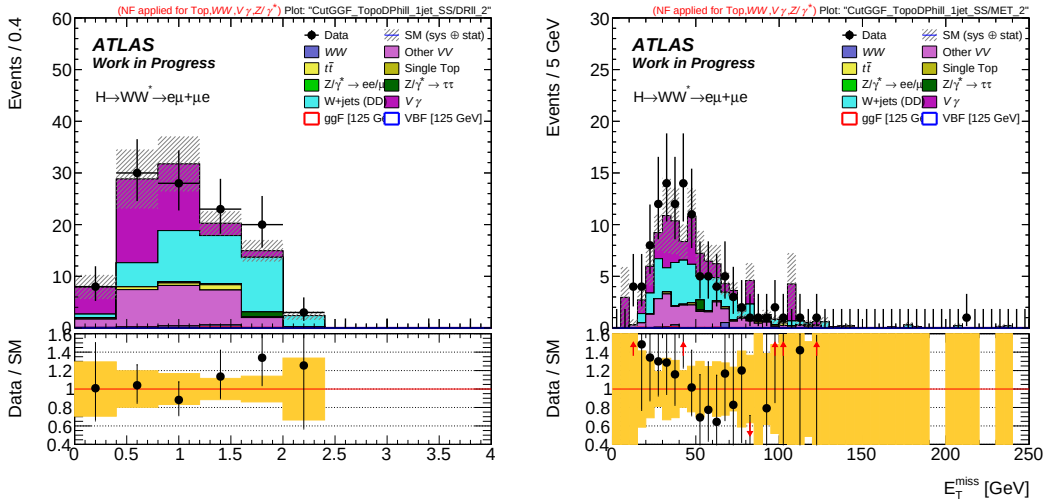

(a) $\Delta R(ll)$ *(b)* E_T^{miss}

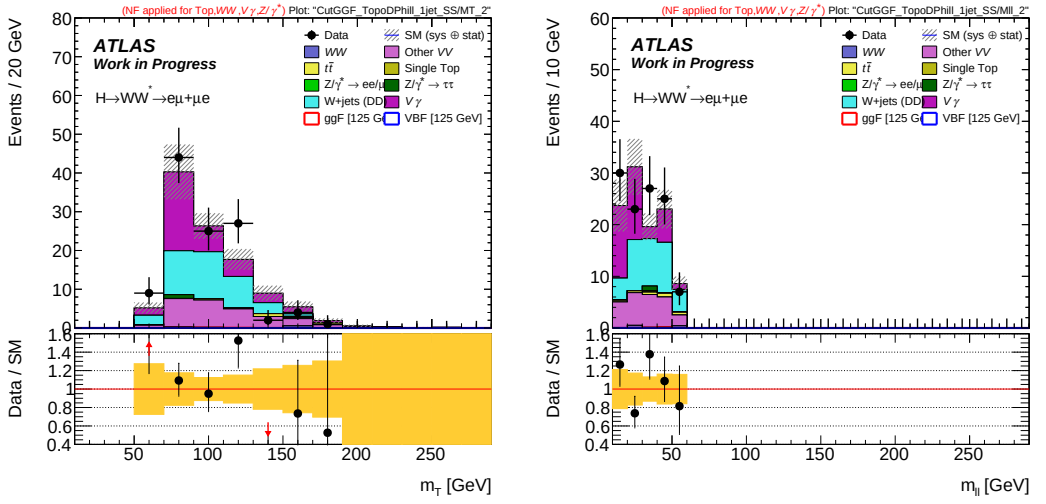

(c) m_T *(d)* m_{ll}

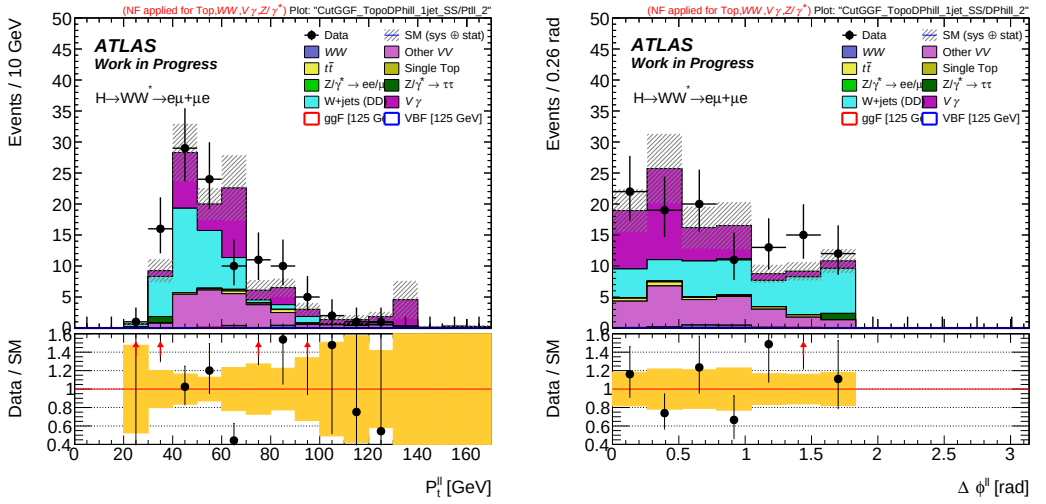

(e) $p_T ll$ *(f)* $\Delta\phi_{ll}$

Figure 7.22 *Distributions of $\Delta R(ll)$, E_T^{miss}, m_T, m_{ll}, p_T^{ll} and $\Delta\phi_{ll}$ in the same-sign control region in the $N_{jet} = 1$ category, from which the $V\gamma$ background in the signal region is normalized. The hatched band in the upper plot, and the shaded band in the ratio plot, give the quadrature sum of statistical and experimental systematic rate uncertainties on the signal and backgrounds. Only the integrated systematic normalization uncertainty is used in this figure.*

7.4 Systematic Uncertainties

7.4.1 Theoretical Uncertainties

The theoretical uncertainty estimation for both signal and background processes in the Run 2 analysis follows the one in Run 1 (see Section 5.4) but with different generators. Table 7.10 summarizes the evaluation of various inputs of theoretical uncertainties. For the signal, the uncertainties on the absolute expected yields in each signal region are needed, properly correlated to account for migrations between the signal regions. In contrast, many backgrounds are normalized using data control regions, as described in the previous sections, and do not require theoretical cross sections. The theoretical uncertainties in this case are on the extrapolation from the control to the signal regions.

For each process, the theoretical uncertainties considered are QCD scale variations, PS/UE differences and PDF model uncertainties. Other uncertainties specific to the process are considered in some cases (see Table 7.10).

WW background

The scale uncertainties are evaluated by varying the renormalization and factorization scales in POWHEG independently up and down by a factor of two. PDF uncertainties are evaluated using 68% C.L. CT10 PDF eigenvectors and the differences of the CT10 PDFs to the MSTW2008 and NNPDF3.0 PDFs, added in quadrature. For the QCD scales and PDF uncertainties, the generator weights within POWHEG are used to evaluate the uncertainties at truth level.

The PS/UE uncertainty is evaluated by comparing the extrapolation factors for the nominal POWHEG+PYTHIA8 sample using the AZNLO tune to the predictions from POWHEG interfaced to HERWIG++ using the UEEE5 tune. The NLO MC matching uncertainty is taken from the comparison of POWHEG+PYTHIA8 and SHERPA.

The electroweak correction uncertainty is evaluated by comparison of the nominal extrapolation factors to those derived after reweighting to account for kinematic effects of higher-order electroweak corrections. The uncertainty due to electroweak correction is at most 2%. For the electroweak correction uncertainty the numbers from the Run-1 analysis are reused.

The relative uncertainty on the extrapolation due to the NNLO $gg \to WW$ fraction (5.5%) of the WW background is estimated to be 0.5%.

Top-quark background

Uncertainties from the QCD renormalization, factorization scale and other addition radiation, PDF model, PS/UE, and NLO MC parton matching are all evaluated using the available top samples. Radiation variations are evaluated using POWHEG+PYTHIA6 generated with variables of shower radiation, modified factorization, renormalization

Table 7.10: Overview of the theoretical uncertainties included in the ggF analysis. The column "Reevaluated" shows if this uncertainty is being reevaluated or if the Run 1 number is being used. The column "Included in the statistical analysis" gives information if the uncertainty is already included in the statistical analysis in its final form.

Process	Uncertainty	Reevaluated	Included in the statistical analysis
ggF	jet veto uncertainty	Yes	Yes
	matching	Yes	Yes
	PS/UE	Yes	Yes
	PDF	Yes	Yes
	QCD scale	Yes	Yes
WW	generator/matching	Yes	Yes
	PS/UE	Yes	Yes
	PDF	Yes	Yes
	QCD scale	Yes	Yes
	EW correction	No	Run 1/final
	$gg \to WW$ fraction	No	Run 1/final
$WZ/W\gamma^*$	QCD and merging scales	Yes	Yes
$W\gamma$	NLO correction, QCD scale	Yes	No
top	radiation	Yes	Yes
	PS/UE	Yes	Yes
	matching	Yes	Yes
	Wt diagram removal	Yes	Yes
	single top cross-section	No	No
DY	alternative generators	Yes	Yes

scale and the NLO radiation. The PDF variations are being evaluated using LHAPDF by taking the envelope of the 68% C.L. CT10 PDF eigenvectors and a comparison of the CT10 PDFs to the MSTW2008 and NNPDF3.0 PDF sets.

The PS/UE uncertainty is evaluated by comparing POWHEG+PYTHIA6 with POWHEG+HERWIG++. The NLO matching is evaluated by comparing POWHEG+HERWIG++ with MADGRAPH5+HERWIG++. The uncertainty on the treatment of interference between $t\bar{t}$ and Wt are assessed by comparing samples with two different schemes for removing common diagrams from the MC samples.

The theoretical uncertainties on the $N_{jet} = 0$ top background estimate can be split into two components. One component is the MC correction factor $f_{MC} \equiv N_{CR,MC}/\alpha^2_{MC}$ and the other is the MC extrapolation factor α_{MC} to extrapolate from the zero jet-veto cut level to the final signal region (see Eq. 5.13). In case of the theory uncertainties for the correction factor f_{MC}, the MC samples after detector simulation were used

to properly evaluate the uncertainties with and without a b-tag applied. The theory uncertainties on the extrapolation factor α_{MC} is estimated on truth level.

Z/DY background

To model the Z/DY background, a LO multileg MADGRAPH+PYTHIA8 sample is used. Extrapolation uncertainties were estimated using a NLO POWHEG+PYTHIA8 sample and an NLO multileg SHERPA sample.

Diboson background

The diboson processes other than WW are $W\gamma$, $W\gamma^*/Z$, and ZZ, and $Z\gamma$. Since the statistic of the same-sign control region is still limited, all other diboson backgrounds are currently normalized to theory prediction. The contribution from ZZ and $Z\gamma$ is negligible, the focus here is on the theoretical uncertainties on $W\gamma^*/Z$ and $W\gamma$.

The strategy for the evaluation of the theoretical uncertainties of $W\gamma^*/Z$ differs from the strategy used in the Run 1 analysis. For the Run 2 analysis, one SHERPA sample models the $lll\nu$ final state which includes both the WZ and $W\gamma^*$ contributions. Since this SHERPA sample is already at NLO precision, the $W\gamma^*$ rate with MCFM does not need to be re-evaluated. For the SHERPA sample the following uncertainty samples are used: variations of the renormalization scale by a factor of two, variations of the factorization scale by a factor of two, variations of the resummation scale by a factor of two, and variations of the matching scale choice using 15 GeV or 30 GeV instead of 20 GeV.

Signal process

For the signal process, the total cross section and scale and PDF uncertainties are given by the LHC Higgs Cross Section Working Group [22]. Cross-section fractions in the individual jet bins are taken from the POWHEG+PYTHIA8 generator. The uncertainty on the QCD scales is evaluated by independently varying the values of the renormalization and the factorization scales in POWHEG. Both scales are independently multiplied by a factor of 2.0 or 0.5 relative to the nominal value. PDF uncertainties are evaluated using 68% C.L. CT10 PDF eigenvectors, taking the envelope of these variations, and the differences of the CT10 PDFs to the MSTW2008 and NNPDF3.0 PDFs, added in quadrature. Both QCD scale and the PDF uncertainties are evaluated using generator weights corresponding to these variations.

Another uncertainty is arising due to the underlying event and parton-shower modelling. The ggF sample is showered with PYTHIA8 using the AZNLO tune. To estimate an uncertainty on the chosen tune we evaluate 4 up-and-down variations of parameters set in that tune. In addition, the uncertainty on the parton shower modelling was also evaluated by comparing the nominal POWHEG+PYTHIA8 to

POWHEG+HERWIG7 using the UEEE5 tune.

The uncertainty on the jet multiplicity distribution is evaluated using the Stewart-Tackmann method [129]. Here, the QCD scale uncertainties on the inclusive cross sections for events with $N_{jet} \geq 0$, $N_{jet} \geq 1$ and $N_{jet} \geq 2$ are assumed to be independent. Those uncertainties are approximately 8%, 15%, and 70%, respectively. In case of the $N_{jet} \geq 0$, the inclusive NNLO+NNLL cross section is used. The cross sections for $N_{jet} \geq 1$ and $N_{jet} \geq 2$ are calculated using the MCFM program. The uncertainties on the inclusive cross sections are shared across the exclusive jet multiplicity categories. The sum in quadrature of those uncertainties are 18% and 46% for $N_{jet} \geq 0$ and $N_{jet} \geq 1$, respectively.

7.4.2 Experimental Uncertainties

Variations of the physics objects are applied in order to evaluate the systematic uncertainty on the number of expected signal and background events. The uncertainty is evaluated varying by $\pm 1\sigma$. The experimental uncertainties on the objects are given below

- *Lepton uncertainties*: $J/\psi \to ll$, $W \to l\nu$ and $Z \to ll$ decays in data and simulation are exploited to estimate the uncertainties on lepton reconstruction, identification, momentum/energy scale and resolution, and isolation criteria [125, 130]. Muon momentum resolution and scale calibrations are derived for simulation from a template fit that compares the invariant mass of $Z \to \mu\mu$ and $J/\psi \to \mu\mu$ candidates in data and MC.
- *Jet uncertainties*: JES and JER uncertainties are derived as a function of p_T and η of the jet, as well as on the pileup conditions and the jet flavour composition of the selected jet sample. They are determined using a combination of simulated and data samples, as measurements of the jet response balance in dijet, Z+jets and γ+jets events [131].
- *b-tagging uncertainties*: the uncertainties on the b- and c-tagging efficiencies and the mistag acceptance [132] are taken into account.
- E_T^{miss} *uncertainties*: the E_T^{miss} systematic uncertainties [131], relative to the soft term, for Run 2 data analysis have been estimated using different MC generators, instead of the data-driven techniques deployed in Run 1. This systematic uncertainties are estimated by propagating the uncertainties on the energy and momentum scale of each of the physics objects, as well as the uncertainties on the soft term resolution and scale.
- *Pile-up reweighting*: as the MC samples are generated with a generic spectrum of average interactions per crossing $\langle\mu\rangle$, the simulation should be corrected to match the corresponding distribution in data by applying a scale factor of 1/1.16. To estimate the uncertainty due to this reweighting, the $\langle\mu\rangle$ scale factor is varied to 1/1.09 and 1/1.23 as $\pm 1\sigma$ variation.

- *Luminosity*: the relative uncertainties on the individual luminosity values are ±2.1% and ±3.7% for 2015 and 2016, respectively, and they are combined as uncorrelated, which results in an uncertainty of ±2.0% on the total luminosity.

7.5 Results of the Run-2 Analysis

7.5.1 Summary of the Event Selection

The expected numbers of signal and background events as well as the numbers of events observed in data at several selection stages are shown in Table 7.11 for the $N_{jet} \leq 1$ categories. Figures 7.23 and 7.24 show the cut variables for the $N_{jet} = 0$ and $N_{jet} = 1$ signal region before the corresponding cuts. These figures can be compared with Figures 7.8 and 7.9 which have blinding criteria applied to the data. General agreement was found between MC predictions and data, except the low region in m_{ll} and $\Delta\phi_{ll}$.

Figure 7.25 and Figure 7.26 show the m_T and m_{ll} variable distributions in the $N_{jet} \leq 1$ signal regions. The blinding criteria is applied on both data and MC modelling in order to avoid any bias in the analysis.

7.5.2 Fit Procedure

For all signal region categories, the transverse mass m_T is used as a discriminating variable in the fit for the cross section. Table 7.12 summarizes the predicted signal and backgrounds for events after the selection in the signal regions which are used in the fit.

The signal regions are split into 8 signal region categories each to extract the results, as shown in Table 7.13, split in $e\mu$ and μe as well as in two bins each of m_{ll} and $p_T^{sublead}$. The resulting bin boundaries in m_T for all signal regions are shown in Table 7.14.

The fit procedure in general follows the description in Section 5.5. The fit is performed over signal and control regions (including $N_{jet} = 1$ top control region). The binning of the m_T distribution is chosen such that it gives a close to flat signal distribution across the full $0 < m_T < \infty$ range. That is, the expected number of signal events is approximately equal in each bin. To this end, for each signal region, histograms with 50 bins of equal size in the range $80\,\text{GeV} < m_T < 130\,\text{GeV}$ are constructed. Neighboring bins, including two additional bins with $m_T < 80\,\text{GeV}$ and $m_T > 130\,\text{GeV}$, are then combined using a using a heuristic tree-search algorithm until there are eight bins left in each signal region. Figure 7.27 shows the remapped m_T distributions all signal regions.

Table 7.11: The expected numbers of signal and background events as well as the numbers of events observed in data at several selection stages of the $N_{jet} \leq 1$ $e\mu + \mu e$ signal and control regions. Uncertainties are statistical only.

	ggF [125 GeV]	VBF [125 GeV]	WW	Other VV	$t\bar{t}$	Single Top	$Z/\gamma^* \to ee/\mu\mu$	$Z/\gamma^* \to \tau\tau$	W+jets (DD)	$V\gamma$	Total Bkg	Data/bkg	Data
Channel Selection	430.01 ± 3.26	41.67 ± 0.40	7238.33 ± 43.09	3411.60 ± 25.98	66798.76 ± 80.76	6071.83 ± 22.71	6906.39 ± 279.86	22232.77 ± 311.22	325837.66 ± 940.65	2434.23 ± 43.18	440931.57 ± 1035.10	0.51 ± 0.00	224962
GRL Selection	430.01 ± 3.26	41.67 ± 0.40	7238.33 ± 43.09	3411.60 ± 25.98	66798.76 ± 80.76	6071.83 ± 22.71	6906.39 ± 279.86	22232.77 ± 311.22	318190.66 ± 936.57	2434.23 ± 43.18	432284.57 ± 1031.40	0.51 ± 0.00	221166
Jet Cleaning	429.34 ± 3.26	41.49 ± 0.40	7225.96 ± 43.05	3406.20 ± 25.97	66668.20 ± 80.68	6059.79 ± 22.69	6891.10 ± 279.79	22200.79 ± 311.08	316844.07 ± 935.55	2427.62 ± 43.09	431723.73 ± 1030.39	0.51 ± 0.00	220415
Overlap, Vgamma/Vjets	429.34 ± 3.26	41.49 ± 0.40	7225.96 ± 43.05	3406.20 ± 25.97	66668.20 ± 80.68	6059.79 ± 22.69	4788.01 ± 208.93	21980.37 ± 309.14	327541.64 ± 851.89	2427.62 ± 43.09	440097.79 ± 936.13	0.50 ± 0.00	220415
Trigger Selection	400.83 ± 3.19	39.40 ± 0.39	7029.94 ± 42.75	3181.09 ± 25.53	64463.22 ± 79.82	5891.00 ± 22.48	4486.59 ± 204.65	19844.71 ± 298.73	158489.18 ± 728.11	2071.52 ± 39.61	265457.24 ± 819.87	0.62 ± 0.00	165613
Trigger Matching	390.11 ± 3.16	38.71 ± 0.39	6961.63 ± 42.62	3041.32 ± 25.11	63774.74 ± 79.47	5841.39 ± 22.41	3950.76 ± 188.06	18723.68 ± 291.60	147252.26 ± 699.49	1969.04 ± 38.08	251454.82 ± 787.66	0.63 ± 0.00	159250
Only two Leptons	389.90 ± 3.15	38.63 ± 0.39	6958.16 ± 42.61	1679.69 ± 16.67	62809.31 ± 78.86	5779.58 ± 22.29	2216.47 ± 151.15	18714.16 ± 291.57	147739.18 ± 671.23	1594.50 ± 36.97	247491.05 ± 754.04	0.63 ± 0.00	154893
$p_{\mathrm{T}}^{lead} > 25/22$ GeV ($e\mu/\mu e$)	388.04 ± 3.14	38.55 ± 0.39	6946.18 ± 42.56	1673.83 ± 16.64	62746.13 ± 78.81	5774.89 ± 22.27	2208.69 ± 150.99	18540.37 ± 289.55	145906.61 ± 667.80	1585.01 ± 36.74	245381.68 ± 750.16	0.63 ± 0.00	154010
$p_{\mathrm{T}}^{sublead} > 15$	388.04 ± 3.14	38.55 ± 0.39	6946.18 ± 42.56	1673.83 ± 16.64	62746.13 ± 78.81	5774.89 ± 22.27	2208.69 ± 150.99	18540.37 ± 289.55	145906.61 ± 667.80	1585.01 ± 36.74	245381.68 ± 750.16	0.63 ± 0.00	154010
OS Leptons	385.77 ± 3.13	38.28 ± 0.39	6873.98 ± 42.33	869.78 ± 12.52	61675.80 ± 78.13	5697.19 ± 22.13	1254.83 ± 109.21	18312.00 ± 288.19	99786.27 ± 602.75	932.11 ± 29.16	195401.96 ± 683.87	0.69 ± 0.00	134189
$M_{\ell\ell} > 12/10$ GeV	371.99 ± 3.08	36.51 ± 0.38	6833.28 ± 42.20	812.70 ± 12.12	61286.92 ± 77.87	5665.34 ± 22.06	1238.89 ± 109.01	18270.45 ± 288.10	80847.16 ± 584.79	842.33 ± 27.08	175797.07 ± 667.90	0.72 ± 0.00	127270
Leptons ID, W+jets 1 anti-ID,1 ID	319.25 ± 2.87	31.61 ± 0.35	6096.99 ± 40.06	556.85 ± 10.32	53044.61 ± 72.66	5012.90 ± 20.82	484.50 ± 70.21	15435.07 ± 265.53	27646.05 ± 311.23	594.60 ± 23.08	108871.56 ± 424.57	0.78 ± 0.00	85093
W+jets 0-jet CR	319.25 ± 2.87	31.61 ± 0.35	6096.99 ± 40.06	556.85 ± 10.32	53044.61 ± 72.66	5012.90 ± 20.82	484.50 ± 70.21	15435.07 ± 265.53	11235.18 ± 234.47	594.60 ± 23.08	92460.70 ± 371.98	0.92 ± 0.00	85093
W+jets 1-jet CR	319.25 ± 2.87	31.61 ± 0.35	6096.99 ± 40.06	556.85 ± 10.32	53044.61 ± 72.66	5012.90 ± 20.82	484.50 ± 70.21	15435.07 ± 265.53	5847.91 ± 121.63	594.60 ± 23.08	87073.43 ± 313.35	0.98 ± 0.00	85093
Triggered by muon only	92.43 ± 1.48	7.35 ± 0.16	953.35 ± 14.58	146.54 ± 4.76	7698.82 ± 25.67	665.48 ± 6.92	221.13 ± 42.58	5472.29 ± 156.00	17006.46 ± 237.26	263.10 ± 15.23	32427.17 ± 289.17	0.57 ± 0.01	18466
Triggered by electron only	107.36 ± 1.62	9.33 ± 0.19	1450.39 ± 19.16	154.69 ± 4.53	13077.02 ± 35.44	1220.89 ± 10.05	109.01 ± 22.69	5020.90 ± 145.18	8665.06 ± 149.64	135.76 ± 11.76	29833.72 ± 214.17	0.84 ± 0.01	25147
Triggered by both	119.46 ± 1.85	14.94 ± 0.25	3693.25 ± 32.01	255.61 ± 7.96	32268.77 ± 58.01	3126.54 ± 16.86	154.36 ± 51.00	4941.88 ± 158.41	1974.53 ± 134.84	195.74 ± 12.74	46610.68 ± 225.34	0.89 ± 0.01	41480
Apply fake factor	319.25 ± 2.87	31.61 ± 0.35	6096.99 ± 40.06	556.85 ± 10.32	53044.61 ± 72.66	5012.90 ± 20.82	484.50 ± 70.21	15435.07 ± 265.53	5403.23 ± 64.77	594.60 ± 23.08	86628.74 ± 295.95	0.98 ± 0.00	85093
Z validation region	319.25 ± 2.87	31.61 ± 0.35	6096.99 ± 40.06	556.85 ± 10.32	53044.61 ± 72.66	5012.90 ± 20.82	484.50 ± 70.21	15435.07 ± 265.53	5403.23 ± 64.77	594.60 ± 23.08	86628.74 ± 295.95	0.98 ± 0.00	85093
SF: $E_{\mathrm{T}}^{\mathrm{miss}} > 45$ GeV, DF: $p_{\mathrm{T}}^{\mathrm{miss}} > 20$ GeV	298.80 ± 2.78	29.89 ± 0.34	5148.03 ± 36.71	448.29 ± 9.41	49329.47 ± 70.06	4682.91 ± 20.12	252.78 ± 36.91	4005.25 ± 108.99	3427.64 ± 43.48	372.78 ± 18.43	67667.14 ± 149.06	1.00 ± 0.00	67493
Scale factors			NF = 1.10 ± 0.06		NF = 0.91 ± 0.03	NF = 0.91 ± 0.03	NF = 0.96 ± 0.03	NF = 0.96 ± 0.03		NF = 1.32 ± 0.26			
0-jet	126.27 ± 1.82	1.35 ± 0.07	2937.67 ± 29.32	146.64 ± 4.14	552.06 ± 7.18	254.85 ± 4.50	131.09 ± 27.94	1306.23 ± 79.10	1006.45 ± 23.42	168.49 ± 14.45	6503.50 ± 93.50	1.01 ± 0.02	6539
Scale factors			NF = 1.10 ± 0.06		NF = 0.91 ± 0.03	NF = 0.91 ± 0.03	NF = 0.96 ± 0.03	NF = 0.96 ± 0.03		NF = 1.32 ± 0.26			
$\Delta\Phi_{\ell\ell,\mathrm{MET}} > 1.57$	125.51 ± 1.81	1.32 ± 0.07	2918.26 ± 29.25	137.76 ± 3.96	534.87 ± 7.07	251.20 ± 4.47	124.68 ± 27.60	1217.41 ± 77.09	942.63 ± 22.90	162.87 ± 14.37	6289.67 ± 91.52	1.01 ± 0.02	6367
Scale factors			NF = 1.10 ± 0.06		NF = 0.91 ± 0.03	NF = 0.91 ± 0.03	NF = 0.96 ± 0.03	NF = 0.96 ± 0.03		NF = 1.32 ± 0.26			
$p_{\mathrm{T}}^{\ell\ell} > 30$ GeV	111.85 ± 1.71	1.21 ± 0.07	2351.62 ± 26.17	107.20 ± 3.43	491.00 ± 6.80	227.99 ± 4.26	50.50 ± 17.59	203.09 ± 34.26	638.38 ± 15.22	100.47 ± 11.20	4170.25 ± 51.00	1.01 ± 0.02	4222
Scale factors			NF = 1.10 ± 0.06		NF = 0.91 ± 0.03	NF = 0.91 ± 0.03	NF = 0.96 ± 0.03	NF = 0.96 ± 0.03		NF = 1.32 ± 0.26			
$M_{\ell\ell} < 55$ GeV	95.87 ± 1.58	1.03 ± 0.06	583.93 ± 12.59	36.93 ± 2.03	79.03 ± 2.77	39.39 ± 1.73	23.29 ± 13.72	19.05 ± 10.49	175.81 ± 9.12	53.26 ± 8.75	1010.69 ± 25.13	1.09 ± 0.04	1100
Scale factors			NF = 1.10 ± 0.06		NF = 0.91 ± 0.03	NF = 0.91 ± 0.03	NF = 0.96 ± 0.03	NF = 0.96 ± 0.03		NF = 1.32 ± 0.26			
$\Delta\Phi_{\ell\ell} < 1.8$	88.60 ± 1.53	0.95 ± 0.06	522.86 ± 11.77	34.00 ± 1.97	76.12 ± 2.73	38.44 ± 1.71	3.49 ± 3.49	0.92 ± 0.51	139.18 ± 7.68	46.43 ± 8.21	861.45 ± 17.07	1.13 ± 0.04	975
Scale factors			NF = 1.10 ± 0.06		NF = 0.91 ± 0.03	NF = 0.91 ± 0.03	NF = 0.96 ± 0.03	NF = 0.96 ± 0.03		NF = 1.32 ± 0.26			
WW CR 0-jet	13.82 ± 0.59	0.16 ± 0.02	846.05 ± 15.69	35.05 ± 1.96	148.02 ± 3.70	76.99 ± 2.50	18.24 ± 10.25	70.67 ± 20.37	176.04 ± 7.78	17.37 ± 3.96	1388.42 ± 29.43	1.00 ± 0.03	1389
Scale factors			NF = 1.10 ± 0.06		NF = 0.91 ± 0.03	NF = 0.91 ± 0.03	NF = 0.96 ± 0.03	NF = 0.96 ± 0.03		NF = 1.32 ± 0.26			
Ztt CR 0-jet	6.97 ± 0.41	0.08 ± 0.02	168.40 ± 7.09	36.79 ± 2.42	9.88 ± 0.95	6.65 ± 0.77	92.06 ± 19.19	7446.09 ± 199.03	953.15 ± 37.70	137.83 ± 12.15	8850.86 ± 203.98	1.00 ± 0.03	8859
Scale factors					NF = 1.01 ± 0.01	NF = 1.01 ± 0.01							
Top0 CR any-jet	270.22 ± 2.63	28.38 ± 0.34	3881.87 ± 31.69	344.76 ± 8.64	40960.78 ± 64.06	3915.99 ± 18.49	120.66 ± 23.07	1847.06 ± 55.21	2330.08 ± 34.53	262.34 ± 15.43	53603.54 ± 102.64	1.00 ± 0.00	53590
Scale factors			NF = 1.10 ± 0.06		NF = 0.91 ± 0.03	NF = 0.91 ± 0.03	NF = 0.96 ± 0.03	NF = 0.96 ± 0.03		NF = 1.32 ± 0.26			
$\Delta\Phi_{\ell\ell} < 1.8$	0.17 ± 0.05	0.00 ± 0.00	3.54 ± 0.99	31.69 ± 1.73	1.10 ± 0.35	0.60 ± 0.25	6.34 ± 4.15	1.10 ± 0.97	59.59 ± 6.25	46.18 ± 7.42	150.14 ± 10.79	1.06 ± 0.11	159
Scale factors			NF = 0.88 ± 0.07				NF = 0.78 ± 0.07	NF = 0.78 ± 0.07		NF = 1.37 ± 0.21			
1-jet	107.06 ± 1.67	9.17 ± 0.19	1426.19 ± 18.07	150.50 ± 4.85	6346.09 ± 25.41	1686.41 ± 12.16	44.78 ± 14.50	1135.65 ± 45.86	892.60 ± 21.80	186.24 ± 14.89	11868.46 ± 64.45	0.98 ± 0.01	11606
Scale factors			NF = 0.88 ± 0.07		NF = 1.03 ± 0.03	NF = 1.03 ± 0.03	NF = 0.78 ± 0.07	NF = 0.78 ± 0.07		NF = 1.37 ± 0.21			
b-jet veto	99.67 ± 1.60	8.55 ± 0.19	1332.18 ± 17.39	141.29 ± 4.70	1293.67 ± 11.18	410.70 ± 5.83	38.00 ± 14.32	1001.35 ± 42.98	721.39 ± 18.70	174.65 ± 14.49	5113.22 ± 55.64	1.00 ± 0.02	5113
Scale factors			NF = 0.88 ± 0.07		NF = 1.03 ± 0.03	NF = 1.03 ± 0.03	NF = 0.78 ± 0.07	NF = 0.78 ± 0.07		NF = 1.37 ± 0.21			
$Z \to \tau\tau$ veto	78.15 ± 1.42	5.94 ± 0.15	898.64 ± 14.19	80.41 ± 3.70	858.07 ± 9.02	277.16 ± 4.77	7.49 ± 3.60	145.83 ± 19.22	287.80 ± 10.79	77.56 ± 9.07	2632.96 ± 30.00	1.03 ± 0.02	2710
Scale factors			NF = 0.88 ± 0.07		NF = 1.03 ± 0.03	NF = 1.03 ± 0.03	NF = 0.78 ± 0.07	NF = 0.78 ± 0.07		NF = 1.37 ± 0.21			
$M_{\ell\ell} < 55$ GeV	66.80 ± 1.31	5.21 ± 0.15	232.15 ± 7.12	32.19 ± 2.36	199.61 ± 4.31	69.72 ± 2.40	0.73 ± 0.66	73.55 ± 15.96	103.81 ± 7.07	41.31 ± 6.94	753.08 ± 20.83	1.04 ± 0.05	780
Scale factors			NF = 0.88 ± 0.07		NF = 1.03 ± 0.03	NF = 1.03 ± 0.03	NF = 0.78 ± 0.07	NF = 0.78 ± 0.07		NF = 1.37 ± 0.21			
$\Delta\Phi_{\ell\ell} < 1.8$	61.36 ± 1.25	4.91 ± 0.14	214.29 ± 6.89	28.91 ± 2.28	184.98 ± 4.14	66.90 ± 2.36	0.73 ± 0.66	12.69 ± 4.01	77.76 ± 6.22	37.66 ± 6.65	623.93 ± 13.22	1.08 ± 0.05	671
Scale factors			NF = 0.88 ± 0.07		NF = 1.03 ± 0.03	NF = 1.03 ± 0.03	NF = 0.78 ± 0.07	NF = 0.78 ± 0.07		NF = 1.37 ± 0.21			
WW CR 1-jet	0.39 ± 0.10	0.03 ± 0.01	683.90 ± 12.63	47.73 ± 2.49	718.65 ± 8.36	213.84 ± 4.17	6.94 ± 3.58	23.45 ± 5.60	170.47 ± 7.71	29.18 ± 4.98	1894.16 ± 19.53	1.01 ± 0.03	1905
Scale factors			NF = 0.88 ± 0.07		NF = 1.03 ± 0.03	NF = 1.03 ± 0.03	NF = 0.78 ± 0.07	NF = 0.78 ± 0.07		NF = 1.37 ± 0.21			
Ztt CR 1-jet	5.72 ± 0.39	0.64 ± 0.05	54.03 ± 3.48	9.03 ± 1.11	42.47 ± 2.01	12.12 ± 1.04	9.95 ± 5.87	496.32 ± 32.40	101.26 ± 8.56	26.19 ± 6.33	751.38 ± 34.87	1.01 ± 0.06	756
Scale factors			NF = 0.88 ± 0.07				NF = 0.78 ± 0.07	NF = 0.78 ± 0.07		NF = 1.37 ± 0.21			
Top1 CR 1-jet (runlike)	4.58 ± 0.39	0.33 ± 0.04	46.83 ± 3.39	3.30 ± 0.59	2993.53 ± 17.63	781.62 ± 8.42	0	18.63 ± 6.00	85.67 ± 8.04	3.99 ± 2.03	3933.59 ± 22.32	0.96 ± 0.02	3792
Scale factors			NF = 0.88 ± 0.07		NF = 1.03 ± 0.03	NF = 1.03 ± 0.03	NF = 0.78 ± 0.07	NF = 0.78 ± 0.07		NF = 1.37 ± 0.21			
$\Delta\Phi_{\ell\ell} < 1.8$	0.22 ± 0.07	0.03 ± 0.01	1.32 ± 0.53	25.56 ± 1.69	2.36 ± 0.46	0.40 ± 0.19	0	0.98 ± 0.98	37.48 ± 4.40	37.98 ± 7.29	106.08 ± 8.77	1.06 ± 0.13	112

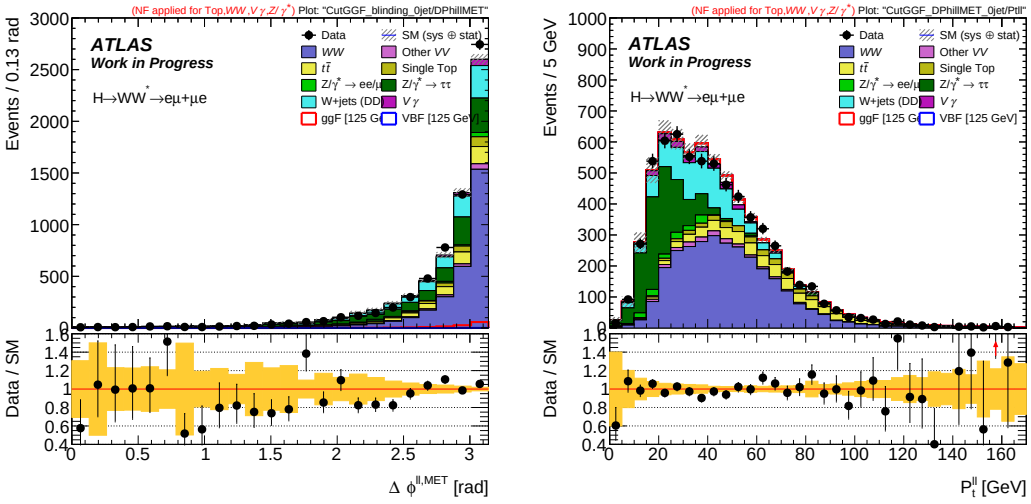

(a) $\Delta\phi_{ll,MET}$ *after the cut* $N_{jet} = 0$ *(b)* p_T^{ll} *after the cut* $\Delta\phi_{ll,MET} > 1.57$

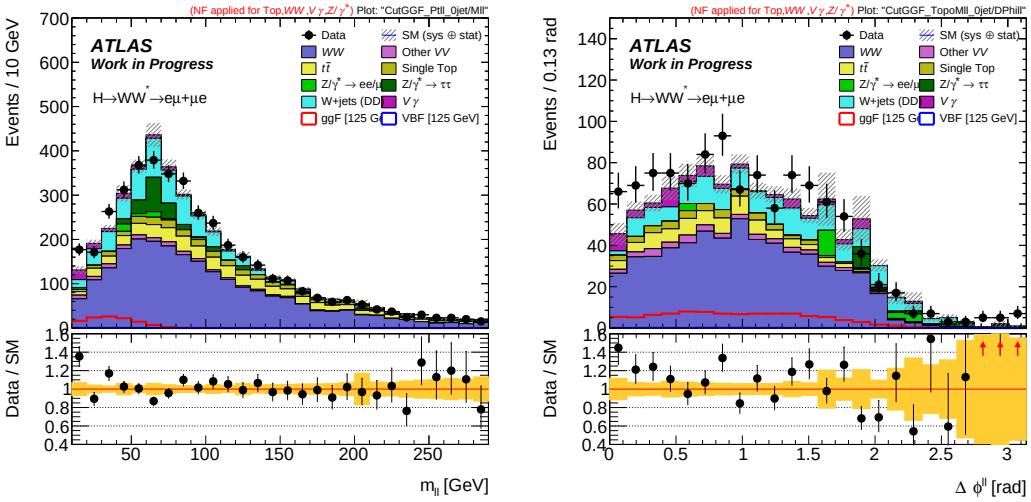

(c) m_{ll} *after the cut* $p_T^{ll} > 30$ *GeV* *(d)* $\Delta\phi_{ll}$ *after the cut* $m_{ll} < 55$ *GeV*

Figure 7.23 *Distributions of the cut variables* $\Delta\phi_{ll,MET}$, p_T^{ll}, m_{ll}, *and* $\Delta\phi_{ll}$ *before the corresponding cut is applied in the* $N_{jet} = 0$ *signal region. The uncertainty band is the quadratic sum of the statistical uncertainty and the experimental systematic rate uncertainties.*

Table 7.12: Summary of predicted signal and background yields for 13 TeV data for events in the signal region. The observed (N_{obs}) and the expected (N_{exp}) yields for the signal (N_{sig}) and background (N_{bkg}) processes are given in the signal region noted in Section 7.3.3. The N_{sig} sums the ggF and VBF contributions. The composition of N_{bkg} is given in the right part of the table.

N_{jet}	N_{obs}	N_{bkg}	N_{ggF}	N_{VBF}	N_{WW}	N_{VV}	$N_{t\bar{t}}$	N_t	N_{Z/γ^*}	$N_{W+\text{jets}}$
$= 0$	975	861 ± 17	89 ± 2	1 ± 0	523 ± 12	80 ± 9	76 ± 3	38 ± 2	4 ± 4	139 ± 8
$= 1$	671	624 ± 13	61 ± 1	5 ± 0	214 ± 7	67 ± 8	185 ± 4	67 ± 2	13 ± 4	78 ± 6

The full likelihood can be written as

$$\mathcal{L}(\mu, \vec{\theta}) = \{ \prod_{i=e\mu,\mu e} \prod_{j=0}^{N_{p_T\text{bins}}} \prod_{k=0}^{N_{m_{ll}\text{bins}}} \prod_{l=0}^{N_{\text{jets}}} \prod_{m=1}^{N_{\text{bins}}} P(N_{ijklm} | \mu s_{ijklm} + \sum_{n}^{N_{bg}} b_{ijklmn}) \} \times \{ \prod_{i=1}^{N_\theta} N(\tilde{\theta}|\theta) \} \quad (7.3)$$

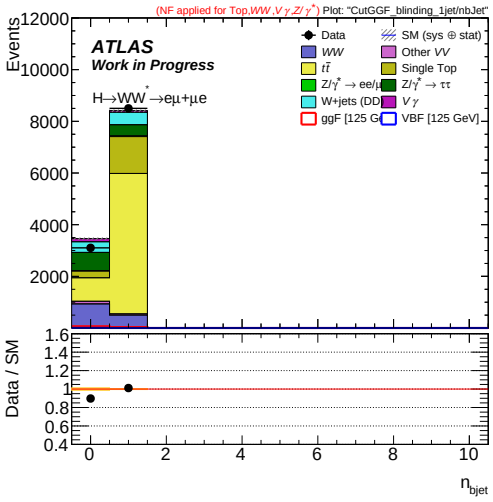

(a) N_{b-jets} *after the cut* $N_{jet} = 1$

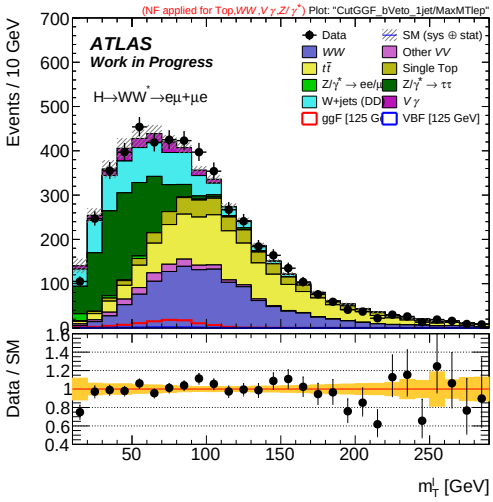

(b) $max(m_T^l)$ *after the b-jet veto*

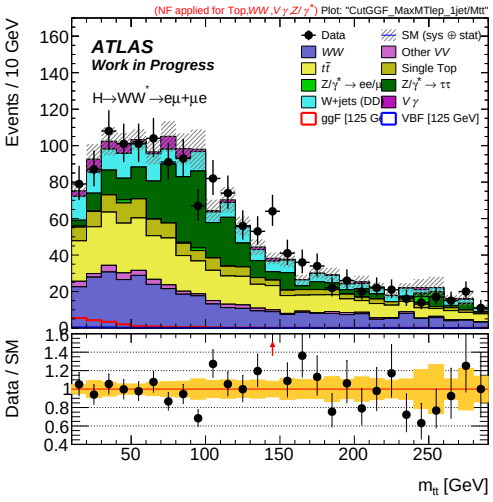

(c) $m_{\tau\tau}$ *after cut* $max(m_T^l) > 50$ *GeV*

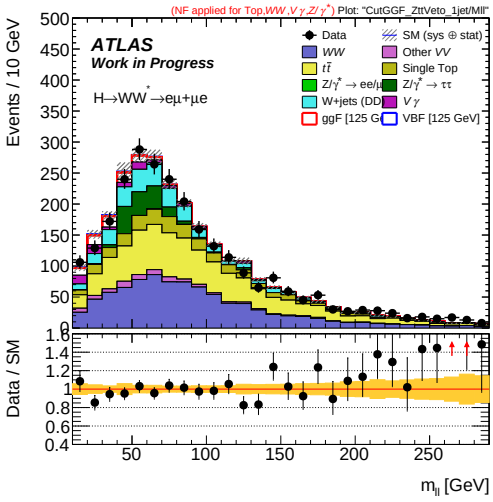

(d) m_{ll} *after the cut* $m_{\tau\tau} < m_Z - 25$ *GeV*

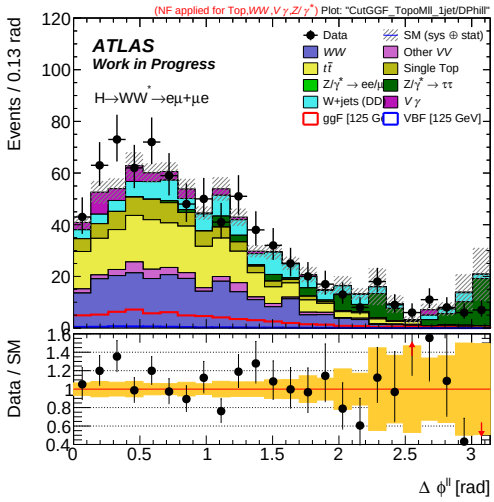

(e) $\Delta\phi_{ll}$ *after the cut* $m_{ll} < 55$ *GeV*

Figure 7.24 *Distributions of the cut variables* N_{b-jets}, $max(m_T^l)$, $m_{\tau\tau}$, m_{ll}, *and* $\Delta\phi_{ll}$ *before the corresponding cut is applied in the* $N_{jet} = 1$ *signal region. The uncertainty band is the quadratic sum of the statistical uncertainty and the experimental systematic rate uncertainties.*

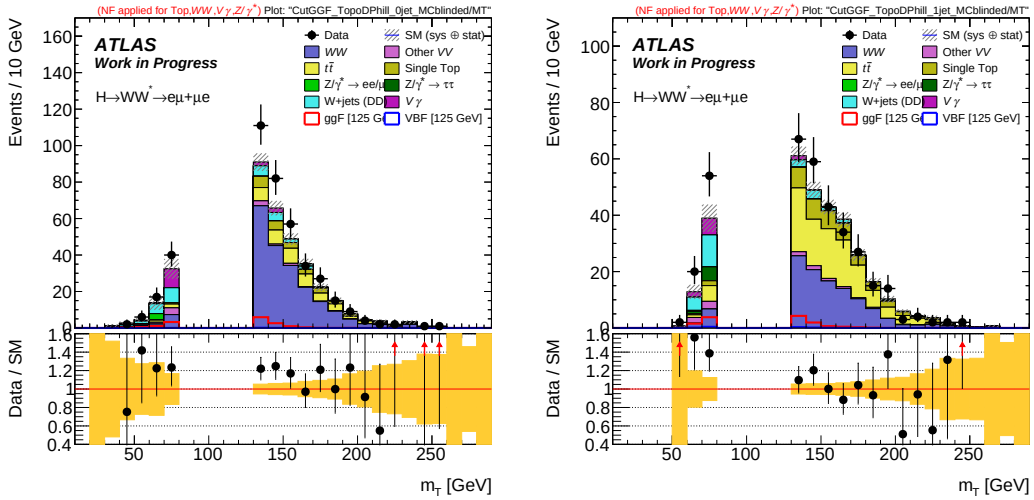

Figure 7.25 *Distributions of the m_T in the $N_{jet} = 0$ (left) and $N_{jet} = 1$ (right) signal regions for $e\mu + \mu e$. The blinding criteria has been applied on both data and MC modelling. The hatched band in the upper plot, and the shaded band in the ratio plot, give the quadratic sum of the statistical uncertainty and the experimental rate systematic uncertainties on the MC.*

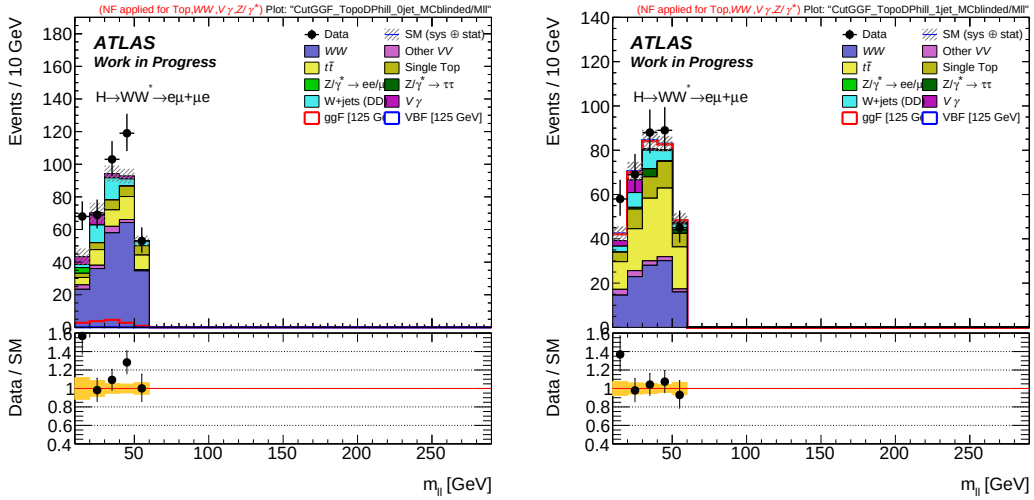

Figure 7.26 *Distributions of the m_{ll} in the $N_{jet} = 0$ (left) and $N_{jet} = 1$ (right) signal regions for $e\mu + \mu e$. The blinding criteria has been applied on both data and MC modelling. The hatched band in the upper plot, and the shaded band in the ratio plot, give the quadratic sum of the statistical uncertainty and the experimental rate systematic uncertainties on the MC.*

Table 7.13: Signal region categories of the ggF analysis. There are eight categories per signal region ($N_{jet} = 0$ and $N_{jet} = 1$).

N_{jet}	$\otimes m_{ll}$	$\otimes p_T^{sublead}$	$\otimes l^{sublead}$
$N_{jet} = 0$	$\otimes[10, 30, 55]$	$\otimes[15, 20, \infty]$	$\otimes[e, \mu]$
$N_{jet} = 1$	$\otimes[10, 30, 55]$	$\otimes[15, 20, \infty]$	$\otimes[e, \mu]$

Table 7.14: m_T bin boundaries of histograms used in the $N_{jet} = 0$ and $N_{jet} = 1$ signal regions in GeV. The convention for the region names is as follows: SR_0j_DF are $N_{jet} = 0$ signal regions with different lepton flavor, SR_1j_DF are the same, but for the $N_{jet} = 1$ signal regions. $Mll1$ denotes the regions with $10 < m_{ll} < 30\,\text{GeV}$, while $Mll2$ denotes the regions with $30 < m_{ll} < 55\,\text{GeV}$. $PtSubLead2$ denotes the regions where the sub-leading lepton has $15 < p_T^{sublead} < 20\,\text{GeV}$, whereas $PtSubLead3$ denotes the regions with $p_T^{sublead} > 20\,\text{GeV}$. The final suffix e denotes that the subleading lepton is an electron while the suffix m corresponds to a muon.

Region	Bin Boundaries								
SR_0j_DF_Mll1_PtSubLead2_e	0	80	89	95	101	107	113	120	inf
SR_0j_DF_Mll1_PtSubLead2_m	0	84	92	98	103	109	115	124	inf
SR_0j_DF_Mll2_PtSubLead2_e	0	85	94	99	104	109	115	124	inf
SR_0j_DF_Mll2_PtSubLead2_m	0	86	94	101	106	112	119	127	inf
SR_0j_DF_Mll1_PtSubLead3_e	0	91	100	106	112	118	124	130	inf
SR_0j_DF_Mll1_PtSubLead3_m	0	94	102	108	113	118	124	130	inf
SR_0j_DF_Mll2_PtSubLead3_e	0	93	102	108	113	118	124	130	inf
SR_0j_DF_Mll2_PtSubLead3_m	0	93	101	107	112	117	123	130	inf
SR_1j_DF_Mll1_PtSubLead2_e	0	80	90	98	106	112	120	129	inf
SR_1j_DF_Mll1_PtSubLead2_m	0	80	89	97	104	110	118	128	inf
SR_1j_DF_Mll2_PtSubLead2_e	0	83	92	98	104	111	117	126	inf
SR_1j_DF_Mll2_PtSubLead2_m	0	84	91	99	106	112	118	127	inf
SR_1j_DF_Mll1_PtSubLead3_e	0	81	91	100	107	114	121	130	inf
SR_1j_DF_Mll1_PtSubLead3_m	0	82	91	98	104	111	118	129	inf
SR_1j_DF_Mll2_PtSubLead3_e	0	87	96	103	109	116	123	130	inf
SR_1j_DF_Mll2_PtSubLead3_m	0	86	95	102	109	115	122	130	inf

where the product over m_{ll} and subleading lepton p_T is written out explicitly to emphasize the 3D fit used.

The control regions are included in the fit as a single-bin histogram. These control regions are used to estimate the NFs for which are applied in the signal region.

Several sources of systematic uncertainties which are considered to affect the normalization of signal and background and/or the shape of their corresponding final discriminant distributions are included. Individual sources of systematics uncertainty are considered uncorrelated. Correlation of a given systematic uncertainty are maintained across processes and channels. It is important to note that both normalization and shape systematics are defined on the individual background sources. Therefore, because the individual backgrounds are not equally distributed across the m_T spectrum, the shape of the total background will still vary for each systematic source.

Systematic variations changing the normalization of a sample in the signal regions are determined from $qq \to WW$ MC samples which provide the highest number of unweighted Monte Carlo events in the $N_{jet} = 0$ and $N_{jet} = 1$ signal regions. The relative changes of the normalization of each signal region are also applied to the remaining background processes as the respective systematic variation. Exempt from this treatment are the W+jet background in the $N_{jet} = 0$ and $N_{jet} = 1$ categories as well as the

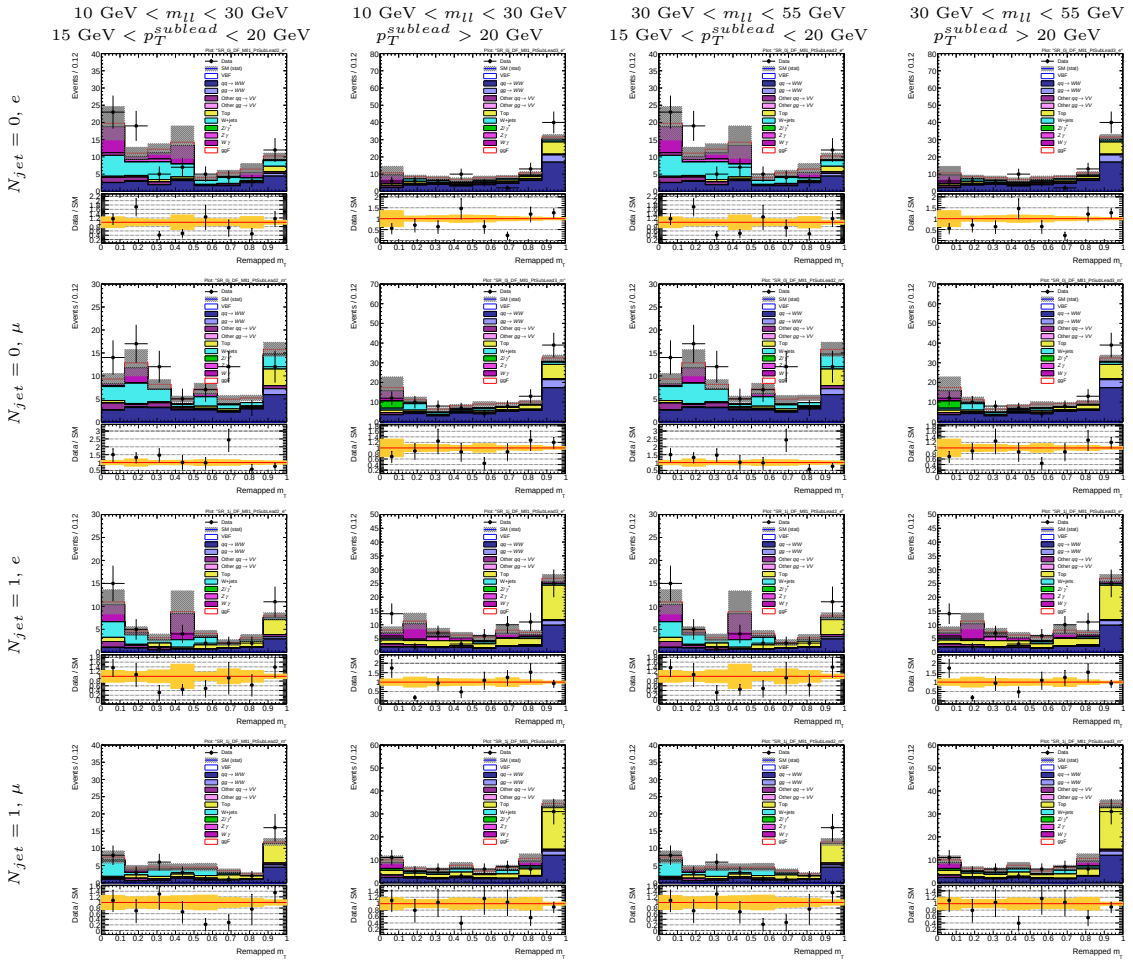

Figure 7.27 *Pre-fit distributions of the remapped m_T in each m_{ll} and subleading lepton p_T bin in the $N_{jet}=0$ and $N_{jet}=1$ signal regions. e and μ denote the subleading electron and muon channels, respectively.*

top-quark backgrounds in the $N_{jet}=1$ category. This is due to these processes being either estimated through a data-driven method (W+jets) or providing a sufficiently large number of raw Monte Carlo events ($N_{jet}=1$ top-quark). The latter one is not used to determine the systematic variations for other samples in the $N_{jet}=1$ category since the remaining backgrounds are topologically more similar to $(qq\rightarrow)WW$ events.

The effect on the normalization due to any experimental systematic uncertainty is pruned in any region if its effect on the normalization of the respective sample in the respective region is below 0.5%.

7.5.3 Performance of the Fit

Expected performance of the fit has been studied using the so-called Asimov dataset approach; this procedure replaces the ensemble testing performed with MC pseudo-experiments with a single "representative" dataset which returns the true value for each estimated parameter. The Asimov dataset allows to study the constraints on the nuisance parameters that could be obtained with the expected data distributions and

statistical uncertainties. Any difference in constraints of a given nuisance parameter between the result of the Asimov dataset fit and the data helps to diagnose unexpected over-constraints from data in the fit.

Figure 7.28 shows the post-fit values and uncertainties of fit parameters based on a fit to the Asimov and observed datasets. All expected NPs corresponding to systematic uncertainties are centered on zero and the normalization scale factors are all centered around 1. For observed NPs, there is some pulls in the theoretical top, fake and JES systematic uncertainties. Correlations between NPs which have a correlation of more than 20% with at least one other NP in the fit are shown in Figure 7.29 and 7.30 for Asimov and observed datasets, respectively. From these figures, there are some (anti)correlations between the theoretical generators and the NFs of Z+jets and top backgrounds. There is an anticorrelation between the NFs of top and $N_{jet} = 1$ WW backgrounds, which are expected because the top background has large contribution in the $N_{jet} = 1$ WW CR. In addition, the $N_{jet} = 1$ WW NF is also anticorrelated with b-tagging with the same reason.

The impact of each uncertainty on the μ result is shown in Figure 7.31. The leading source of systematics uncertainties are the uncertainty on normalization of $N_{jet} = 0$ WW background, QCD scale of signal sample and fake factor sample composition. This can be understood since most of the contribution of the signal is in the $N_{jet} = 0$ category and WW is the dominating background here. Therefore, if the $N_{jet} = 0$ WW background shifts due to systematic, there is not much else from other backgrounds that can compensate this. While in the $N_{jet} = 1$ category, WW and top backgrounds can counter balance each other. The fake factor uncertainties are also large since there is a lot of W+jets background in the SRs with similar shape to the signal, therefore a large impact on μ from fake factor is expected.

Table 7.15 shows the post-fit yields for all of the fitted categories. Table 7.16 shows the post-fit NFs and comparison with the ones obtained from cut-based CRs. There are differences between post-fit and cut-based CR extracted NFs because the fit has more freedom with systematic NPs and can thus compensate NFs shifts with those while the cut-based CRs do not. The post-fit remapped m_T distributions are shown in Figure 7.32. The final post-fit m_T distributions in $N_{jet} = 0$ (left) and $N_{jet} = 1$ (right) signal regions are shown in Figure 7.33.

Table 7.15: Summary of post-fit signal and background yields for 13 TeV data for events in the signal region. The observed (N_{obs}) and the expected (N_{exp}) yields for the signal (N_{sig}) and background (N_{bkg}) processes are given in the signal region noted in Section 7.3.3. The N_{sig} sums the ggF and VBF contributions. The composition of N_{bkg} is given in the right part of the table.

N_{jet}	N_{obs}	N_{bkg}	N_{ggF}	N_{VBF}	N_{WW}	N_{VV}	$N_{t\bar{t}}$	N_t	N_{Z/γ^*}	$N_{W+\text{jets}}$
$= 0$	975	924	33	1	580	73	76	38	10	146
$= 1$	671	653	22	5	265	55	170	62	18	84

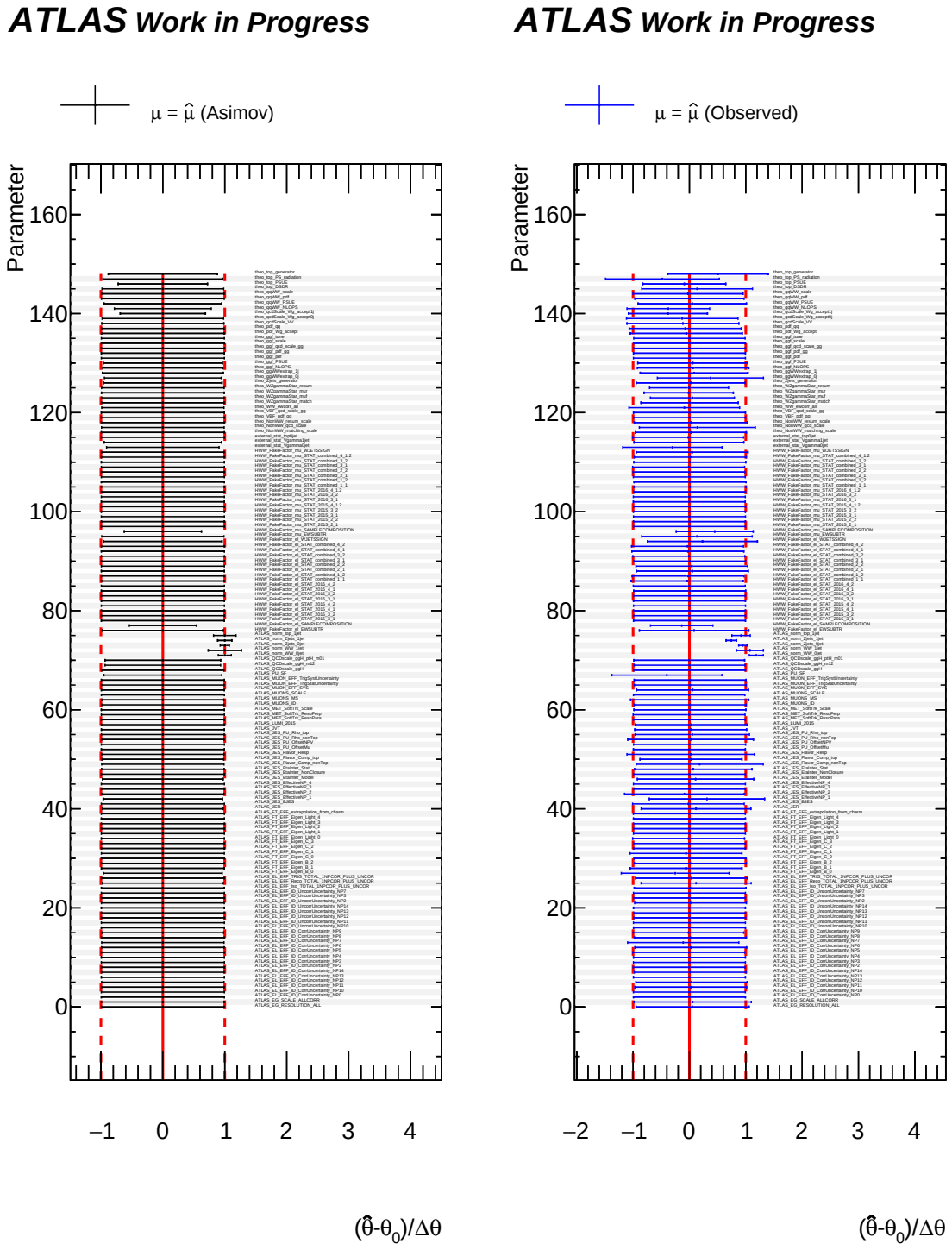

Figure 7.28 *The pull distributions of the nuisance parameters in the analysis using Asimov (left) and observed (right) datasets.*

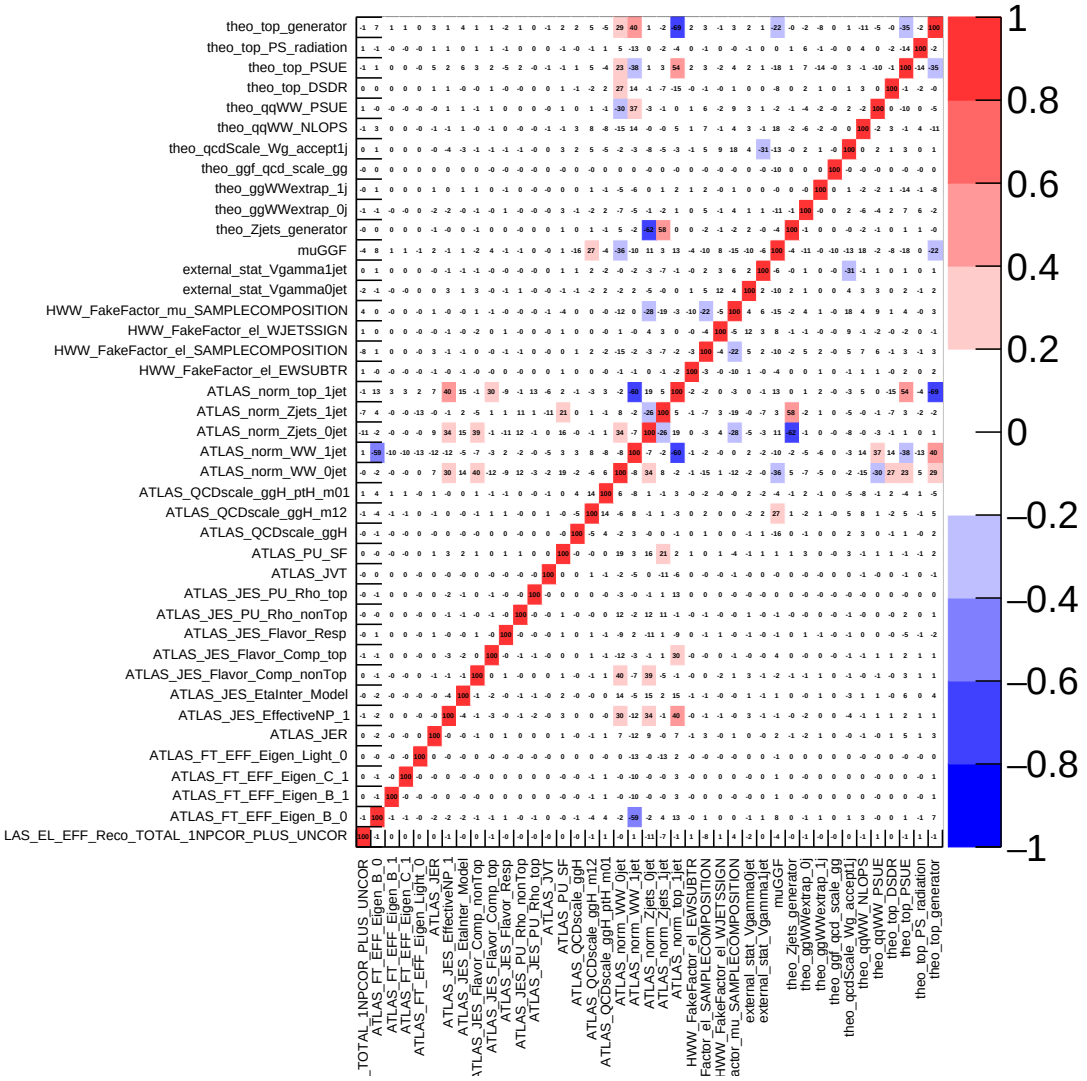

Figure 7.29 *Post-fit correlations of nuisance parameters which have a correlation of $> 20\%$ with at least one other nuisance parameter in the Asimov dataset.*

Table 7.16: Comparison between the post-fit normalization factors and the cut-based control region extraction ones.

Normalization factor	Post-fit value	CR extracted value
WW ($N_{jet} = 0$)	1.19 ± 0.12	1.10 ± 0.06
WW ($N_{jet} = 1$)	1.07 ± 0.40	0.88 ± 0.07
$Z/\gamma^* \to ll$ ($N_{jet} = 0$)	0.95 ± 0.07	0.96 ± 0.03
$Z/\gamma^* \to ll$ ($N_{jet} = 1$)	0.74 ± 0.09	0.78 ± 0.07
Top ($N_{jet} = 1$)	0.92 ± 0.16	1.03 ± 0.03

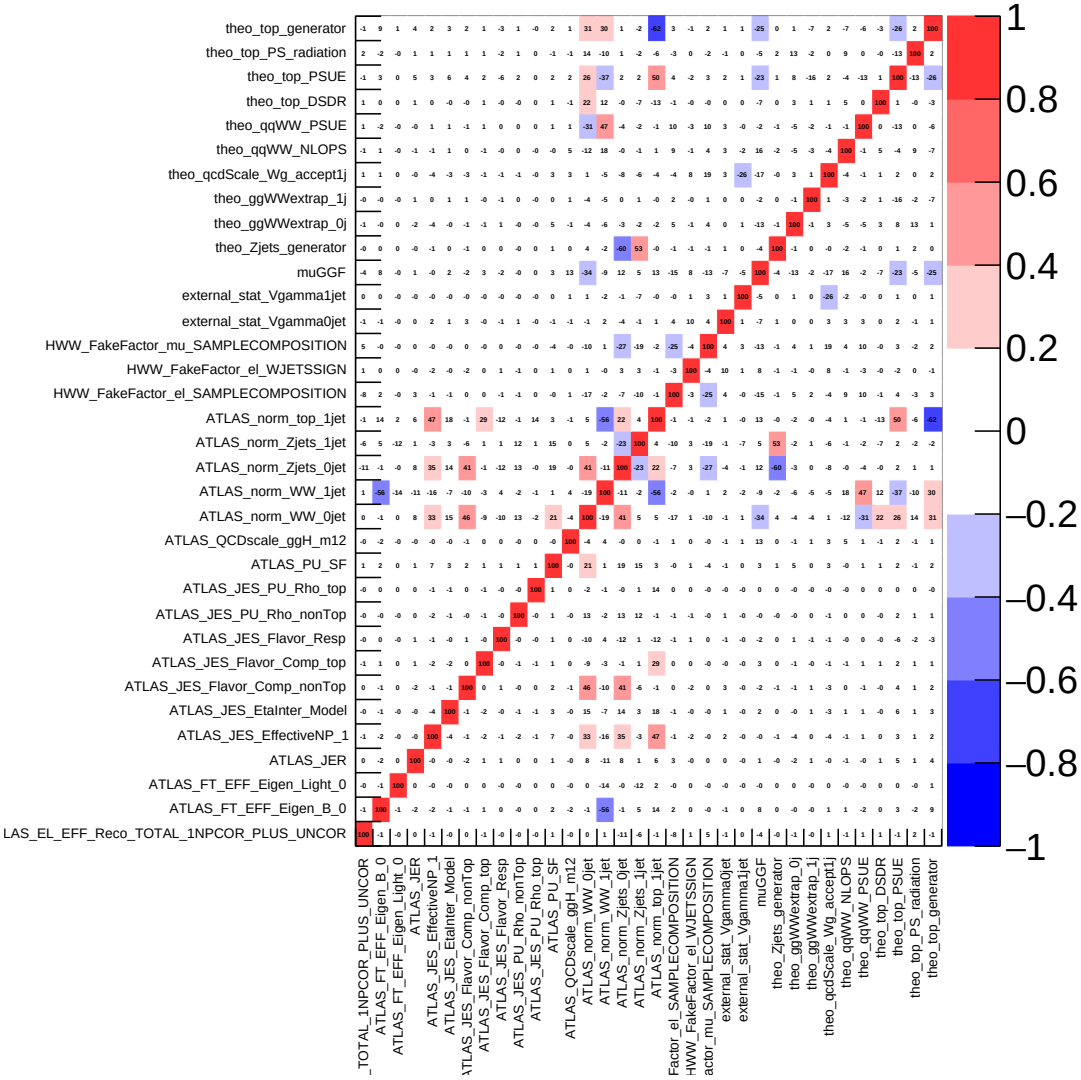

Figure 7.30 *Post-fit correlations of nuisance parameters which have a correlation of* $> 20\%$ *with at least one other nuisance parameter in the observed dataset.*

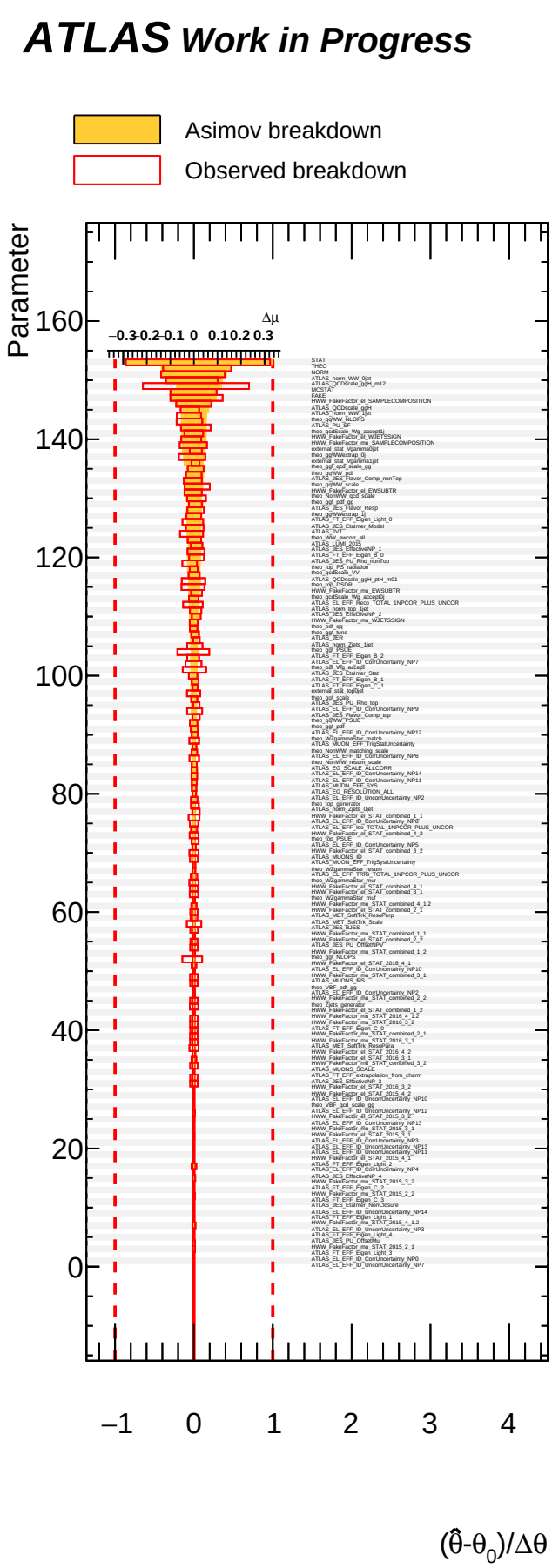

Figure 7.31 *The impact of each nuisance parameter on the μ result in Asimov and observed datasets. STAT, THEO, MCSTAT and FAKE represent the impact of all statistical, theoretical, MC statistical and fake nuisance parameters, respectively.*

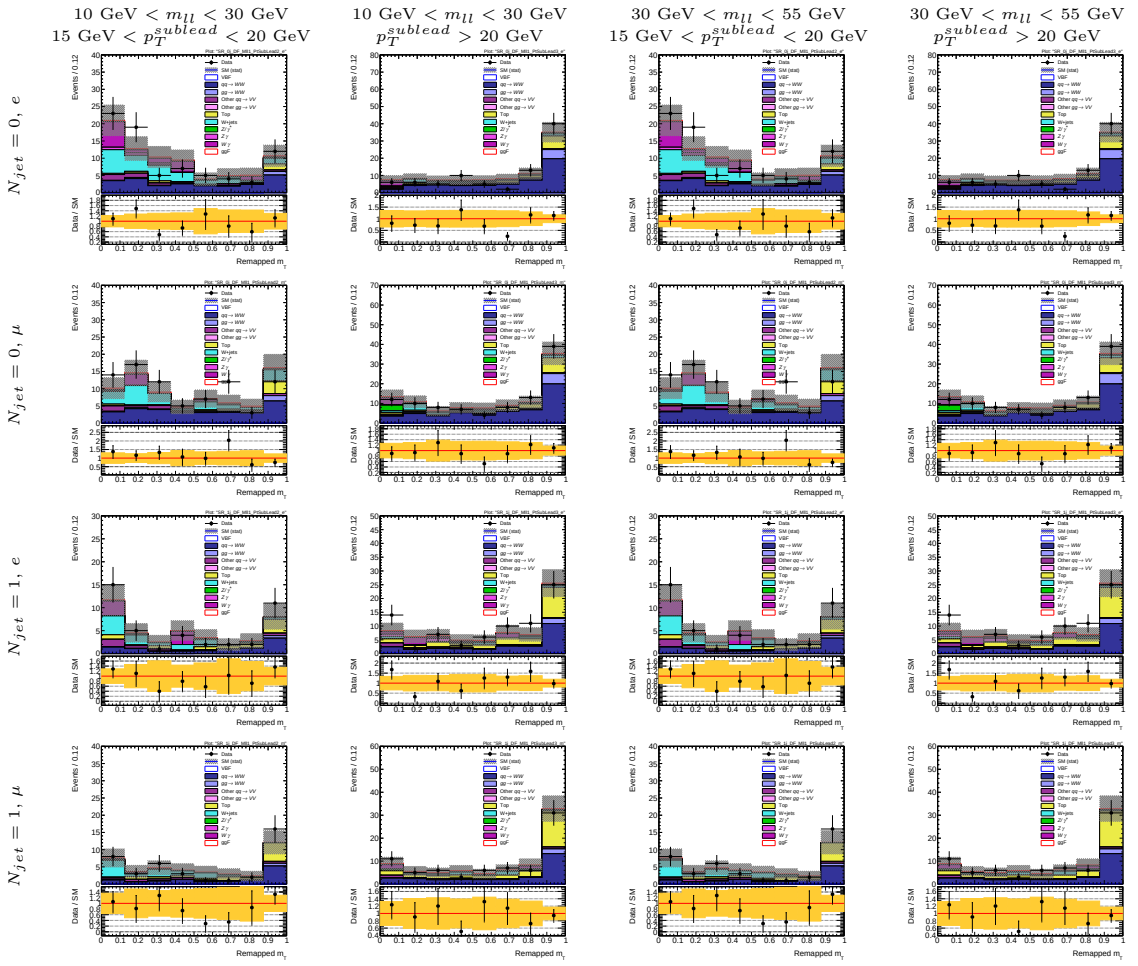

Figure 7.32 *Post-fit distributions of the remapped m_T in each m_{ll} and subleading lepton p_T bin in the $N_{jet}=0$ and $N_{jet}=1$ signal regions. e and μ denote the subleading electron and muon channels, respectively.*

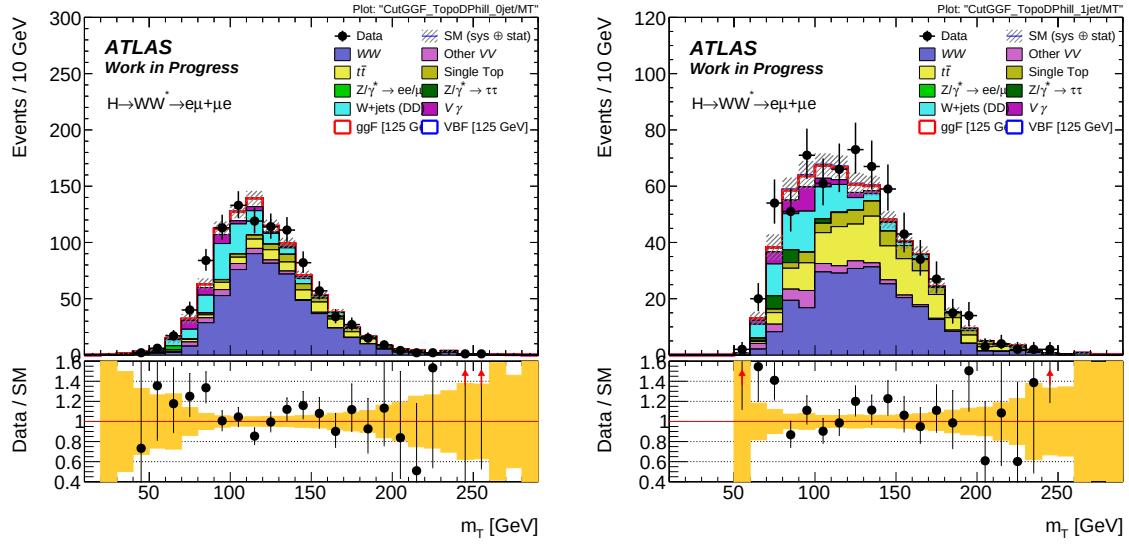

Figure 7.33 *Post-fit distributions of the m_T in $N_{jet}=0$ (left) and $N_{jet}=1$ (right) categories. The hatched band in the upper plot, and the shaded band in the ratio plot, give the quadratic sum of the statistical uncertainty and the experimental rate systematic uncertainties on the MC.*

7.5.4 Results

The expected significance from the Asimov dataset for a Higgs boson signal with the mass $m_H = 125$ GeV is 2.8 s.d. ($p_0 = 0.003$) and the corresponding observed significance is 1.0 s.d. ($p_0 = 0.16$). The best-fit value of the signal strength is

$$\begin{aligned} \mu &= 0.37 \ {}^{+0.23}_{-0.22}\,(\text{stat.}) \ {}^{+0.32}_{-0.29}\,(\text{syst.}) \\ &= 0.37 \ {}^{+0.40}_{-0.37}. \end{aligned} \tag{7.4}$$

The signal strength μ can be further separated and fitted independently in the $N_{jet} = 0$ and $N_{jet} = 1$ categories

$$\begin{aligned} \mu_{0j} &= 0.44 \ {}^{+0.52}_{-0.44} \\ \mu_{1j} &= 0.28 \ {}^{+0.61}_{-0.28}. \end{aligned} \tag{7.5}$$

The corresponding observed (expected) significances are 0.9 (2.2) and 0.5 (1.9) for the $N_{jet} = 0$ and $N_{jet} = 1$ categories, respectively.

7.5.5 Discussion of the Results

The signal strength $\mu = 0.37^{+0.40}_{-0.37}$ obtained in this analysis is the first result of the measurement of the SM Higgs boson decaying to WW at $\sqrt{s} = 13$ TeV in the ATLAS experiment. The observed signal strength is at the 1-sigma level and compatible with both the expectation from the Standard Model and the no-signal hypothesis.

As both the nuisance parameters for the top theory uncertainties, as well as the ones for the fake-lepton uncertainties, are pulled in the observed result, an additional test has been performed. In order to test the impact of these pulls on the final result, the fit was repeated with either of these two systematic uncertainty categories turned off. The results

$$\begin{aligned} \mu &= 0.43 \ {}^{+0.36}_{-0.34} \quad \text{(no theoretical top uncertainties)} \\ \mu &= 0.40 \ {}^{+0.38}_{-0.36} \quad \text{(no fake uncertainties)} \end{aligned} \tag{7.6}$$

are within agreement of the nominal result, but show a slight shift. This shift is however well within the quoted systematic uncertainty of the main result.

Another issue is the currently limited number of generated events available for some processes. This can be seen in Figure 7.31, where it is shown that the impact of the MC statistical uncertainty on the uncertainty of μ is the largest "experimental" uncertainty. It is also clearly visible in the right plot of Figure 7.33 that the WW background exhibits rather large bin-to-bin fluctuations, which are due to the limited raw number of events of this background sample.

In the Run-1 analysis, the expected significance for the Higgs boson at the mass $m_H = 125$ GeV is 5.76 s.d. However, this expected significance is the combined sig-

nificance when treating ggF and VBF together as signal. It also integrates over all N_{jet} categories, including the ggF-enriched $N_{jet} \geq 2$ category, the VBF category and the same-flavour lepton categories. When treating only ggF as signal, but still integrating over all categories, the expected significance is 4.34 s.d. The ggF $N_{jet} \geq 2$ category has an expected significance of 1.21 s.d., the same-flavour $N_{jet} = 1$ category 1.02 s.d., the same-flavour $N_{jet} = 0$ category 1.43 s.d., the different-flavour $N_{jet} = 1$ category 2.56 s.d., the different-flavour $N_{jet} = 0$ category with a subleading muon (electron) 2.89 s.d. (2.36 s.d.) and the VBF category 3.38 s.d. In addition, all of the above numbers include the $\sqrt{s} = 7$ TeV and $\sqrt{s} = 8$ TeV data. Thus, the expected combined sensitivity of the Run-1 analysis on 20.3 fb^{-1} of data collected at $\sqrt{s} = 8$ TeV for the ggF production in the different-flavour $N_{jet} \leq 1$ categories, i.e. the same categories as the 13 TeV analysis presented in this chapter, can be estimated to be around 4 s.d.

The worse expected significance of this Run-2 result compared to the Run-1 result is largely caused by the smaller integrated luminosity (5.8 fb^{-1} compared to 20.3 fb^{-1} in Run 1). This luminosity is not yet large enough to extract conclusive results. More data is needed to extract more reliable Higgs boson properties and production strength at 13 TeV. Even when taking into account the different amount of produced Higgs bosons (the ratio of expected ggF production cross sections between $\sqrt{s} = 13$ TeV and $\sqrt{s} = 8$ TeV is approximately 2.3), the expected sensitivity of the Run-1 analysis, extrapolated (arcording to simple scaling $\sqrt{N}$) to 5.8 fb^{-1} collected at $\sqrt{s} = 13$ TeV, is approximately 3.2 s.d. Additional reasons for this discrepancy are:

- The higher subleading lepton p_T threshold (15 GeV instead of 10 GeV) reduces the signal acceptance in the analysis presented in this chapter, compared to the Run-1 results.
- The higher centre-of-mass energy increases background yields, especially the top-quark backgound (e.g. the ggF signal production cross section at 13 TeV increases by a factor of about 2.3 compared to the one at 8 TeV while the $t\bar{t}$ background increases by a factor of about 3.3).

In addition, the CMS collaboration has also reported the first results in the same $H \to WW^* \to l\nu l\nu$ channel using a data sample corresponding to an integrated luminosity of 2.3 fb^{-1} at $\sqrt{s} = 13$ TeV collected in 2015 [133]. According to the report, the observed (expected) significance for a SM Higgs boson with a mass of 125 GeV is 0.7 s.d. (2.0 s.d.), corresponding to an observed signal strength of 0.3 ± 0.5. One should be notice that when scaling to 5.8 fb^{-1} (according to $\sqrt{N}$) the CMS results gives an expected significance of $\sim$3.2, while ours is only 2.8. The better expected significance can come from the lower lepton p_T requirements which are 10(13) GeV for subleading muons (electrons) and 20 GeV for leading leptons.

There are some improvements that can be done for the ATLAS $H \to WW^* \to l\nu l\nu$ analysis for the full 2015 and 2016 datasets

- Including dilepton triggers to gain in acceptance, especially since now, the single

lepton triggers start at 26 GeV.

- Improving the fake-lepton estimate and its uncertainties by using Z+jets sample instead of dijet one or using the matrix method which are described in Chapter 6.
- Getting WW samples with higher number of generated events, and signal samples with higher order calculation (e.g. NNLOPS simulation of Higgs boson production via gluon-gluon fusion).
- Going down to subleading lepton $p_T > 10$ GeV again and adding same-flavor channels (ee and $\mu\mu$ channels) into the analysis.

8

Summary

The Higgs mechanism is employed to incorporate the masses of elementary particles into the Standard Model via spontaneously breaking of the electroweak symmetry, and gives rise to the appearance of a physical scalar particle, the Higgs boson. The observation of this boson was announced on July 4$^{\text{th}}$ 2012 by the ATLAS and CMS experiments at the LHC. Nowadays, its mass is known to be 125.09 $\pm$ 0.21 (stat.) $\pm$ 0.11 (sys.) GeV [134].

In this thesis, a search for the Higgs boson production via gluon fusion in the $H \to WW^* \to l\nu l\nu$ decay mode with the ATLAS experiment has been presented. The analysis is based on data corresponding to an integrated luminosity of 4.5 fb^{-1} and 20.3 fb^{-1} collected at centre-of-mass energies of 7 TeV and 8 TeV, respectively. Due to the decay topology, the signature of this analysis is two isolated, oppositely charged leptons and large missing transverse momentum caused by the two neutrinos. Since the signal and background rates and their compositions depend on the number of jets in the final state, the analysis is divided into $N_{jet} = 0$, $N_{jet} = 1$ and $N_{jet} \leq 2$ categories. The combined results obtained from the analysis show an excess with a significance of 6.1 standard deviations, corresponding to a background fluctuation probability of about 10^{-9} for a Higgs boson mass of $m_H = 125.36$ GeV. Assuming the existence of a Standard Model Higgs boson, the ratio of the measured cross section to that predicted by the Standard Model is observed to be consistent with unity

$$\mu = 1.09\,^{+0.16}_{-0.15}\,(\text{stat.})\,^{+0.17}_{-0.14}\,(\text{syst.}) = 1.09\,^{+0.23}_{-0.21}.$$

Several Standard Model processes, such as WW, $t\bar{t}$, single top-quark production, Z/γ^*, W+jets and other non-WW diboson, contribute as sources for background events to this analysis. Amongst them, the W+jets background contribution in the final signal region of the $H \to WW^* \to l\nu l\nu$ analysis is at a similar level as the Higgs boson signal itself. Therefore, it is very important to reliably determine the shape and normalization of the W+jets background in the signal region. The fake factor method used in this analysis has a large systematic uncertainty due to the differences in flavour

compositions and kinematic and topological distributions between control and signal regions. A new matrix method was proposed in order to provide a way to determine the W+jets background directly in the dilepton data sample. The main advantage of this method is the absence of the uncertainty on the sample dependence. This matrix method result was used as a cross-check to the fake factor method in the analysis.

The studies performed in the Run-2 analysis focus on the $N_{jet} = 0$ and $N_{jet} = 1$ categories in the different-flavour final state, which provide the best sensitivity to the gluon fusion production mode. A dataset corresponding to an integrated luminosity of 5.8 fb^{-1} at a centre-of-mass energy of 13 TeV is used. The signal event selection is mostly similar to the Run-1 analysis. However, since Run 2 exhibits a higher centre-of-mass energy, the object reconstruction and event selection criteria are re-optimized and validated in order to obtain a good expected signal significance. The strategy of this optimization was not to perform a rigorous optimization of all selection criteria, but rather to validate that the selection criteria obtained in the Run-1 analysis are also good selection criteria for the Run-2 analysis. The modelling of the Monte Carlo and data-driven predictions were validated in many (essentially signal-free) dedicated control and validation regions. Monte Carlo yields were normalized to observed data yields in several control regions using multiple techniques. General agreement was found between Monte Carlo predictions and data. All signal and background processes are fitted simultaneously to reflect the correlation amongst them in the signal strength fit.

The first results of the measurement of the Higgs boson decaying to WW at a centre-of-mass energy of $\sqrt{s} = 13$ TeV is presented. The observed (expected) significance for the gluon-gluon fusion production mode is 1.0 (2.8) standard deviations, corresponding to a background fluctuation probability of 0.16 (0.003). The best-fit signal strength is

$$\mu = 0.37\,^{+0.23}_{-0.22}\,(\text{stat.})\,^{+0.32}_{-0.29}\,(\text{syst.}) = 0.37\,^{+0.40}_{-0.37}$$

and thus compatible with both the expectation from the Standard Model and the no-signal hypothesis. Further analysis with more data is needed to be performed to extract more reliable Higgs boson properties and production strength at 13 TeV.

A

Additional plots for the matrix method

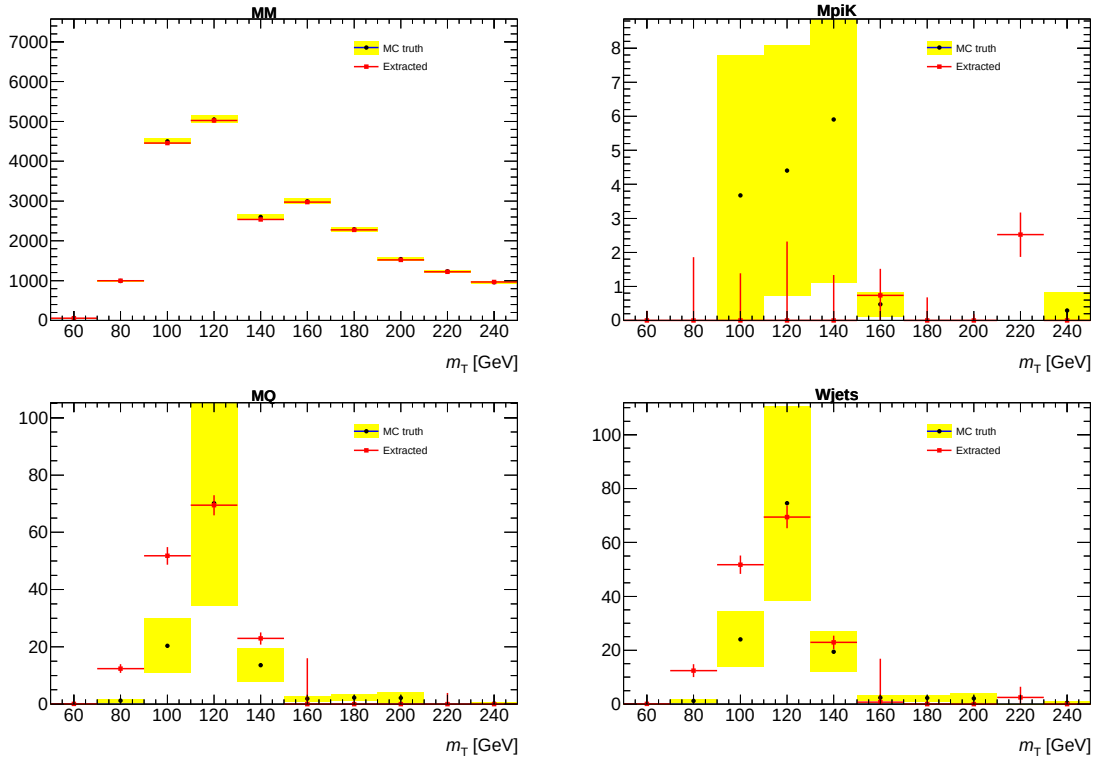

Figure A.1 *Comparison between MC truth and extracted results for the variable m_T in the $H \to WW^* \to \mu\nu\mu\nu$ channel after the pre-selection. Shown are the $\mu\mu$ component (top left), the μh component (top right), the μQ component (bottom left), and the final $W+$*jets *component (bottom right).*

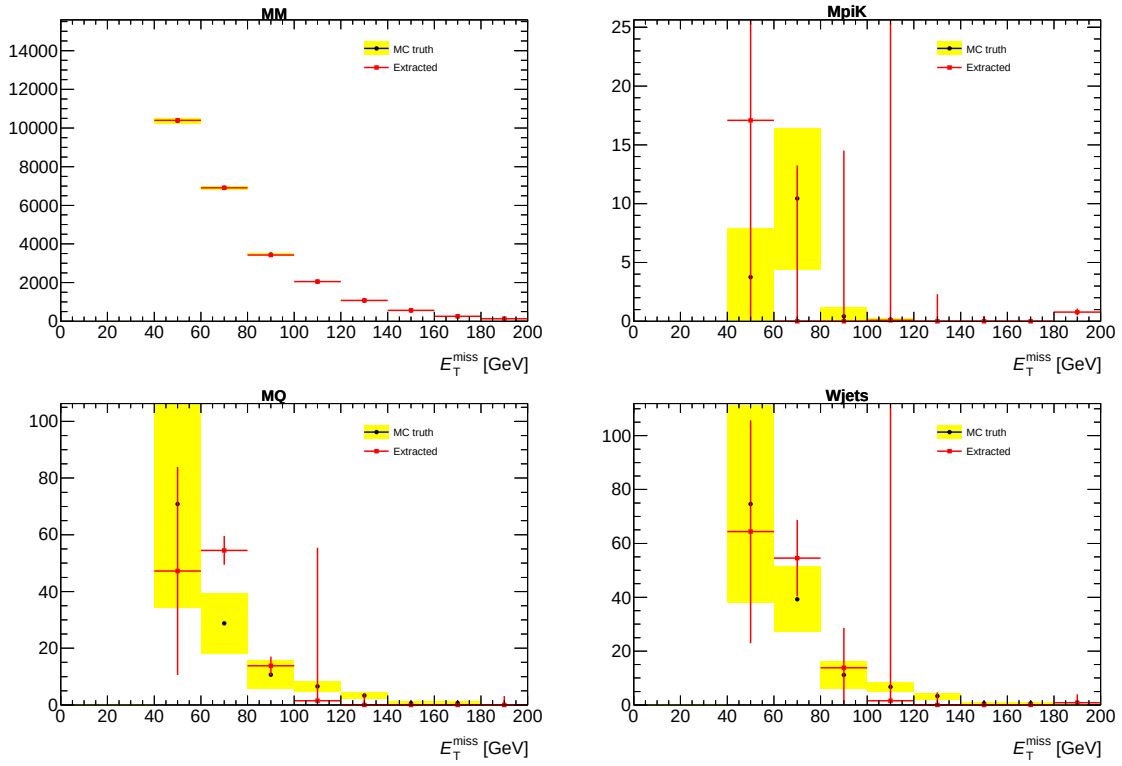

Figure A.2 *Comparison between MC truth and extracted results for the variable E_T^{miss} in the $H \to WW^* \to \mu\nu\mu\nu$ channel after the pre-selection. Shown are the $\mu\mu$ component (top left), the μh component (top right), the μQ component (bottom left), and the final $W +$ jets component (bottom right).*

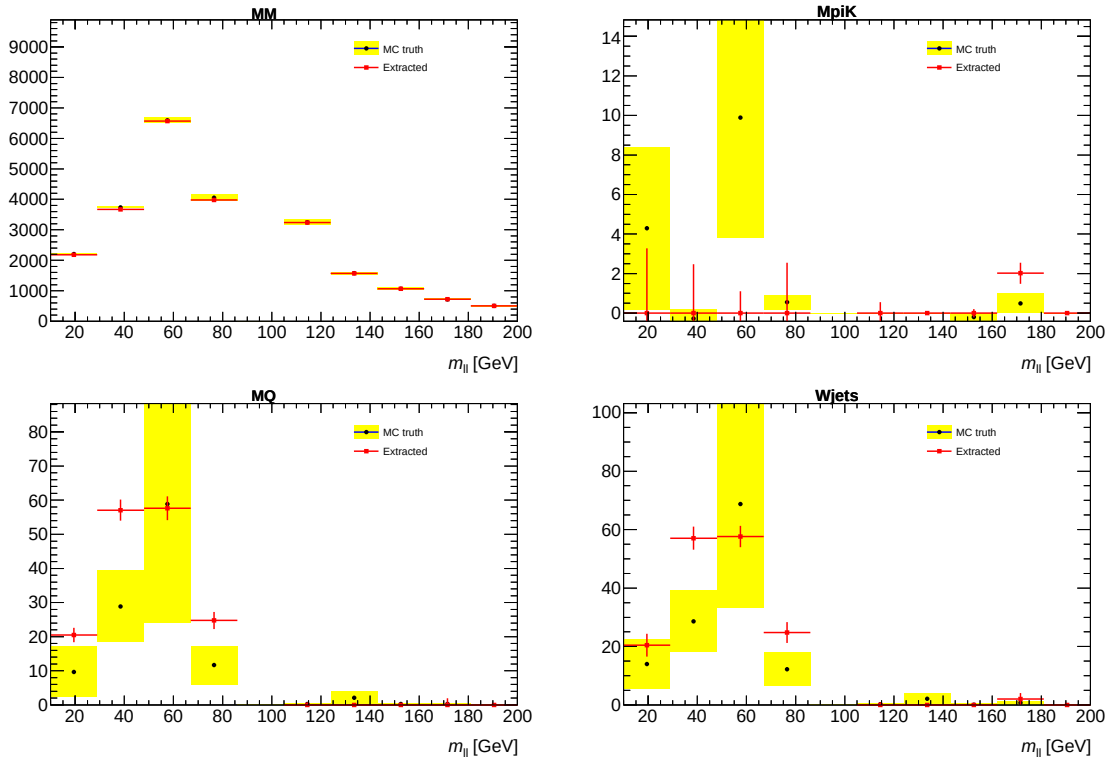

Figure A.3 *Comparison between MC truth and extracted results for the variable m_{ll} in the $H \to WW^* \to \mu\nu\mu\nu$ channel after the pre-selection. Shown are the $\mu\mu$ component (top left), the μh component (top right), the μQ component (bottom left), and the final $W+$ jets component (bottom right).*

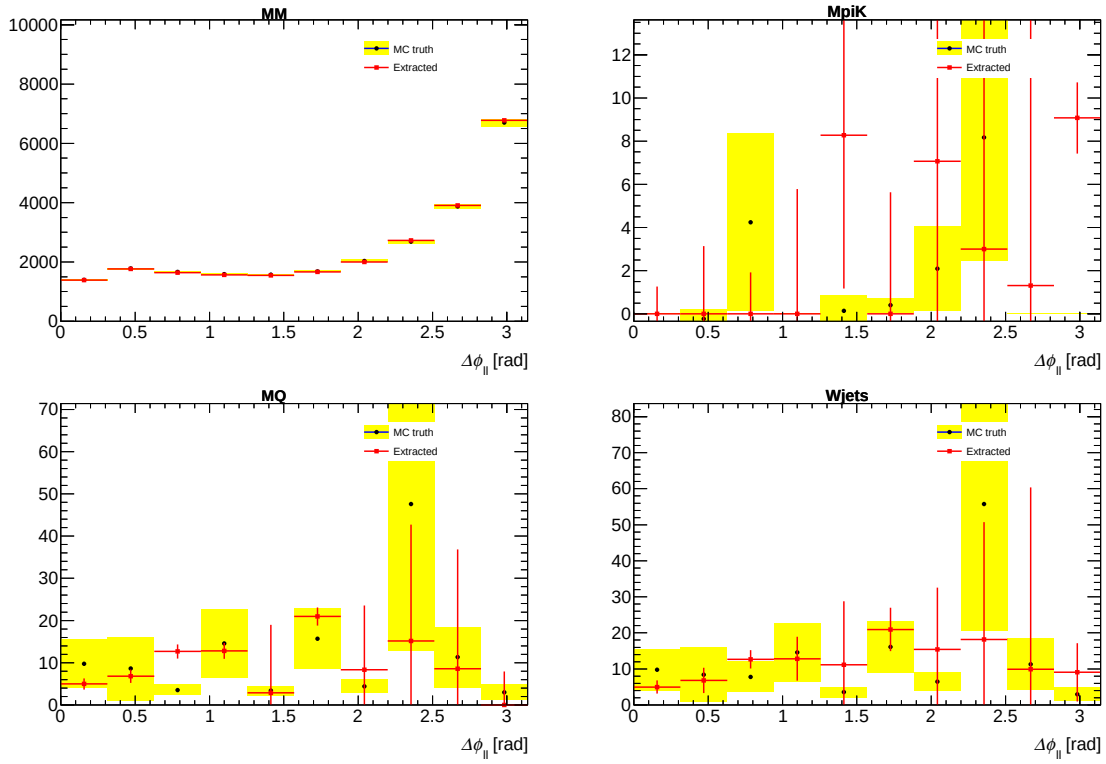

Figure A.4 *Comparison between MC truth and extracted results for the variable* $\Delta\phi_{ll}$ *in the* $H \to WW^* \to \mu\nu\mu\nu$ *channel after the pre-selection. Shown are the* $\mu\mu$ *component (top left), the* μh *component (top right), the* μQ *component (bottom left), and the final* $W + \text{jets}$ *component (bottom right).*

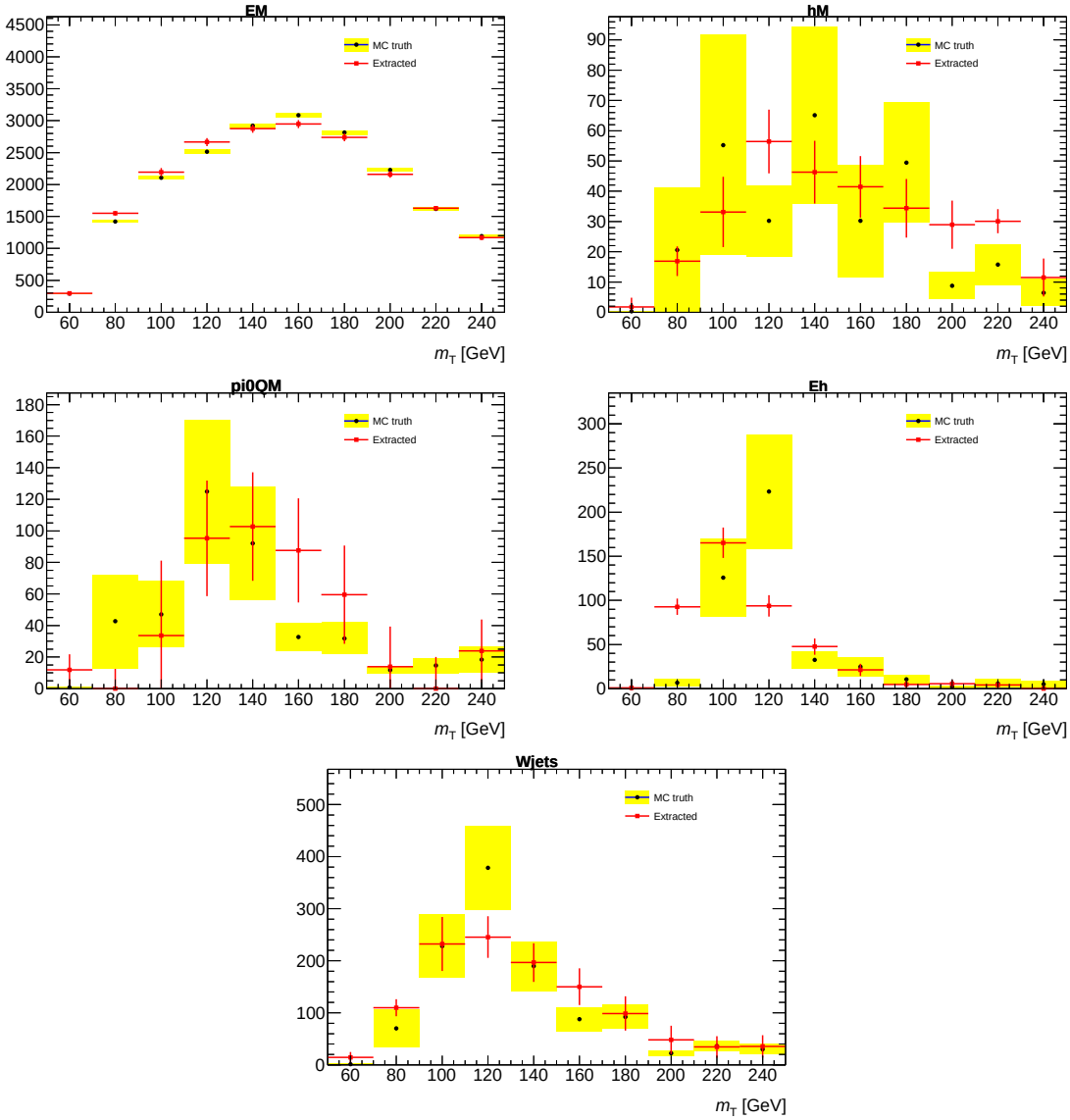

Figure A.5 *Comparison between MC truth and extracted results for the variable m_T in the $H \to WW^* \to e\nu\mu\nu$ channel after the pre-selection. Shown are the $e\mu$ component (top left), the μh component (top right), the $\pi^0 Q\mu$ component (middle left), the eh component (middle right), and the final $W+$ jets component (bottom).*

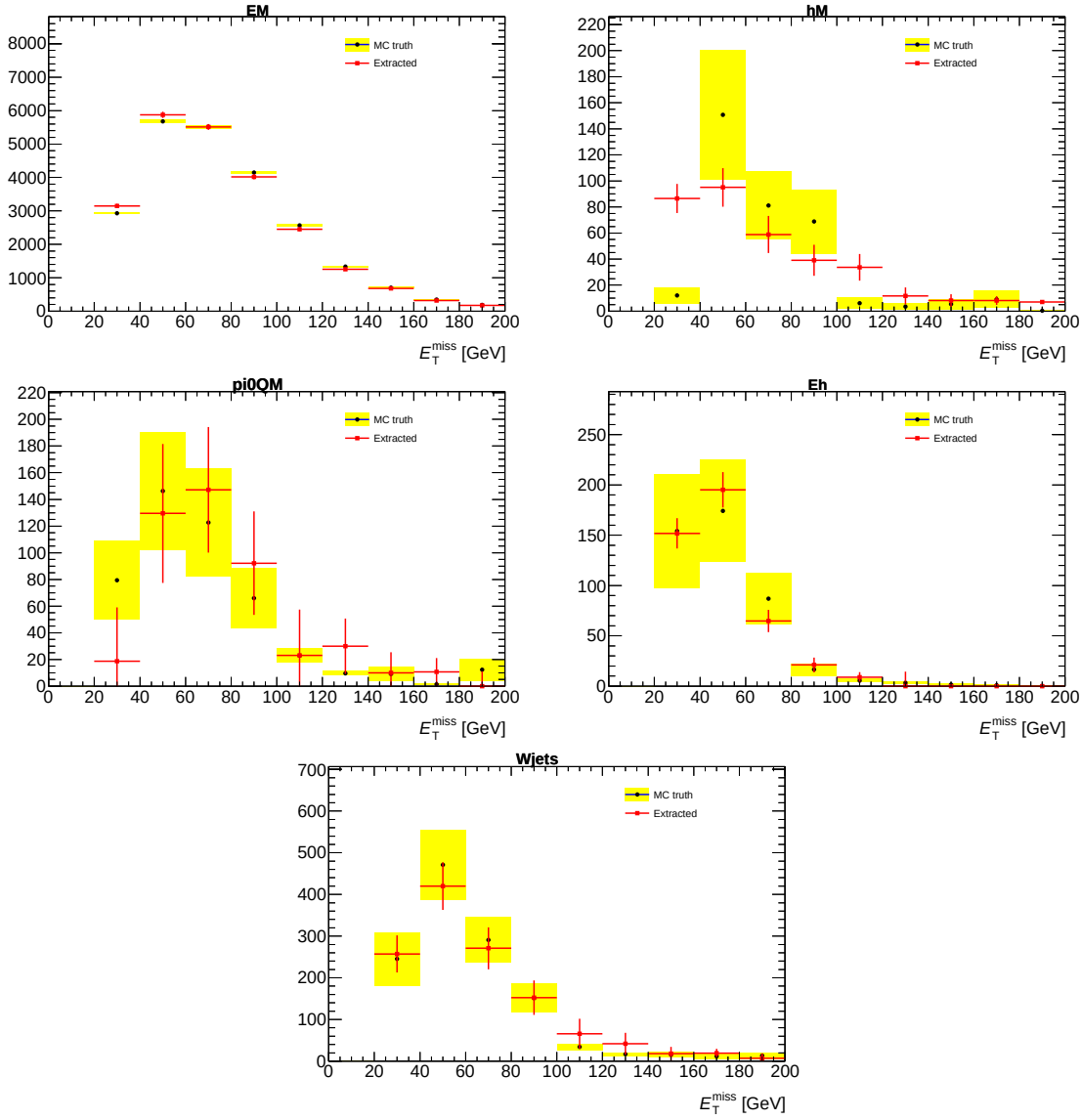

Figure A.6 *Comparison between MC truth and extracted results for the variable* E_T^{miss} *in the* $H \to WW^* \to e\nu\mu\nu$ *channel after the pre-selection. Shown are the* $e\mu$ *component (top left), the* μh *component (top right), the* $\pi^0 Q\mu$ *component (middle left), the* eh *component (middle right), and the final* $W + \text{jets}$ *component (bottom).*

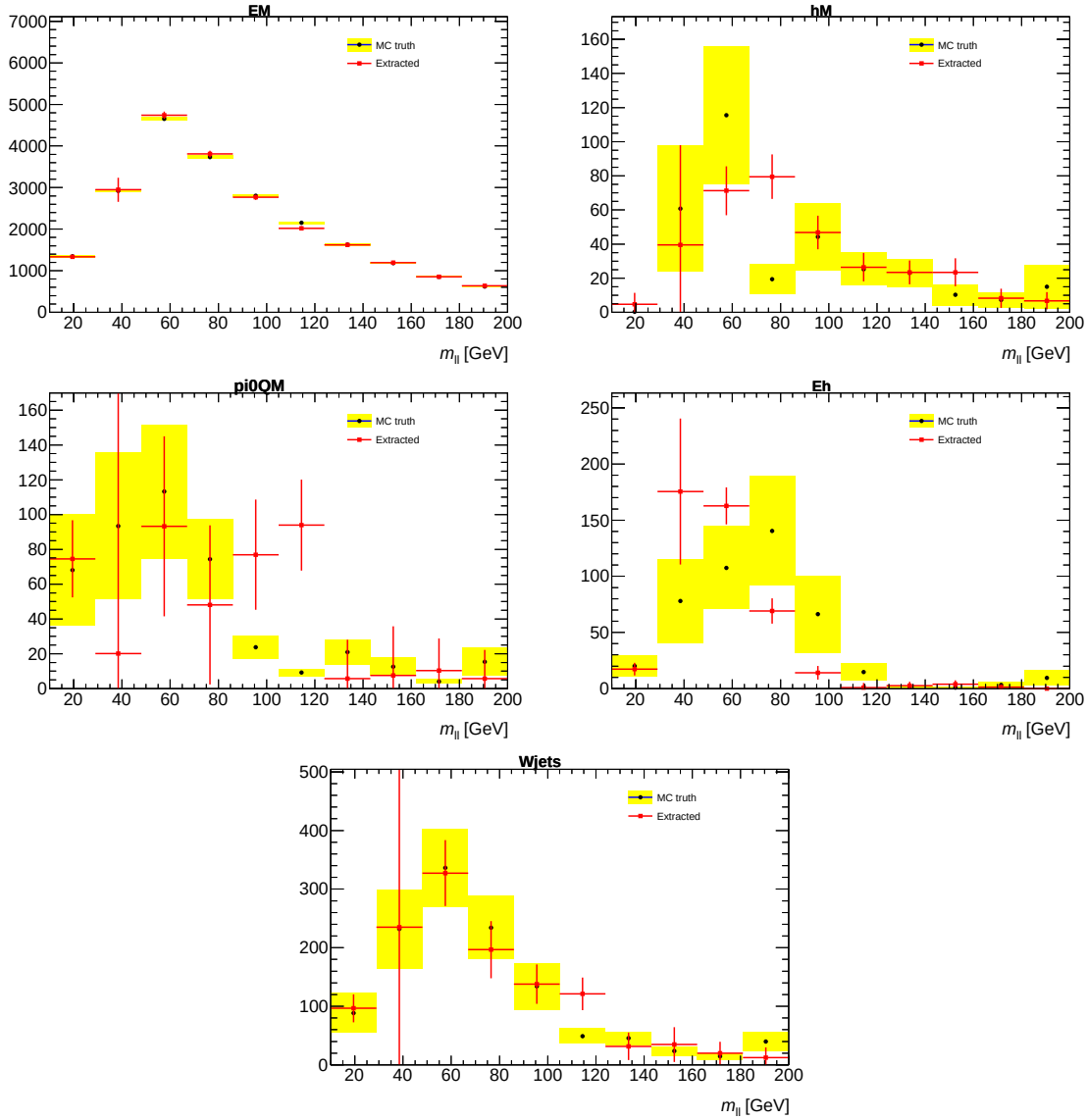

Figure A.7 *Comparison between MC truth and extracted results for the variable m_{ll} in the $H \to WW^* \to e\nu\mu\nu$ channel after the pre-selection. Shown are the $e\mu$ component (top left), the μh component (top right), the $\pi^0 Q\mu$ component (middle left), the eh component (middle right), and the final $W+$ jets component (bottom).*

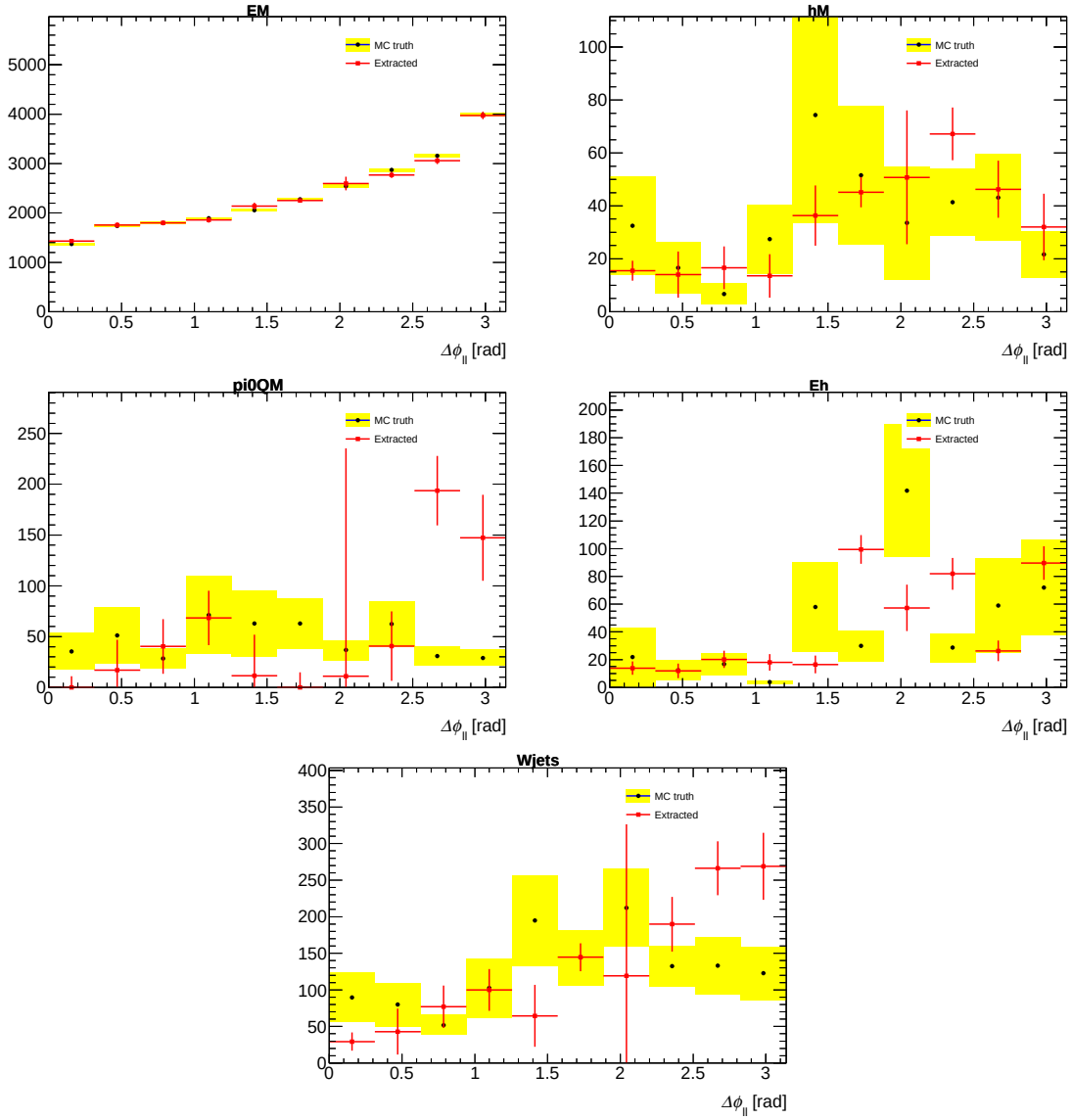

Figure A.8 *Comparison between MC truth and extracted results for the variable* $\Delta\phi_{ll}$ *in the* $H \to WW^* \to e\nu\mu\nu$ *channel after the pre-selection. Shown are the* $e\mu$ *component (top left), the* μh *component (top right), the* $\pi^0 Q\mu$ *component (middle left), the* eh *component (middle right), and the final* $W + \text{jets}$ *component (bottom).*

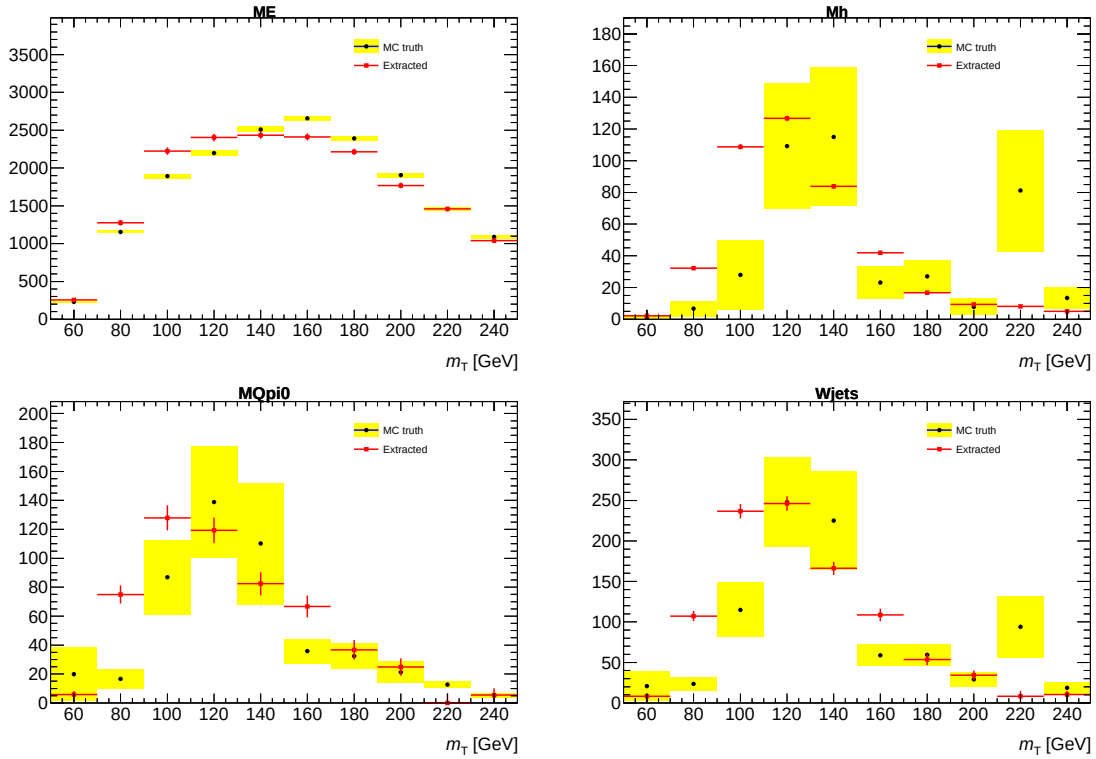

Figure A.9 *Comparison between MC truth and extracted results for the variable m_T in the $H \to WW^* \to \mu\nu e\nu$ channel after the pre-selection. Shown are the μe component (top left), the μh component (top right), the $\mu\pi^0 Q$ component (bottom left), and the final $W+$ jets component (bottom right).*

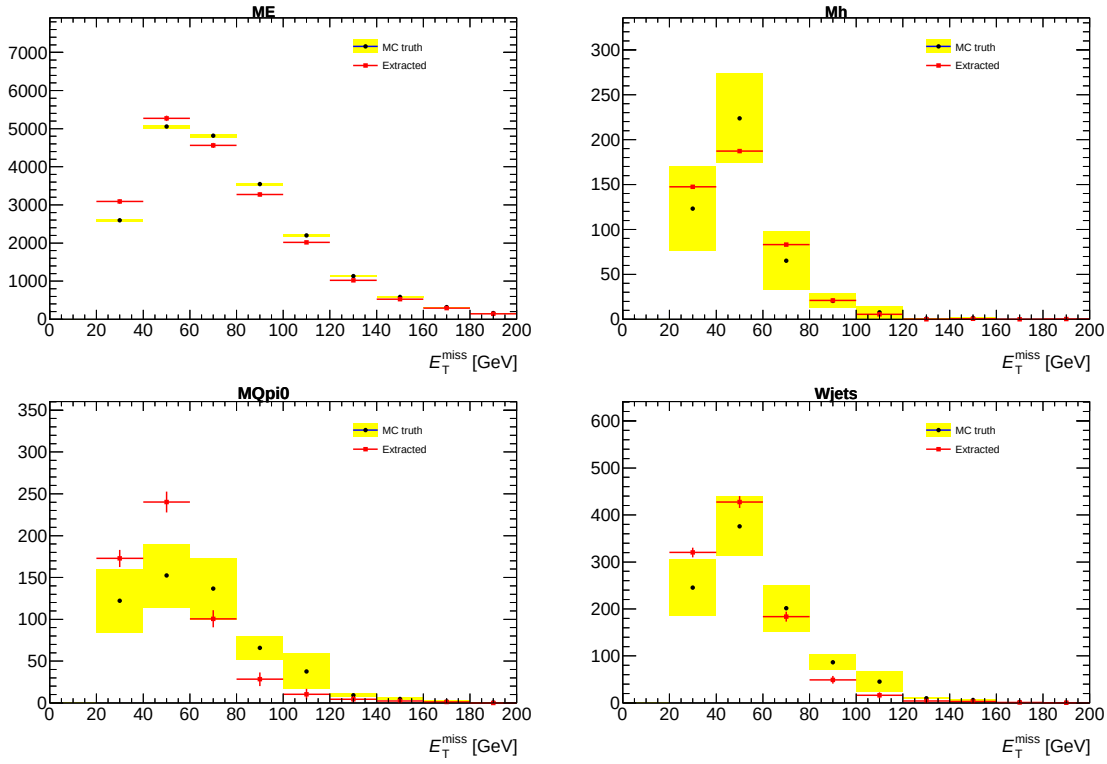

Figure A.10 *Comparison between MC truth and extracted results for the variable* E_T^{miss} *in the* $H \to WW^* \to \mu\nu e\nu$ *channel after the pre-selection. Shown are the* μe *component (top left), the* μh *component (top right), the* $\mu\pi^0 Q$ *component (bottom left), and the final* $W + \text{jets}$ *component (bottom right).*

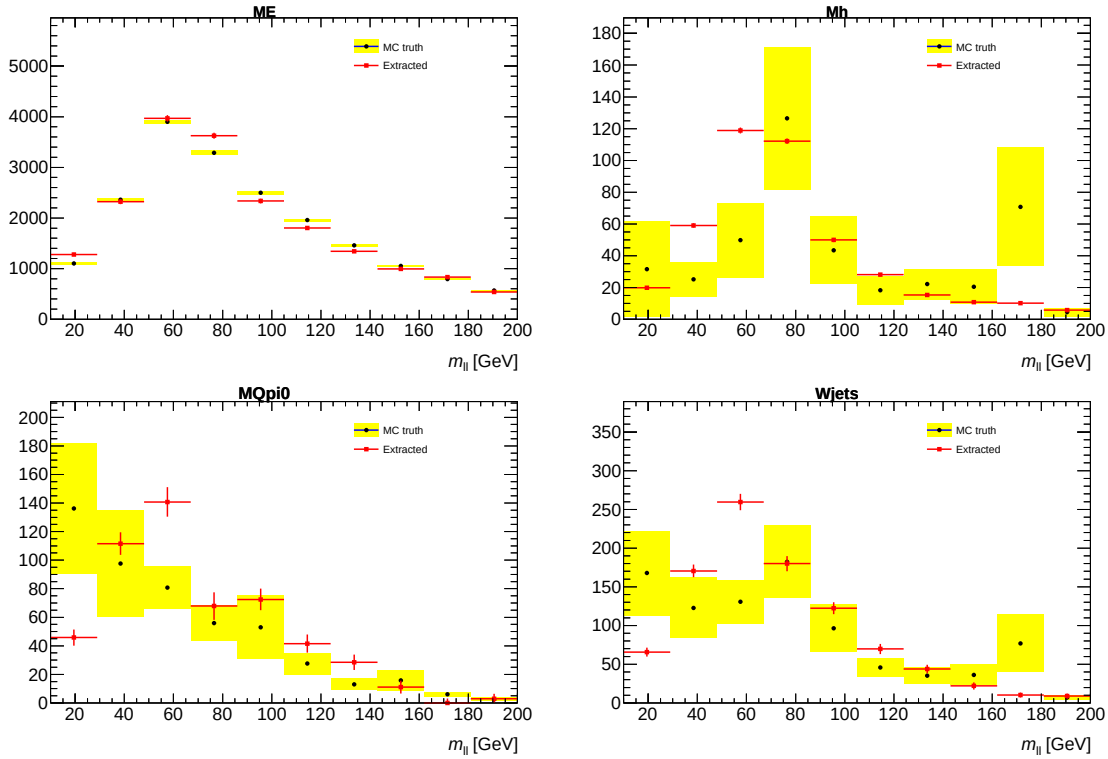

Figure A.11 *Comparison between MC truth and extracted results for the variable m_{ll} in the $H \to WW^* \to \mu\nu e\nu$ channel after the pre-selection. Shown are the μe component (top left), the μh component (top right), the $\mu\pi^0 Q$ component (bottom left), and the final $W +$ jets component (bottom right).*

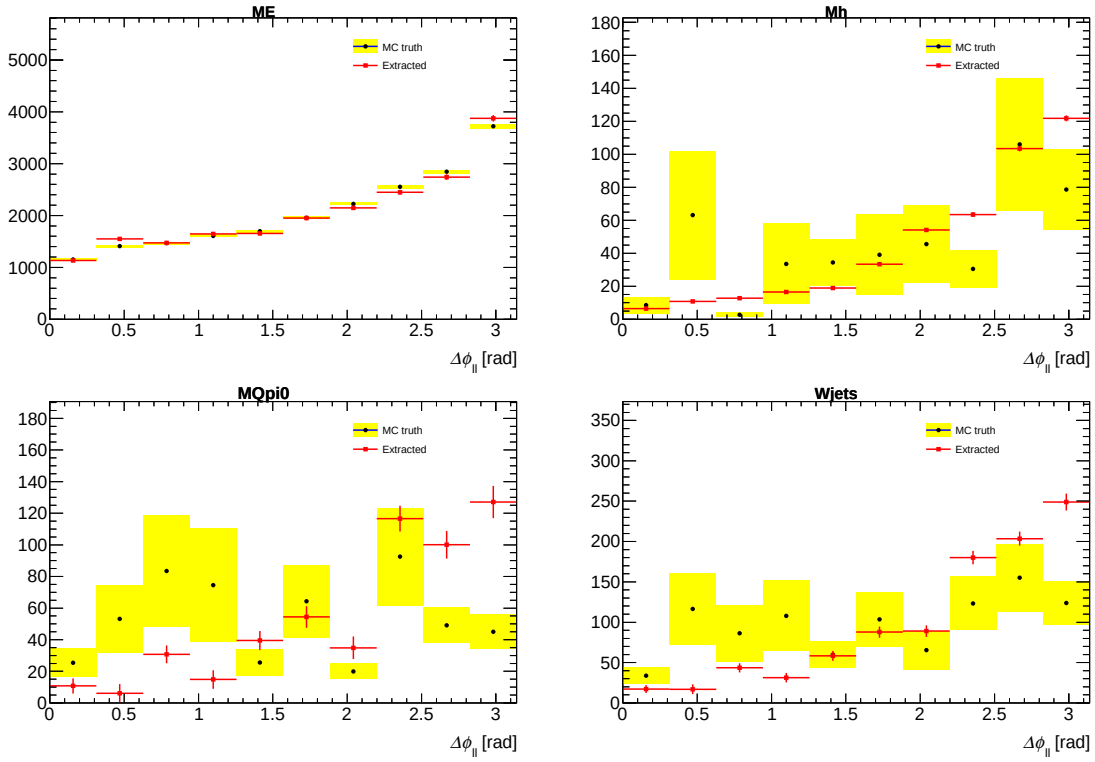

Figure A.12 *Comparison between MC truth and extracted results for the variable* $\Delta\phi_{ll}$ *in the* $H \to WW^* \to \mu\nu e\nu$ *channel after the pre-selection. Shown are the* μe *component (top left), the* μh *component (top right), the* $\mu\pi^0 Q$ *component (bottom left), and the final* $W + \text{jets}$ *component (bottom right).*

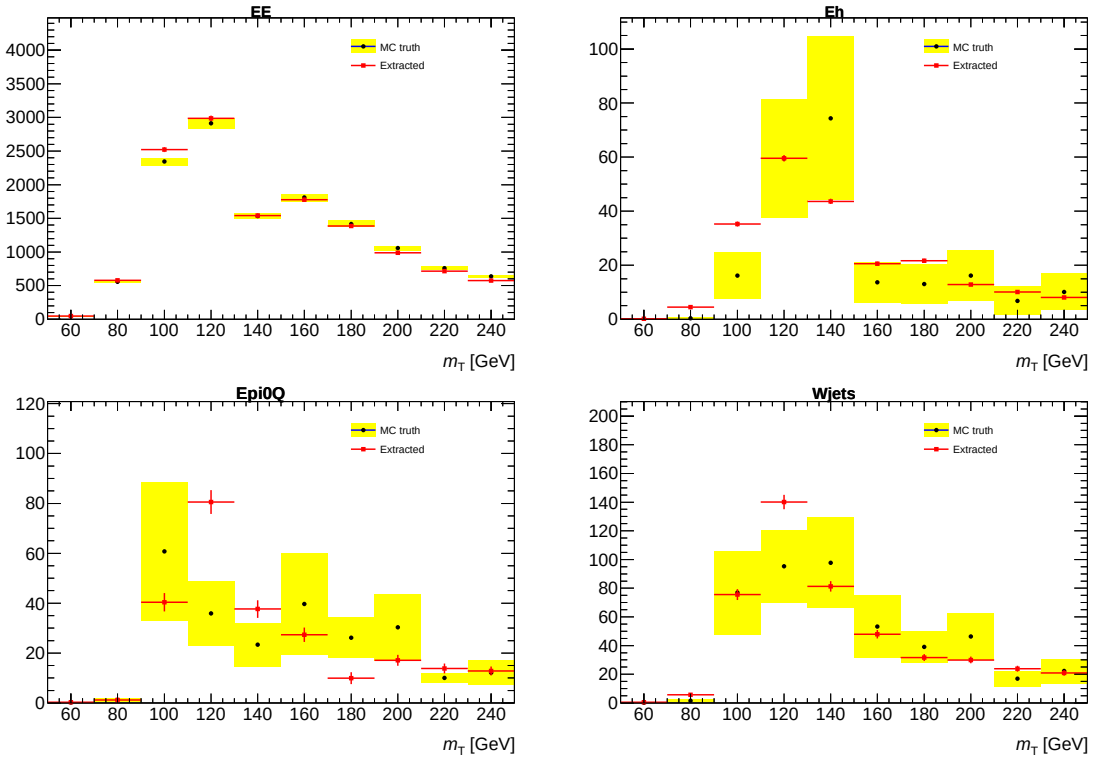

Figure A.13 *Comparison between MC truth and extracted results for the variable m_T in the $H \to WW^* \to e\nu e\nu$ channel after the pre-selection. Shown are the ee component (top left), the eh component (top right), the $e\pi^0 Q$ component (bottom left), and the final $W+$ jets component (bottom right).*

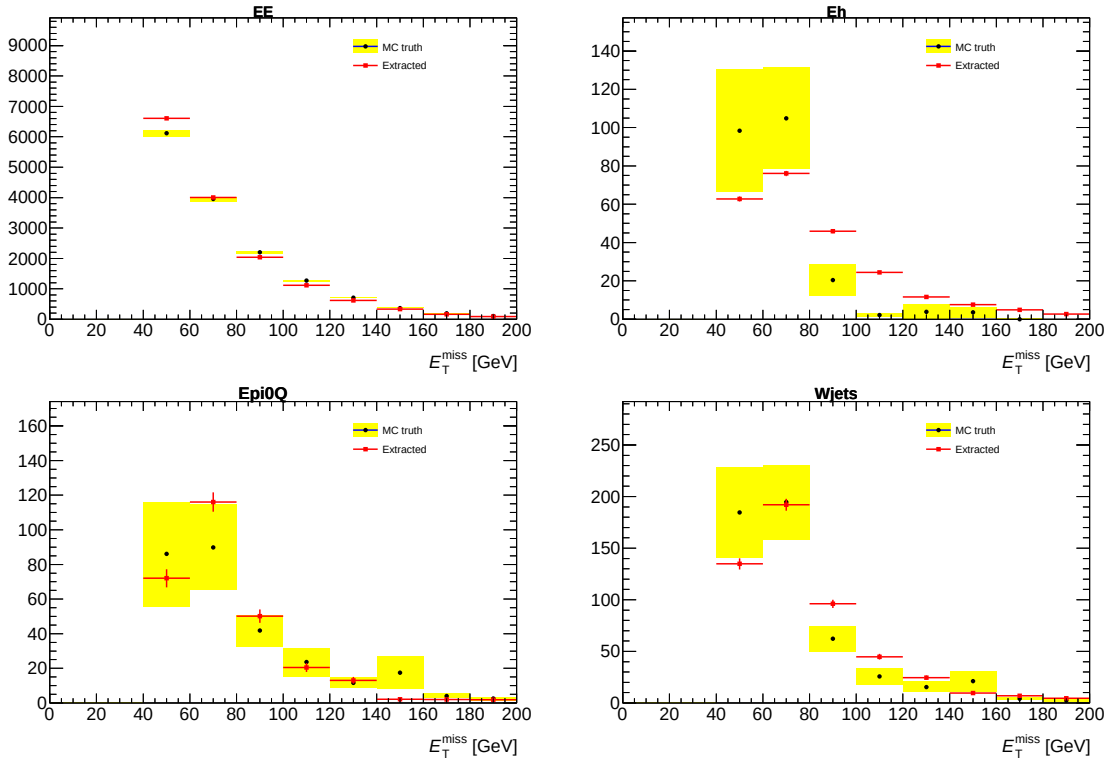

Figure A.14 *Comparison between MC truth and extracted results for the variable E_T^{miss} in the $H \to WW^* \to e\nu e\nu$ channel after the pre-selection. Shown are the ee component (top left), the eh component (top right), the $e\pi^0 Q$ component (bottom left), and the final $W +$ jets component (bottom right).*

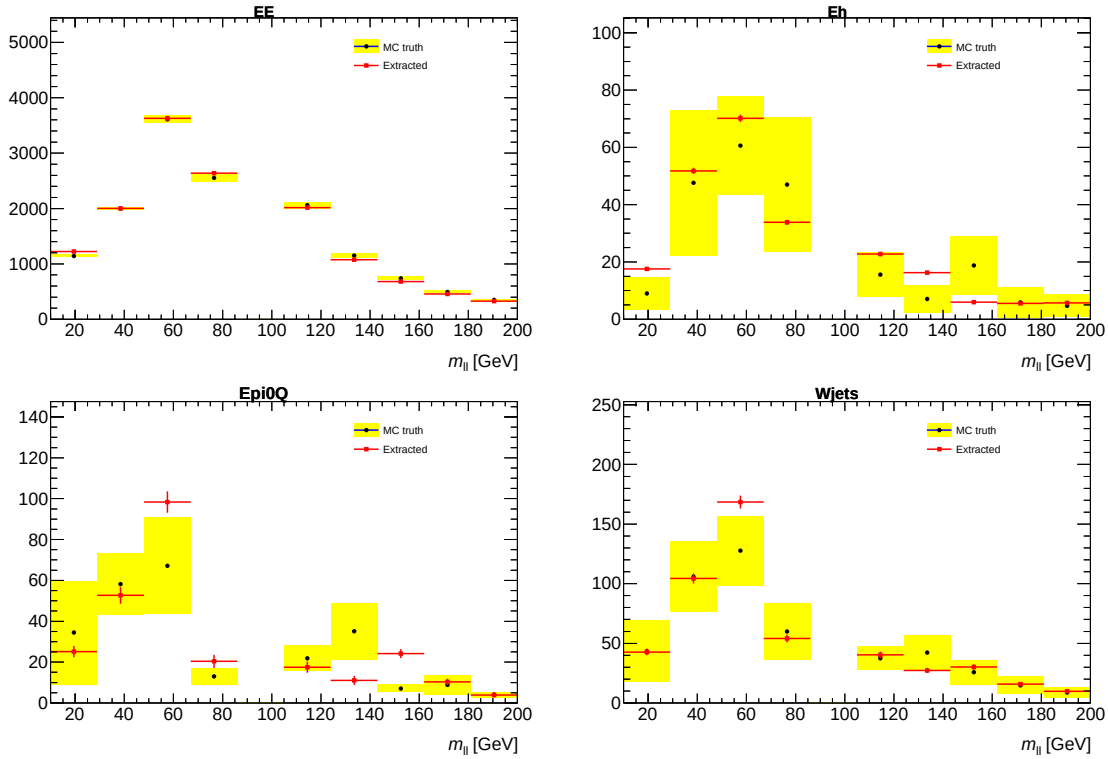

Figure A.15 *Comparison between MC truth and extracted results for the variable m_{ll} in the $H \to WW^* \to e\nu e\nu$ channel after the pre-selection. Shown are the ee component (top left), the eh component (top right), the $e\pi^0 Q$ component (bottom left), and the final $W +$ jets component (bottom right).*

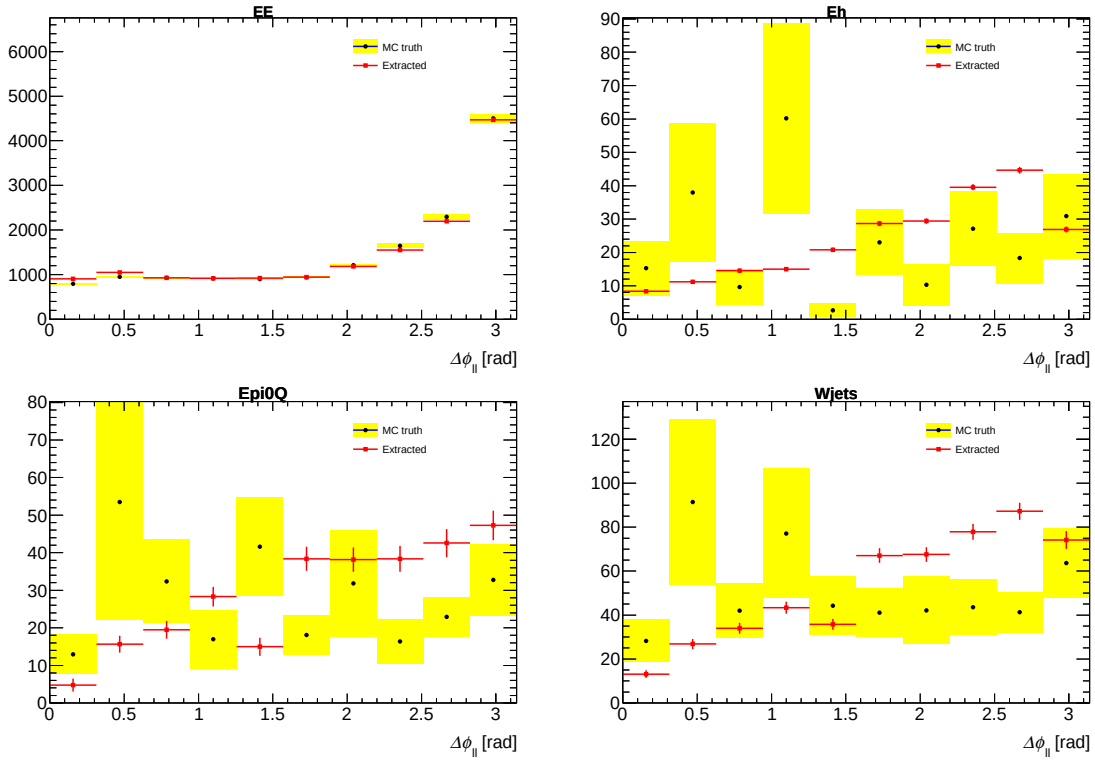

Figure A.16 *Comparison between MC truth and extracted results for the variable* $\Delta\phi_{ll}$ *in the* $H \to WW^* \to e\nu e\nu$ *channel after the pre-selection. Shown are the ee component (top left), the eh component (top right), the* $e\pi^0 Q$ *component (bottom left), and the final* $W + \text{jets}$ *component (bottom right).*

B

Additional plots at pre-selection level

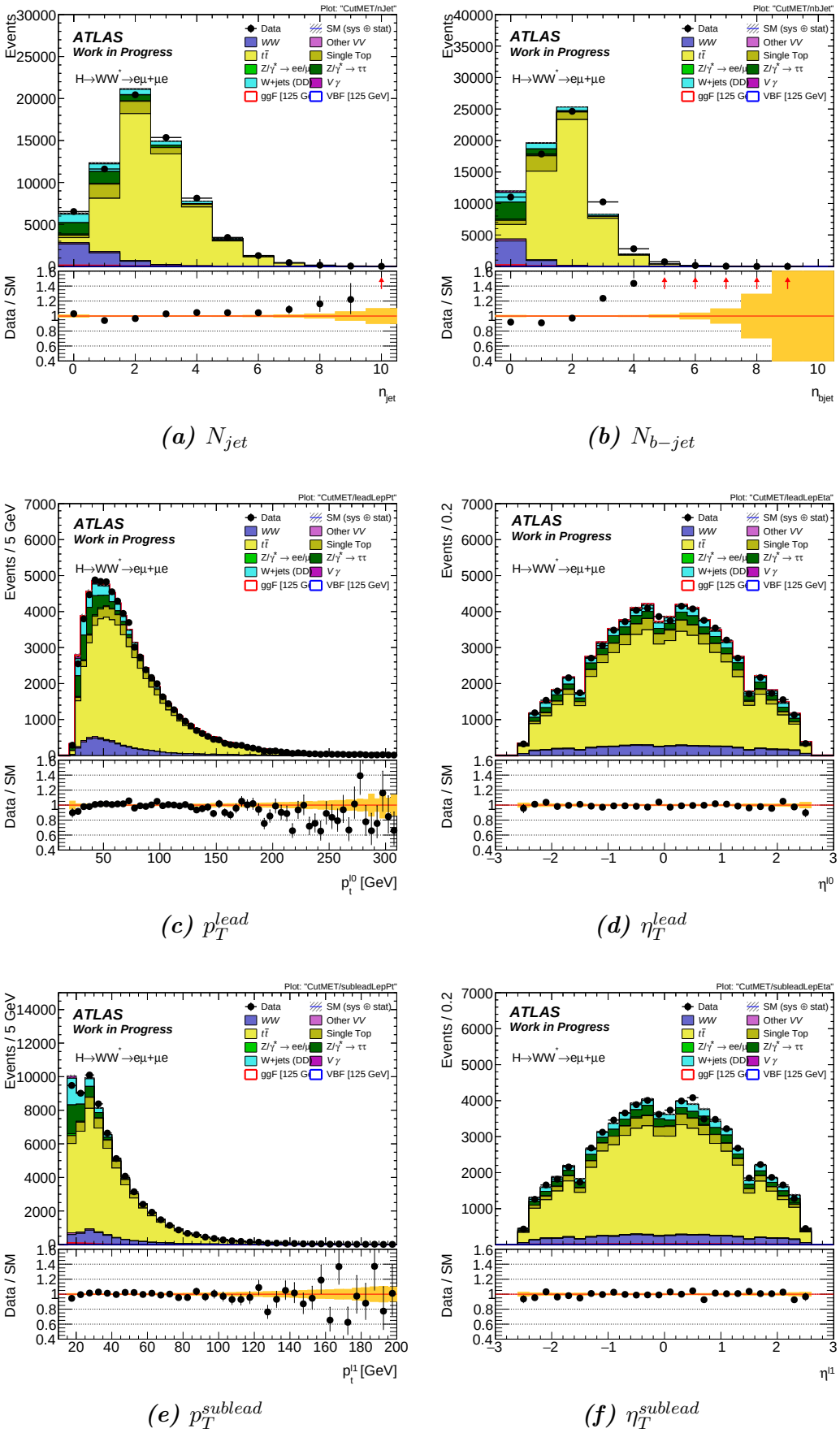

(a) N_{jet} *(b)* N_{b-jet}

(c) p_T^{lead} *(d)* η_T^{lead}

(e) $p_T^{sublead}$ *(f)* $\eta_T^{sublead}$

Figure B.1 *Comparison of data and MC at pre-selection level. Signal and background processes are normalized to predictions. The hatched band in the upper plot, and the shaded band in the ratio plot, give the quadrature sum of statistical and experimental systematic rate uncertainties on the signal and backgrounds.*

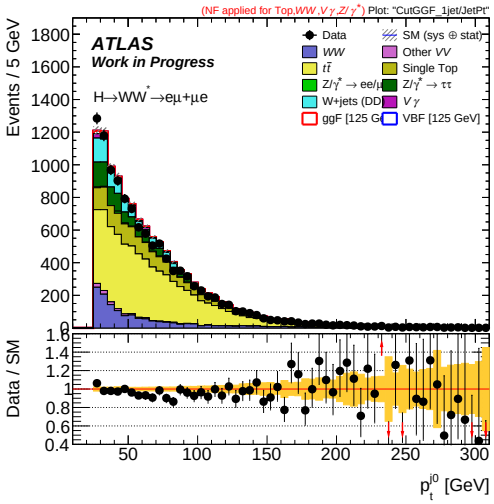

(a) p_T^{j0}

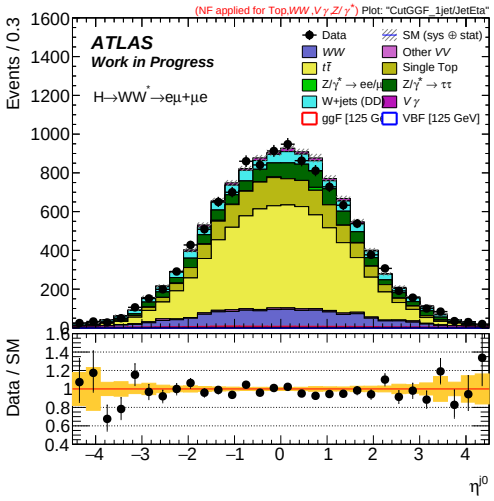

(b) η^{j0}

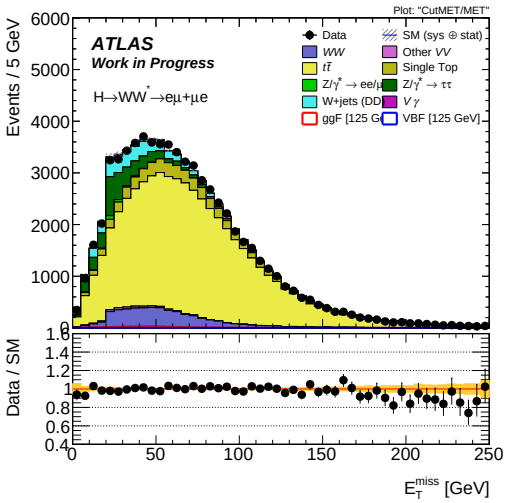

(c) E_T^{miss}

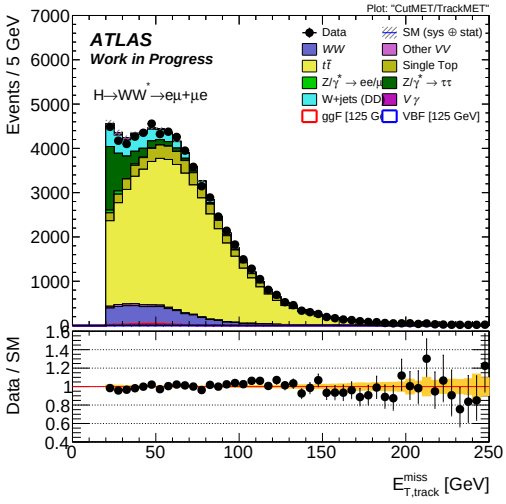

(d) $E_T^{miss,TRK}$

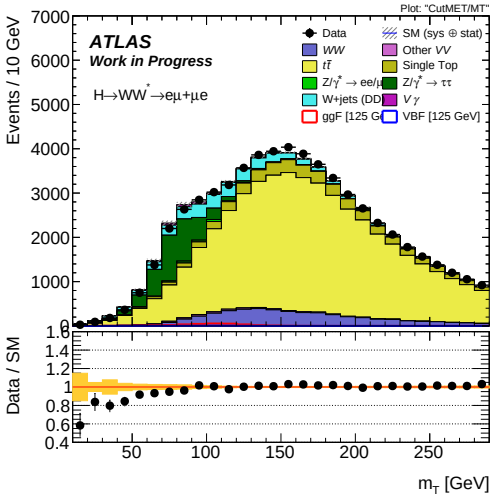

(e) m_T

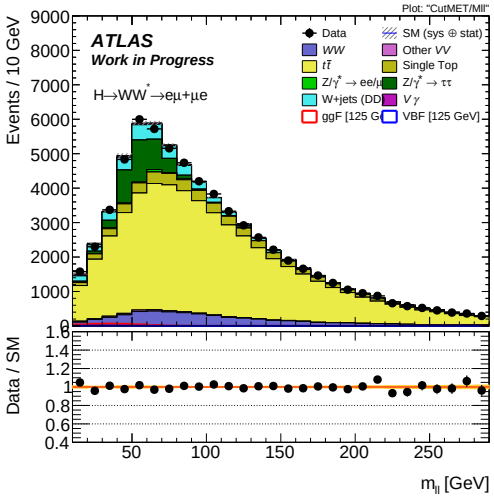

(f) m_{ll}

Figure B.2 *Comparison of data and MC at pre-selection level. Signal and background processes are normalized to predictions. The hatched band in the upper plot, and the shaded band in the ratio plot, give the quadrature sum of statistical and experimental systematic rate uncertainties on the signal and backgrounds.*

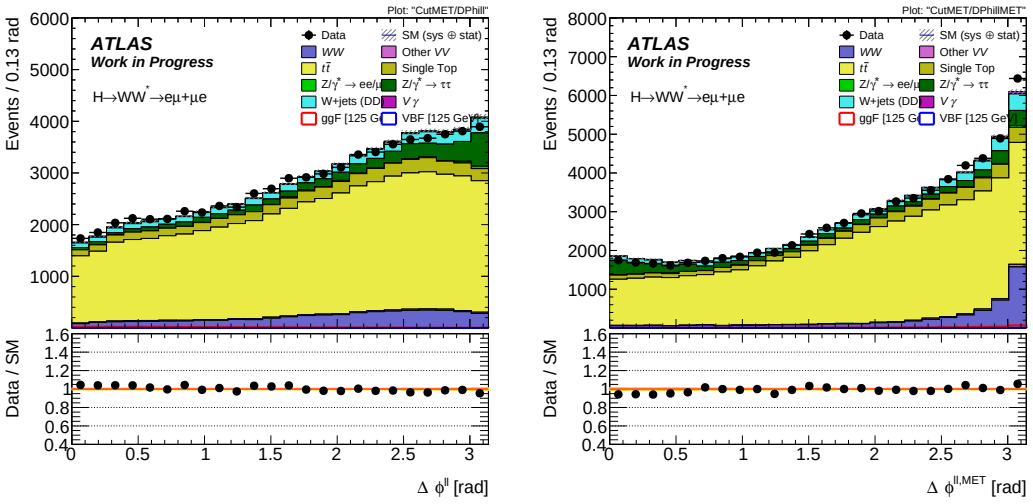

(a) $\Delta\phi_{ll}$ *(b)* $\Delta\phi_{ll,MET}$

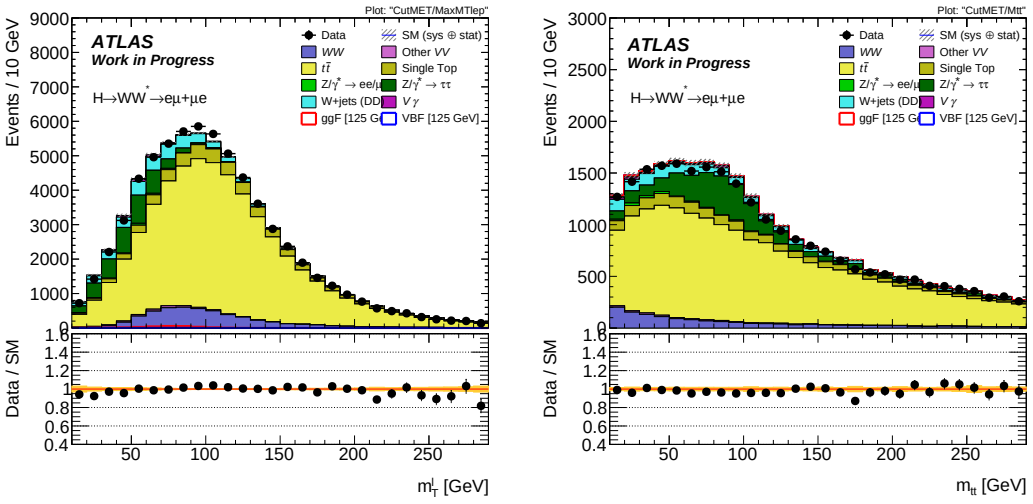

(c) m_T^l *(d)* $m_{\tau\tau}$

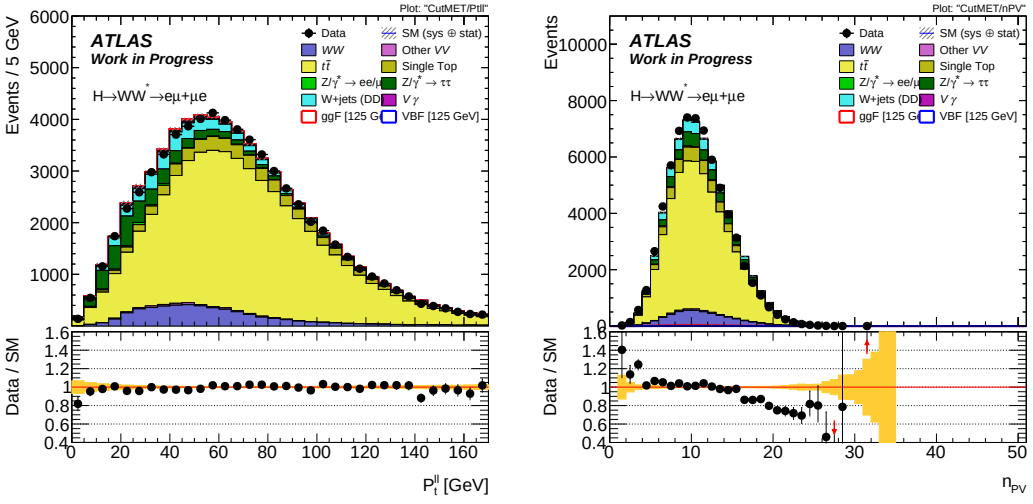

(e) p_T^{ll} *(f)* $n_{\text{primary vertex}}$

Figure B.3 *Comparison of data and MC at pre-selection level. Signal and background processes are normalized to predictions. The hatched band in the upper plot, and the shaded band in the ratio plot, give the quadrature sum of statistical and experimental systematic rate uncertainties on the signal and backgrounds.*

Bibliography

[1] F. Halzen and A. D. Martin, *Quarks and Leptons: An Introductory Course in Modern Particle Physics*. Wiley, 1984.

[2] M. E. Peskin and D. V. Schroeder, *An Introduction to Quantum Field Theory*. Westview Press, 1995.

[3] A. Pich, *The Standard Model of Electroweak Interactions*, arXiv:0705.4264 [hep-ph].

[4] S. Dittmaier and M. Schumacher, *The Higgs Boson in the Standard Model — From LEP to LHC: Expectations, Searches, and Discovery of a Candidate*, arXiv:1211.4828 [hep-ph].

[5] K. Olive et al., *Review of Particle Physics*, Chinese Physics C **38** (2014) 090001.

[6] C. Textbook, *Nuclear and Particle Physics, An Introduction*. 2015.

[7] D. Gross and F. Wilczek, *Asymptotically Free Gauge Theories. 1*, Phys.Rev. D **8** (1973) 3633.

[8] H. Politzer, *Asymptotic Freedom: An Approach to Strong Interactions*, Phys.Rept. **14** (1974) 129.

[9] M. G.-M. H. Fritzsch and H. Leutwyler, *Advantages of the Color Octet Gluon Picture*, Phys.Lett. B **47** (1973) 365.

[10] S. Glashow, *Partial-Symmetries of Weak Interactions*, Nucl.Phys. **22** (1961) 579.

[11] S. Weinberg, *A Model of Leptons*, Phys.Rev.Lett. **19** (1967) 1264.

[12] A. Salam, *Weak and Electromagnetic Interactions*, Conf.Proc. C680519 (1968) 367.

[13] P. W. Higgs, *Broken Symmetries and the Masses of Gauge Bosons*, Phys.Rev.Lett. **13** (1964) 508.

[14] P. W. Higgs, *Spontaneous Symmetry Breakdown without Massless Bosons*, Phys.Rev. **145** (1966) 1156.

[15] F. Englert and R. Brout, *Broken Symmetry and the Mass of Gauge Vector*

Mesons, Phys.Rev.Lett. **13** (1964) 321.

[16] C. H. G. Guralnik and T. Kibble, *Global Conservation Laws and Massless Particles*, Phys.Rev.Lett. **13** (1964) 585.

[17] I. van Vulpen, *The Standard Model Higgs Boson*, Lecture Particle Physics II, 2013.

[18] C. Kolda and H. Murayama, *The Higgs Mass and New Physics Scales in the Minimal Standard Model*, JHEP **0007** (2000) 035.

[19] S. Myers and H. Schopper, *Accelerators and Colliders*. Springer, 2013.

[20] A. D. Martin, W. J. Stirling, R. S. Thorne, and G. Watt, *Parton distributions for the LHC*, Eur. Phys. J. C **63** (2009) 189, `arXiv:0901.0002 [hep-ph]`.

[21] J. W. H. J. M. Campbell and W. J. Stirling, *Hard Interactions of Quarks and Gluons: A Primer for LHC Physics*, Rept. Prog. Phys. **70** (2007) 89.

[22] `https://twiki.cern.ch/twiki/bin/view/LHCPhysics/CrossSections`.

[23] S. Dawson, *Radiative corrections to Higgs boson production*, Nucl.Phys. **B359** (1991) 283–300.

[24] A. Djouadi, M. Spira, and P. M. Zerwas, *Production of Higgs bosons in proton colliders: QCD corrections*, **264** (1991) 440.

[25] M. Spira, A. Djouadi, D. Graudenz, and P. Zerwas, *Higgs boson production at the LHC*, Nucl.Phys. **B453** (1995) 17–82, `arXiv:hep-ph/9504378 [hep-ph]`.

[26] R. V. Harlander and W. B. Kilgore, *Next-to-next-to-leading order Higgs production at hadron colliders*, Phys.Rev.Lett. **88** (2002) 201801, `arXiv:hep-ph/0201206 [hep-ph]`.

[27] C. Anastasiou and K. Melnikov, *Higgs boson production at hadron colliders in NNLO QCD*, Nucl.Phys. **B646** (2002) 220–256, `arXiv:hep-ph/0207004 [hep-ph]`.

[28] V. Ravindran, J. Smith, and W. L. van Neerven, *NNLO corrections to the total cross-section for Higgs boson production in hadron hadron collisions*, Nucl.Phys. **B665** (2003) 325–366, `arXiv:hep-ph/0302135 [hep-ph]`.

[29] M. Ciccolini, A. Denner, and S. Dittmaier, *Strong and electroweak corrections to the production of Higgs+2 jets via weak interactions at the LHC*, Phys. Rev. Lett. **99** (2007) 161803, `arXiv:0707.0381 [hep-ph]`.

[30] P. Nason and C. Oleari, *NLO Higgs boson production via vector-boson fusion matched with shower in POWHEG*, JHEP **1002** (2010) 037, `arXiv:0911.5299 [hep-ph]`.

[31] P. Bolzoni, F. Maltoni, S.-O. Moch, and M. Zaro, *Higgs production via vector-boson fusion at NNLO in QCD*, Phys.Rev.Lett. **105** (2010) 011801, `arXiv:1003.4451 [hep-ph]`.

[32] T. Han and S. Willenbrock, *QCD correction to the $pp \to WH$ and ZH total cross-sections*, Phys.Lett. **B273** (1991) 167–172.

[33] O. Brein, A. Djouadi, and R. Harlander, *NNLO QCD corrections to the*

Higgs-strahlung processes at hadron colliders, Phys.Lett. **B579** (2004) 149–156, arXiv:hep-ph/0307206 [hep-ph].

[34] M. L. Ciccolini, S. Dittmaier, and M. Krämer, *Electroweak radiative corrections to associated WH and ZH production at hadron colliders*, Phys. Rev. D **68** (2003) 073003, arXiv:hep-ph/0306234.

[35] W. Beenakker et al., *NLO QCD corrections to t anti-t H production in hadron collisions.* , Nucl. Phys. B **653** (2003) 151–203, arXiv:hep-ph/0211352.

[36] S. Dawson, L. H. Orr, L. Reina, and D. Wackeroth, *NLO QCD predictions for associated t anti-t h production in hadronic collisions*, Nucl. Phys. Proc. Suppl. **116** (2003) 207, arXiv:hep-ph/0211373.

[37] S. Dawson, C. Jackson, L. H. Orr, L. Reina, and D. Wackeroth, *Associated Higgs production with top quarks at the Large Hadron Collider: NLO QCD corrections*, Phys. Rev. D **68** (2003) 034022, arXiv:hep-ph/0305087.

[38] http://public.web.cern.ch/public/en/research/.

[39] https://timeline.web.cern.ch/timelines/The-Large-Hadron-Collider.

[40] https://home.cern/about/updates/.

[41] ATLAS Collaboration, *The ATLAS Experiment at the CERN Large Hadron Collider*, JINST **3** (2008) S08003.

[42] ATLAS Collaboration, *ATLAS : technical proposal for a general-purpose pp experiment at the Large Hadron Collider at CERN*. 1994. CERN-LHCC-94-43.

[43] ATLAS Collaboration, *Expected Performance of the ATLAS Experiment − Detector, Trigger and Physics*. 2008. arXiv:0901.0512.

[44] M. D. Matthias Schott, *Review of single vector boson production in pp collisions at $\sqrt{s} = 7$ TeV*, Eur.Phys.J. C **74** (2014) 2916.

[45] B. Aubert et al., *Performance of the ATLAS electromagnetic calorimeter end-cap module 0*, Nucl. Instrum. Meth. A **500** (2003) 178.

[46] E. Abat et al., *Combined performance studies for electrons at the 2004 ATLAS combined test-beam*, JINST **5** (2010) P11006.

[47] W. Buttinger, *The ATLAS Level-1 Trigger System*, Journal of Physics: Conference Series **3 96** (2012) 012010.

[48] V. Cindro et al., *The ATLAS beam conditions monitor*, JINST **3** (2008) P02004.

[49] ATLAS Collaboration, *Concepts, Design and Implementation of the ATLAS New Tracking (NEWT)*, Tech. Rep. ATL-SOFT-PUB-2007-007, 2007.

[50] ATLAS Collaboration, *Performance of the ATLAS Inner Detector Track and Vertex Reconstruction in the High Pile-Up LHC Environment*, Tech. Rep. ATLAS-CONF-2012-042, 2012.

[51] ATLAS Collaboration, *Performance of primary vertex reconstruction in proton-proton collisions at $\sqrt{s} = 7$ TeV in the ATLAS experiment*, Tech. Rep. ATLAS-CONF-2010-069, 2010.

[52] W. W. R. Frühwirth and P. Vanlaer, *Adaptive vertex fitting*, J. Phys. G **34**

(2007) N343.

[53] ATLAS Collaboration, *Expected electron performance in the ATLAS experiment*, Tech. Rep. ATL-PHYS-PUB-2011-006, 2011.

[54] ATLAS Collaboration, *Electron identification efficiency measured with $Z \to ee$ events using 2016 data*, Tech. Rep. ATL-COM-PHYS-2016-1046, 2016.

[55] H. H. W. M. Hance and D. Olivito, *Performance Studies of e/gamma Calorimeter Isolation*, Tech. Rep. ATL-COM-PHYS-2011-1186, 2011.

[56] ATLAS Collaboration, *Electron shower shapes, tracking, isolation and invariant mass distributions from $Z \to ee$ and $J/\psi \to ee$ events*, Tech. Rep. ATL-COM-PHYS-2015-728, 2015.

[57] ATLAS Collaboration, *Muon reconstruction efficiency in reprocessed 2010 LHC proton-proton collision data recorded with the ATLAS detector*, Tech. Rep. ATL-CONF-2011-063, 2011.

[58] ATLAS Collaboration, *Muon reconstruction performance of the ATLAS detector in protonproton collision data at $\sqrt{s} = 13$ TeV*, Eur.Phys.J. C **76** (2016) 292.

[59] M. Cacciari and G. P. Salam, *The anti-kt jet clustering algorithm*, JHEP **0804** (2008) 063.

[60] ATLAS Collaboration, *Jet energy measurement with the ATLAS detector in proton-proton collisions at $\sqrt{s} = 7$ TeV*, tech. rep., 2013.

[61] G. Corcella et al., *HERWIG 6: An event generator for hadron emission reactions with interfering gluons (including super-symmetric processes)*, JHEP **0101** (2001) 010.

[62] ATLAS Collaboration, *Data-Quality Requirements and Event Cleaning for Jets and Missing Transverse Energy Reconstruction with the ATLAS Detector in Proton-Proton Collisions at a Center-of-Mass Energy of $\sqrt{s} = 7$ TeV*, Tech. Rep. ATLAS-CONF-2010-038, 2010.

[63] ATLAS Collaboration, *Performance of the ATLAS Secondary Vertex b-tagging Algorithm in 7 TeV Collision Data*, Tech. Rep. ATLAS-CONF-2010-042, 2010.

[64] ATLAS Collaboration, *Performance of b-Jet Identification in the ATLAS Experiment*, . arXiv:1512.01094v2 [hep-ex].

[65] ATLAS Collaboration, *Measurement of the b-tag Efficiency in a Sample of Jets Containing Muons with 5 fb^{-1} of Data from the ATLAS Detector*, Tech. Rep. ATLAS-CONF-2012-043, 2012.

[66] ATLAS Collaboration, *Measurement of the Mistag Rate of b-tagging algorithms with 5 fb^{-1} of Data Collected by the ATLAS Detector*, Tech. Rep. ATLAS-CONF-2012-040, 2012.

[67] ATLAS Collaboration, *Performance of missing transverse momentum reconstruction with the ATLAS detector in the first proton-proton collisions at $\sqrt{s} = 13$ TeV*, Tech. Rep. ATL-PHYS-PUB-2015-027, 2015.

[68] B. G. A. J. Barr and C. G. Lester, *Measuring the Higgs boson mass in*

dileptonic W-boson decays at hadron colliders, JHEP **0907** (2009) 072.

[69] `https://twiki.cern.ch/twiki/bin/view/AtlasPublic/LuminosityPublicResults`.

[70] A. Bredenstein, A. Denner, S. Dittmaier, and M. Weber, *Precise predictions for the Higgs-boson decay $H \to WW/ZZ \to 4$ leptons*, Phys.Rev. **D74** (2006) 013004, `arXiv:hep-ph/0604011 [hep-ph]`.

[71] A. Bredenstein, A. Denner, S. Dittmaier, and M. Weber, *Radiative corrections to the semileptonic and hadronic Higgs-boson decays $H \to WW/ZZ \to 4$ fermions*, JHEP **0702** (2007) 080, `arXiv:hep-ph/0611234`.

[72] A. Djouadi, J. Kalinowski, and M. Spira, *HDECAY: A program for Higgs boson decays in the Standard Model and its supersymmetric extension*, Comput. Phys. Commun. **108** (1998) 56, `arXiv:hep-ph/9704448`.

[73] ATLAS Collaboration, *Measurements of the properties of the Higgs-like boson in the $WW^{(*)} \to l\nu l\nu$ decay channel with the ATLAS detector using 25 fb^{-1} of proton-proton collision data*, Tech. Rep. ATLAS-CONF-2013-030, 2013.

[74] S. Alioli, P. Nason, C. Oleari, and E. Re, *NLO Higgs boson production via gluon fusion matched with shower in POWHEG*, JHEP **0904** (2009) 002, `arXiv:0812.0578 [hep-ph]`.

[75] T. Sjöstrand, S. Mrenna, and P. Z. Skands, *A brief introduction to PYTHIA 8.1*, Computer Physics Communications **178** (2008) no. 11, 852–867.

[76] T. Binoth, M. Ciccolini, N. Kauer and M. Krämer, *Gluon-induced W-boson pair production at the LHC*, JHEP **0612** (2006) 046, `arXiv:hep-ph/0611170`.

[77] S. Frixione and B. R. Webber, *Matching NLO QCD computations and parton shower simulations*, JHEP **0206** (2002) 029, `arXiv:hep-ph/0204244`.

[78] B. P. Kersevan and E. Richter-Was, *The Monte Carlo event generator AcerMC version 2.0 with interfaces to PYTHIA 6.2 and HERWIG 6.5*, TPJU-6/2004, 2004. `arXiv:hep-ph/0405247`.

[79] T. Sjostrand, S. Mrenna, and P. Z. Skands, *PYTHIA 6.4 physics and manual*, JHEP **0605** (2006) 026, `arXiv:hep-ph/0603175`.

[80] M. L. Mangano et al., *ALPGEN, a generator for hard multi-parton processes in hadronic collisions*, JHEP **0307** (2003) 001, `arXiv:hep-ph/0206293`.

[81] J. Alwall et al., *MadGraph/MadEvent v4: The new web generation*, JHEP **0709** (2007) 028, `arXiv:0706.2334 [hep-ph]`.

[82] J. Alwall, M. Herquet, F. Maltoni, O. Mattelaer, and T. Stelzer, *MadGraph 5 : going beyond*, JHEP **1106** (2011) 128, `arXiv:1106.0522 [hep-ph]`.

[83] R. C. Gray, C. Kilic, M. Park, S. Somalwar, and S. Thomas, *Backgrounds to Higgs boson searches from $W\gamma^* \to l\nu l(l)$ asymmetric internal conversion*, (2011) , `arXiv:1110.1368 [hep-ph]`.

[84] A. Djouadi, M. Spira, and P. Zerwas, *Production of Higgs bosons in proton colliders: QCD corrections*, Phys.Lett. **B264** (1991) 440–446.

[85] R. Harlander and W. B. Kilgore, *Next-to-next-to-leading order Higgs production at hadron colliders*, Phys. Rev. Lett. **88** (2002) 201801, arXiv:hep-ph/0201206.

[86] U. Aglietti, R. Bonciani, G. Degrassi, and A. Vicini, *Two loop light fermion contribution to Higgs production and decays*, Phys.Lett. **B595** (2004) 432–441, arXiv:hep-ph/0404071 [hep-ph].

[87] S. Actis, G. Passarino, C. Sturm, and S. Uccirati, *NLO electroweak corrections to Higgs boson production at hadron colliders*, **670** (2008) 12, arXiv:0809.1301 [hep-ph].

[88] S. Catani, D. de Florian, M. Grazzini, and P. Nason, *Soft-gluon re-summation for Higgs boson production at hadron colliders*, JHEP **0307** (2003) 028, arXiv:hep-ph/0306211.

[89] C. Anastasiou, S. Buehler, F. Herzog, and A. Lazopoulos, *Inclusive Higgs boson cross-section for the LHC at 8 TeV*, JHEP **1204** (2012) 004, arXiv:1202.3638 [hep-ph].

[90] D. de Florian and M. Grazzini, *Higgs production at the LHC: updated cross sections at* $\sqrt{s} = 8$ *TeV*, (2012) , arXiv:1206.4133 [hep-ph].

[91] J. Baglio and A. Djouadi, *Higgs production at the LHC*, JHEP **1103** (2011) 055, arXiv:1012.0530 [hep-ph].

[92] M. Ciccolini, A. Denner, and S. Dittmaier, *Electroweak and QCD corrections to Higgs production via vector-boson fusion at the LHC*, Phys. Rev. D **77** (2008) 013002, arXiv:0710.4749 [hep-ph].

[93] K. Arnold et al., *VBFNLO: A parton level Monte Carlo for processes with electroweak bosons*, Comput. Phys. Commun. **180** (2009) 1661, arXiv:0811.4559 [hep-ph].

[94] J. M. Butterworth, J. R. Forshaw, and M. H. Seymour, *Multiparton interactions in photoproduction at HERA*, Z. Phys. **C72** (1996) 637, arXiv:hep-ph/9601371.

[95] J. Alwall et al., *Comparative study of various algorithms for the merging of parton showers and matrix elements in hadronic collisions*, Eur. Phys. J. C **53** (2008) 473, arXiv:0706.2569 [hep-ph].

[96] T. Gleisberg et al., *Event generation with SHERPA 1.1*, JHEP **0902** (2009) 007, arXiv:0811.4622 [hep-ph].

[97] J. M. Campbell and R. K. Ellis, *An update on vector boson pair production at hadron colliders*, Phys. Rev. D **60** (1999) 113006, arXiv:hep-ph/9905386.

[98] H.-L. Lai et al., *New parton distributions for collider physics*, Phys. Rev. D **82** (2010) 074024, arXiv:1007.2241 [hep-ph].

[99] P. M. Nadolsky et al., *Implications of CTEQ global analysis for collider observables*, Phys. Rev. D **78** (2008) 013004, arXiv:0802.0007 [hep-ph].

[100] S. Agostinelli et al., *GEANT 4, a simulation toolkit*, Nucl. Instrum. Meth.

A506 (2003) 250.

[101] ATLAS Collaboration, *Muon reconstruction efficiency in reprocessed 2010 LHC proton-proton collision data recorded with the ATLAS detector*, ATLAS-CONF-2011-063 (2011) . https://cdsweb.cern.ch/record/1345743.

[102] M. Cacciari, G. P. Salam, and G. Soyez, *The anti-k_t jet clustering algorithm*, JHEP **0804** (2008) 063, arXiv:0802.1189 [hep-ex].

[103] ATLAS Collaboration, *Update of the $H \to WW^{(*)} \to e\nu\mu\nu$ analysis with 13 fb^{-1} of $\sqrt{s} = 8$ data collected with the ATLAS Detector*, ATLAS-CONF-2012-158, 2012. https://cdsweb.cern.ch/record/1493601.

[104] ATLAS Collaboration, *Observation and measurement of Higgs boson decays to WW^* with the ATLAS detector*, tech. rep., 2015.

[105] ATLAS Collaboration, *Commissioning of the ATLAS high-performance b-tagging algorithms in the 7 TeV collision data*, ATLAS-CONF-2011-102 (2011) . https://cdsweb.cern.ch/record/1369219.

[106] R.K. Ellis et al., *Higgs decay to $\tau^+\tau^-$: A possible signature of intermediate mass Higgs bosons at the SSC*, Nucl. Phys. B **297** (1988) 221.

[107] ATLAS Collaboration, *Observation of an excess of events in the search for the Standard Model Higgs boson in the $H \to WW^{(*)} \to \ell\nu\ell\nu$ channel with the ATLAS detector*, ATLAS-CONF-2012-098, 2012. https://cdsweb.cern.ch/record/1462530.

[108] LHC Higgs Cross Section Working Group, S. Dittmaier, C. Mariotti, G. Passarino, and R. Tanaka (Eds.), *Handbook of LHC Higgs Cross Sections: 1. Inclusive Observables*, CERN-2011-002 (CERN, Geneva, 2011) , arXiv:1101.0593 [hep-ph].

[109] LHC Higgs Cross Section Working Group, S. Dittmaier, C. Mariotti, G. Passarino, and R. Tanaka (Eds.), *Handbook of LHC Higgs Cross Sections: 2. Differential Distributions*, CERN-2012-002 (CERN, Geneva, 2012) , arXiv:1201.3084 [hep-ph].

[110] J. Butterworth et al., *Les Houches 2013: Physics at TeV Colliders: Standard Model Working Group Report*, arXiv:1405.1067 [hep-ph].

[111] ATLAS Collaboration, *Measurement of the b-tag efficiency in a sample of jets containing muons with 5 fb^{-1} of data from the ATLAS detector*, ATLAS-CONF-2012-043 (2012) . https://cdsweb.cern.ch/record/1435197.

[112] ATLAS Collaboration, *Improved luminosity determination in pp collisions at $\sqrt{s} = 7$ TeV using the ATLAS detector at the LHC*, arXiv:1302.4393 [hep-ex].

[113] L. H. C. S. W. Group, *Handbook of LHC Higgs Cross Sections: 3. Higgs Properties*, arXiv:1307.1347 [hep-ph].

[114] A.L. Read, *Presentation of search results: the CL_s technique*, J. Phys. G **28** (2002) 2693.

[115] ATLAS Collaboration, *Update of the $H \to WW^{(*)} \to \ell\nu\ell\nu$ Analysis with 21 fb^{-1} of $\sqrt{s}$ = 8 TeV Data Collected with the ATLAS Detector*, ATL-COM-PHYS-2013-158 .

[116] F. James, M. Winkler, *Minuit User's Guide*, 2004.

[117] `https://twiki.cern.ch/twiki/bin/view/AtlasPublic/LuminosityPublicResultsRun2`.

[118] P. M. Nadolsky, *Implications of CTEQ global analysis for collider observables*, Phys. Rev. D **78** (2008) 013004, `arXiv:0802.0007 [hep-ph]`.

[119] ATLAS Collaboration, G. Aad et al., *Measurement of the Z/γ^* boson transverse momentum distribution in pp collisions at $\sqrt{s}$ = 7 TeV with the ATLAS detector*, JHEP **09** (2014) 145, `arXiv:1406.3660 [hep-ex]`.

[120] *ATLAS Run 1 Pythia8 tunes*, Tech. Rep. ATL-PHYS-PUB-2014-021, CERN, Geneva, Nov, 2014. `https://cds.cern.ch/record/1966419`.

[121] T. Gehrmann, M. Grazzini, S. Kallweit, P. Maierhfer, A. von Manteuffel, S. Pozzorini, D. Rathlev, and L. Tancredi, *W^+W^- Production at Hadron Colliders in Next to Next to Leading Order QCD*, Phys. Rev. Lett. **113** (2014) no. 21, 212001, `arXiv:1408.5243 [hep-ph]`.

[122] P. Z. Skands, *Tuning Monte Carlo Generators: The Perugia Tunes*, Phys. Rev. **D82** (2010) 074018, `arXiv:1005.3457 [hep-ph]`.

[123] D. J. Lange, *The EvtGen particle decay simulation package*, Nucl. Instrum. Meth. **A462** (2001) 152–155.

[124] M. Czakon and A. Mitov, *Top++: A Program for the Calculation of the Top-Pair Cross-Section at Hadron Colliders*, Comput. Phys. Commun. **185** (2014) 2930, `arXiv:1112.5675 [hep-ph]`.

[125] *Electron identification measurements in ATLAS using $\sqrt{s}$ = 13 TeV data with 50 ns bunch spacing*, Tech. Rep. ATL-PHYS-PUB-2015-041, CERN, Geneva, Sep, 2015. `https://cds.cern.ch/record/2048202`.

[126] ATLAS Collaboration, *Tagging and suppression of pileup jets*, . `https://cds.cern.ch/record/1700870`.

[127] ATLAS Collaboration, G. Aad et al., *Performance of b-Jet Identification in the ATLAS Experiment*, `arXiv:1512.01094 [hep-ex]`.

[128] ATLAS Collaboration, *2015 start-up trigger menu and initial performance assessment of the ATLAS trigger using Run-2 data*, Tech. Rep. ATL-DAQ-PUB-2016-001, 2016.

[129] I. Stewart and F. Tackmann, *Theory uncertainties for Higgs mass and other searches using jet bins*, Phys. Rev. D **85** (2012) 034011, `arXiv:1107.2117 [hep-ph]`.

[130] ATLAS Collaboration, *Muon reconstruction performance in early 13 TeV data*, Tech. Rep. ATL-PHYS-PUB-2015-037, 2015.

[131] *Jet Calibration and Systematic Uncertainties for Jets Reconstructed in the*

ATLAS Detector at $\sqrt{s} = 13$ *TeV*, Tech. Rep. ATL-PHYS-PUB-2015-015, CERN, Geneva, Jul, 2015. http://cds.cern.ch/record/2037613.

[132] *Optimisation of the ATLAS b-tagging performance for the 2016 LHC Run*, Tech. Rep. ATL-PHYS-PUB-2016-012, CERN, Geneva, Jun, 2016. http://cds.cern.ch/record/2160731.

[133] CMS Collaboration, *First results on Higgs to WW at* $\sqrt{s}$*=13 TeV*, CMS-PAS-HIG-15-003 (2016) .

[134] ATLAS and CMS Collaborations, *Combined Measurement of the Higgs Boson Mass in pp Collisions at* $\sqrt{s}$*=7 and 8 TeV with the ATLAS and CMS Experiments*, Phys. Rev. Lett. **114** (2015) 191803.

Acknowledgements

I would like to take the opportunity to thank those people that I had the chance to work with during the time of my PhD program.

First of all I would like to thank Prof.Dr. Karl Jakobs for giving me the opportunity to come to Freiburg and work in such a wonderful group. I am grateful for his help and support through all the years of my PhD program.

I would like to thank Dr. Ralf Bernhard for introducing me the very first step to particle physics area, and sharing his experience on the Higgs analysis. Im very thankful to Dr. Vu Anh Tuan for his guidance and fruitful discussions in W + jets background estimation. I am also deeply thankful to Dr. Karsten Köneke for taking care of me during the last part of my PhD and for proofreading my thesis.

A special thank to Carsten Burgard, Valerio Dao, Ralf Gugel, Evelyn Schmidt and Andreas Walz for all your help, assistance with technical problems of HWW framework and cooperation on the Higgs analysis. I cannot accomplish my studies without your invaluable support.

During my qualification work on the E_T^{miss} physics validation, I had a lot of help from Daniel Buscher and Dr. Tien Jiang Khoo.

Im thankful to all members of the Freiburg group, for the friendly, constructive and positive atmosphere. I would like to thank Vakhtang Tsiskaridze for cheering me up so many times and for your invaluable chat. Many thanks to my colleagues at CERN, Tatsuya Masubuchi, Keisuke Yoshihara, Doug Schäfer, Olivier Arnaez, Pamela Ferrari, Thomas Maier, Claudia Bertella and Ruchi Gupta for their help with the analysis.

A big thank to Christina Skorek for her kind and support in all administrative matters.

Last but not least I would like to thank my family, my parents, brother, wife and daughter, for the huge support through my experiences. I couldn't have made it without you.